



HAL
open science

Commande d'un bras de chargement de gaz naturel liquéfié en milieu marin

Pierre Besset

► **To cite this version:**

Pierre Besset. Commande d'un bras de chargement de gaz naturel liquéfié en milieu marin. Automatique / Robotique. Ecole nationale supérieure d'arts et métiers - ENSAM, 2017. Français. NNT : 2017ENAM0011 . tel-01596140

HAL Id: tel-01596140

<https://pastel.hal.science/tel-01596140>

Submitted on 27 Sep 2017

HAL is a multi-disciplinary open access archive for the deposit and dissemination of scientific research documents, whether they are published or not. The documents may come from teaching and research institutions in France or abroad, or from public or private research centers.

L'archive ouverte pluridisciplinaire **HAL**, est destinée au dépôt et à la diffusion de documents scientifiques de niveau recherche, publiés ou non, émanant des établissements d'enseignement et de recherche français ou étrangers, des laboratoires publics ou privés.

École doctorale n° 432 : Sciences des Métiers de l'ingénieur

Doctorat ParisTech

THÈSE

pour obtenir le grade de docteur délivré par

l'École Nationale Supérieure d'Arts et Métiers

Spécialité " Automatique "

présentée et soutenue publiquement par

Pierre BESSET

Le 27 avril 2017

**Automatic control of a marine loading arm for offshore LNG
offloading**

-

**Commande d'un bras de chargement de gaz naturel liquéfié en
milieu marin**

Directeur de thèse : **Olivier GIBARU**

Co-encadrement de la thèse : **Richard BEAREE et Adel OLABI**

Jury

M. Gabriel Abba, Professeur, LCFC, ENI de Metz

M. Olivier Brûls, Professeur, LTAS, Université de Liège

Mme Hélène Chanal, Maître de conférences, Institut Pascal, SIGMA Clermont

M. Bruno Siciliano, Professeur, PRISMA, University of Naples Federico II

M. Olivier Gibaru, Professeur, LSIS, Arts et Métier ParisTech - Lille

M. Richard Béarée, Maître de conférences, LSIS, Arts et Métier ParisTech - Lille

M. Adel Olabi, Maître de conférences, LSIS, Arts et Métier ParisTech - Lille

M. Adrien Vannesson, Ingénieur, TechnipFMC

Président

Rapporteur

Rapporteur

Examineur

Examineur

Examineur

Invité

Invité

À mes parents



Remerciements

Cette thèse a été réalisée au centre des Arts et Métiers ParisTech de Lille au sein de l'équipe INSM du Laboratoire des Sciences de l'Information et des systèmes (LSIS), en partenariat avec la société FMC Technologies, devenue TechnipFMC.

En premier lieu je tiens à remercier Gabriel ABBA, professeur à l'ENI de Metz, d'avoir présider le jury lors de ma soutenance de thèse. Je remercie de plus Madame Hélène Chanal et Monsieur Olivier Brûls, respectivement maître de conférence HDR à l'Institut Pascal de Clermont et professeur à l'université de Liège, d'avoir rapporté ma thèse, me permettant ainsi d'améliorer mon travail par leurs commentaires constructifs. Je remercie également Bruno Siciliano, professeur à l'université de Naples Frédéric II, d'avoir pris part à mon jury de thèse.

Je tiens à remercier chaleureusement Olivier Gibaru, professeur aux Arts et Métiers de Lille, qui a dirigé ma thèse en m'assurant d'excellentes conditions de travail et un encadrement de qualité. Je suis sincèrement reconnaissant envers Richard Béaré, maître de conférence HDR aux Arts et Métiers de Lille, qui m'a encadré au quotidien et qui s'est fortement impliqué dans mon projet. Sa motivation envers mes travaux, ses conseils scientifiques et son soutien moral m'ont permis d'aller au bout de ce projet de doctorat dans les meilleures conditions. Je remercie chaudement Adel Olabi, maître de conférence aux Arts et Métiers de Lille, pour son encadrement, et plus particulièrement pour son aide avec la partie étalonnage, aussi bien théorique qu'expérimentale. Olivier Thomas, professeur aux Arts et Métiers de Lille, m'a apporté un grand appui scientifique concernant la mécanique vibratoire, l'organisation et la mise en place des analyses modales expérimentales. Son aide et son implication m'ont été précieuses et je l'en remercie sincèrement.

L'équipe des ingénieurs de TechnipFMC, m'a réservé un excellent accueil et leur collaboration m'a été indispensable. Pour cela je remercie tout mes collègues du site de Sens m'ayant soutenu dans ce projet. Plus particulièrement, je souhaite exprimer ma reconnaissance envers Adrien Vannesson, pour sa collaboration et sa bonne humeur au quotidien, son excellence technique et son aide avec les bras de chargement et les études expérimentales.

Je suis infiniment reconnaissant envers mes collègues de l'Ecole pour leur bonne humeur, l'excellente ambiance de travail et bien sur leur assistance technique et scientifique dans leurs domaines respectifs. Je ne saurais tous les citer ici,

je tiens cependant à remercier David Busson, Emmanuel Cottanceau, Nadim El Hayek, Julian Freytes, Franck Hernoux, Gil Boye de Sousa, Hussein Zahr, Jorge Palos, Joris Guérin, Tiago dos Santos Moraes , Tian Tian, et bien sur Juliette Morin, qui m'a soutenu et encouragé tout au long de ces trois années de doctorat.

Je remercie enfin mes parents, qui m'ont transmis leur passion pour la science et la technologie et qui m'ont encouragé et soutenu tout au long de mes études.

Contents

General introduction	1
1 Introduction to marine loading arms and automatic connection	5
1.1 Floating Liquefied Natural Gas	6
1.2 Marine loading arms	8
1.2.1 Description	8
1.2.2 Targeting system	11
1.3 Problem Statement	14
1.3.1 Automatic or semi-automatic connection	15
1.3.2 Technical requirements	20
1.4 Presentation of the marine loading arms	21
1.4.1 OLAF scaled model	21
1.4.2 Full scale DCMA	23
1.5 Placement of the project regarding the literature	25
2 Accurate positioning of a loading arm	27
2.1 Measurement systems	27
2.1.1 Candidate solutions	28
2.1.2 Data fusion	31
2.1.3 Proposed solution	31
2.2 Kinematic calibration of serial mechanisms	31
2.2.1 Generic geometric calibration for a serial robot	33
2.2.2 Application to a collaborative robot	36
2.2.3 Application to marine loading arms	46
3 Experimental study of an offshore loading arm	53
3.1 Experimental modal analysis	54
3.2 Experimental study of the joints	61
3.2.1 Step responses of the joints	62
3.2.2 Bandwidth of the joints	64
3.2.3 Oscillation of joint 4	65

CONTENTS

3.2.4	Conclusion and recommendations	67
3.3	Influence of the wind and the sea	68
3.3.1	Influence of the wind	69
3.3.2	Vessels motions simulation	69
3.3.3	Influence of the inertial effects	73
4	Jerk limited time optimal online trajectory generation	82
4.1	Online trajectory generation with jerk limitation	84
4.1.1	Acceleration-limited trajectory generator	88
4.1.2	Adaptation of the initial AL profile for FIR filtering	89
4.1.3	FIR Filtering and jerk patterns	91
4.2	Time-optimal jerk-limited trajectories	92
4.2.1	Jerk-limited full-stop	93
4.2.2	Sign change	94
4.2.3	Adaptation of the AL profiles	95
4.2.4	Filtering	96
4.3	Online constraints change	97
4.4	Time-fixed trajectory: Axis Synchronization	98
4.5	Results	100
4.5.1	Simulation	100
4.5.2	Experimental validation with a 7 axis robot	101
4.5.3	Marine loading arms	103
5	Active motion compensation with delay removal	105
5.1	Predictive planning	109
5.2	Vessel motion prediction	116
5.2.1	Structure of the neural network	117
5.2.2	Training of the neural network	119
5.2.3	Results	120
5.3	Experimental validation	127
5.3.1	Joints controllers synthesis	127
5.3.2	Final tests	131
6	General conclusion and perspectives	141
6.1	Summary of the results	141
6.2	Perspectives	144
	Bibliography	145
	Appendices	152
A	Inverse kinematics of a marine loading arm	153

CONTENTS

B	Résumé en Français	157
B.1	Présentation des bras de chargement et de la connexion automatique	158
B.2	Positionnement précis d'un bras de chargement	164
B.3	Etude expérimentale d'un bras de chargement	166
B.4	Génération de dynamique trajectoires	169
B.5	Compensation active avec annulation du retard	172
	B.5.1 Méthodologie	172
	B.5.2 Validation expérimentale	175
B.6	Conclusion	176

List of Figures

1.1	The Prelude FLNG.	7
1.2	Prelude, Shell's FLNG moored by a LNG carrier. [Credit Shell].	7
1.3	Offshore Loading Arm Footless (OLAF) - Prelude's loading arm.	8
1.4	Prelude's loading arm: OLAF.	9
1.5	Actuation system of the inboard joint.	10
1.6	Coupler.	10
1.7	The current targeting system. This system requires the setup of cables and alignment for every manifold of the LNGC. [Credit: FMC Technologies].	12
1.8	The targeting system requires a cone and a winch on the Style 80 [Credit: FMC Technologies].	12
1.9	The manifold.	13
1.10	Simplified hydraulic diagram of a joint.	13
1.11	Main frames and positions notations.	15
1.12	Initial configuration: the loading arm is in its parking position, in front of the flanging area.	17
1.13	Deployment stage.	18
1.14	Pursuit stage.	19
1.15	Prelude's loading arms.	20
1.16	The OLAF scaled model connected to the manifold.	22
1.17	The scaled manifold on its hexapod.	22
1.18	A full scale marine loading arm is used for the final tests of automatic connection.	24
1.19	3 DoF test bench is fitted with a manifold.	25
2.1	A total station and its reflector.	28
2.2	Total station set-up.	29
2.3	Frames placement for a serial manipulator.	35
2.4	iiwa robot in zero position: Modified DH parameters.	38

LIST OF FIGURES

2.5 Example of the joints model with joint 4. In order to take into account the joints compliance, each joint j is modeled as a spring of stiffness k_j 39

2.6 Examples of robot configurations with high torques for joints 2, 3 and 4. 40

2.7 Picture of the robot during the measurements stage. A spherical reflector associated with the laser tracker is installed on the tip of the robot. 41

2.8 The laser tracker measures accurately the tip position, while the robot goes to all selected configurations. 41

2.9 Samples of the recorded evolution of position and torque in joint 2 while the robot goes through the calibration configurations. The laser tracker waits for both the position and the torque to be steady before measuring. 42

2.10 The base frame R_0 of the robot is built by fitting circles on circular path virtually drawn by the tip of the robot when moving successively joint 1 (blue circle) and joint 2 (pink circle). 42

2.11 Diagram of the implementation of the online geometric and compliance errors correction. 45

2.12 Simplified Jacobian transpose method for solving the inverse geometric problem. The management of the joints bounds is not shown, for the sake of clarity. 45

2.13 MLA in zero position: Modified DH model. 47

2.14 Angles notations Red: robotic convention. Green: actual joints positions 48

2.15 The total station measures the position of the coupler. Picture of the OLAF scaled model. 49

2.16 The reflector of the total station is set up on the coupler. Left picture: full scale DCMA. Right picture: scaled model. 49

2.17 Calibration points. 51

3.1 The laser vibrometer measures the velocity of all measurement points of the mesh. Left and bottom pictures: Head of the laser vibrometer. Right picture: Acquisition and generation system. . . 55

3.2 The structures of the scaled model and the full-scale loading arm are meshed with measurement points. 56

3.3 The excitator excites the structure of the arm via the coupler, and the transmitted force is calculated from the current in the coil. . . 56

3.4 Pictures of the sensors set up at the excitement point. 57

3.5 Set up of the modal analysis for the full scale arm. 57

LIST OF FIGURES

3.6	Temporal evolution of the force input (top graph) and the associate velocity response (bottom graph) at the excitation point of the full scale DCMA. Example of a chirp with a logarithmic evolution of the frequency (red lines).	58
3.7	Experimental frequency response functions of the arms	59
3.8	Setup of the full scale DCMA.	61
3.9	Step responses.	63
3.10	Experimental identification of the steady state gains of joints 1, 2 and 3. One can observe dead zones and offsets. Left graph: OLAF scaled model, zoom on the dead zones. Right graph: full scale DCMA.	64
3.11	Gain Bode diagrams of the actuated joints.	66
3.12	The gain Bode diagrams of the joints (blue lines, full: joint 1, dashed: joint 2, dot-dashed: joint 3) are compared to the average FRF of the structures of the arms (red lines). The measured frequencies of the oscillation of the Style 80 are plotted as the vertical orange lines.	68
3.13	JONSWAP wave power density spectrum for the reference sea state.	70
3.14	Simulation of a vessel motion.	71
3.15	FLNG motion spectra.	72
3.16	The surge spectrum (blue) and the FRFs of the arms structures (red) do not share frequencies. Left graph: OLAF scaled model. Right graph: full scale DCMA.	72
3.17	Diagram of a generic loading arm for dynamic modeling.	74
3.18	Joints torques induced by the FLNG motion. Top graph: total torques. Middle graph: Gravity only. Bottom graph: all inertia effects except gravity.	79
3.19	Joints torques induced by the FLNG motion and joints motions. Top graph: total torques. Bottom graph: torques induced by joints motions only.	80
3.20	Frequency spectra of the joints torques induced by the inertia effects. These frequencies are below the first measured mode of the structure of the arm.	81
4.1	FIR filtering principle for jerk-limited trajectories synthesis.	85
4.2	Proposed online trajectory generation algorithm based on FIR filtering of adapted acceleration-limited profiles.	86
4.3	Examples of trajectories resulting from FIR filtering	87
4.4	A classic acceleration-limited profile.	88
4.5	Principle of initial conditions definition for FIR filtering trajectory	90
4.6	Example of an adaptation: Type II.	91

LIST OF FIGURES

4.7 The initial acceleration-limited trajectory (blue dashed line) is filtered to give a jerk-limited profile (solid red line). 92

4.8 Example of trajectories with different jerk patterns. 92

4.9 Time-optimal jerk-limited profile with non-zero initial conditions, each derivative saturates at its bound. 93

4.10 Examples of full-stop acceleration profiles. 93

4.11 Example of an acceleration profile with a sign change at $t = T_p$ 94

4.12 Example of an adaptation: Type III-b (see Fig. 4.13). To the left: non-adapted profile, $T_d < T_{jd}$. To the right, adapted profile, $T_d = T_{jd}$ and $|d_r| < d_{max}$ 95

4.13 Decision table for the selection of the adaptation of the AL profile. 96

4.14 Decision tree which shows the possible successive adaptations. 96

4.15 Example of a trajectory with a deceleration stage. Dashed blue line: acceleration. Full green line: velocity. The kinematic bounds are lowered at $t = 5.3$ s (vertical full line). A deceleration stage ensures that the velocity respects its new limit. 98

4.16 The approach chosen to deal with joint synchronization is to constrain the value of the jerk j_{max} for the first acceleration stage and the filter length T_{jd} for the second one. 100

4.17 Synchronization of time-optimal trajectories: initial trajectories to the left, synchronized trajectories to the right. 100

4.18 Experimental setup for the validation of the jerk-constrained trajectory generation. 101

4.19 Experimental results for non-synchronized trajectories (only three joints shown). New targets are given on vertical lines. j_{max} is lowered at the vertical full line. Dashed lines: reference acceleration, full lines: actual acceleration. 101

4.20 Experimental results for synchronized trajectories (7 joints). 102

4.21 Setup of the master / slave experiment. 103

4.22 Typical joints responses to AL and JL trajectories. 104

5.1 Simple jerk-limited tracking algorithm for a single joint. 106

5.2 Evolution of the angular references q_{ref} of the three first joints (blue lines) with the target positions q_t (dashed red lines). 108

5.3 Evolution of the position error of the coupler. The maximum simulated error is 1.3 m for the full scale DCMA and 0.25 for the scaled OLAF. The red lines represent the tolerance of the coupling systems. 109

5.4 Predictive control. 111

5.5 The predictive planning sends inputs to the trajectory generator. 112

LIST OF FIGURES

5.6 The predictive planning algorithm uses the jerk-limited trajectory generator as a model. 113

5.7 Predictive planning: simulation results. Evolution of the angular position q of the three first joints (blue lines) with the target positions q_t (dashed red lines). The set-points $u_{k|k}$ generated by the optimization algorithm is plotted by the dot-dashed green lines. . . 114

5.8 Evolution of the coupler position error $X_{err}(t)$ with the predictive planning operating. The red lined represents the tolerance of the coupling systems. 115

5.9 Generic structure of a three-layered feedforward neural network. . 118

5.10 Estimated samples are used as inputs to make multiple step ahead prediction. 119

5.11 Generic diagram for the training of artificial neural networks [MV06].120

5.12 Six one-dimension artificial neural networks are trained for the motion prediction. Each of them follow the structure shown in Figure 5.9. 121

5.13 A single six-dimension artificial neural network is trained for the motion prediction. 122

5.14 Example of heave prediction by the one-dimension ANN. This prediction is only based on the past heave motion (blue samples), and previous predictions (green samples) to predict multiple steps ahead. Bottom graph: prediction error 123

5.15 Study of the evolution of the prediction error regarding the length of the prediction j : Case of the heave prediction by a one-dimension ANN. 124

5.16 Study of the evolution of the prediction error regarding the length of the prediction j : Case of the heave prediction by a six-dimension ANN. 125

5.17 Comparison of the one-dimension ANN and the six-dimension ANN for heave prediction at one time sample. 126

5.18 Diagram of a joint controller. 128

5.19 Typical effect of the dry friction in the joint: the joint "sticks" to its position when its velocity changes of sign. Example of the slewing joint (joint 1) of the OLAF scaled model. 129

5.20 Typical joints responses to jerk-limited trajectories, example of the inboard joints. Left graphs: full scale DCMA, right graphs: OLAF scaled model. 130

5.21 Architecture of the hierarchical framework developed and implemented for the OLAF scaled model and the full scale DCMA. . . 133

LIST OF FIGURES

5.22 Evolution of the joint position q (blue line), controller set-point q_{ref} (orange line) and the reference w (red line). The predictive planning is switched on at $t = 140$ s. Top graph: inboard joint ($q = \alpha$), bottom graph: outboard joint ($q = \beta$). 134

5.23 Evolution of the controller error $q_{ref} - q$ (orange line), planning error $w - q_{ref}$ (red line) and total error $w - q$ (blue line). Top graph: inboard joint ($q = \alpha$), bottom graph: outboard joint ($q = \beta$). The predictive planning is switched on at $t = 140$ s (vertical line). 135

5.24 Evolution of the total error in terms of coupler position $X_{err}(t) = \|\mathbf{X}_c(t) - \mathbf{X}_m(t)\|$. Red line: coupler tolerance. 135

5.25 The OLAF scaled model automatically follows the manifold. 136

5.26 Evolution of the controller error $q_{ref} - q$ (orange line), planning error $w - q_{ref}$ (red line) and total error $w - q$ (blue line). Top graph: inboard joint ($q = \alpha$), bottom graph: outboard joint ($q = \beta$). 138

5.27 Evolution of the calculated total error in terms of coupler position $X_{err}(t) = \|\mathbf{X}_c(t) - \mathbf{X}_m(t)\|$ 138

5.28 The full scale DCMA automatically follows the manifold. 139

5.29 The loading arm moves very closely (<4 cm) to the manifold, to make the flanging possible. 140

5.30 The full scale DCMA is successfully connected to the manifold. 140

Acronyms

AL	Acceleration-Limited.
ANN	Artificial Neural Network.
DCMA	Double Counterweight Marine Arm.
DGPS	Differential Global Positioning System.
DH	Denavit-Hartenberg.
DoF	Degree of Freedom.
FFT	Fast Fourier Transform.
FLNG	Floating LNG facility.
FRF	Frequency Response Function.
IMU	Inertial Measurement Unit.
JL	Jerk-Limited.
LNG	Liquefied Natural Gas.
LNGC	LNG Carrier.

- LPG** Liquefied Petroleum Gas.
- MLA** Marine Loading Arm.
- MPC** Model Predictive Control.
- OLAF** Offshore Loading Arm Footless.

General introduction

A new kind of vessels called Floating Liquefied Natural Gas platforms (FLNGs) is emerging from the industry to exploit offshore gas fields. These giant vessels are able extract, liquefy and store the natural gas onboard. The resulting liquefied natural gas (LNG) is then offloaded to shuttle tankers (LNGCs). Marine loading arms (MLAs) are structures embedding articulated rigid pipes in which the LNG flows at cryogenic temperature to stay liquid. These MLAs are located on the decks of FLNGs vessels, and can connect the manifold of the moored shuttle tankers thanks to a cable based targeting system. This connection operation is conducted manually from a remote control.

This thesis aims to investigate how to turn these loading arms into robotic systems, and give them the ability to connect the manifolds of the tankers automatically. This project, conducted by the designer and manufacturer FMC Technologies, is motivated by the issues raised by the existing targeting system in terms of safety, convenience and performance. To achieve the automatic connection of loading arms, many challenges are to be overcome. First of all any experimental study of a marine loading arm is a challenge by itself. The size, the mass and the power of these systems, which are respectively over 15 meters, 100 tons and 100 kilo Watts, make them extremely difficult to deal with. Then the many and very low vibration modes in the mechanical structures and hydraulic circuits of loading arms make them difficult to control without oscillation. Indeed the accuracy required to make the automatic connection possible is very high regarding the size and the low stiffness of loading arms. Therefore any oscillation or control error is to be prevented. Non-linearities in the hydraulic actuation system of the loading arms is also a difficulty. Another major challenge comes from the asynchronous motion of the FLNG and LNGC due to sea waves and wind, which makes an active motion compensation necessary. In other words, the MLA has to dynamically follow its target with minimum position error. Moreover the low dynamic capabilities of loading arms regarding the relative motion of the vessels in case of harsh sea conditions leads to detrimental pursuit delay in the active compensation. This pursuit delay is also to be prevented. Finally the estimation of the orientation

and the relative position of the vessels is not straightforward. The choice of an adequate monitoring system is made difficult by the environmental and industrial constraints. This thesis dissertation proposes an original approach to overcome these challenges. The development of a technical solution is conducted during this project through theoretical and experiment studies. The final methodology is implemented and successfully tested on real marine loading arms.

Thesis organization

This document is organized as follow.

Chapter 1 presents the economic and industrial context of this study. Offshore loading arms are introduced and their hardware architecture is detailed. Then the objectives of this project are presented. Finally the desired automatic connection procedure is described.

Chapter 2 first investigates appropriate technical solutions to estimate the orientation and relative position of the FLNG and LNGC. Then the methodology of geometric and non-geometric calibration to improve the accuracy of serial mechanisms is discussed. An adaptation to collaborative robots is proposed. Finally loading arms are calibrated.

Chapter 3 is dedicated to the experimental study of offshore loading arms. In particular, modal analyses are conducted on the structures of loading arms, and the behavior and capabilities of their joints is studied. The methodology according to which the motions of the vessels are simulated is presented, and the influence of these motions on the MLAs is investigated.

Chapter 4 details the development of a jerk-limited trajectory generator. This algorithm can to produce smooth trajectories useful to drive robotic systems, including loading arms. This trajectory generator is able to compute time-optimal jerk-limited trajectories with non-zero initial conditions. It is also able to deal with axis synchronization. The implementation of this program is optimized so that its calculation time is very short and it may be used for real-time systems.

Chapter 5 proposes an approach to make the loading arm able to compensate the relative motion of the vessels without time delay. This approach combines classic predictive control with the trajectory generator developed in Chapter 3. This combination results in a so-called predictive planning algorithm which gives

the ability to the loading arm to anticipate the vessels motions. Hence it can perform active compensation without time delay. This predictive planning algorithm requires a prediction of the vessels motions to work. This prediction is achieved by using artificial neural networks. Finally an experimental validation of the whole methodology is conducted.

Thesis contributions

In a general manner this thesis contributes to the field of loading arms and similar systems, as the first academic research study investigating the robotization of MLAs. More specific contributions are present, evenly distributed across the chapters of this document.

The results presented in Chapter 2 are mostly specific of the particular design to the loading arms available for this study and their generalization to other systems is not obvious. However, the qualitative discussions and conclusions about frequency considerations, as well as the generic rigid-body dynamic model with its simulation results, contribute to the understanding of their inner working.

The trajectory generator developed during this project differs from the state-of-the-art as it combines all classic features of a time-optimal jerk-limited trajectory generator with a very low computational time and a filter-based methodology straightforward to implement on most industrial systems. Smooth trajectories reduce the oscillation in the structure of the arm, which is calibrated according to methods from industrial robotic. As a result the position errors of the end-effector of the system is greatly reduced.

Then, the modification of the classic model predictive control methodology, where the model is replaced by a trajectory generator with kinematic limits, prevents one from modeling all joints. It also ensures that the planned trajectories are respected by the system and that these trajectories take advantage of the full capabilities of the system, given the low-level controllers.

The vessels motion predictor used to supply the predictive planning algorithm improves existing vessel motion prediction methods, by taking advantage of the coupling effects of the vessels motion without any hydromechanic model.

Finally this project presents the first automatic connection of an offshore marine loading arm, hence fulfilling the objectives of the project.

Thesis publications

Conference publications

- P. Besset, R. Béarée and O. Gibaru, "FIR Filter-Based Online Jerk-Controlled Trajectory Generation", in *IEEE International Conference on Industrial Technology (ICIT 2016)*, Taipei 2016.
- P. Besset, A. Olabi and O. Gibaru, "Advanced calibration applied to a collaborative robot", in *IEEE International Power Electronics and Motion Control Conference (PEMC 2016)*, Varna 2016.

Journal publications

Submitted:

- P. Besset and R. Béarée, "FIR filter-based online jerk-constrained trajectory generation", in *Control Engineering Practice*.

Patents

Submitted:

- P. Besset and A. Vannesson, "Dispositif de commande de déplacement, procédé et dispositif d'acquisition et de calcul pour celui-ci, ainsi que bras articulé de chargement de fluide le comportent."

Chapter 1

Introduction to marine loading arms and automatic connection

The global market, and particularly the East-Asian one, will demand a large amount of energy in the next decades to follow the demographic trend, as well as the evolution of the standard of living. As the nowadays oil reservoirs are expected to run low soon, new reservoirs, less economically interesting, will have to be tapped. Another challenging consideration which has to be accounted for in the global energy supply management is the environmental issue. Carbon emissions should be reduced in order to stabilize the global climate [Mar15]. Natural gas is an hydrocarbon gas mixture which essentially consists of methane (CH_4). This gas is extracted and liquefied to be easily transported. Natural gas is present in large amounts in underground fields. Moreover it is the cleanest burning fuel available [LWL13]. For these reasons, natural gas is expected to play a key role in the global economy, and its demand significantly rises in all forecasting scenarios [IEA15]. The current exploitation scheme for offshore gas fields consists of pipelines, that run from the wellheads to onshore facilities built on the coasts. The gas is then treated and liquefied to form LNG (Liquefied Natural Gas), more transportable. However so-called "stranded" offshore gas fields located far from the coasts, or too small, are not economically interesting with the current exploitation scheme. Moreover underwater pipelines raise environmental issues such as corals destruction or disturbance of whales. Many of the largest energy companies are developing as a solution a new generation of vessels, named Floating Liquefied Natural Gas platforms.

1.1 Floating Liquefied Natural Gas

Floating Liquefied Natural Gas platforms (FLNGs) are large vessels designed to make it economically [Mar14] and ecologically possible to exploit stranded gas fields. FLNGs moor above the fields to be exploited and collect the natural gas directly from the underwater wells. The gas is processed, liquefied and stored by on-board facilities. LNG carriers (LNGCs) are tanker vessels that can store and transport large quantities of LNG. Such tankers may moor side-by-side to the FLNG in order to be loaded with LNG. Loading arms set up on the FLNG deck connect to the carrier manifolds and transfer the liquefied gas at cryogenic temperature: -162°C (-260°F). Once loaded, the LNGC leaves and may be replaced by another.

In December 2014 the construction of the hull of the Prelude FLNG started. This FLNG owned by the company Royal Dutch Shell is being built in South Korea by the Technip / Samsung Consortium (TSC). The Prelude FLNG is expected to start operating in 2017 in gas fields at 200 kilometers of the north coasts of Australia, as pictured by Figure 1.1. The planned production rate of Prelude is 5.3 million tonnes per annum of liquids: LNG, condensate and liquefied petroleum gas (LPG). This vessel is 488 meters long and is fitted with seven loading arms of the kind OLAF (Offshore Loading Arm Footless), designed and manufactured by the company FMC Technologies in Sens, France. Figure 1.2 shows the Prelude FLNG moored by a LNG carrier.

Other FLNG projects are currently undergoing in Australia and South East Asia, but that technology is becoming an increasingly viable option in other regions. In particular FLNG are being expected in Latin America, Africa and Middle East.

CHAPTER 1. INTRODUCTION TO MARINE LOADING ARMS AND AUTOMATIC CONNECTION

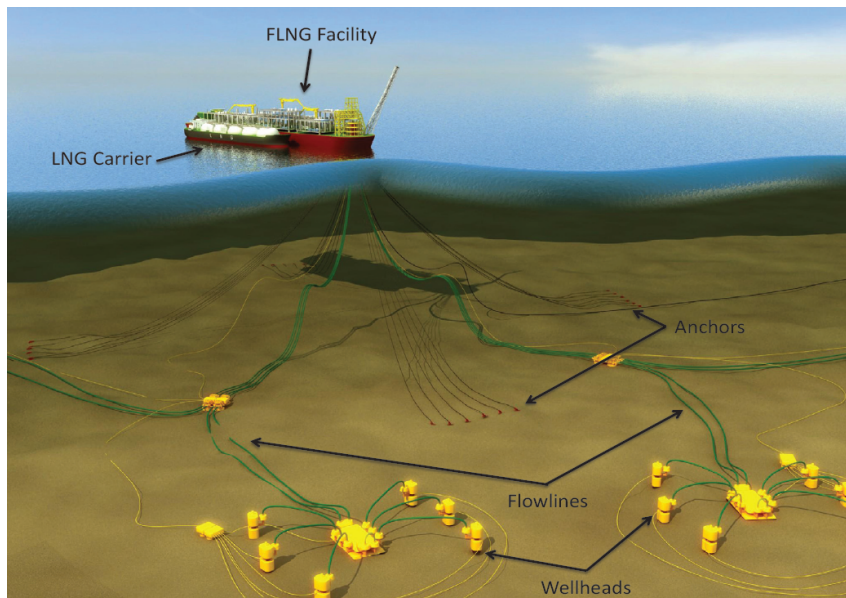


Figure 1.1: The Prelude FLNG will moor above gas field at the north of the Australian coasts.

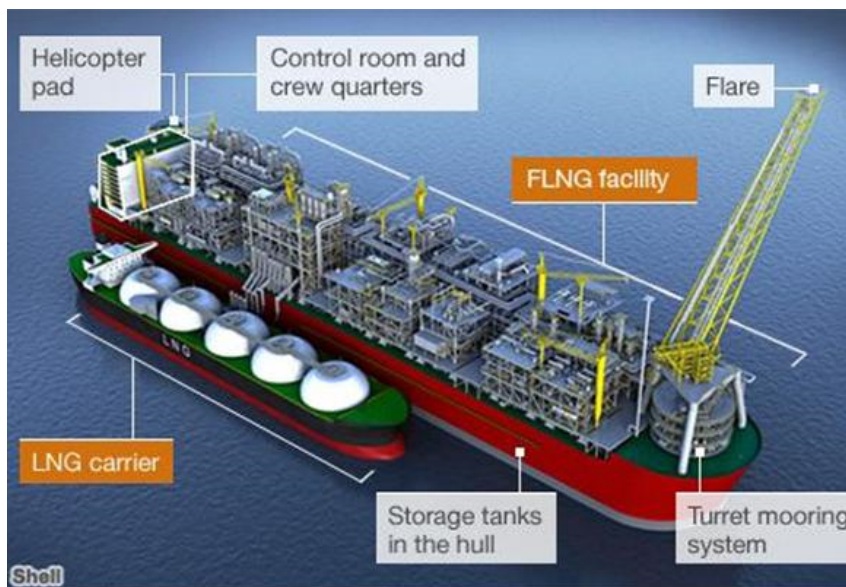


Figure 1.2: Prelude, Shell's FLNG moored by a LNG carrier. [Credit Shell].

1.2 Marine loading arms

Marine loading arms (MLAs) are systems designed to transfer LNG or LPG from one vessel to another. The generic architecture of an MLA consists of an articulated mechanical structure supporting an equally articulated pipe called product line. The product line, in which the LNG flows, ends with a flanging system called coupler. The whole structure is balanced thanks to a double counterweight system which ensures that the arm is statically balanced in any configuration. The actuation system of offshore loading arms is fully hydraulic. Figure 1.3 shows an OLAF on a test bench before its shipment to the Prelude's FLNG.



Figure 1.3: Offshore Loading Arm Footless (OLAF) - Prelude's loading arm.

1.2.1 Description

Figure 1.4 summarizes the hardware design of a generic marine loading arm, with the example of the OLAF.

The foot of the loading arm, also called riser, is fixed on the FLNG deck. The slewing joint, or joint 1, can rotate the complete structure of the arm around the axis z_0 via the link 1. This joint is actuated by a hydraulic cylinder, and its angular position is noted ϕ . The inboard link is actuated by a second rotary joint called

CHAPTER 1. INTRODUCTION TO MARINE LOADING ARMS AND AUTOMATIC CONNECTION

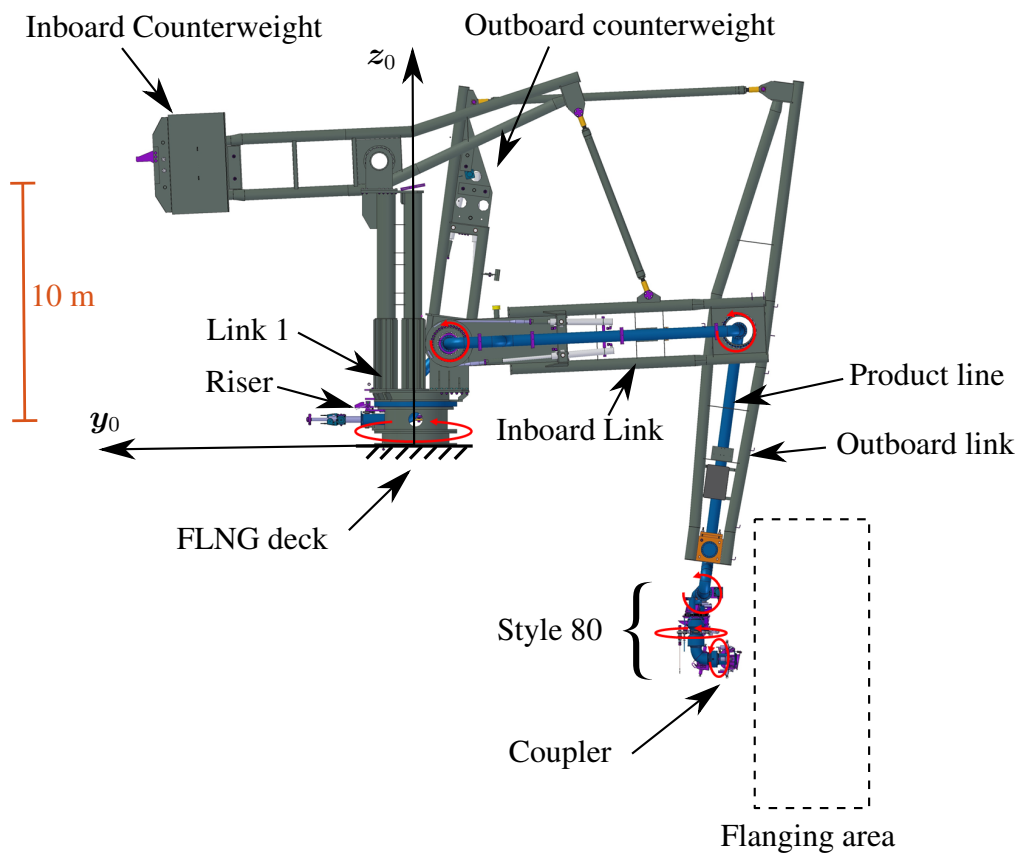


Figure 1.4: Prelude's loading arm: OLAF.

inboard joint, or joint 2. This joint is driven by two cylinders pulling a cable, as shown on Figure 1.5, and its angular position is noted α . The outboard link is connected to the inboard link by a third rotary joint: the outboard joint or joint 3. This joint is driven by a similar dual cylinder system placed on the outboard counterweight. Its angular position is noted β . It is important to note that, unlike classic robotic joints, the outboard link is not driven relatively to the inboard link, but relatively to the link 1 via the outboard counterweight parallelogram system.

To the end of the outboard link is connected a system called Style 80. The fourth joint, which links the outboard link to the Style 80, is left free, i.e. it does not transmit any torque around its axis, except friction. Therefore the Style 80 is free to oscillate as a pendulum. Its inclination regarding the gravity axis, measured by an inclinometer, is noted θ . The Style 80 consists of the end of the product line, with an actuated fifth joint of position γ and finally the coupler. The coupler is a flanging system designed to clamp on carriers manifolds in order to connect

CHAPTER 1. INTRODUCTION TO MARINE LOADING ARMS AND AUTOMATIC CONNECTION

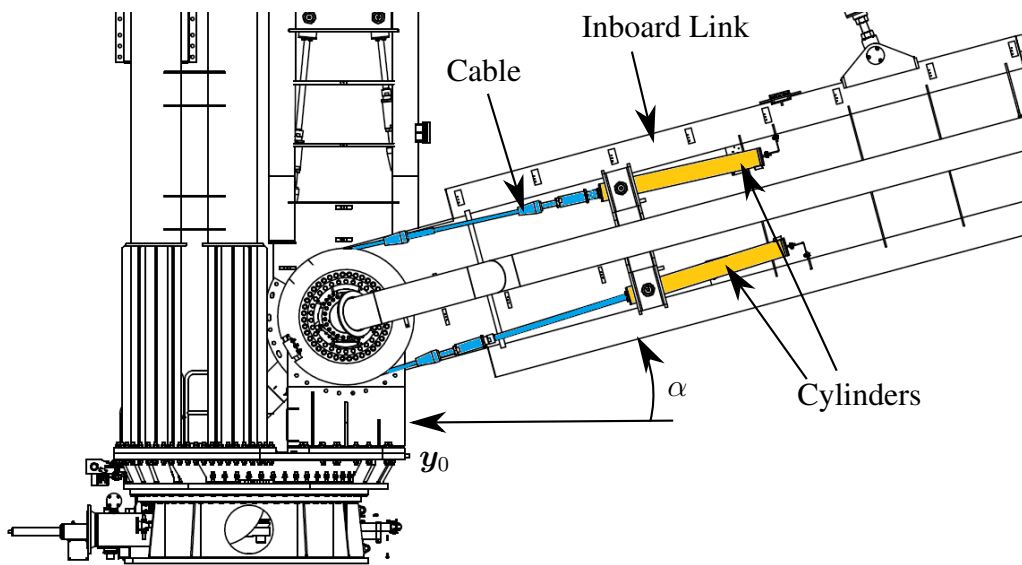


Figure 1.5: Actuation system of the inboard joint.

the MLA product line the the carriers tanks. Figure 1.6 shows a coupler and a Style 80. Table 1.1 summarizes the joints of the system.

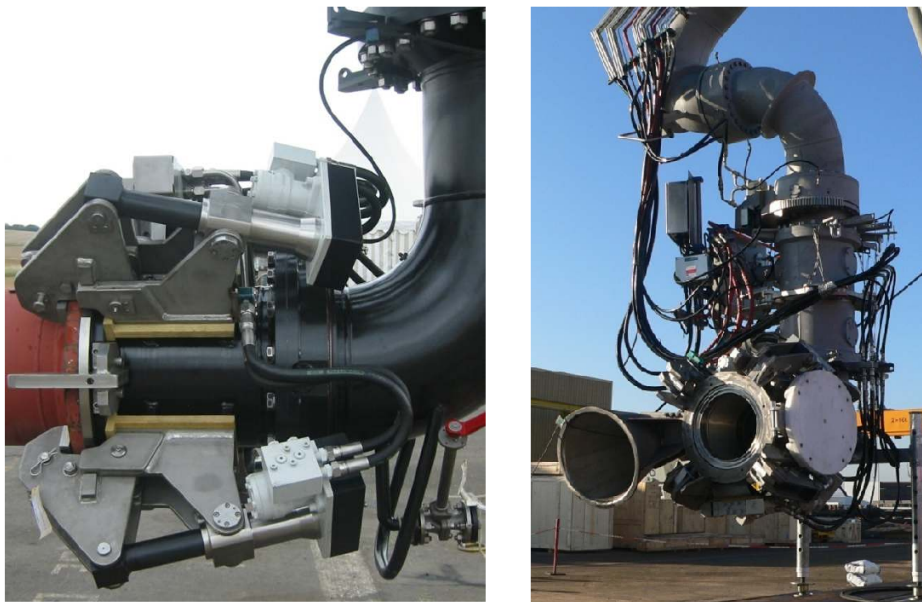


Figure 1.6: Left: the coupler connects the product line (black) to the carrier manifold (red). Right: picture of a Style 80.

Table 1.1: Hardware: joints

Joint	Name	Actuator	Sensor
1	Slewing	hydraulic cylinder	rod position transducer: ϕ
2	Inboard	dual cylinder system	rod position transducer: α
3	Outboard	dual cylinder system	rod position transducer: β
4	/	none	Inclinometer: θ
5	/	Hydraulic motor	none: γ
(6	Coupler rotation	none	none)

An inboard and an outboard counterweight systems are respectively used to balance the inboard and outboard links. In the OLAF architecture, these systems are designed as parallelograms. Finally is associated with the loading arm a flanging area, inside which the client manifold is during the connection.

1.2.2 Targeting system

The targeting system is used to guide the coupler to the LNG manifold. A cable links the MLA riser to the carrier manifold. An hydraulic winch fitted on the Style 80 is used to pull the arm along the cable to the manifold. Accurate positioning of the coupler on the manifold is ensured by male and female alignment cones respectively set up on the manifold and the coupler. Figures 1.7 and 1.8 present the targeting system while Figure 1.9 details a generic carrier manifold.

While the winch pulls the loading arm along the cable, the hydraulic system is set in freewheel mode. This mode makes the cylinders compliant so that the arm can move according to the external forces applied on the coupler. In this mode the cylinders are used as dampers. The system is kept in freewheel mode while the arm is connected to the tanker. Hence the arm can comply to the relative motion between the FLNG and the LNGC. When disconnecting, the winch pulls the arm backward along the cable. The "selected mode", for which the cylinders are used as actuators driven by proportional spool valves, is only used to move the arm when the cable is set up and removed. In the latter mode, the loading arm is manually driven by an operator, via a control deck or a remote control. Figure 1.10 presents a simplified hydraulic diagram of a joint.

CHAPTER 1. INTRODUCTION TO MARINE LOADING ARMS AND AUTOMATIC CONNECTION

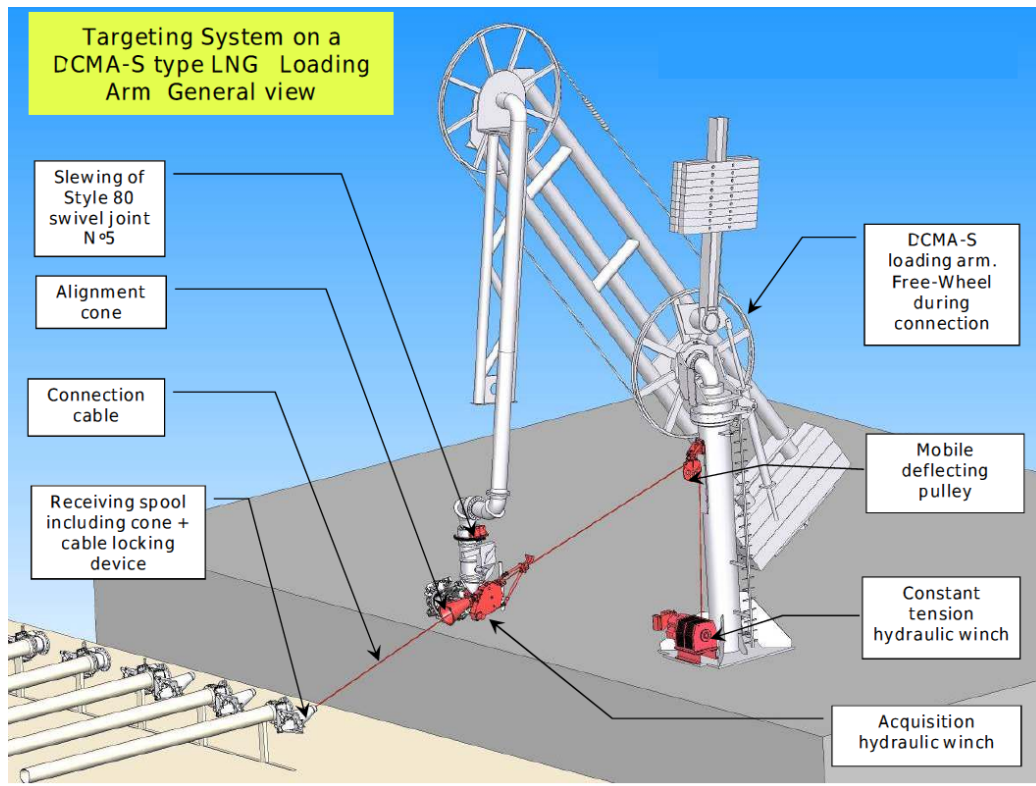


Figure 1.7: The current targeting system. This system requires the setup of cables and alignment for every manifold of the LNGC. [Credit: FMC Technologies].

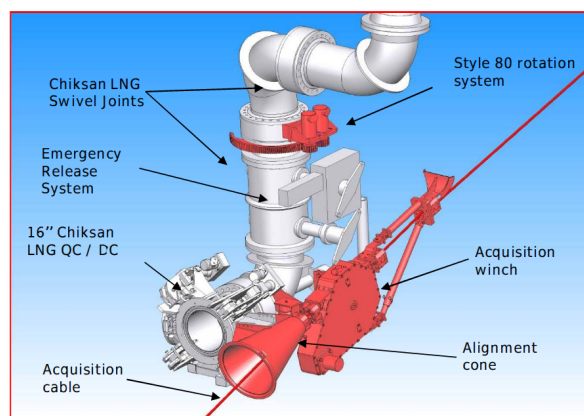


Figure 1.8: The targeting system requires a cone and a winch on the Style 80 [Credit: FMC Technologies].

CHAPTER 1. INTRODUCTION TO MARINE LOADING ARMS AND AUTOMATIC CONNECTION

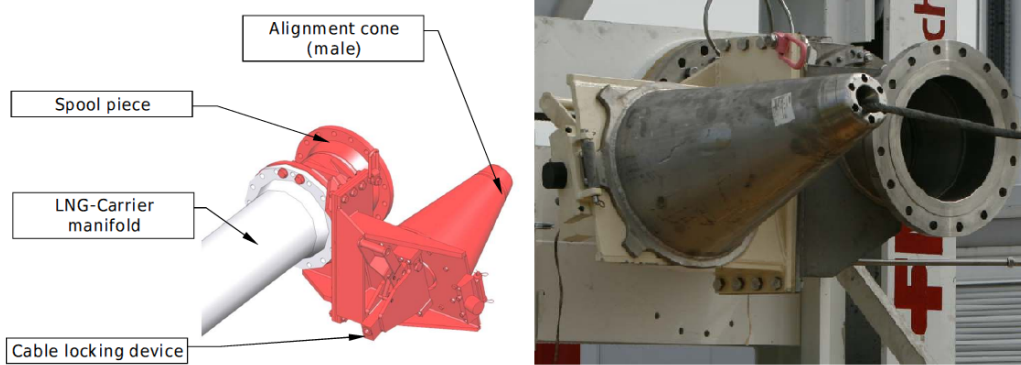


Figure 1.9: The manifold is the interface to the LNGC tanks. It has to be fitted with an alignment cone and a cable locking device to use the targeting system.

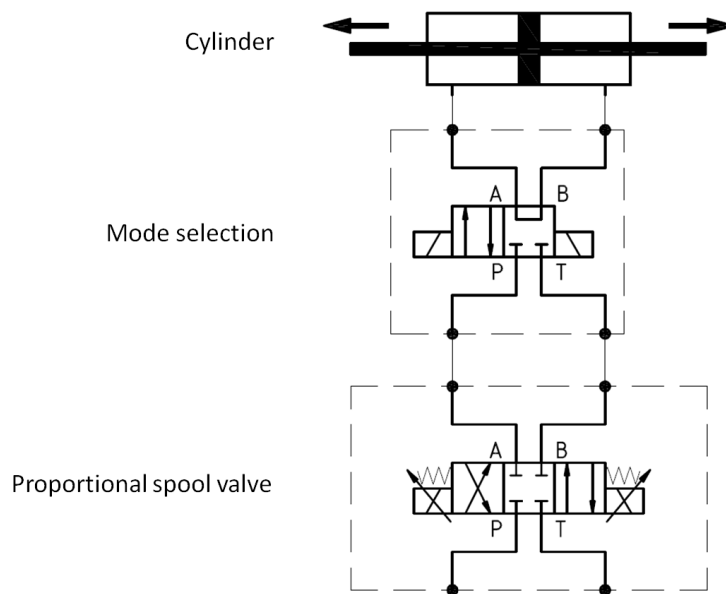


Figure 1.10: Simplified hydraulic diagram of a joint. In freewheel mode, the cylinder chambers are connected together. In "selected" mode, the proportional spool valve makes it possible to adjust the rod velocity.

1.3 Problem Statement

The current targeting system, although operational, does not provide full satisfaction:

- The targeting system require hardware to be set up on the shuttle tanker, e.g. alignment cones, cable. For this operation crew members and heavy parts have to be transferred from one vessel to the other. In addition to the difficulties in terms of logistics, the transfer of crew members is disapproved by the vessels captains and may raise legal issues.
- The cable may damage the manifold in case of overtension. Also, the legislation drastically constraints the forces that are transmitted by the cable to the manifold. For example, the maximum allowed load on a 16" LNG manifold is 50 kN, axially and radially.
- The winch and the cone attached to the manifold weight over 500 kg. This weight is not wished since it leads to oversizing the counterweights and the whole structure.
- The targeting system is very expensive relatively to the overall price of the loading arm, especially, the hydraulic power unit necessary to supply the winch.

For these reasons another way to manage the MLA connection is looked for. In this study the robotization of loading arms is investigated, in view to get rid of the current targeting system and automatize the connection operation.

1.3.1 Automatic or semi-automatic connection

The overall procedure of the desired automatic or semi-automatic connection is described in this section. This new procedure aims to connect the loading arms of an FLNG to the manifolds of the client LNGC, and no longer requires the original targeting system. For safety reasons, the loading arms present on the deck of the FLNG are connected one by one, as detailed on Figure 1.15. The connection procedure described below stands for a single loading arm. In this section, the relative pose (See Figure 1.11) of the manifold 0P_m with respect to the FLNG deck frame, i.e. frame R_0 is assumed known at all time, from some measurement system. This latter point is discussed in Section 2.1. The main frames used in this study are shown on Figure 1.11.

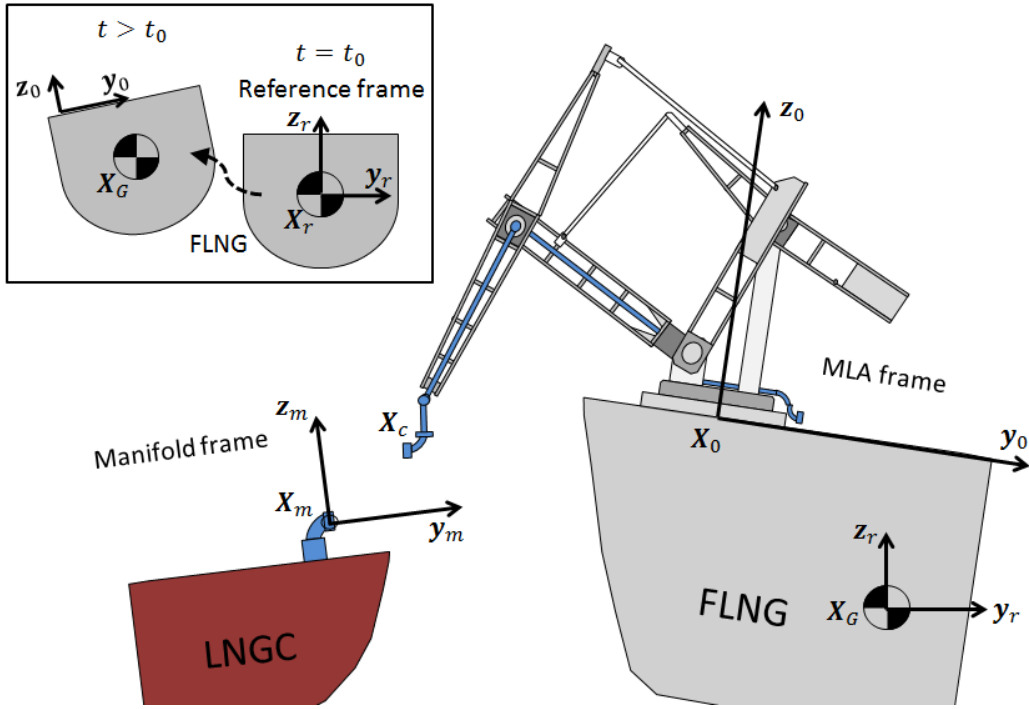


Figure 1.11: Main frames and positions notations.

In this study the notations are as following:

- \mathbf{X} is a 3×1 vector which denotes a position,
- \mathbf{q} is a 3×1 vector which denotes an orientation,
- \mathbf{P} is a 6×1 vector which denotes a pose: $\mathbf{P} = \begin{bmatrix} \mathbf{X} \\ \mathbf{q} \end{bmatrix}$,

CHAPTER 1. INTRODUCTION TO MARINE LOADING ARMS AND AUTOMATIC CONNECTION

- ${}^f v$, denotes the expression of any vector v in the frame f ,

The main frames used in this document are defined below:

- A reference frame noted R_r is constructed as (X_r, x_r, y_r, z_r) , with X_r the center of gravity at an initial time t_0 , x_r the longitudinal axis of the FLNG at t_0 projected on the horizontal plan, and z_r the vertical axis. The Galilean invariance is assumed in the reference frame.
- The loading arm frame R_0 is attached to the arm foot, with z_0 the axis of the first joint, orthogonal to the deck of the FLNG.
- The manifold frame R_m is attached to the center X_m of the manifold of the LNGC. Its orientation is noted q_m .
- The center of the coupler is noted X_c and the center of mass of the FLNG is noted X_G .

1.3.1.1 Initial configuration

The connection procedure starts with a particular initial configuration. The LNG carrier is moored to the FLNG such as the manifolds are located in front of their associated loading arms, inside their respective flanging areas. The arms are parked in their standard parking positions, defined as $(\alpha, \beta, \phi) = (90^\circ, 80^\circ, 0^\circ)$. Figure 1.12 presents an initial configuration for an OLAF parked in front of its flanging area.

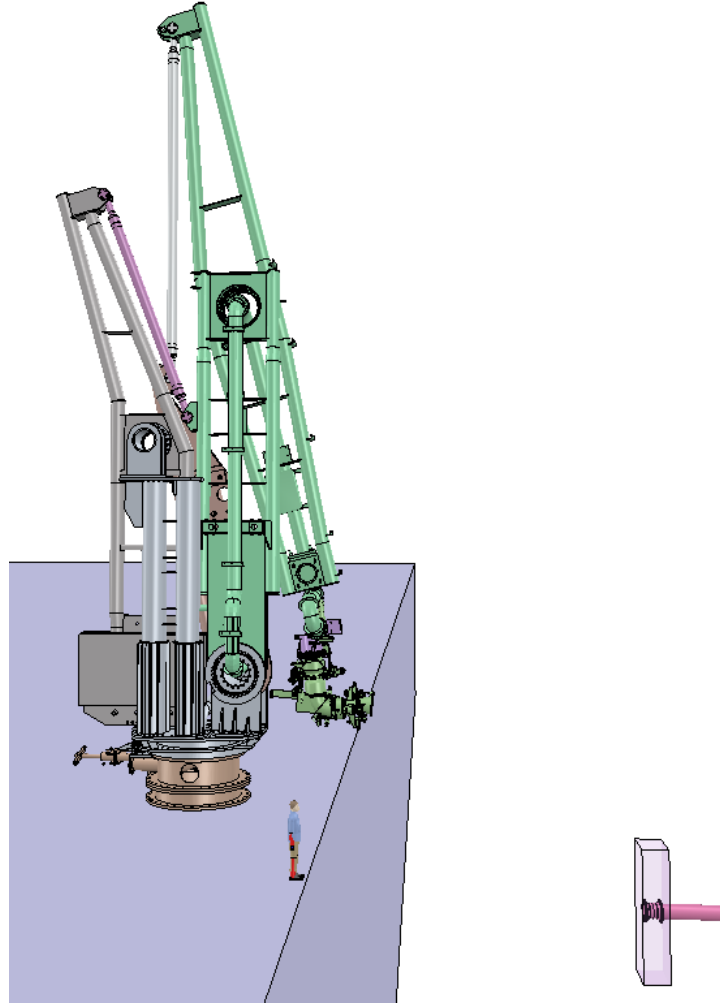


Figure 1.12: Initial configuration: the loading arm is in its parking position, in front of the flanging area.

1.3.1.2 Deployment

The deployment stage starts on the operator's command. The path of the coupler is calculated between its current pose and a target pose P_t in front of the manifold at a distance d_p :

$$\begin{cases} \mathbf{X}_t = \mathbf{X}_m + d_p \cdot \mathbf{y}_0 \\ \mathbf{q}_t = \mathbf{q}_m \end{cases}, \quad (1.1)$$

The value of d_p is to be defined latter in the project. This safety distance should take into account the delay of the arm over the manifold to prevent any collision. As the manifold move, P_t and the path are updated online. On the operator command, the loading arm is automatically driven from its parking position to P_t . The

CHAPTER 1. INTRODUCTION TO MARINE LOADING ARMS AND AUTOMATIC CONNECTION

motion is updated online to follow the evolution of P_m . Figure 1.13 illustrates the deployment stage. When the coupler reaches P_t , the loading arm continues to track it in the pursuit stage.

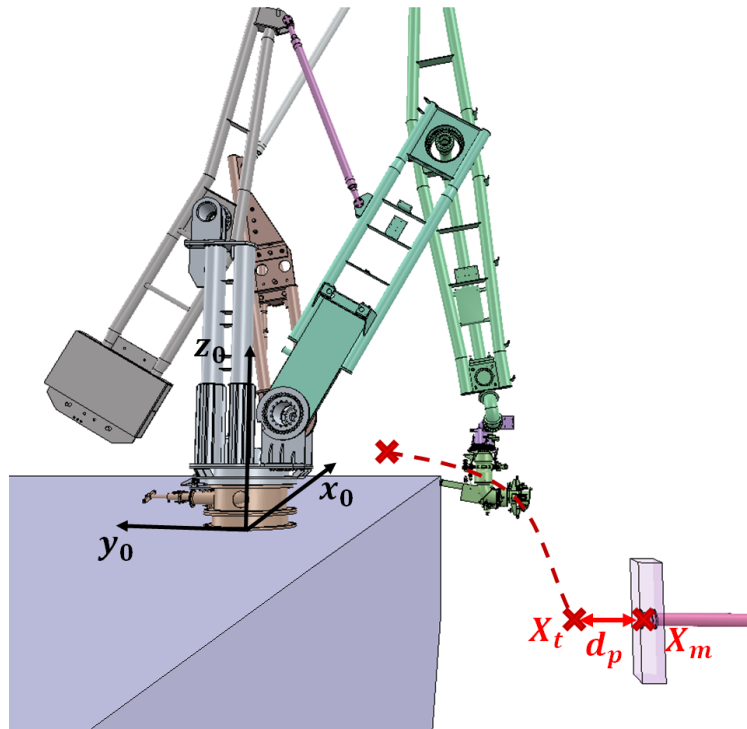


Figure 1.13: Deployment stage: the arm goes from its parking position to a dynamic position, in front of the manifold.

1.3.1.3 Pursuit

The pursuit stage is a transition stage where the loading arm waits for the flanging command. The robot tracks the target pose P_t in order to keep the coupler in front of the manifold, at a distance d_p . Figure 1.14 illustrates the pursuit stage.

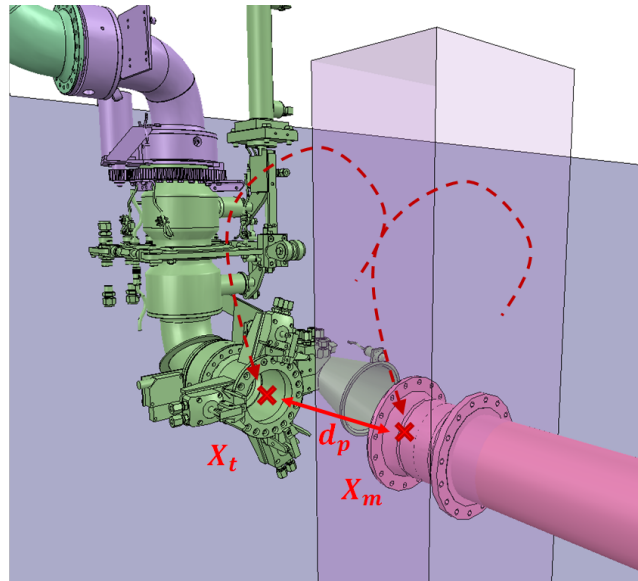


Figure 1.14: Pursuit stage: the coupler (green) follows the manifold (pink) at a distance d_p .

1.3.1.4 Flanging

The final stage of the connection procedure is the flanging stage, where the coupler is connected to the manifold. On the operator's command the coupler moves forward until the coupler frame coincide with the manifold frame, i.e. $P_t = P_m$. Once the coupler is in the right position, it automatically clamps on the manifold.

When the coupler is clamped to the manifold, the arm automatically switches in freewheel mode. Thus the loading arm is still able to comply with the relative motion between the two vessels. Any failure to switch to freewheel mode at the connection would lead to severe damage to the hardware, as the arm stays rigid while the vessels have a relative motion.

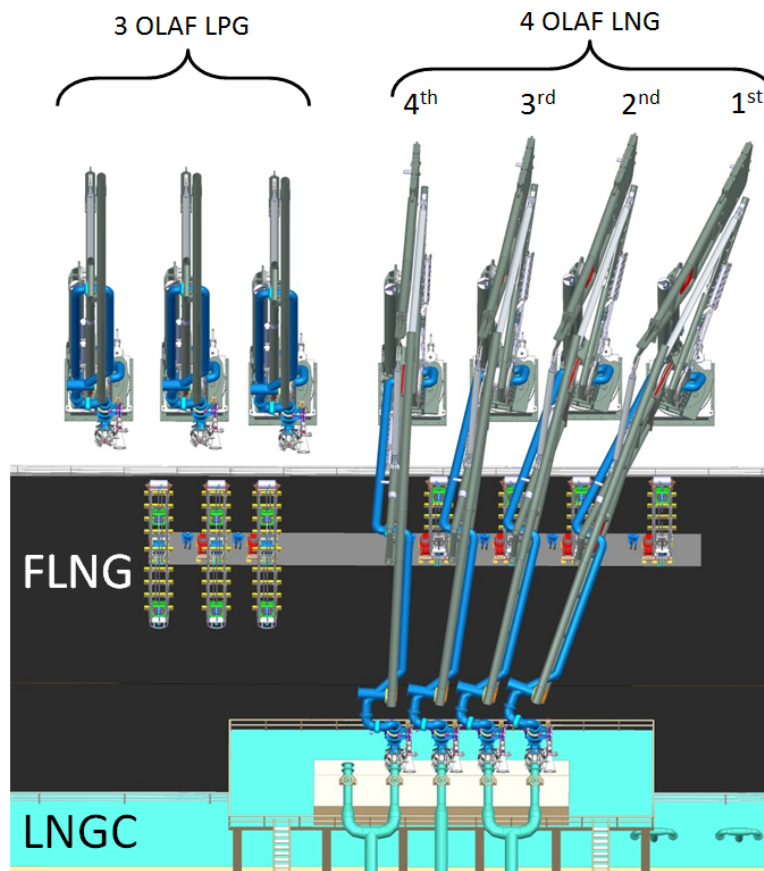


Figure 1.15: The four LNG loading arms of the FLNG Prelude are connected to the LNGC. The numbers above the arms indicate their order of connection: from right to left.

1.3.2 Technical requirements

This project aims to develop and implement a system that makes the described automatic connection of the MLA possible. The requirements under which the project is led are:

- No major change should be done to the structure of the loading arm,
- The chosen solution should minimize the hardware necessary on the LNGC.
- Any additional hardware should be certified compatible with an explosive atmosphere (ATEX directive).

The main foreseen obstacles in the realization of this project are:

CHAPTER 1. INTRODUCTION TO MARINE LOADING ARMS AND AUTOMATIC CONNECTION

- The accuracy required for the connection is very high regarding the size of the MLA: the position tolerance of the flanging system is 10 cm and its orientation tolerance 5 degrees. This value is estimated from the design of the coupler.
- The automatic connection should work under the oceanic weather conditions, including the motion of the vessels and the wind.
- Loading arms are not designed as industrial robotic systems. Their structures have a low stiffness, include backlashes and non-linearities such as dry friction and hystereses.

To conduct this project a 1/4 scaled OLAF model is available for experiments, as described in Section 1.4.1. Such a scaled model is easier to deal with than a full scale loading arm, regarding its size, its availability and the typical setup time. A full scale MLA, presented in Section 1.4.2 is available for the final validation of this study, at the very end of this project.

1.4 Presentation of the marine loading arms

1.4.1 OLAF scaled model

This loading arm is 1/4 model of an OLAF arm, presented in Section 1.2. Originally built for commercial and communication purposes, this is nevertheless a true replica of a real loading arm. It is fitted with a complete position monitoring system, and a functional actuation system. This arm can be controlled from a nearby control deck or a remote control, both connected to a dedicated industrial PLC (programmable logic controller), for manual connection. Because full scale loading arms are not available for research, this scaled model is used for all the experimental aspects of this project. Picture 1.16 shows the OLAF scaled model connected to the manifold. The scaled OLAF model is set up on a 6 DoF hexapod table which is used to simulate the FNLG motion. An equally scaled manifold, shown on Figure 1.17, is set up in front of the arm, in its flanging area so that the connection is possible. This manifold is installed on a second hexapod table which can simulate the LNGC motion.

The actuation system of the scaled loading arm is powered by a 4 kW pump, which makes available a maximum flow rate of oil of 10 L/min at 200 bars. This pump corresponds to the one of a full scale arm. Also, the masses and inertia of the parts can be assumed $4^3 = 64$ times lower than the ones of a full scale arm.

CHAPTER 1. INTRODUCTION TO MARINE LOADING ARMS AND AUTOMATIC CONNECTION



Figure 1.16: The OLAF scaled model connected to the manifold.



Figure 1.17: The scaled manifold on its hexapod.

CHAPTER 1. INTRODUCTION TO MARINE LOADING ARMS AND AUTOMATIC CONNECTION

Consequently, the dynamical performances of the scaled OLAF are greater than the ones of full scale arms, as highlighted in Section 3.2.

1.4.1.1 Robotization of the arm

In order to use this scaled model for the automatic connection project, minor changes are brought. First of all the PLC programming is adapted to transmit data from the sensor of the arm to a development computer, and to this computer to the hydraulic spool valves. The communication rate ensured by the PLC is 30 ms. A low-level communication client is developed on the development computer, with care for code robustness and safety. Second the hydraulic circuit is redesigned, with servo-valves, to make a better control of the oil flow in the cylinders possible. These servo-valves are installed the closest possible of the cylinders, with care to minimize flexible hoses, in order to keep the circuit stiff. Finally inclinometers for the original position monitoring system are replaced by incremental position encoders. The inclinometers are pendulum based and badly respond to during motion, hence cannot be used for this project. Unfortunately the joint 5 was not included in this robotization stage, and had to be left aside in this project.

1.4.2 Full scale DCMA

After the promising results of this project, and in particular after the tests presented in Section 5.3.2.1, a full scale marine loading arm was made available in order to apply the developed methodology on a real system. The author would like to emphasize the anachronism of this document. While the experimental results collected on the two systems are presented together across the chapters, this full scale arm was only available for a few days at the end of the project. Hence the methodology presented in this document is exclusively based on simulations and experimental study of the 1/4 scaled loading arm.

This loading arm is a DCMA: Double Counterweight Marine Arm. Its design only slightly differs from the one of the OLAF:

- its internal counterweight is part of the internal link,
- the external parallelogram structure of the OLAF is replaced by a cable and pulleys,
- the DCMA is set up on a 10 meters riser.

Figure 1.18 shows a picture of the full scale DCMA available at the end of the project.

CHAPTER 1. INTRODUCTION TO MARINE LOADING ARMS AND AUTOMATIC CONNECTION



Figure 1.18: A full scale marine loading arm is used for the final tests of automatic connection.

This loading arm is connected to a PLC, as the scaled model is. Its hydraulic circuit is powered by a 300 bars - 100 L/min pump, which is in turn powered by a 120 kVA generator. The structure of the arm weights about 100 tons and each of its links is 10 meters long. The joint 5 of this arm is not instrumented and not adequately actuated, and was left aside during this project. In front of the arm is set up a 3 DoF test bench fitted with a manifold, as shown on Figure 1.19. This test bench is placed in the flanging area of the loading arm, and is used to reproduce the relative vessel motion ${}^0X_m(t)$ (no rotation possible).



Figure 1.19: 3 DoF test bench is fitted with a manifold.

1.5 Placement of the project regarding the literature

Robotic systems are increasingly popular in most sectors of the industry. Traditional stiff industrial robots, mobile robots, collaborative and soft robots are used for an amazingly wide scope of operations. However it is not easy to judge in which category a robotized marine loading arm belongs. Indeed the literature offers few examples of similar systems.

CHAPTER 1. INTRODUCTION TO MARINE LOADING ARMS AND AUTOMATIC CONNECTION

First of all some research studies exist about the automatization of marine cranes. K uchler *et al.* [KMN⁺11] propose a method which makes easier for the operator to drive a tower crane set up on the deck of a ship. This method combines active heave prediction and compensation and results with a significant reduction of the vertical position error of the payload. This approach of "predictive compensation" can be considered to solve the tracking problem of MLAs. Other studies involving cranes mainly focus on the reduction of the swing of the payload, as in [K o05]. However this studies only focus on the motion of the load, attached at the end of a cable, and do not consider the structure of the crane. Then From *et al.* present in [FGLA11] a very interesting research study about the control of motion planning of industrial manipulators set up on seaborne platforms. This work focuses on the inertia effects of the vessel motion on the robotic system, and how to deal with this disturbance by using adequate control. From *et al.* go even further and propose a way to take advantage of these inertia effects to reduce the joints torques required for a given task. Although industrial robots are very different of loading arms in terms of size, mass and stiffness, the methodology is still valid for MLAs.

Then different systems with technical similarities may be interesting to study. For example flexible space manipulators, e.g. CANADARM, present unique characteristics such as joints and links flexibility, large size and mobile base, as highlighted by Kim [Kim99]. As significant amount of research studies applied to these space systems can be found, particularly about active vibration damping [SGMP12]. Another similarity can be found in active compensation tools for beating heart surgery. Kettler *et al.* [KPN⁺07] developed a robotic instrument that measures and compensates the motion of the target tissue, resulting in an increased dexterity for the user. Such a motion compensation may be applied to loading arms for reducing the position error induced by the relative motion of the vessels.

More specific research topics will be reviewed across this document when relevant.

Chapter 2

Accurate positioning of a loading arm

To make the automatic connection of the loading arm to the manifold possible, accurate estimations of the manifold pose ${}^0\mathbf{P}_m$ and the coupler pose ${}^0\mathbf{P}_c$ in the arm frame are needed. The accuracy of these estimations is of primary importance, since they serve as reference when the loading arm is driven. More precisely, the accuracy of the estimations of ${}^0\mathbf{P}_m$, and ${}^0\mathbf{P}_c$ should be sufficiently high so that the final position error of the coupler lays within its tolerance. The first section of this chapter deals with technical ways to estimate the pose of the manifold ${}^0\mathbf{P}_m$. In Section 2.2, a method to calibrate the loading arm is developed, in order to improve its accuracy.

2.1 Measurement systems

In order to give a target to the loading arm when connecting, the relative pose of the manifold with respect to the arm frame, ${}^0\mathbf{P}_m$, is required. The orientation of the FLNG deck in the reference frame R_r is also necessary to compute the configuration of the arm from the measurement of the Style 80 inclinometer . Finally, the measurement of the FLNG pose ${}^r\mathbf{P}_0$ can be used to estimate the inertia effects induced in the arm, as simulated in Section 3.3.3.

Some constraints , due to the context, are to be respected when choosing suitable measurement systems:

- The measurement systems should have a high accuracy regarding the tolerance of the coupler, i.e. under 10 mm in position and 1° in orientation.
- The measurement systems should provide data in real time, at a rate of

at least 1 Hz, according the vessels motion frequency spectra presented in Section 3.3.2.

- The measurement systems should be robust to the marine environment, i.e. to heavy rain, wind, intense sunlight.
- The measurement systems should be suitable to operate in explosive atmosphere (ATEX certification).

Moreover, one should note that it is wished to minimize the equipment that is needed on the shuttle vessel, for the reasons detailed in Section 1.3.2. The cost of the hardware is also to be considered.

2.1.1 Candidate solutions

Some technical solutions are discussed below.

2.1.1.1 Total station

Total stations are electronic devices used for topography operations such as surveying or building construction. Such devices consist of a laser emitter and receptor set up on a two-DoF articulated frame. The total station is able to locate a dedicated reflector target with an accuracy less than $1 \text{ mm} + 1.5 \text{ ppm}$ for ranges up to 2000 meters, and provides position data at a rate up to 10 Hz. The two rotary joints are actuated so that the system is able to automatically follow its target. Total stations are designed for outdoor use, and are robust to harsh weather conditions. Figure 2.1 shows a total station and its reflector.

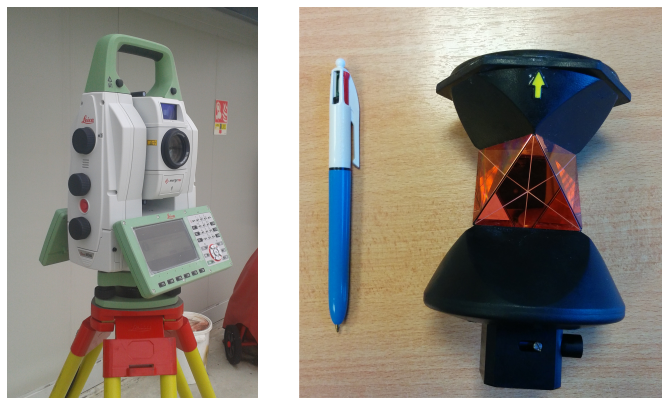


Figure 2.1: A total station and its reflector.

CHAPTER 2. ACCURATE POSITIONING OF A LOADING ARM

By setting up a total station on the FLNG deck, and a reflector on the LNGC manifold, the relative manifold position 0P_m can be known at all time. Adding two extra reflectors on the manifold, in the plan (z_m, x_m) , makes it possible to also obtain the manifold orientation, if the total station alternatively measures the three reflectors positions.

Besides locating the manifold frame, the station total may solve another technical problem. If an additional reflector is fitted on the Style 80 of the arm, the total station can measure the coupler position. Such data can prove itself useful to adjust the arm calibration before the connection. Indeed it is likely that the factory calibration loses its accuracy over time, and from some other effects such as thermal expansion. A quick re-calibration procedure could be designed to restore the original accuracy of the arm. Figure 2.2 illustrates the possible use of a total station. Calibration is detailed in Section 2.2.

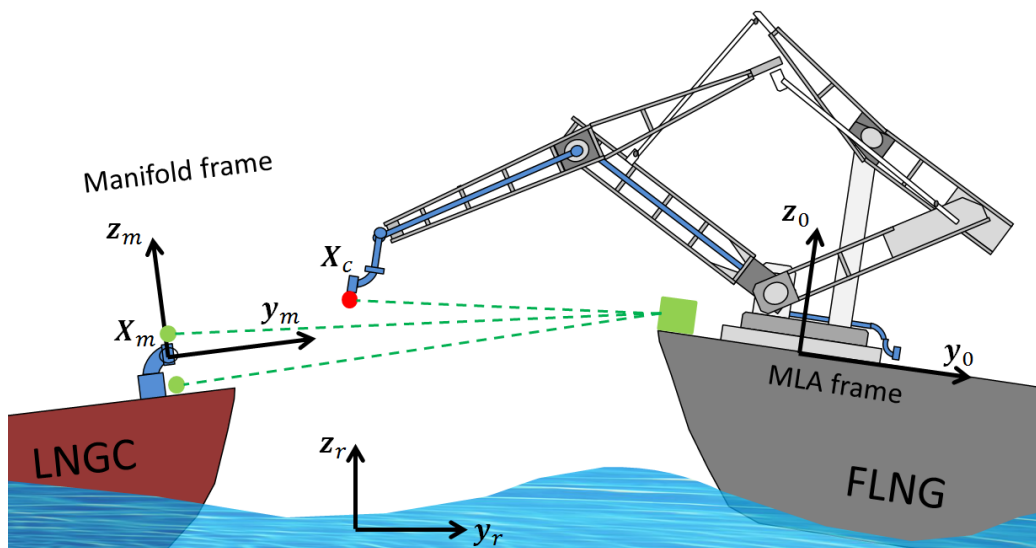


Figure 2.2: The total station (green box) locates accurately the reflectors on the manifold (green circles) or on the coupler (red circle).

Total stations meet the requirements in terms of measurement performance, to measure the relative position and orientation of the shuttle tanker. Moreover this solution does not require any hardware on the tanker except reflectors. At the best of the author's knowledge, no manufacturer presently proposes ATEX certified total stations. This certification is expensive but can be obtained.

2.1.1.2 Inertial measurement unit

Inertial measurement units (IMU) are electronic devices which embed accelerometers, gyroscopes and magnetometers. From these sensors the IMU can accurately estimate its orientation in the Earth frame. It also can estimate the evolution of its motion, i.e. heave, surge and sway, by integration. For example, an IMU set up at the foot of the loading arm can measure the orientation of the loading arm frame in the Earth frame. IMU are already popular for vessel motion monitoring [FGLA11], [KMN⁺11].

2.1.1.3 Differential Global Positioning System

Differential Global Positioning System (DGPS) is an improvement of the classic GPS system. This device communicates with satellites and is able to estimate its position in the Earth frame, with an accuracy of a few centimeters. If DGPS systems are installed on both the LNGC and FLNG decks, the position of the manifold in the arm frame 0X_m can be known. An experimental study has shown that, besides its insufficient accuracy (4 cm) when following a vessel motion, a DGPS antenna cannot be set up at the foot of a loading arm. Indeed the structure of the arm would shadow the DGPS antenna and interfere with its position estimation. This drawback may be fixed by installing the antenna away from the arm, but then it would be difficult to know accurately the position of the antenna in the arm frame.

2.1.1.4 Machine vision

Cameras set up on the FLNG deck or on the Style 80 are a possible solution, together with a pattern recognition software, to locate the manifold. This solution is cheaper than the ones presented above, and no hardware on the LNGC is required. The main challenge of this solution is to make it robust to external condition, e.g. mist, water, sunlight and darkness.

2.1.1.5 Connected loading arms

Before offloading LNG or LPG, three or four loading arms have to be successively connected to the LNG carrier. Once the first arm is connected, its geometric model can be used to calculate the pose of its coupler, hence the pose of the manifold. This data can be used as a redundancy or to improve the estimation of the pose of the other manifolds. Since once connected the arm sustains external forces, the accuracy of the geometric model may be lowered by mechanical distortion. The validity of this method may be checked by connecting a loading arm to a moving

test bench and comparing the actual position of the manifold with the calculated one.

2.1.2 Data fusion

For the sake of safety, several sensors can be used to locate the LNGC manifolds. These sensors can be set up as simple redundancies, or can improve the estimation of the manifolds pose by data fusion. Data fusion consists in gathering data from several sensors, and use these data together to improve the estimation of the measured quantity. The sensors can be of the same kind, or different. For example the position variation measured by an IMU can be merged with position information from a DGPS system, as proposed by Caron *et al.* [CDPV06].

2.1.3 Proposed solution

According to the current state of the art and the discussion hereinbefore, the solution proposed by the author consists of an inertial measurement unit installed on the FLNG deck, next to a total station. From the IMU the FLNG absolute orientation is known at all times, as well as its velocity and acceleration. From the total station the relative position and orientation of the manifold are known. Together, these devices gather all needed information, while minimizing the hardware on the LNGC deck.

2.2 Kinematic calibration of serial mechanisms

Loading arms are large structures regarding the position accuracy required for an automatic connection. While the length of the links of MLA are up to ten meters, the coupler should be located in front of the manifold with an accuracy of a few millimeters. Nowadays loading arms are not designed for accurate positioning since it is not needed for the current targeting system. This problem is solved by using a position calibration method originally designed for industrial robotic manipulators. Orientation accuracy is left aside in this project, because the accuracy of the loading arms in terms of orientation is assumed much greater than the coupler orientation tolerance, from nominal specifications. This section first presents the calibration methodology. Then a collaborative robot is first used to validate this methodology for practical reasons. Indeed the calibration operation is difficult to set up on a MLA so a preliminary validation is wished. Finally marine loading arms are calibrated. To the best of the author's knowledge, this is the first geometric calibration of a MLA.

The first industrial robots were used to replace humans to realize fastidious, difficult and hazardous tasks such as material handling, welding and assembling. These operations are programmed as point to point operations, which are defined by few points only. In this case, robots are programmed by teaching: the robot is manually driven to the point to be learned, and the corresponding joints configuration is recorded. Thanks to their good repeatability, which ranges from 0.03 to 0.1mm for small and medium sized robots, industrial robots are able to reproduce the taught positions with a good accuracy. In this case the robot accuracy is equal to its repeatability. Manually teaching points to the robot is a sufficient method when the task trajectories are made of few points. This approach is not adapted for continuous operations such as the pre-machining of cast parts as well as the end-machining of middle tolerance parts, or point to point operations with large number of positions to be reached, e.g. riveting huge pieces in aircraft manufacturing. Off-line programming (OLP) is more suitable for the latter operations. OLP uses a geometric model of the robot, and is able to translate points expressed in the task space to robot configurations expressed in the joint space. Many dedicated CAD softwares include this feature and automatically generate the desired trajectories. While the repeatability of industrial robots is usually less than 0.1 mm, their accuracy is often up to several millimeters [ODB⁺12]. This poor accuracy is caused by an accumulation of small errors coming from various sources that add up and may lead to significant position errors. Such a pose error can be corrected by some sensor-based methods: the error is measured and injected in a control loop for correction. In particular, vision-based correction, i.e. visual servoing, shows good results and has become popular in many industrial applications, such as robotic assembly [NPK96]. However sensor-based methods often require extra hardware which may be expensive and difficult to set up. Other approaches include model-based calibration methods. A model of the robot to be calibrated is built, which embeds all error sources to be compensated, e.g. dimensional parameters, misalignments, stiffness parameters for deflections. The model parameters are evaluated by solving a nonlinear optimization problem with as reference a series of measurements of the real position of the robot, classically the position of its end-effector. The model is then used to anticipate the positioning errors and adjust the control law to correct it.

The present study focuses on static model-based global position calibration. This type of calibration is classified as geometric or non-geometric calibration. The former type adjusts only dimensional parameters of the robot model, e.g. links length, joints offset, misalignments and tool definition. In that case, the robot joints and links are assumed as perfectly rigid [EGZ⁺04]. Non-geometric calibration takes into account, in addition to geometric parameters, other phenomena such as joints and links deflections or thermal effects, e.g. dilatation.

The choice of the parameters to be included into the model depend on the level of accuracy needed. Khalil *et al.* [KB02] build a model based on flexible joints and beams and uses the Newton-Euler algorithm to compute the needed forces and moments. This method requires to know the mass and the center of gravity for each link. Nubiola *et al.* [NB13] takes account of a backlash in one joint, which may be necessary for MLAs. Gong *et al.* [GYN00] uses 12 thermistor sensors to identify thermal effects in addition to joints compliance. Santolaria *et al.* [SYJA09] also incorporates thermal effects in the model of an articulated arm measuring machine in order to reach a high accuracy level. Thermal effects may be non-negligible for marine loading arms, as these systems are to be used in polar or tropical environments. However this is beyond the scope of this study.

Although some calibration methods do not need a model of the robot, as the one presented in [DJC07] which uses genetic programming, most calibration methods are model-based. The complete procedure of robot calibration consists of four stages: modeling, measurement, identification, and compensation [CFC⁺08]:

1. A model of the robot has to be chosen according to the possible non-geometric effects to be accounted for.
2. A sufficient number of measurements of the robot position has to be collected in order to provide enough equations to solve the optimization problem.
3. The model parameters are identified to minimize the errors between the model and the real system.
4. The commanded articular positions of the robot are corrected according to these new parameters.

2.2.1 Generic geometric calibration for a serial robot

2.2.1.1 Modeling

The common robot calibration technique requires a model of the robot, in which all error types to be compensated are included. The main error source is the geometric difference between the real robot parts and the nominal ones. Therefore the chosen structure for the robot model is a geometric model. Typically, this geometric model relies on the Denavit–Hartenberg (D-H) parametrization, with which a minimum number of parameters is needed to represent the geometry of the robot. DH parameters include parts dimensions and joints offset. In addition to geometric parameters, some non-geometric effects may be taken into account

in the calibration process, if these effects are known to lead to significant position errors. The most frequently modeled non-geometric effect is joints compliance, since for most robots it is the main non-geometric source of inaccuracy. Then, in a few cases links deflection or thermal effects or also accounted for. The set of the parameters of the model is noted ξ .

2.2.1.2 Measurements

The second stage of the calibration process is to select a set of n calibration configurations $(\mathbf{q}_1, \dots, \mathbf{q}_n)$. Each configuration \mathbf{q}_i is a $m \times 1$ vector, with m the number of joints of the robot: $\mathbf{q}_i = [q_{i,1}, \dots, q_{i,m}]^T$ and $q_{i,j}$ the position of the j^{th} joint for the i^{th} configuration. This stage is of primary importance since it will significantly impact the quality of the parameters identification. While handbooks generally propose to simply cover the taskspace with measurement points, many methods are proposed in the literature to select an optimal or near optimal set of calibration configurations. Wu *et al.* [WKP⁺12] proposes a dedicated selection method for elasto-static calibration. However the latter uses known loads for each configuration and do not take the weight of the robot into account. [ZWR94] and [JB13] present selection methods based on observability indices. Observability indices measure the possibility to identify all model parameters for a given set of configurations. The common drawback of these selection methods is that the taskspace should be numerically modeled, so that no configuration is generated through an obstacle, e.g. a wall, the floor or any part in the environment of the robot.

The robot then is successively driven in each configuration $\mathbf{q}_i, \forall i \in \{1, \dots, n\}$, and the Cartesian position of the tool tip of the robot \mathbf{x}_i is measured. The accuracy of these measurements should be high regarding the repeatability of the robot.

2.2.1.3 Global identification

Geometric calibration consists in estimating dimensional parameters such as joint offsets or link lengths. In this study it is chosen to include all identifiable DH parameters in the calibration process. The tool center point (TCP), which represents the position of the tool tip with respect to the robot last frame R_m , is also included in the parameters ξ to be identified as a vector of three parameters $[t_x, t_y, t_z]^T$. Frames placement is illustrated on Figure 2.3.

For each configuration \mathbf{q}_i , the theoretical tool tip Cartesian position $\mathbf{x}_{th,i}$ can be obtained by using homogeneous matrices. Let us note ${}^{j-1}\mathbf{T}_j(\xi, q_j)$ the transformation matrix which defines the frame R_j of the j^{th} link of the robot, with respect to the frame R_{j-1} . Together, these matrices are used to build ${}^0\mathbf{T}_m(\xi, \mathbf{q}_i)$, which

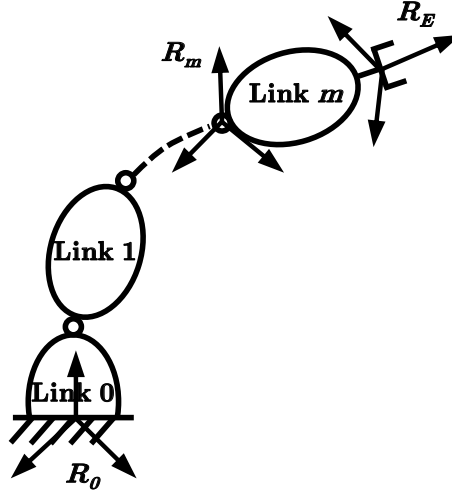


Figure 2.3: Frames placement for a serial manipulator.

defines the frame R_m with respect to the frame R_0 :

$${}^0T_m(\xi, q_i) = {}^0T_1(\xi, q_{i,1}) \dots {}^{m-1}T_m(\xi, q_{i,m}). \quad (2.1)$$

The TCP of the robot is defined by its transformation matrix ${}^mT_E(\xi)$:

$${}^mT_E(\xi) = \begin{bmatrix} 0 & 0 & 0 & t_x \\ 0 & 0 & 0 & t_y \\ 0 & 0 & 0 & t_z \\ 0 & 0 & 0 & 1 \end{bmatrix}, \quad (2.2)$$

The theoretical tool tip positions $x_{th,i}(\xi)$ can then be calculated in the frame R_0 :

$${}^0T_E(\xi, q_i) = {}^0T_m(\xi, q_i)E(\xi) = \begin{bmatrix} {}^0R_E & {}^0x_{th,i}(\xi) \\ 0 & 0 & 0 & 1 \end{bmatrix}. \quad (2.3)$$

The (3×1) vector representing the error in position is given by:

$$\Delta x_i(\xi) = x_i - x_{th,i}(\xi). \quad (2.4)$$

Let us note $\Delta X(\xi)$ the $(3n \times 1)$ column vector of the $\Delta x_i(\xi)$:

$$\Delta X(\xi) = \begin{bmatrix} \Delta x_1(\xi) \\ \vdots \\ \Delta x_n(\xi) \end{bmatrix} \quad (2.5)$$

In order to minimize $\Delta X(\xi)$, i.e. minimize the position errors, several methods can be used. [NB13] proposes to solve this nonlinear optimization problem by using an iterative method based on the pseudo-inverse of the observation matrix. [NZK15] uses an extended Kalman filter to identify the geometric parameters and an artificial neural network for the non-geometric parameters. In this study the Levenberg-Marquardt algorithm has been chosen for the identification of the parameters of the model. This algorithm is a classic method to minimize a parameterized function in the least square sense. The Levenberg-Marquardt is an iterative method which combines the gradient descent method and the Gauss-Newton method [Mor78]. The output of the Levenberg-Marquardt algorithm is a set of new parameters that minimizes the position errors. These new parameters can be used to drive the robot with an improved accuracy.

To quantify the quality of the identification, the norm d_i of the position error $\Delta x_i(\xi)$, i.e. the distance between the calculated and measured tip position is derived :

$$\forall i, d_i = \|\Delta x_i(\xi)\| \quad (2.6)$$

Three values are used to evaluate the quality of the identification. The maximal error $\max_i(d_i)$ represents the higher inaccuracy. The average $\text{mean}_i(d_i)$ and standard deviation $\text{std}_i(d_i)$ represent the distribution of the position errors.

2.2.1.4 Correction and validation

The updated values of the model parameters are used in the model of the robot to drive the robot more accurately, by compensating the position errors online. Validation configurations, different from the calibration configurations, should be used to verify that the accuracy of the robot is improved by making new measurements.

Before applying the methodology above to marine loading arms, it is wished to validate it on another system for practical reasons. For this purpose a collaborative manipulator is chosen, as a similar polyarticulated serial mechanism with some joint flexibility. This application is also used to investigate how one can use joints torques measurements to improve the calibration process.

2.2.2 Application to a collaborative robot

A new generation of so-called collaborative robots comes with embedded joint torque sensors. The LBR iiwa Kuka robot, for example, is a seven degrees-of-freedom (DoF) polyvalent manipulator. Its "collaborative" features include artificial joints compliance, collision detection and hand-guiding. The easy access to joint torques data makes it possible to perform many studies of the robot which

would be difficult with a classic robot. For example [JGJ14] proposes a method to identify the dynamic parameters of the robot, while [GFDL14] identifies the dynamic model used by the manufacturer by reverse engineering. In this study, the torque sensors values are exploited to easily identify the joints stiffnesses with no need to derive the joints torques. One notes that the direct measurement of the joints torques can be replaced by the measurement of the motors current in case of missing sensors, as propose by [JAG14]. The calibration method presented in this study was applied to a 7 DoF ($m = 7$) iiwa LBR Kuka robot. This collaborative manipulator is fitted with torque sensors on each of its seven rotary joints.

2.2.2.1 Setup of the experiment

The iiwa robot was vertically installed on a massive metallic structure, for rigidity purposes. It is important that the base of the robot does not to move during the experiment, to not induce non modeled position errors. No load is attached to the robot, the joints torques are induced by the weight of the robot itself. The whole experiment was led at ambient temperature (19°C) assumed constant. Thermal errors compensation is beyond the scope of this research, and such errors are assumed negligible.

2.2.2.2 Modeling

The geometric model of the robot with the modified D-H parametrization [KD04] as shown on Figure 2.4. The nominal modified D-H parameters ξ_n provided by the manufacturer of the robot are given by Table 2.1. The parameters definitions are given in Appendix A. Each parameter θ_j represents the offset of joint j .

Table 2.1: Nominal parameters

j	α_j (rd)	θ_j (rd)	d_j (mm)	r_j (mm)
1	0	0	0	360
2	$-\pi/2$	0	0	0
3	$\pi/2$	0	0	420
4	$\pi/2$	0	0	0
5	$-\pi/2$	0	0	400
6	$-\pi/2$	0	0	0
7	$\pi/2$	0	0	126

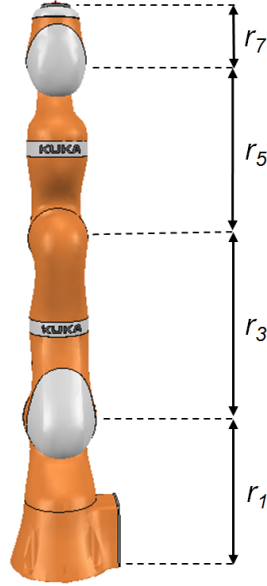


Figure 2.4: iiwa robot in zero position: Modified DH parameters.

For most industrial robots, joints compliance is recognized as the non-geometric phenomenon leading to largest inaccuracies [SK16], [WKP⁺12], [Lee13]. In this study, it is chosen to take joints compliance, twist only, into account in the calibration process. The model chosen for the joints is a simple rotary spring characterized by its stiffness, as illustrated in Figure 2.5. For each joint j and joint torque τ_j , the deflection $\delta\theta_{j,def}(\tau_j)$ of the joint is given by Hooke's law:

$$\delta\theta_{j,def}(\tau_j) = \frac{\tau_j}{k_j}. \quad (2.7)$$

The joints stiffnesses are assumed to be constant, although in the case of large deflections, a more sophisticated model might be needed. [NGM⁺15] also includes damping parameters in the joints model, to carry out an identification in the frequency domain. However no damping effect is necessary for a static calibration.

In order to incorporate the joints compliance into the model of the robot, the robot joints positions are updated with the deflections given by relation (2.7). A set of joints torques (τ_1, \dots, τ_n) is needed. Each $m \times 1$ joints torque vector $\boldsymbol{\tau}_i = [\tau_{i,1}, \dots, \tau_{i,m}]^T$ represents the static torque in the joints of the robot for the configuration \boldsymbol{q}_i . Relation (2.1) becomes:

$${}^0\boldsymbol{T}_m(\boldsymbol{\xi}, \boldsymbol{q}_i, \boldsymbol{\tau}_i) = {}^0\boldsymbol{T}_1(\boldsymbol{\xi}, q_{i,1} + \frac{\tau_{i,1}}{k_1}) \dots {}^{m-1}\boldsymbol{T}_m(\boldsymbol{\xi}, q_{i,m} + \frac{\tau_{i,m}}{k_m}) \quad (2.8)$$

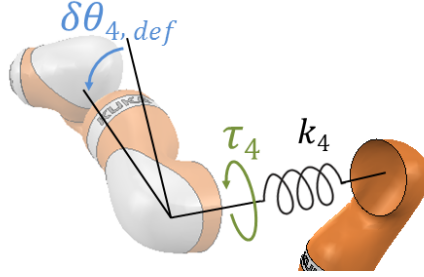


Figure 2.5: Example of the joints model with joint 4. In order to take into account the joints compliance, each joint j is modeled as a spring of stiffness k_j .

and the theoretical robot tip position $x_{th,i}(\xi, \tau_i)$ takes the joints deflection into account. The joints stiffness parameters (k_1, \dots, k_m) are added in ξ as parameters to be identified.

2.2.2.3 Selection of the calibration configurations

The methods presented in 2.2.1.2 require to build the observability matrix of the model of the robot, with all parameters. For a non-geometric calibration, a mass model and a resolution algorithm such as Newton-Euler would be required. In this study, a more practical way to obtain calibration configurations is chosen. By using its collaborative features, the robot is hand-guided through a large set of configurations covering the workspace of the robot. Special care is taken to put the robot in configurations maximizing the joints torques, in order to make the joints compliance errors identifiable, as shown in Figure 2.6. The manual manipulation makes it straightforward to avoid the potential obstacles, e.g. walls, floor, self-collisions, and keep the tool visible by the laser tracker. During this operation the evolution of the joints position is continuously recorded. This motion, from which the calibration configurations are sampled, is reproduced in the measurement stage.

2.2.2.4 Measurements

The second step of the experiment is, for each of the $n = 50$ calibration configurations, to measure the tool tip position and the joints torques. Laser tracker is a popular choice as a 3D position measurement tool [NB13], [ODB⁺12]. This measurement tool is based on laser interferometry and its accuracy is $15 \mu\text{m/m}$, which is under the repeatability of the iiwa manipulator. Thus such a measurement tool is suitable for the experiment presented in this section. The laser tracker measures the position of a dedicated spherical reflector, which is installed on the tip of the

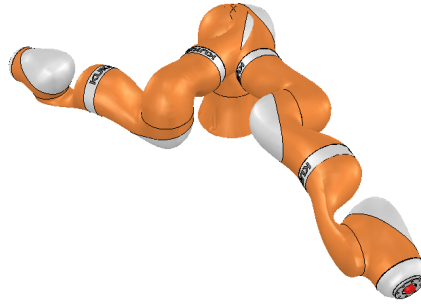


Figure 2.6: Examples of robot configurations with high torques for joints 2, 3 and 4.

robot, as show on Figure 2.7. The laser tracker is set up 2 meters away from the robot, on a rigid tripod glued on the floor to make sure that it will not move in case of any disturbance.

In order to obtain the joints torques, many methods are available in the literature. The Newton-Euler algorithm and the Lagrangian approach are popular choices [KD04], but the needed inertial parameters, e.g. masses, centers of mass, are most of the time difficult to obtain from the manufacturer or experimentally [JGJ14], [GFDL14]. These difficulties are bypassed by using the technology embedded in the collaborative robot. Since the joint torques values are available in real-time from sensors, the problem is simplified and the torques values more accurate.

The robot is programmed to automatically go in each of the n chosen configurations $(\mathbf{q}_1, \dots, \mathbf{q}_n)$, as illustrated in Figure 2.8. When the robot reaches a configuration \mathbf{q}_i , it pauses and measures the joint torques τ_i while the laser tracker measures the tool position \mathbf{x}_i . The laser tracker waits for the robot to be steady before measuring. Figure 2.9 shows a sample of the recorded torque and joint position for the joint 2. The data collection ends up with, for each configuration \mathbf{q}_i in the joint space, an associated joints torque τ_i and a measured Cartesian position \mathbf{x}_i .

To make sure that the base of the robot is rigid and does not present any deflection from the torque induced by the weight of the robot, additional measurements were made. The reflector of the laser tracker was installed on the base of the robot, and its position was monitored for different configurations. In particular, the arm was driven in fully extended horizontal positions to maximize the static torque in the base of the robot. A difference below $50 \mu m$ was measured,



Figure 2.7: Picture of the robot during the measurements stage. A spherical reflector associated with the laser tracker is installed on the tip of the robot.

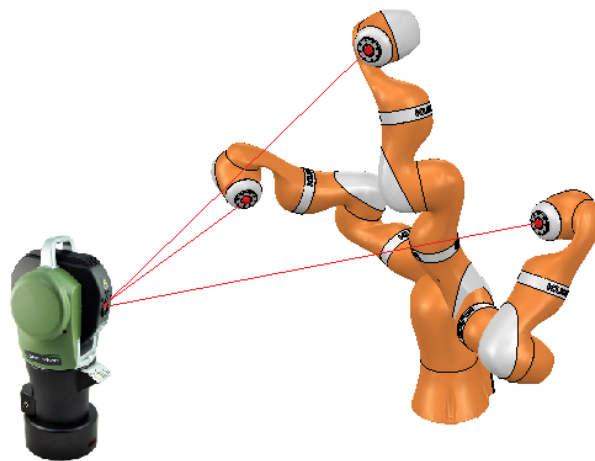


Figure 2.8: The laser tracker measures accurately the tip position, while the robot goes to all selected configurations.

which is under the repeatability of the robot. Therefore the base of the robot can be assumed steady.

2.2.2.5 Construction of the base frame

In order to express the points (x_1, \dots, x_n) in the frame R_0 , that frame can be identified by using the laser tracker. By continuously measuring the tip of the

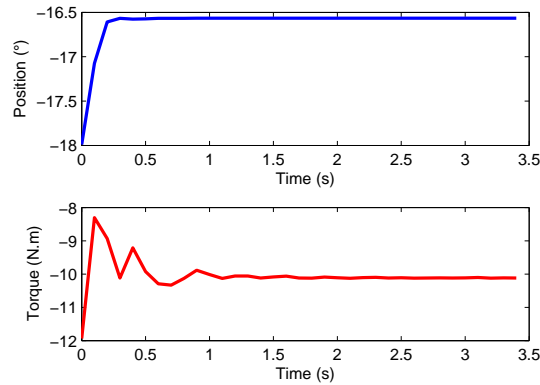


Figure 2.9: Samples of the recorded evolution of position and torque in joint 2 while the robot goes through the calibration configurations. The laser tracker waits for both the position and the torque to be steady before measuring.

robot while driving its first joint, a circular path around the z_0 vertical axis of the robot is drawn, as shown on Figure 2.10. This operation is repeated for the second joint with $\theta_1 = 0$ in order to obtain another circular path around the y_0 axis of the robot. By fitting circles to the latter paths, z_0 and y_0 are built as the axes of these circles. x_0 is obtained by :

$$\mathbf{x}_0 = \mathbf{y}_0 \wedge \mathbf{z}_0. \quad (2.9)$$

Another solution is to identify the frame R_0 along the parameters ξ .

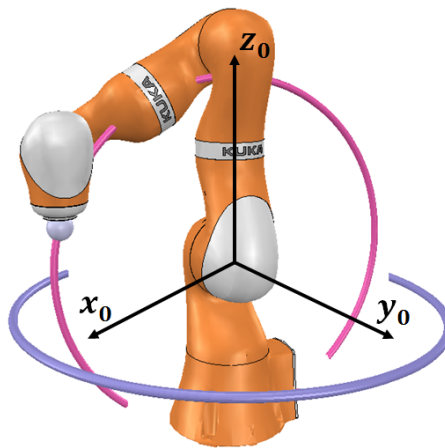


Figure 2.10: The base frame R_0 of the robot is built by fitting circles on circular path virtually drawn by the tip of the robot when moving successively joint 1 (blue circle) and joint 2 (pink circle).

Table 2.2: Identification results

$n = 50$	ξ_n	ξ_{geo}	ξ_{comp}
$\max_i(d_i)$ (mm)	2.529	0.503	0.235
$\text{mean}_i(d_i)$ (mm)	2.211	0.257	0.138
$\text{std}_i(d_i)$ (mm)	0.161	0.106	0.054

 Table 2.3: Identified parameters ξ_{geo}

j	α_j (rd)	θ_j (rd)	d_j (mm)	r_j (mm)
1	1.926e-0	-3.112e-05	0.187	359.368
2	-1.571	-0.002	0.423	-0.365
3	1.570	8.250e-05	0.693	420.768
4	1.571	-7.767e-04	-0.200	1.275
5	-1.572	6.367e-04	-0.732	399.950
6	-1.567	0	-0.642	0.068
7	1.571	-0.316	0.586	126
TCP (t_x, t_y, t_z) (mm) = (-1.609, 0.769, 74.462)				

2.2.2.6 Identification

The third stage of this experiment consists in processing the data previously collected. The Levenberg-Marquardt algorithm used in this stage is available in many development frameworks or libraries. For example, this algorithm is implemented in the *lsqnonlin* Matlab function. By using this method, the parameters ξ which minimize $\Delta X(\xi)$ are found. The calculation time of the algorithm was 1.2 seconds in the worst case. However, this calculation time is not a problem since the identification of the parameters is made off-line.

Let us note ξ_{geo} the identified parameters when only the geometric parameters are accounted for, and ξ_{comp} the identified parameters when the joints stiffnesses are included in the identification. Table 2.2 presents a comparison of the position errors on the calibration configurations using the different sets of parameters. One can note that taking the joint compliance into account reduces by half the position errors in comparison to a simple geometric calibration. It should be born in mind that the accuracy of the robot before calibration is only 2.5 mm accurate. Tables 2.3 and 2.4 respectively detail the identified parameters ξ_{geo} and ξ_{comp} .

Table 2.4: Identified parameters ξ_{comp}

j	α_j (rd)	θ_j (rd)	d_j (mm)	r_j (mm)	k_j (N.m/rd)
1	6.401e-04	-3.851e-04	0.009	360.074	∞
2	-1.571	-4.252e-04	0.078	-0.321	3.959e04
3	1.571	3.535e-04	0.428	420.085	1.22e04
4	1.571	-0.002	-0.068	-0.059	2.023e04
5	-1.570	-3.542e-04	-0.972	399.863	0.804e04
6	-1.567	0	-0.214	0.393	0.378e04
7	1.571	-0.294	0.061	126	∞
TCP (t_x, t_y, t_z) (mm) =			(-1.608, 0.745, 74.545)		

2.2.2.7 Correction

The last stage of the calibration process is to include the identified parameters in the program used to drive the robot. When a Cartesian position \mathbf{x}_t is given to the robot as new target, this Cartesian position has to be translated to a configuration \mathbf{q}_t expressed in the joint space by using an inverse geometric function. This function relies on the geometric model of the robot and its geometric parameters. Since the joints torques are measured in real time and not estimated via a model, by contrast with the literature, the joints compliance is not predicted and has to be corrected in real time. Once the robot has reached the target configuration \mathbf{q}_t , the joints torques $\boldsymbol{\tau}$ are measured, and the compliance is compensated to give a new target configuration \mathbf{q}'_t . The compliance error is corrected by using relation (2.10):

$$\mathbf{q}'_t = \mathbf{q}_t - \mathbf{c} \cdot \boldsymbol{\tau}, \quad (2.10)$$

where $\boldsymbol{\tau}$ is the $m \times 1$ current joints torques vector and \mathbf{c} the $m \times m$ compliance matrix defined as:

$$\mathbf{c} = \begin{bmatrix} 1/k_1 & 0 & \dots & 0 \\ 0 & 1/k_2 & \dots & 0 \\ \vdots & \vdots & \ddots & \vdots \\ 0 & 0 & \dots & 1/k_m \end{bmatrix}. \quad (2.11)$$

Figure 2.11 summarizes the implementation of the correction.

Let us note \mathbf{f} the forward geometric function which calculates the pose of the robot for a given configuration \mathbf{q} . The function \mathbf{f} essentially relies on relation (2.3). The inverse geometric function \mathbf{f}^{-1} gives a robot configuration \mathbf{q} for a given robot pose \mathbf{p} :

$$\mathbf{q} = \mathbf{f}^{-1}(\mathbf{p}) \quad (2.12)$$

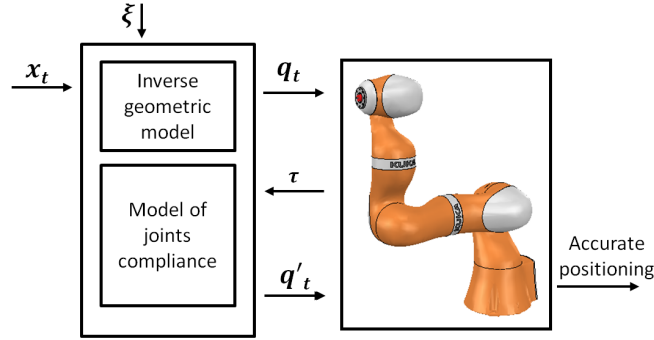


Figure 2.11: Diagram of the implementation of the online geometric and compliance errors correction.

In the case of the iiwa robot, no closed-form expression of f^{-1} can be found, for redundancy reasons. Many alternatives are available in the literature, as iterative resolution algorithms [Bus04]. The transpose jacobian method is selected in our study for its simplicity and its robustness against singularities. Figure 2.12 summarizes this approach.

```

function  $f^{-1}(p, q_{ini})$ 
     $p_c \leftarrow f(q_{ini})$ 
     $\Delta p \leftarrow p - p_c$ 
    while  $\|\Delta p\| > e$  do
         $\delta q \leftarrow \alpha J^T \Delta p$ 
         $q \leftarrow q + \delta q$ 
         $p_c \leftarrow f(q)$ 
         $\Delta p \leftarrow p - p_c$ 
    end while
    return  $q$ 
end function
    
```

- ▷ q_{ini} current or zero configuration
- ▷ e error tolerance
- ▷ J Jacobian matrix
- ▷ Check for joints bounds

Figure 2.12: Simplified Jacobian transpose method for solving the inverse geometric problem. The management of the joints bounds is not shown, for the sake of clarity.

In order to validate the correction, the accuracy of the robot after calibration has been measured on 30 new points. Table 2.5 presents the results. It can be noted that the robot is less accurate for configurations which are not part of the identification stage. This is due to the fact that the configurations used to identify the parameters let gaps in the workspace. However an accuracy of 0.4 mm is still

sufficient for many industrial applications. The author strongly believes that, for applications using a limited area of the workspace, a dedicated calibration can significantly improve the accuracy of the robot in that area.

Table 2.5: Validation

30 points	ξ_{comp}
$\max_i(d_i)$ (mm)	0.426
$\text{mean}_i(d_i)$ (mm)	0.292
$\text{std}_i(d_i)$ (mm)	0.069

2.2.2.8 Conclusion

This study proposes an advanced robot calibration method applied on a collaborative robots. Through the hand-guiding feature, there is no need to use a selection algorithm to choose the calibration configurations. Moreover, the embedded joint torque sensors of the robot are used to estimate the joints deflection, with no mass model or resolution algorithm required. Therefore the overall calibration process is straightforward to set up. Experimental results show that an accuracy up to 0.4 mm can be obtained with LBR iiwa Kuka robot against an accuracy higher than 2.5 mm before calibration. These results are presented in the conference article: P. Besset, A. Olabi and O. Gibaru, "Advanced calibration applied to a collaborative robot", in *IEEE International Power Electronics and Motion Control Conference (PEMC 2016)*, Varna 2016.

2.2.3 Application to marine loading arms

Marine loading arms are articulated structures that can be seen as robotic manipulators, in a geometric point of view. They can therefore be calibrated with similar methods. MLAs are not designed to be controlled as robots. In particular, the low stiffness of the links, cables and joints induces deflections that lead to position errors up to several decimeters on the end-effector. On the other hand, the flanging area, i.e. the volume in which the loading arm has to be accurate, is small in terms of range of the joints position. Thus in this area, the change of deflections in the structure of the arm are small, and directly compensated in the DH parameters. Experimental results presented below concur with this hypothesis, as a geometric calibration proves sufficient.

A geometric model of an MLA is built using the classic modified D-H parametrization [KD04]. Figure 2.13 shows the geometric model chosen. One can note that this model is suitable to represent the geometric structure of many types of loading arms, including OLAF, RCMA and DCMA.

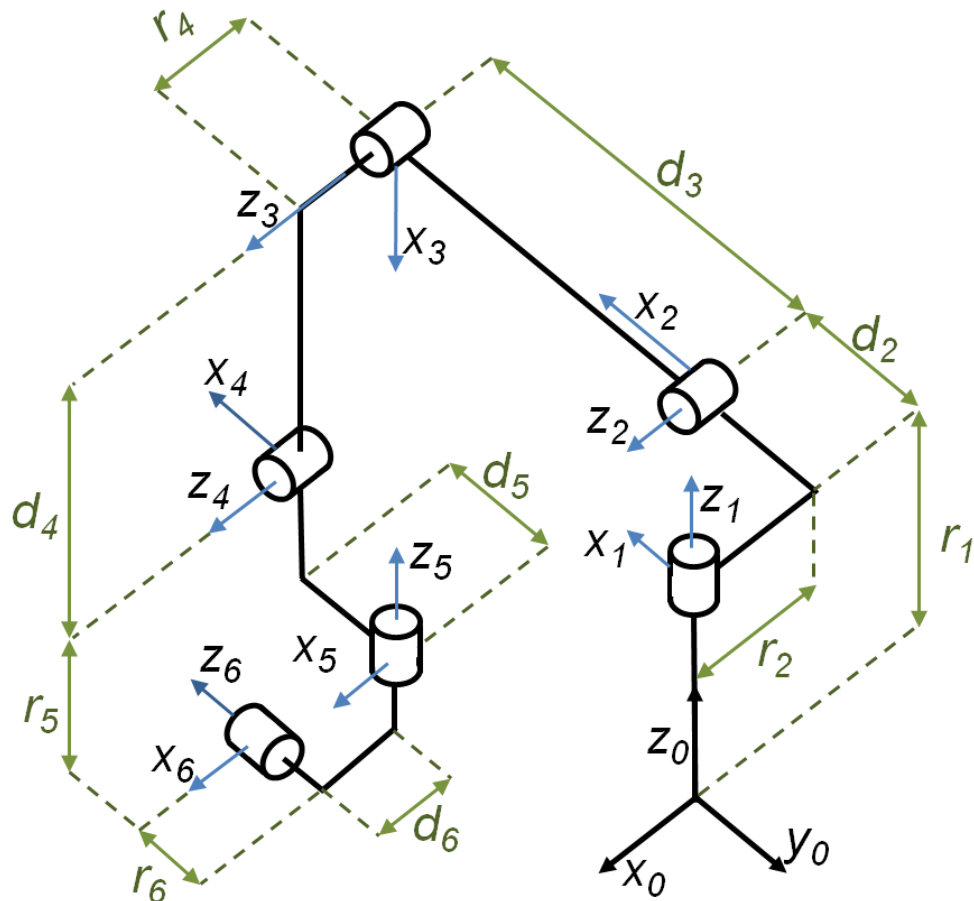


Figure 2.13: MLA in zero position: Modified DH model.

It is convenient to introduce a conventional DH joints notation for the loading arm. Figure 2.14 shows the true joint notation (green) and the joints notation following the DH convention (red). Table 2.6 shows the relation between both notations.

The repeatability and calibration experiments are conducted on the scaled OLAF model and the full scale DCMA, presented in Section 1.4. For these experiments a robotic total station, as presented in 2.1, is chosen instead of a classic metrology laser tracker. Although less accurate, the total station is robust to sun-

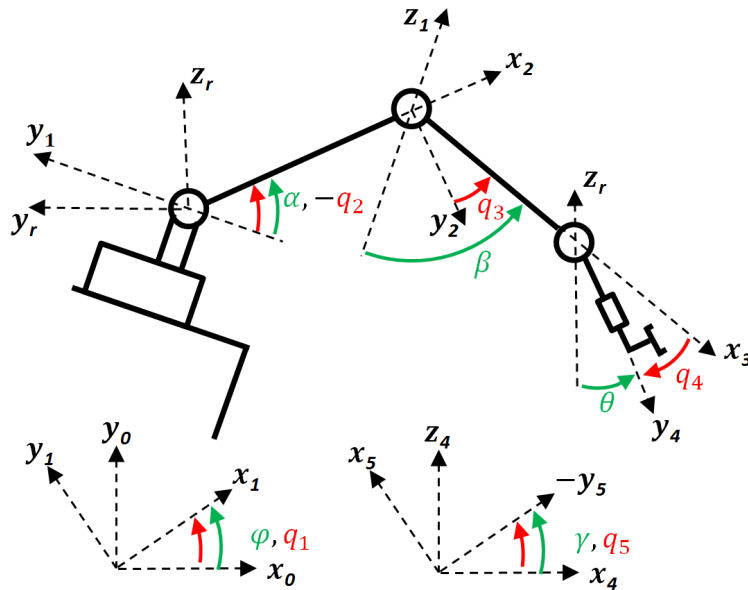


Figure 2.14: Angles notations Red: robotic convention. Green: actual joints positions .

Table 2.6: Joints position calculation

q_1	=	ϕ
q_2	=	$-\alpha$
q_3	=	$\alpha - \beta$
q_4	=	$\beta - \theta - (z_1 \wedge z_r) \cdot x_1$
q_5	=	γ

light, rain and mist, which is convenient for these outdoor experiments. The long range of this device is necessary, regarding the size of the loading arm and its layout. Finally this measurement system has the ability to automatically find and follow its target, which makes these operations easier. Figure 2.15 shows the total station measuring the position of its reflector, which is set up on the couplers of the arms, as shown on Figure 2.16.

First the repeatability of the arms is estimated. Five configurations which correspond to positions inside the flanging area are chosen, as shown on Figure 2.17. The joints controllers developed in Section 5.3.1 are used to drive the arm to each configuration successively. The configurations are sorted so that all joints are exercised during movement between them (except the fifth joint, not available as

CHAPTER 2. ACCURATE POSITIONING OF A LOADING ARM



Figure 2.15: The total station measures the position of the coupler. Picture of the OLAF scaled model.

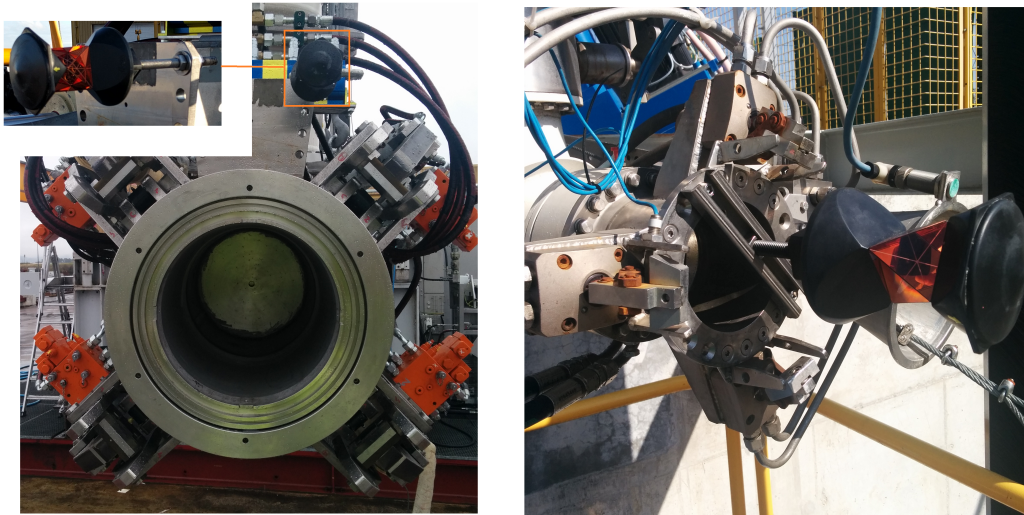


Figure 2.16: The reflector of the total station is set up on the coupler. Left picture: full scale DCMA. Right picture: scaled model.

explained in Section 1.4). When the arm reaches a configuration and is steady, the position of the coupler is measured, as well as the joints positions. The operation is automated and repeated $n_r = 30$ times. For each position the repeatability RP is calculated, according to the ISO 9283 definition [ISO98], as:

$$RP = \bar{l} + 3S_l, \quad (2.13)$$

where \bar{l} is the mean distance to the barycenter \bar{X} of the measured points:

$$l_i = \|X_i - \bar{X}\|, \quad \bar{l} = \frac{1}{n_r} \sum_{i=1}^{n_r} l_i, \quad (2.14)$$

and S_l the standard deviation:

$$S_l = \sqrt{\frac{\sum (l_i - \bar{l})^2}{n_r - 1}}. \quad (2.15)$$

Table 2.7 presents the results for the five positions.

Table 2.7: Repeatability results for the OLAF scaled model and the DCMA.

Position	scaled model RP (mm)	full scale DCMA RP (mm)
1	21	9
2	27	9
3	9	4
4	18	5
5	21	9

The results presented in Table 2.7 are unexpected. The 1/4 scaled tolerance of the coupler is 25 mm while the worst calculated repeatability is 27 mm, i.e. 108% of the tolerance. That makes the repeatability of the scaled arm too poor for the automatic connection. However the full scale DCMA presents significantly better results. The worst calculated repeatability for this arm is 9 mm, i.e. 9% of the full scale tolerance. The poor repeatability of the OLAF scaled model mainly comes from dry friction in joint 4, which keeps the Style 80 to settle, from the gravity, in its zero position. After investigation, the repeatability of joint 4 for the scaled model is 3.3 degrees, which corresponds to a 30 mm position error of the coupler .

The accuracy of the loading arms are estimated according to the method previously developed. $n = 24$ points are chosen to cover the flanging area, as shown

Table 2.8: Accuracy of the loading arms before calibration

$n = 24$	ξ_n (scaled model)	ξ_n (full scale DCMA)
$\max_i(d_i)$ (mm)	40.1	421
$\text{mean}_i(d_i)$ (mm)	24.0	217
$\text{std}_i(d_i)$ (mm)	9.1	114

on Figure 2.17. Table 2.8 presents the accuracy measured before calibration.

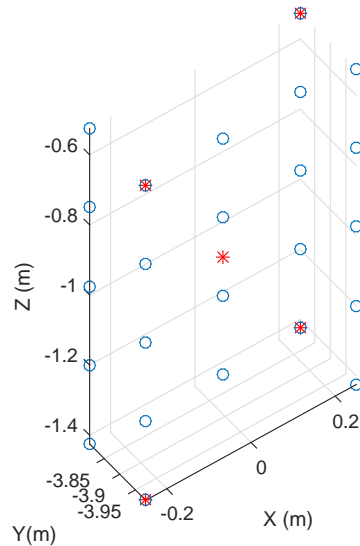


Figure 2.17: Calibration points (blue circles) and repeatability points (red stars) in the frame R_0 , for the OLAF scaled model. The calibration points map the flanging area (see Figure 1.4).

In this study the frame R_0 is identified thanks to features of the total station, which takes z_0 as the vertical axis, and y_0 from a motion of the manifold. The position of the frame R_0 is then adjusted by a least square fitting. The overall identification is performed according to the method previously presented, and the resulting DH parameters are updated in the inverse kinematics functions of the arms (See Appendix A). In order to validate this identification, sets of 50 points in the flanging areas, different from the calibration points, are chosen to measure the new accuracies. Table 2.9 presents the measured accuracies of the arms after

calibration.

Table 2.9: Accuracy of the loading arms after calibration

$n = 50$	ξ_n (scaled model)	ξ_n (full scale DCMA)
$\max_i(d_i)$ (mm)	27.1	25.5
$\text{mean}_i(d_i)$ (mm)	13.8	14.7
$\text{std}_i(d_i)$ (mm)	6.1	6.4

The calibration conducted on the OLAF scaled model and the full scale DCMA gave unexpected results. The performance of the full scale arm in terms of repeatability is much better than the scaled model. After calibration, the worst measured accuracy of the full scale DCMA is 25.5% of the tolerance of the coupler (100 mm). This value is acceptable for the automatic connection, since there is 74.5% of the tolerance left for errors from other sources, e.g. tracking error, oscillation.

Chapter 3

Experimental study of an offshore loading arm

Offshore loading arms are designed to operate with the current targeting system, that guides and stabilizes the coupler during the connection stage. The automatic connection system that is developed in this project requires an actuation system able to compensate the motion of the vessel, as well as the possibility to accurately move the loading arm. These performances, not necessary for the initial targeting system, are not guaranteed. An investigation of the MLAs hardware capabilities is therefore needed. Besides, such a study also helps to improve any simulation model used by the manufacturer. This chapter proposes an experimental study of the hardware of a loading arm. First a modal analysis of the structure of the arm is carried out, in order to evaluate how this structure will react under internal and external disturbances. Then the actuated joints of the system are studied to evaluate their dynamic capabilities. Finally, the influence of the sea and wind on the system is studied.

3.1 Experimental modal analysis

The mechanical structure of the loading arm operates under many different disturbances that can induce vibration. First of all, under the influence of sea heave and waves, the FLNG on which the MLA operates is unsteady and its motion may affect the MLA. Another source of disturbance is the wind gusts incoming on the structure of the loading arm, which could induce bending and vibration. The actuation system itself may also generate oscillation along with the desired "rigid" motion. Vibration may lead to significant error in the estimation of the position of the end-effector. Also, vibration may reduce the hardware lifetime and raise safety issues in case of large oscillation. The knowledge of the vibratory behavior of the system is therefore important to estimate the influence of the different incoming disturbances. An experimental modal analysis is performed on both the 1/4 OLAF scaled model detailed in Section 1.4.1, and a full scale DCMA presented in 1.4.2. The objective of this experiment is to determine the vibration modes of the structure of the loading arm, with their shapes and frequencies.

The frequency response function of the structure can be obtained by mechanically exciting it with signals covering the studied frequency range, and measuring its response at multiple points of the structure. Classically, e.g. in the aircraft industry, arrays of accelerometers are set up along the structure of the system, in the three spatial directions. However for a loading arm, such a method would prove costly in terms of hardware, time and complexity of setup. As an alternative, a laser vibrometer is chosen to measure the structure response. This electronic device produces a laser beam to a target point and makes use of the doppler effect to measure the velocity of this point. The velocity is measured along the beam direction, and is corrected to be expressed along a constant direction, \boldsymbol{x}_0 in this study. Figure 3.1 shows the laser vibrometer set up for the experiment. This contactless technology is convenient regarding the size and layout of the loading arm. The direction \boldsymbol{x}_0 , i.e. the surge, is chosen because the most detrimental vibration seems to be along \boldsymbol{x}_0 , regarding the general design of the structure. Also, the layout of the test yard makes it difficult to measure along other directions.

The structures of both studied arms are meshed with reflective targets to help the vibrometer to operate outdoor. Figure 3.2 shows the meshes of the structures. The scaled OLAF is set up in operating configuration $(\phi, \alpha, \beta) = (0^\circ, 5^\circ, 5^\circ)$ on a 6 DoF hexapod platform. The hexapod is used to excite the system with sinusoidal displacements along \boldsymbol{x}_0 . The acceleration of the hexapod displacement $u_1(t)$ is measured by an accelerometer. Classically, the input force is measured to obtain velocity / force transfer functions, but that was not practically possible with the

CHAPTER 3. EXPERIMENTAL STUDY OF AN OFFSHORE LOADING ARM



Figure 3.1: The laser vibrometer measures the velocity of all measurement points of the mesh. Left and bottom pictures: Head of the laser vibrometer. Right picture: Acquisition and generation system.

available hardware.

The setup of the modal analysis for the full-scale loading arm differs from the previous one, for practical reasons. The arm is set up in a configuration such as its coupler is at one meter above the yard floor, shown by Figure 3.8. In that way, a 1000 Kilo Newtons capable electromechanical exciter is anchored on the floor and excites the loading arm via the coupler, as show on Figure 3.3. Several sensors are set up to measure the input excitation. First, three accelerometers measure the acceleration of the excited point along the three spatial directions. Unfortunately no data could be exploited from these accelerometers because they are incompatible with low frequencies. The same issue is found with the force sensor set up on the exciter rod. However the intensity of the current running in the coil of the exciter is measured, so that the force $u_2(t)$ transmitted to the structure can be calculated anyway. Finally, a displacement sensor measures the displacement of the excited point of the coupler. Figure 3.4 shows the set up of these sensors. Figure 3.5 shows the overall set up of the experiment.

The two modal analyses are carried out on the frequency range [0.1Hz, 10Hz]

CHAPTER 3. EXPERIMENTAL STUDY OF AN OFFSHORE LOADING ARM



Figure 3.2: The structures of the scaled model and the full-scale loading arm are meshed with measurement points.



Figure 3.3: The excitator excites the structure of the arm via the coupler, and the transmitted force is calculated from the current in the coil.

with a maximal resolution allowed by the hardware: 62.5mHz. The input signals are sent as "periodic chirp", built in the frequency domain with a uniform ampli-

CHAPTER 3. EXPERIMENTAL STUDY OF AN OFFSHORE LOADING ARM



Figure 3.4: Pictures of the sensors set up at the excitement point.

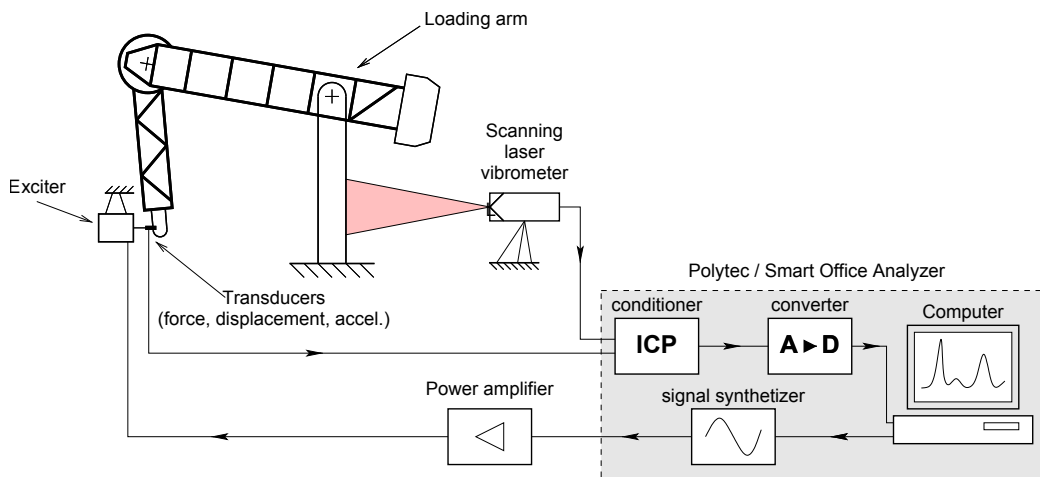


Figure 3.5: Set up of the modal analysis for the full scale arm.

tude spectrum, and obtained by inverse FFT. The velocities of the measurement points $y_{1,i}(t)$, $y_{2,i}(t)$ are measured. Figure 3.6 shows a typical chirp force input with the measured velocity response.

CHAPTER 3. EXPERIMENTAL STUDY OF AN OFFSHORE LOADING ARM

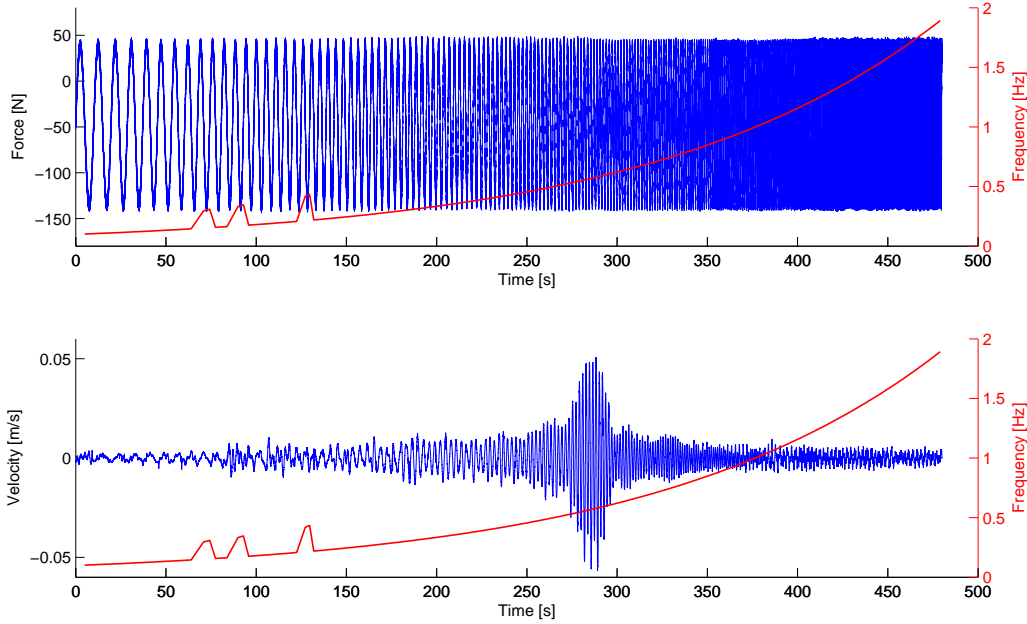


Figure 3.6: Temporal evolution of the force input (top graph) and the associate velocity response (bottom graph) at the excitation point of the full scale DCMA. Example of a chirp with a logarithmic evolution of the frequency (red lines).

The recorded signals are expressed in the frequency domain by using fast Fourier transforms (FFT):

$$\begin{aligned} U_i &= \mathcal{F}(u_i), \quad i \in \{1, 2\} \\ Y_{i,j} &= \mathcal{F}(y_{i,j}) \quad j \text{ index of the measured point} \end{aligned} \quad (3.1)$$

The noise of U_i and $Y_{i,j}$ is reduced by averaging the signals five times with an overlap of 75%. Frequency response functions (FRF) are then automatically calculated by the vibrometer as:

$$G_{i,j}(f) = \frac{Y_{i,j}(f)}{U_i(f)} \quad (3.2)$$

Figure 3.7 shows \hat{G}_1 and \hat{G}_2 the spatial average of the FRFs along the structures (top graphs). The bottom graphs of this figure shows the FRF produced from the response of the coupler: $G_{1,\text{coupler}}$ and $G_{2,\text{coupler}}$. These FRFs are particularly interesting since the oscillation of the coupler directly affects the precision of the arm.

The operational shapes of the structures can then be constructed. Table 3.1 shows the operational shapes of the three first modes of the structures with their

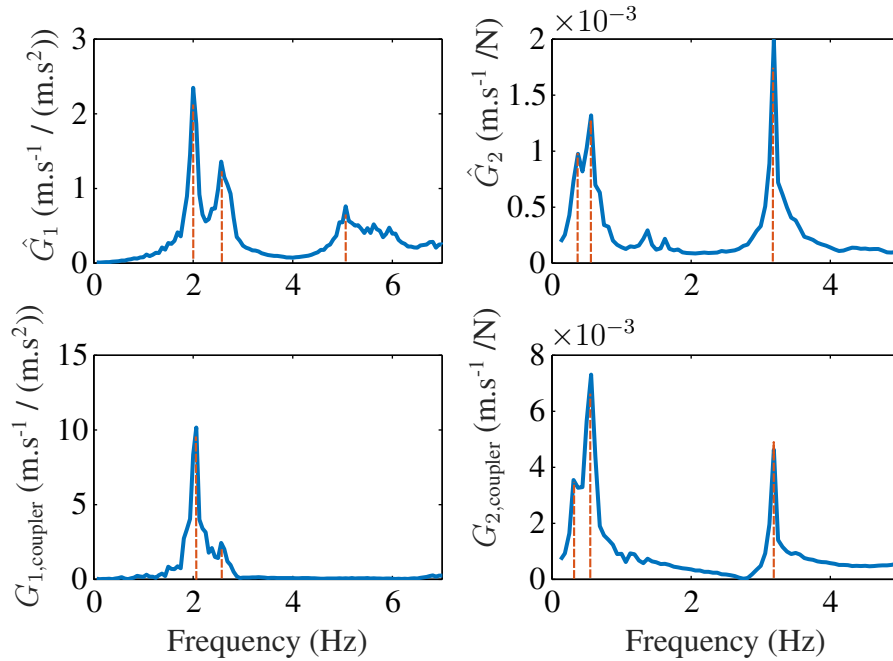


Figure 3.7: Experimental frequency response functions of the arms along x_0 . Left graphs: scaled model, Right graphs: full-scale arm. Top graphs: mean responses, Bottom graphs: responses at the coupler. Frequency resolution = $6.25 \cdot 10^{-2}$ Hz.

frequencies.

The knowledge collected during this experiment will be used in the following sections. In particular, the frequency responses of the structures will be compared to the dynamic capabilities of the actuators and the frequency spectrum of the FLNG motion. Notes :

- The piezoelectric based sensors (force transducers, accelerometers) badly worked at low frequencies (<0.5 Hz), and their data could not be used.
- The laser vibrometer turned out to be an adequate choice. First, it is not limited in low frequencies as accelerometers. The intensity of the laser signal was very good (average 80%) at a range of 40 meters, with reflecting targets. This made it possible to obtain measurements with very low noise.
- Binoculars were necessary when aiming the laser at the reflecting target, in order to record the mesh in the vibrometer.
- The stroke of the exciter should be long enough to support the oscillation of the arm. As a reference, the stroke of the exciter was 75 mm, too short to

CHAPTER 3. EXPERIMENTAL STUDY OF AN OFFSHORE LOADING ARM

comfortably conduct the experiment.

Table 3.1: First measured modes: frequencies and operational shapes

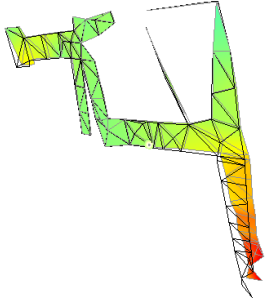
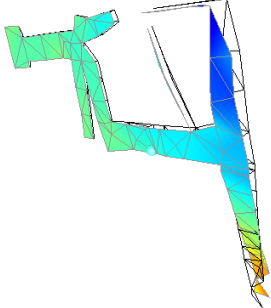
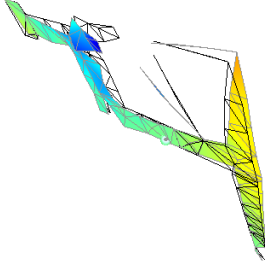
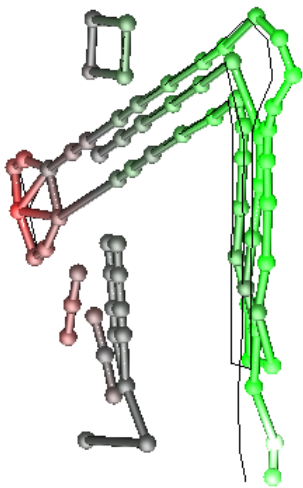
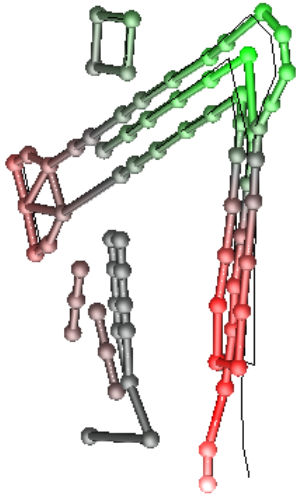
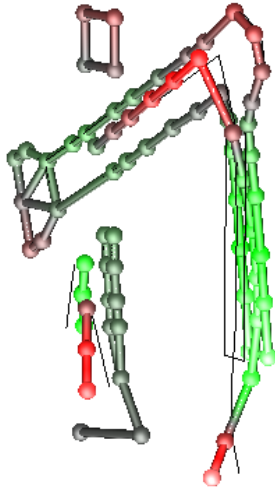
OLAF scaled model		
2.0 Hz	2.56 Hz	5.31 Hz
		
Full scale DCMA		
0.37 Hz	0.56 Hz	3.69 Hz
		



Figure 3.8: Setup of the full scale DCMA.

3.2 Experimental study of the joints

In this Section the term "joint" refers to the set of hardware {hydraulic circuit + valves + cylinder + load}. The knowledge of the dynamic behavior of the joints is important to choose planning and control strategies. It is also interesting to compare the the bandwidth of the joints with the modes of the structure. Indeed vibration may be induced in the structure of the loading arm by simply driving the cylinders. An experimental identification is thus led on both the 1/4 scaled OLAF model and the full scale loading arm. The three first joints of the loading arms are actuated by hydraulic cylinders, as shown on Figure 1.10. The loading arms made available for this research project do not have adequate actuating and monitoring systems for the swivel (5th) joint. Therefore these joints are left aside in this study.

Before this study, the system is warmed up with repetitive motion of all joints,

in order to let the temperature of its oil reach a permanent value. It has been visually observed that the behavior of the joints significantly changes whether the arm is warmed up or not, although no data were collected to support this observation. The hexapod table of the scaled OLAF is motionless and horizontal for all experiment, unless otherwise specified.

3.2.1 Step responses of the joints

First the step responses of the joints are studied. A series of step inputs is sent to each joint, one by one. The input is the opening rate of the proportional spool valve. The position response of the joint is recorded from its sensor. A total station, as presented in Section 2.1, is used to monitor the Cartesian position of the coupler X_c during this experiment on the full scale arm.

Since the positions of the inboard and outboard links change the inertia of the arm about z_1 , the response of the slewing joint may change with α and β . This study focuses on the behavior of the system for "deployed" configurations, where the coupler is inside the flanging area, where accuracy is needed. This scope of configuration being small ($(\Delta\phi, \Delta\alpha, \Delta\beta) < (5^\circ, 15^\circ, 10^\circ)$), the behavior of the arms is assumed constant within this scope. Typical step responses of the joints are given on Figure 3.9. Position transducers responses are given on the top and middle rows (blue lines). The bottom row gives the evolution of the position of the coupler along the appropriate direction. The step inputs (red areas) are set at +15%.

From Figure 3.9 one can observe that the cylinders of the scaled model respond with oscillation to step inputs. That is not the case with the full scale arm, where the no oscillation of the cylinders rods is measured. However one can visually see that the structure of the full scale arm respond with large oscillation, as recorded by the total station.

The mean measured delays on the position response of the joints are given in Table 3.2.

The measured delays presented in Table 3.2 are small regarding the operating frequencies of the joints (see Figure 3.11), and proved not to led to any difficulty in the low level control (see Section 5.3.1).

The evolution of the steady state gain of the joints regarding the value of the valves inputs is measured. Let us note $K_i(u)$, $\forall i \in \{1, 2, 3\}$, the steady state gain of the joint i for the input u . Step inputs are sent on the used range [-15%,

CHAPTER 3. EXPERIMENTAL STUDY OF AN OFFSHORE LOADING ARM

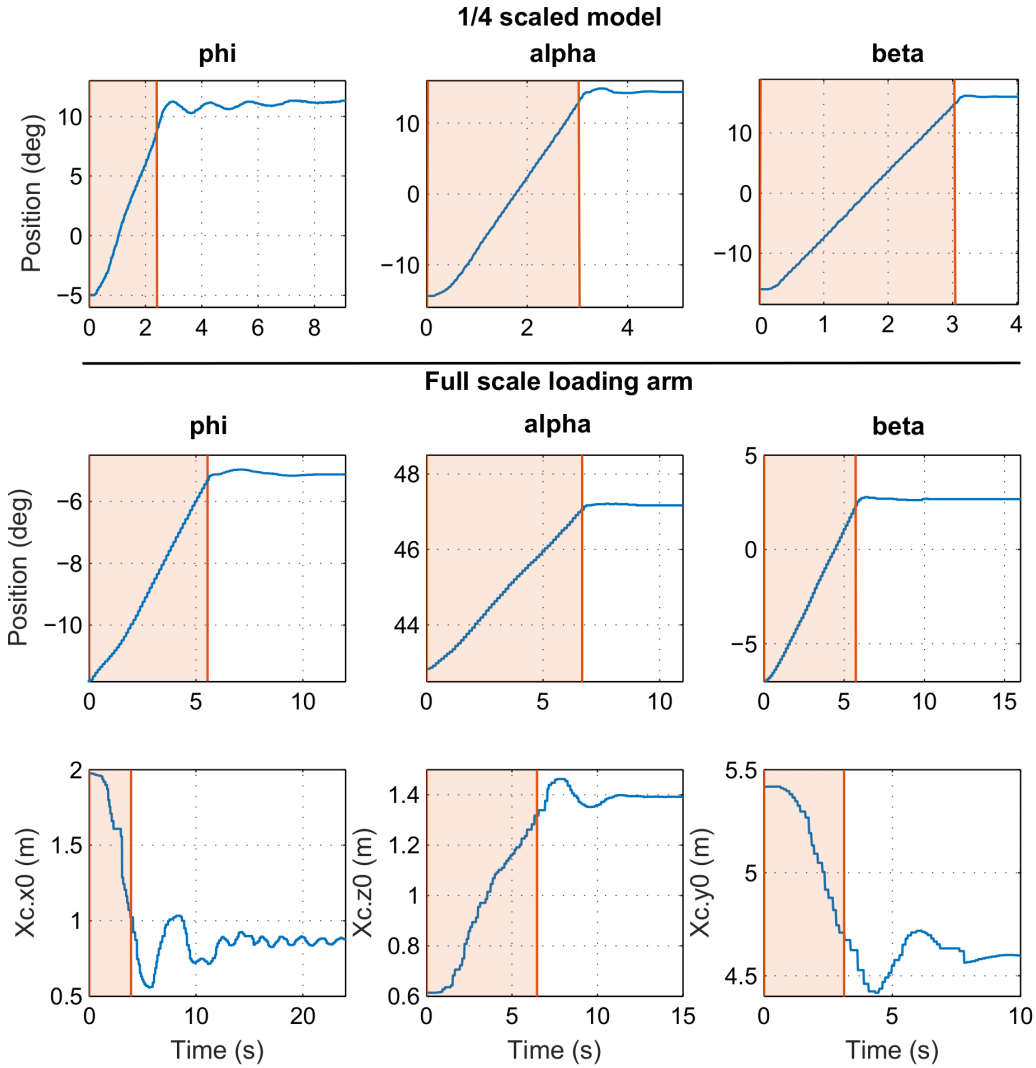


Figure 3.9: Top and middle rows: responses of cylinders position sensors (blue lines) to step inputs. Bottom row: evolution of the position of the coupler X_c along one dimension. Step inputs are set to +15% in term of valve opening rate.

+15%] with a spacing of 0.1% around the zeros and otherwise 1%. For each input the velocity is measured when steady. Figure 3.10 show the results. One can note that the steady state gains of the joints are not constant, and present dead-zones and offsets, for both arms. Functions K_i^{-1} are built in order to compensate these effects when driving the joints. For instance, if a velocity signal $\omega(t)$ is wanted for the i^{th} joint, the right signal $u(t)$ to send to the valve is:

$$u(t) = K_i^{-1}(\omega(t)) \quad (3.3)$$

Table 3.2: Delay of the joints responses.

	Scaled OLAF	Full scale DCMA
Joint 1	0.18 s	<0.10 s
Joint 2	0.15 s	<0.10 s
Joint 3	0.15 s	<0.10 s

These functions are made by fitting polynomials on the curves $u = f(\omega)$. These functions are mainly used for the low level control, in Section 5.3.1.

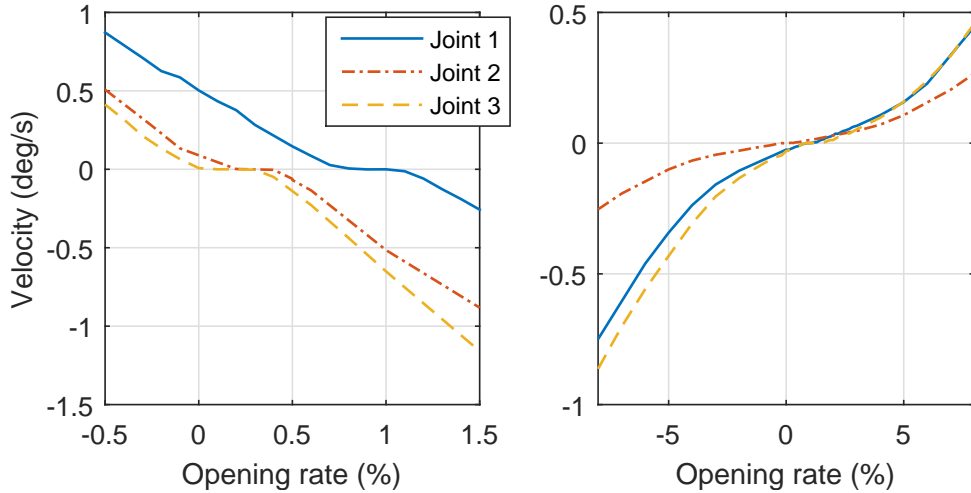


Figure 3.10: Experimental identification of the steady state gains of joints 1, 2 and 3. One can observe dead zones and offsets. Left graph: OLAF scaled model, zoom on the dead zones. Right graph: full scale DCMA.

3.2.2 Bandwidth of the joints

The bandwidths of the joints are evaluated, by plotting experimental gain Bode diagrams. Sine signals w_{in} are sent as inputs such as:

$$\omega_{in}(t) = A_{in} \sin(2\pi ft), \quad (3.4)$$

with $A_{in} = 5$ deg/sec and f the current frequency. These signals are directly sent to the spool valves, in open-loop. The amplitudes of the velocity responses $A_{out}(f)$ are measured. The frequency ranges and resolutions with which the inputs are sent

CHAPTER 3. EXPERIMENTAL STUDY OF AN OFFSHORE LOADING ARM

differ from one joint to another, according to its response. Gain Bode diagrams are plotted as:

$$G_i(f) = 20 \log\left(\frac{A_{out}(f)}{A_{in}}\right), \forall i \in \{1, 2, 3\}. \quad (3.5)$$

The whole operation is done three times for each joint of the scaled OLAF, twice for the first and second joints of the full scale DCMA, and only once for its third joint. These numbers of tests are kept low because this experiment is time consuming regarding the low availability of the hardware. The third joint of the full scale arm is only tested once with a low resolution because resonance phenomena were visually observed. This operation was judged unsafe for the hardware and the operator and was therefore stopped. Figure 3.11 shows the average gain Bode diagrams of the joints. For the slewing joint of the scaled model, the experiment is conducted in both parking and working configurations.

The observation of the graphs of Figure 3.11 gives an estimation of the bandwidth of the joints, summarized in Table 3.3. One can also observe antiresonance on several of these responses. The origin of these phenomena is no further investigated.

Table 3.3: Bandwidth of the joints

	Scaled OLAF	Full scale DCMA
Joint 1 (Hz)	0.56	0.25
Joint 2 (Hz)	0.56	0.54
Joint 3 (Hz)	1.85	0.25

3.2.3 Oscillation of joint 4

The fourth joint, which links the Style 80 to the outboard link, is not actuated. This joint is left free to oscillate as a pendulum. Such oscillations, even with small angles, may induce significant errors of the position of the coupler. For instance an oscillation with an amplitude of 2° induces an oscillation of 95 mm of the position of the coupler. For this reason the oscillation frequency of the coupler is determined for small angles of θ .

The oscillation periods and frequencies are calculated as:

$$T_{calc} = 2\pi \sqrt{\frac{J}{mgl}}, \quad (3.6)$$

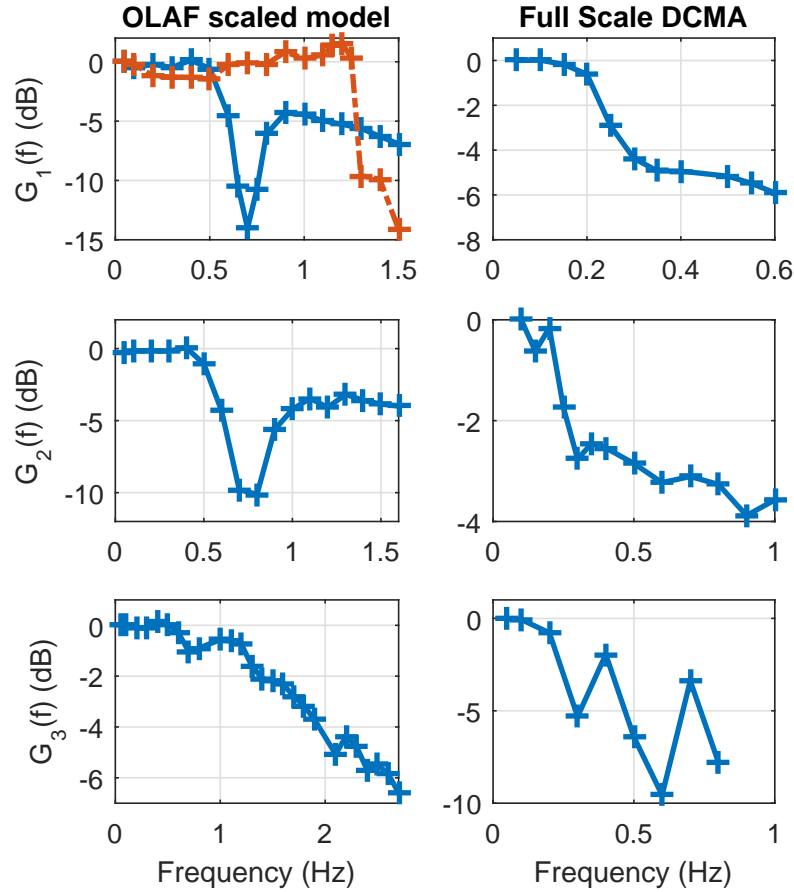


Figure 3.11: Gain Bode diagrams of the actuated joints: 1,2,3,and 5 from the top left to the bottom right. The gain of the first joint (slewing) is plotted both for the parking (dashed red line) and the working configurations.

and

$$f_{calc} = \frac{1}{T_{calc}}, \quad (3.7)$$

where J , m and l respectively denote the inertia about the rotation axis of the joint 4, the mass, and the distance of the center of gravity about the latter axis. These parameters are provided by the manufacturer. g denotes the acceleration of the gravity. The calculation is made for both the scaled OLAF and the full scale DCMA. This oscillation period is also measured by recording the evolution of θ when $\theta < 5^\circ$, after a step motion of the outboard joint. The operation is repeated ten times, for both arms. The average measured period T_{mes} is given in Table 3.4. The standard deviation is, in the two cases, less than 0.02 s.

Table 3.4: Style 80 oscillation frequencies

	Scaled OLAF	Full scale DCMA
T_{calc} (s)	1.50	3.70
f_{calc} (Hz)	0.67	0.27
T_{mes} (s)	1.48	3.44
f_{mes} (Hz)	0.68	0.29

Figure 3.12 compares the frequencies of both Styles 80 with the gain Bode diagrams of the joints. It concurs with the visual observation that:

- the Style 80 of the scaled model easily oscillates from motion of the joint 3.
- the Style 80 of the full scale arm easily oscillates from motion of joints 2 and 3.

3.2.4 Conclusion and recommendations

The observation of the systems shows that the OLAF scaled model and the full scale DCMA behave differently. The mechanical structure of the scaled model may be assumed as rigid when the system is driven, but not its hydraulic circuit. As a result a part of the oscillation, that corresponds to deformation of the hoses an oil compression, is observable from the position transducers of the cylinders. Other oscillation e.g. cables deformation or backlashes remain unseen because undergoing "after" the cylinder encoders. The full scale arm, on the other hand, has a structure very flexible and oscillate easily while the rods of the cylinders stay steady from a stiff hydraulic circuit. As a consequence the oscillation of the full scale arm is not observable. Figure 3.12 compares the gains of the joints with the average frequency responses of the structures obtained from the modal analysis. One can observe that the bandwidths of the joints are below (about 4 times) the first mode of the structure. That is also the case for the full scaled arm, although the gap is smaller (25%). Consequently active vibration damping cannot be implemented by using the cylinders. Moreover it is important to highlight that the modal analysis did only observe the modes of the structure along x_1 , and unknown modes in the plan (y_1, z_1) are also to be considered. From these observations it can be stated that:

- The scaled model and the full scaled arm have a significantly different behavior, and methods developed for the former might not be adequate for the latter.

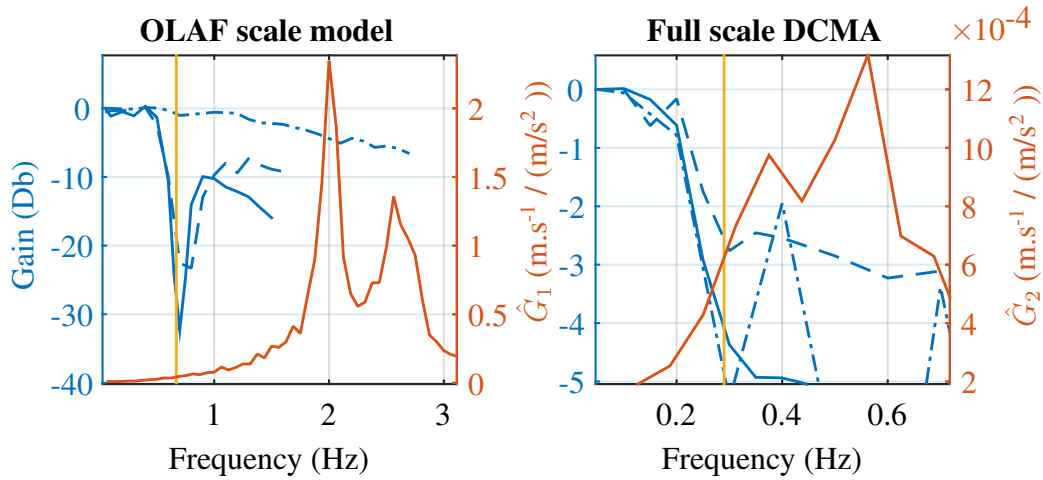


Figure 3.12: The gain Bode diagrams of the joints (blue lines, full: joint 1, dashed: joint 2, dot-dashed: joint 3) are compared to the average FRF of the structures of the arms (red lines). The measured frequencies of the oscillation of the Style 80 are plotted as the vertical orange lines.

- Active damping cannot be implemented on the full scale arm unless adding extra sensors, because the oscillation are not observable by the monitoring system of the arm.
- Smooth trajectories should be used to drive the system, in order not to make it oscillate.

The study of the gains of the joints proved essential to drive the arms. Indeed the measured offsets and zeros have a significant detrimental impact on the control of the joints and must be compensated.

3.3 Influence of the wind and the sea

The sea induces undesired motion of the vessels. This motion may be expressed as evolution of the poses ${}^r P_0$ and ${}^r P_m$. The main detrimental effects that can be forecast are:

- A relative motion between the two vessels, that makes ${}^0 P_m$ unsteady and difficult to follow with the arm,
- Important inertial effects induced in the system,

CHAPTER 3. EXPERIMENTAL STUDY OF AN OFFSHORE LOADING ARM

- The excitement of one or several vibration modes of the structure of the loading arm.

In order to study the effects of the vessels motion on the loading arm, simulated motion is provided by the manufacturer. Indeed, no recorded motion is available for this study. In this section, the simulation method is briefly described. Then the vibratory and dynamical effects induced by of the FLNG motion are studied.

3.3.1 Influence of the wind

One major disturbance in oceanic environment is the wind. It is known from visual observation during the test campaign that end of the full scale arm does move under strong wind. This motion correspond to an oscillation of the external link about y_1 , similar to the first or second operational shape presented on Table 3.1. No data was measured to support this observation because of the lack of adequate sensor. In this project the study of the effects of the wind on the arm is left aside and it is assumed that the automatic connection takes place under no significant wind.

3.3.2 Vessels motions simulation

FLNG and LNGC motions can be simulated, on the basis of a sea state and a so-called Response Amplitude Operator (RAO). The sea state characterizes the sea in terms of waves direction, height and period. A sea state can also be defined by its wave energy density spectrum. A reference sea environment chosen by the manufacturer to validate the overall connection process is given in Table 3.5. Although wind sea, with higher frequencies, is generally included in the sea state, this case takes only the swell into account.

Table 3.5: Reference Sea state

Significant wave height:	2.0 m
Mean wave period:	9.0 s
Waves direction:	$-y_0$

This sea state corresponds to a JONSWAP wave power spectrum given on Figure 3.13. JONSWAP (Joint North Sea Wave Project) is an empirical model of

CHAPTER 3. EXPERIMENTAL STUDY OF AN OFFSHORE LOADING ARM

monodirectional sea waves spectrum [JP02]. The direction of the incoming wave is chosen as $-\mathbf{y}_0$. This direction is considered as a worst case since it maximizes the roll.

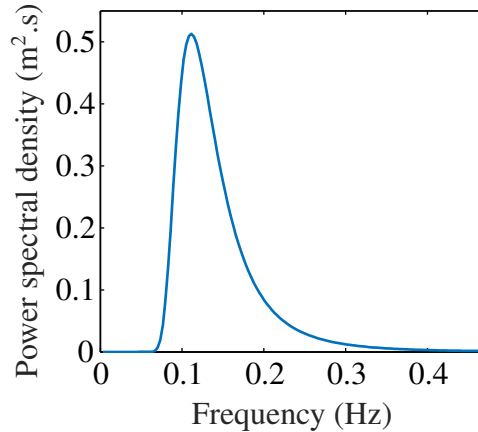


Figure 3.13: JONSWAP wave power density spectrum for the reference sea state.

The RAO is a transfer function that gives the response of the ship motion, for the six DOFs, under the influence of the sea. The RAO of a ship depends on many parameters, e.g. its size, shape, mass distribution, damping. Hence the RAO of a tanker changes according to the quantity of LNG that it carries. In the context of loading arms, the RAOs used in simulations are experimentally determined on scaled models, and are enhanced with nonlinear multiphysic simulations. The study of the RAOs of the FLNG and LNGC is beyond the scope of this project and will not be further described. By using seeds, i.e. random phase values, wave time series may be produced. Figure 3.14 summarizes the simulation of the vessels motions in our study.

The vessel motion thus obtained is a six dimensional time series. Its position is expressed in the initial frame of the vessel R_r . Its orientation is expressed as the nautical angles pitch, roll and yaw, i.e. the Euler angles with the "ZYX" convention. For the FLNG, this signal is transformed to represent the pose ${}^r P_0(t)$ of the foot of the loading arm. For the LNGC, it is transformed to represent the pose of the manifold ${}^r P_m(t)$. The involved frames and notation are presented in Section 1.3.1. These motion time series will be referred as the reference vessel motion in the following of this document.

A fast Fourier transform (FFT) is applied to the time series of ${}^r P_0$. The re-

CHAPTER 3. EXPERIMENTAL STUDY OF AN OFFSHORE LOADING ARM

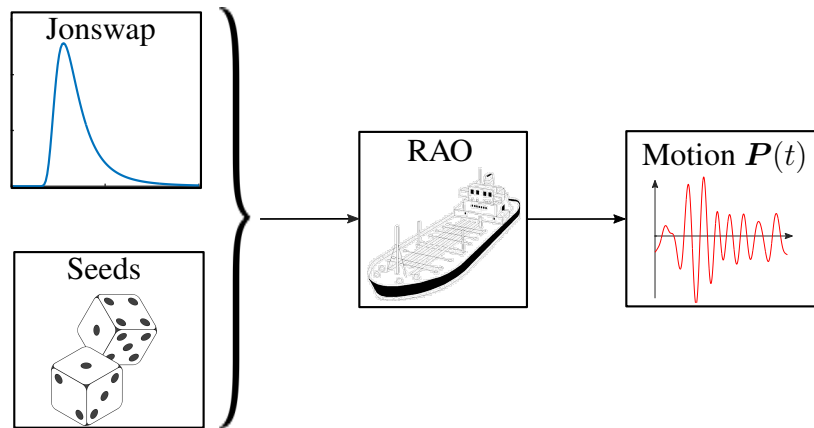


Figure 3.14: Simulation of a vessel motion. The power spectrum and the seeds make a wave time series, which is translated into vessel motion by the RAO.

sulting spectra are shown on Figure 3.15. In particular, the surge spectrum is compared to the FRF of the structure of the loading arm. Figure 3.16 shows that both spectra are on separated frequency ranges. Therefore the modes of the arm structure will not be excited by the FLNG motion.

CHAPTER 3. EXPERIMENTAL STUDY OF AN OFFSHORE LOADING ARM

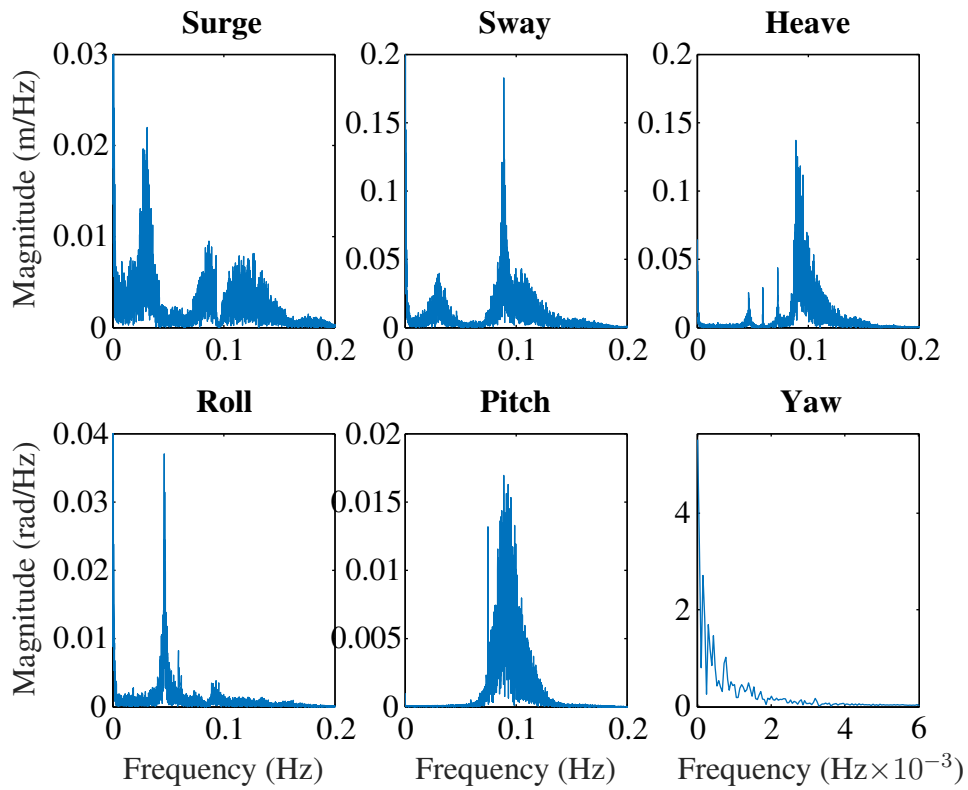


Figure 3.15: FLNG motion spectra.

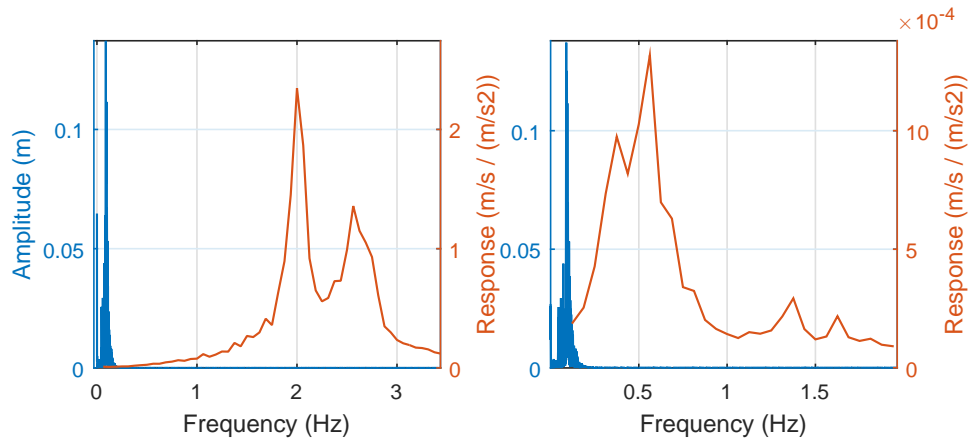


Figure 3.16: The surge spectrum (blue) and the FRFs of the arms structures (red) do not share frequencies. Left graph: OLAF scaled model. Right graph: full scale DCMA.

3.3.3 Influence of the inertial effects

The vessel on which the loading arms are set up moves under the influence of the sea and the wind. Thus this vessel can be seen as a non-inertial base which induces inertia forces in the MLA structure. These inertial effects, which are not measured, may lead to detrimental disturbances for the control of the arm motion. The literature proposes some examples of such cases, for which the motion of a non-inertial base is accounted for. Küchler *et al.* [KMN⁺11] detail a control algorithm applied to an onboard crane system. The position of the payload of the crane is controlled by taking account of the ship motion and prevents detrimental oscillations. The study presented in [FGLA11] proposes to anticipate and take advantage of the inertial effects that apply to an onboard robotic manipulator. In this context the controller of the robot makes sure not to move against the inertia forces and uses them to reduce its energy consumption. In both of these cases, the ship motion is predicted to anticipate the inertial effects that apply to the system.

In order to simulate the inertial effects of the vessel motion on the MLA, the equations of motion of the system are needed. These equations express the joints torques according to the state of each degree of freedom of the system. In our context the chosen system consists of the loading arm, with the five DoFs of the joints, plus the FLNG, with six DoFs. To derive the equations of motion a multi-body dynamic model is needed. Many handbooks propose methods to build such models. In particular, [Cra05] and [KD04] deal with rigid multibody models for serial manipulators. One of the most popular methods is the Lagrangian dynamic formulation. This method consists in using an energetic approach to derive the equations of motion of the robot. Another classic method is the Newton-Euler approach, based on Newton's laws. The latter method is selected for its easiness of implementation with serial mechanisms. Figure 3.17 presents a diagram of a generic loading arm to support the dynamic model developed in this section.

In this section the DH joints notation convention introduced in Chapter 2 (see Figure 2.14) is used, for convenience in the calculation

3.3.3.1 Dynamic modeling

A full rigid multibody model of the arm is built, accounting for all parts, is built. Let us note in this section:

- $\boldsymbol{\tau}$ the joints torques vector: $\boldsymbol{\tau} = [\tau_1, \tau_2, \tau_3, \tau_4, \tau_5]^T$.
- $\boldsymbol{q}_{ext} = [\boldsymbol{q}^T, {}^r\boldsymbol{q}_0^T]^T$ the joint position vector, extended with ${}^r\boldsymbol{q}_0$ the 3 rotation vector of frame R_0 in frame R_r .

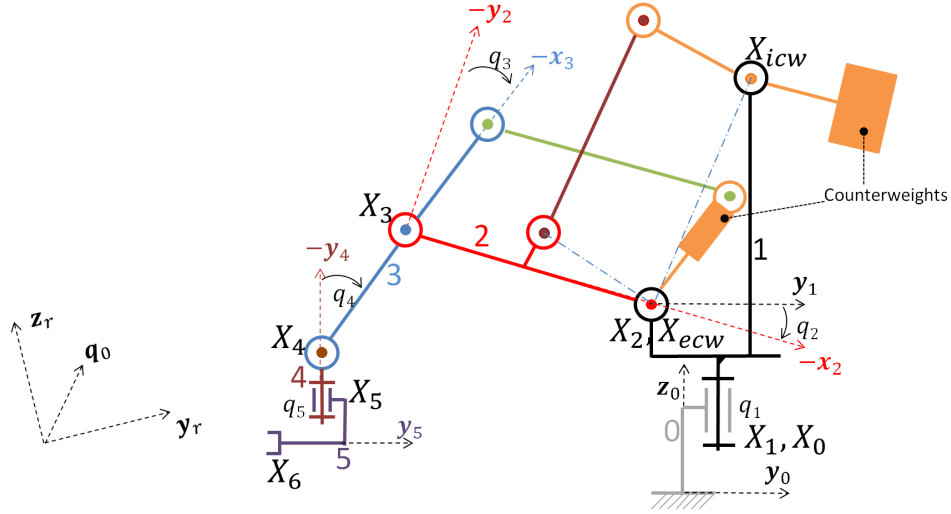


Figure 3.17: Diagram of a generic loading arm for dynamic modeling.

- \dot{V}_0 the acceleration of the FLNG in the frame R_r : $\dot{V}_0 = \frac{d^2 {}^r X_0}{dt^2}$

This dynamic model should account for the FLNG motion, assumed as known in this section. It should lead to the motion equation of the loading arm, such as:

$$\tau = M(q_{ext})\ddot{q} + V(q_{ext}, \dot{q}_{ext}) + G(q_{ext}, \dot{V}_0) + B(q_{ext}, \ddot{q}_0), \quad (3.8)$$

or

$$\ddot{q} = M^{-1}(q_{ext}) \left[\tau - V(q_{ext}, \dot{q}_{ext}) - G(q_{ext}, \dot{V}_0) - B(q_{ext}, \ddot{q}_0) \right], \quad (3.9)$$

with:

- M the 5×5 inertia matrix.
- V the 5×1 vector which represents the centrifugal and Coriolis effects.
- G the 5×1 vector which includes the gravity effects, as well as the acceleration of the FLNG.
- B the 5×1 vector which includes the effects of the rotational acceleration of the FLNG.

This model does not account for external disturbances, e.g. wind.

The first stage of the Newton-Euler algorithm is the derivation of the acceleration of each body of the system.

CHAPTER 3. EXPERIMENTAL STUDY OF AN OFFSHORE LOADING ARM

Derivation of velocities and accelerations

Let us note:

- \mathbf{a}_i the rotation axis of joint i .
- $\boldsymbol{\omega}_i$ the rotational velocity of the frame \mathcal{R}_i regarding the frame \mathcal{R}_r .
- $\dot{\boldsymbol{\omega}}_i$ the rotational acceleration of the frame \mathcal{R}_i regarding the frame \mathcal{R}_r .

For each frame, the rotational velocity is derived.

$${}^0\boldsymbol{\omega}_0 = {}^r\mathbf{R}_0^T \cdot \dot{\mathbf{q}}_0, \quad (3.10)$$

for i from 1 to 5:

$${}^i\boldsymbol{\omega}_i = {}^{i-1}\mathbf{R}_i^T \cdot {}^{i-1}\boldsymbol{\omega}_{i-1} + \dot{\mathbf{q}}_i \cdot {}^i\mathbf{a}_i. \quad (3.11)$$

The angular acceleration can then be calculated.

$${}^0\dot{\boldsymbol{\omega}}_0 = {}^r\mathbf{R}_0^T \cdot \ddot{\mathbf{q}}_0, \quad (3.12)$$

for i from 1 to 5:

$${}^i\dot{\boldsymbol{\omega}}_i = {}^{i-1}\mathbf{R}_i^T \cdot {}^{i-1}\dot{\boldsymbol{\omega}}_{i-1} + {}^{i-1}\mathbf{R}_i^T \cdot {}^{i-1}\boldsymbol{\omega}_{i-1} \wedge \dot{\mathbf{q}}_i \cdot {}^i\mathbf{a}_i + \ddot{\mathbf{q}}_i \cdot {}^i\mathbf{a}_i \quad (3.13)$$

Let us note

- \mathbf{G}_i the center of mass of link i .
- $\dot{\mathbf{v}}_i$ the acceleration of the frame R_i regarding R_r : $\dot{\mathbf{v}}_i = \frac{d^2 {}^r\mathbf{X}_i}{dt^2}$
- $\dot{\mathbf{v}}_{G_i}$ the acceleration of \mathbf{G}_i regarding R_r : $\dot{\mathbf{v}}_{G_i} = \frac{d^2 {}^r\mathbf{G}_i}{dt^2}$
- g the acceleration of gravity, assumed at $9.81 \text{ m}\cdot\text{s}^{-2}$

The accelerations can be successively derived:

$${}^0\dot{\mathbf{v}}_0 = {}^r\mathbf{R}_0^T \cdot ({}^r\dot{\mathbf{V}}_0 + g \cdot {}^r\mathbf{z}_r) \quad (3.14)$$

for i from 1 to 5:

$${}^i\dot{\mathbf{v}}_i = {}^{i-1}\mathbf{R}_i^T \cdot ({}^{i-1}\dot{\boldsymbol{\omega}}_{i-1} \wedge {}^{i-1}\mathbf{X}_i + {}^{i-1}\boldsymbol{\omega}_{i-1} \wedge ({}^{i-1}\boldsymbol{\omega}_{i-1} \wedge {}^{i-1}\mathbf{X}_i) + {}^{i-1}\dot{\mathbf{v}}_{i-1}) \quad (3.15)$$

Also, the acceleration of \mathbf{X}_{icw} et \mathbf{X}_{ecw} are respectively:

$${}^2\dot{\mathbf{v}}_{icw} = {}^1\mathbf{R}_2^T \cdot ({}^1\dot{\boldsymbol{\omega}}_1 \wedge {}^1\mathbf{P}_{icw} + {}^1\boldsymbol{\omega}_1 \wedge ({}^1\boldsymbol{\omega}_1 \wedge {}^1\mathbf{P}_{icw}) + {}^1\dot{\mathbf{v}}_1) \quad (3.16)$$

and

$${}^3\dot{\mathbf{v}}_{ecw} = {}^2\mathbf{R}_3^T \cdot ({}^2\dot{\boldsymbol{\omega}}_2 \wedge {}^2\mathbf{P}_{ecw} + {}^2\boldsymbol{\omega}_2 \wedge ({}^2\boldsymbol{\omega}_2 \wedge {}^2\mathbf{P}_{ecw} + {}^2\dot{\mathbf{v}}_2)) \quad (3.17)$$

Finally, the acceleration of the center of mass of each link is derived.
for i from 1 to 5:

$${}^i\dot{\mathbf{v}}_{G_i} = {}^i\dot{\boldsymbol{\omega}}_i \wedge {}^i\mathbf{G}_i + {}^i\boldsymbol{\omega}_i \wedge ({}^i\boldsymbol{\omega}_i \wedge {}^i\mathbf{G}_i) + {}^i\dot{\mathbf{v}}_i \quad (3.18)$$

The accelerations of the centers or mass of the internal and external counterweights, respectively noted $\dot{\mathbf{v}}_{icw}$ and $\dot{\mathbf{v}}_{ecw}$, are also needed:

$${}^2\dot{\mathbf{v}}_{G_{icw}} = {}^2\dot{\boldsymbol{\omega}}_2 \wedge {}^2\mathbf{G}_{icw} + {}^2\boldsymbol{\omega}_2 \wedge ({}^2\boldsymbol{\omega}_2 \wedge {}^2\mathbf{G}_{icw}) + {}^2\dot{\mathbf{v}}_{icw} \quad (3.19)$$

$${}^3\dot{\mathbf{v}}_{G_{ecw}} = {}^3\dot{\boldsymbol{\omega}}_3 \wedge {}^3\mathbf{G}_{ecw} + {}^3\boldsymbol{\omega}_3 \wedge ({}^3\boldsymbol{\omega}_3 \wedge {}^3\mathbf{G}_{ecw}) + {}^3\dot{\mathbf{v}}_{ecw} \quad (3.20)$$

Derivation of joints torque

The forces and torques induced by the inertia effects \mathbf{F}_i et \mathbf{N}_i , that apply to the link i at its center of gravity are given by Relations (3.21) and (3.22), which correspond to Newton's and Euler's laws:

$$\forall i \in \{1, \dots, 5, icw, ecw\} \quad {}^i\mathbf{F}_i = m_i \cdot {}^i\dot{\mathbf{v}}_{G_i} \quad (3.21)$$

$${}^i\mathbf{N}_i = {}^{G_i}\mathbf{I}_i \cdot {}^i\dot{\boldsymbol{\omega}}_i + {}^i\boldsymbol{\omega}_i \wedge {}^{G_i}\mathbf{I}_i \cdot {}^i\boldsymbol{\omega}_i \quad (3.22)$$

where ${}^{G_i}\mathbf{I}_i$ represents the inertia tensor of link i in the frame having for origine \mathbf{G}_i and directions $(\mathbf{x}_i, \mathbf{y}_i, \mathbf{z}_i)$. At this point the Newton-Euler algorithm as to be modified. Indeed for serial mechanisms the derivation of joints torques is achieve by a simple recurrent equation. However the loading arm is not a serial mechanism, dynamically speaking. The joints torques $\boldsymbol{\tau}$ are then seen as the solution of a classic rigid-body mechanical linear problem:

$$\mathbf{f}(\boldsymbol{\tau}, \boldsymbol{\Theta}, \mathbf{N}_{1..5}, \mathbf{F}_{1..5}) = \mathbf{0}, \quad (3.23)$$

which is manually solved as a set of equations, such as:

$$\tau_i = \sum_k (\boldsymbol{\lambda}_k(\mathbf{q}_{ext}) \cdot \mathbf{F}_k + \boldsymbol{\mu}_k(\mathbf{q}_{ext}) \cdot \mathbf{N}_k) \cdot {}^i\mathbf{a}_i, \quad \forall k \in \{1, \dots, 5, icw, ecw\}, \quad (3.24)$$

where the terms $\boldsymbol{\lambda}_k$ et $\boldsymbol{\mu}_k$ are 3×3 matrices which contains geometrical parameters of the arm. In order to derive the joints accelerations $\ddot{\mathbf{q}}$ from the joints torques $\boldsymbol{\tau}$, The matrix \mathbf{M} should be separated from the terms \mathbf{V} , \mathbf{B} and \mathbf{G} , as shown by Equation (3.9). if Relations (3.10) to (3.24) are symbolically derived, the matrix \mathbf{M} and the vectors \mathbf{V} , \mathbf{G} and \mathbf{B} can be identified. However these closed-form

CHAPTER 3. EXPERIMENTAL STUDY OF AN OFFSHORE LOADING ARM

expressions are difficult to deal with because they are very long (millions of symbols), due to the number of DoFs of the system. Symbolic identification of the elements cannot be performed when running the algorithm numerically. This drawback can be avoided by noticing that \mathbf{F}_i and \mathbf{N}_i may be written as expressions of the form :

$$\sum_{j=1}^5 \left(\sum_{k=1}^5 \mathbf{f}_{Mj,k}(\dot{q}_k) + \mathbf{f}_{Bj}(\ddot{q}_0) + \mathbf{f}_{Gj}(\mathbf{g}, \dot{\mathbf{V}}_0) + \mathbf{f}_{Vj} \right).$$

Hence, the elements \mathbf{M} , \mathbf{V} , \mathbf{B} and \mathbf{G} can be evaluated individually by splitting the terms. Equation (3.13) becomes:

$${}^i\dot{\boldsymbol{\omega}}_i = {}^i\dot{\boldsymbol{\omega}}_{Vi} + {}^i\dot{\boldsymbol{\omega}}_{Bi} + \sum_{j=1}^5 {}^i\dot{\boldsymbol{\omega}}_{Mi,j}, \quad \forall i \in \llbracket 1,5 \rrbracket, \quad (3.25)$$

with

$$\left\{ \begin{array}{l} {}^0\dot{\boldsymbol{\omega}}_{V0} = 0 \\ {}^i\dot{\boldsymbol{\omega}}_{Vi} = {}^{i-1}\mathbf{R}_i^T \cdot {}^{i-1}\dot{\boldsymbol{\omega}}_{Vi-1} + {}^{i-1}\mathbf{R}_i^T \cdot {}^{i-1}\boldsymbol{\omega}_{Vi-1} \wedge \dot{q}_i \cdot {}^i\mathbf{a}_i \\ {}^i\dot{\boldsymbol{\omega}}_{Bi} = {}^{i-1}\mathbf{R}_i^T \cdots {}^r\mathbf{R}_0^T \cdot \mathbf{q}_0 \\ {}^i\dot{\boldsymbol{\omega}}_{Mi,j} = \begin{cases} 0 & \text{if } i < j \\ {}^{i-1}\mathbf{R}_i^T \cdots {}^0\mathbf{R}_1^T \cdot {}^i\mathbf{a}_j & \text{otherwise} \end{cases} \quad (\dot{\boldsymbol{\omega}}_M \text{ is a } 5 \times 5 \text{ matix}) \end{array} \right. \quad (3.26)$$

Likewise, by rewriting (3.15), (3.16) and (3.17), comes:

$${}^i\dot{\mathbf{v}}_i = {}^i\dot{\mathbf{v}}_{Vi} + {}^i\dot{\mathbf{v}}_{Gi} + \sum_{j=1}^5 {}^i\dot{\mathbf{v}}_{Mi,j}, \quad (3.27)$$

$${}^2\dot{\mathbf{v}}_{icw} = {}^2\dot{\mathbf{v}}_{Vicw} + {}^2\dot{\mathbf{v}}_{Gicw} + \sum_{j=1}^5 {}^2\dot{\mathbf{v}}_{Micw,j}, \quad (3.28)$$

$${}^3\dot{\mathbf{v}}_{ecw} = {}^3\dot{\mathbf{v}}_{Vecw} + {}^3\dot{\mathbf{v}}_{Gecw} + \sum_{j=1}^5 {}^3\dot{\mathbf{v}}_{Mecw,j} \quad (3.29)$$

Finally the matrix \mathbf{M} and the vectors \mathbf{V} , \mathbf{G} and \mathbf{B} can be numerically computed. To do so, one should evaluate expressions (3.18) to (3.24) in which the terms $\dot{\boldsymbol{\omega}}_i$ and $\dot{\mathbf{v}}_i$ are replaced by $\dot{\boldsymbol{\omega}}_{Gi}$ and $\dot{\mathbf{v}}_{Gi}$ to obtain \mathbf{G} , $\dot{\boldsymbol{\omega}}_{Mi,j}$ and $\dot{\mathbf{v}}_{Mi,j}$ to obtain $\mathbf{M}_{,j}$ (j^{th} column of \mathbf{M}), etc. With $\forall i, \boldsymbol{\omega}_i = 0$, except when evaluating \mathbf{V} .

At the end of the day, the motion equations (3.8) and (3.9) are available. Relation (3.8) may be used to compute joints torques given the joints and FLNG motions, while relation (3.9) may be used to simulate the joints motions according to the joints torques.

3.3.3.2 Simulation results

Simulation are run to evaluate the joints torques induced by the FLNG motion for the full scale DCMA presented in Section 1.4. The length, mass and inertia parameters are extracted from CAD (computer-aided design) models provided by the manufacturer. These parameters are such that the loading arm is assumed perfectly statically balanced. First the evolution of the joints torques is simulated, for the arm in deployed configuration, with no joint motion. The FLNG moves under the reference sea state presented in Section 3.3.2. The joints torques are thus only generated by the FLNG motion and the gravity. Figure 3.18 shows the result of this simulation.

A second simulation is run assuming the joints are driven to follow the manifold. The inverse kinematics model of the arm, presented in Appendix A, is used to express the relative motion of the vessels ${}^0\mathbf{P}_m(t)$ in terms of joints motions $\mathbf{q}(t)$. This time series are numerically differentiated to obtain the needed velocities and acceleration. Figure 3.19 shows the result of this simulation.

First these results show that the total joints torques are below the actuators capabilities. The highest calculated joint torque is $0,8 \cdot 10^5$ N.m for the inboard joint, which stays under 40% of its nominal cylinder capacity. Then the frequency spectra of the inertia joints torques are obtained by using FFTs. Figure 3.20 shows that the low frequencies of these signals (<0.1 Hz) are below the first measured mode of the structure of the loading arm (0.37 Hz). Hence it can be assumed that the inertia effects do not excite the structure of the arm. In other words, the vessels motion are considered as a purely geometric problem in this project.

Finally these results show that inertia effects consist of about 10% of the total joints torques, assuming the loading arm exactly compensates the relative motion ${}^0\mathbf{P}_m$. Thus these inertia effects cannot be considered as negligible, and an approach similar to the one proposed by [FGLA11] can be considered. The latter approach, as presented at the top of this section, consists in predicting the FLNG motion to plan the arm motion so that the inertia forces reduce the joints torques needed for the motion. This issue is not further investigated in this project. Ho-

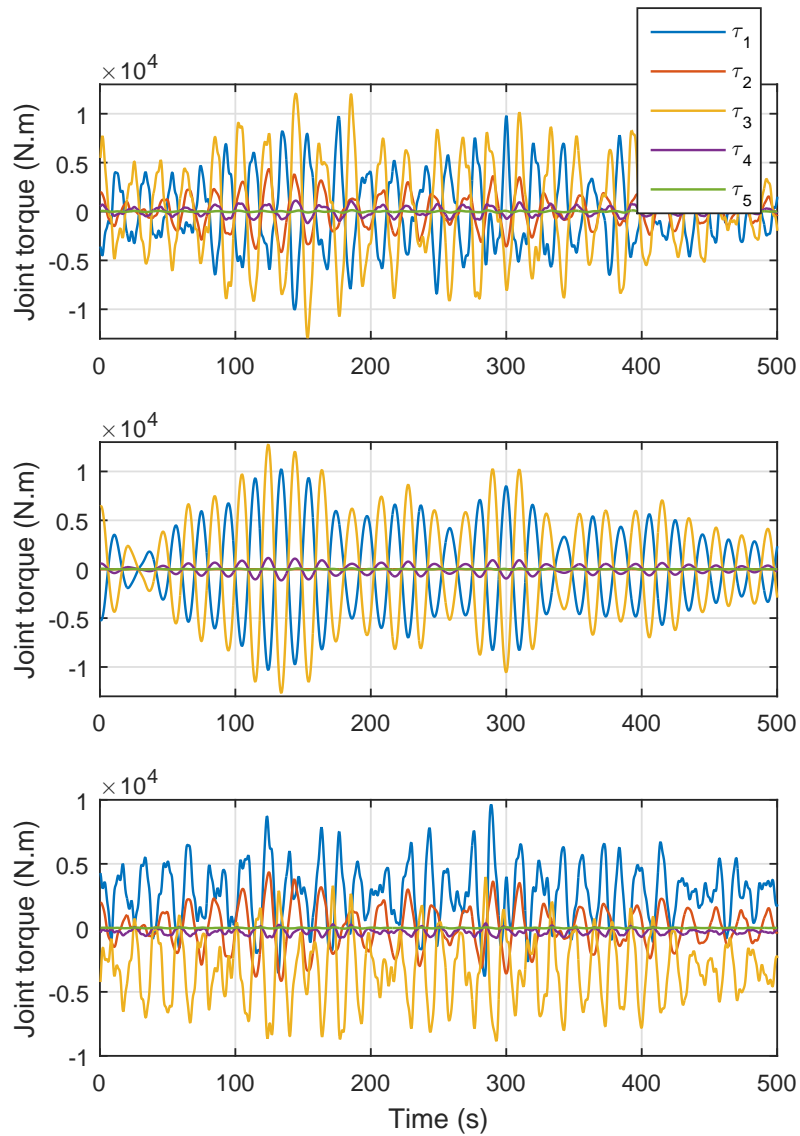


Figure 3.18: Joints torques induced by the FLNG motion. Top graph: total torques. Middle graph: Gravity only. Bottom graph: all inertia effects except gravity.

wever the author suggests:

- to validate this model by fitting the OLAF scaled model with force sensors, and using its hexapod table to reproduce the FLNG motion,
- if needed, to incorporate flexible elements in the model,

CHAPTER 3. EXPERIMENTAL STUDY OF AN OFFSHORE LOADING ARM

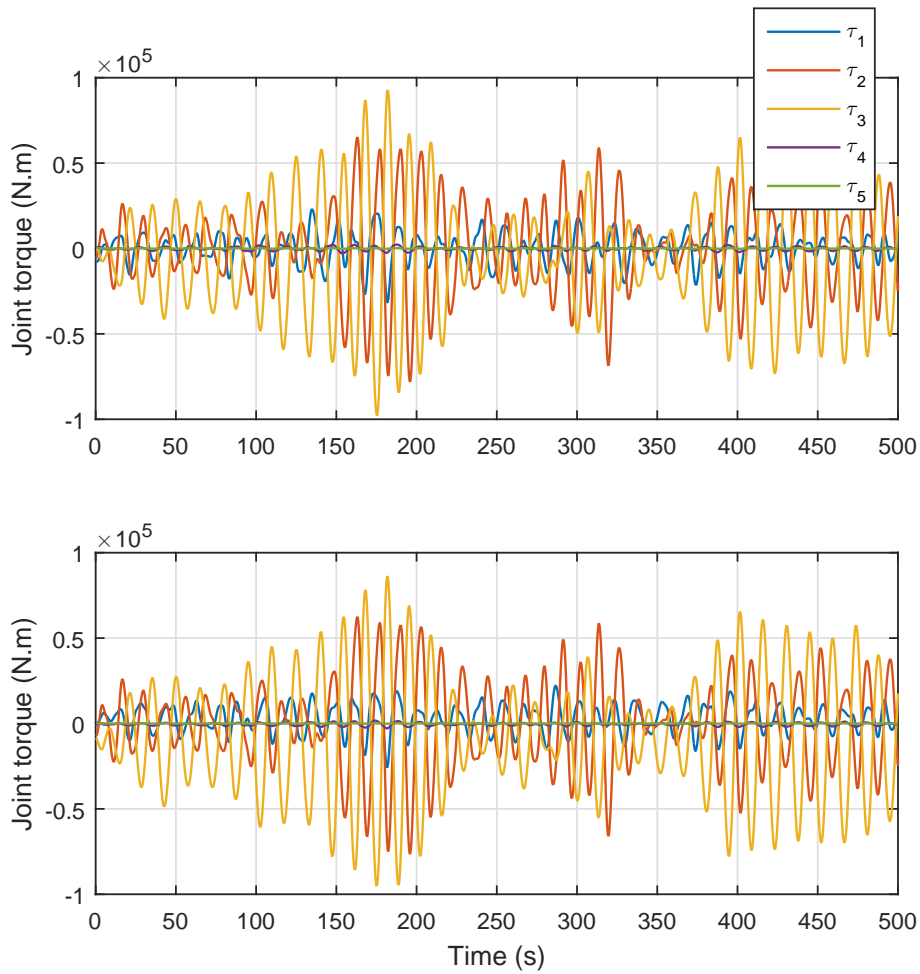


Figure 3.19: Joints torques induced by the FLNG motion and joints motions. Top graph: total torques. Bottom graph: torques induced by joints motions only.

- to apply the methodology proposed by [FGLA11], by using the motion prediction algorithm developed in Section 5.2.

CHAPTER 3. EXPERIMENTAL STUDY OF AN OFFSHORE LOADING ARM

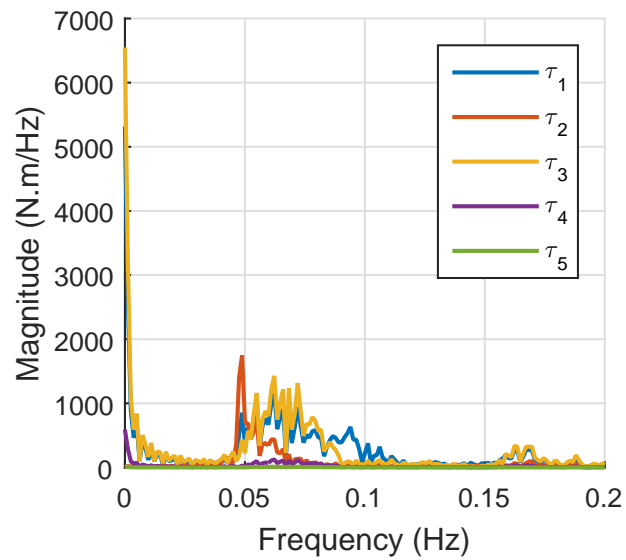


Figure 3.20: Frequency spectra of the joints torques induced by the inertia effects. These frequencies are below the first measured mode of the structure of the arm.

Chapter 4

Jerk limited time optimal online trajectory generation

For the sake of motion accuracy, safety and hardware lifetime, it is important that the vibrations in the loading arm are kept low. In particular, oscillation of the Style 80 around joint 4 is to be prevented, as well as the joint and structure vibration measured in Chapter 3. Indeed it is shown that the structures of the loading arms are easily excited by their actuators. Robotic manipulation classically uses very smooth profiles, such as jerk-limited trajectories, to avoid acceleration discontinuities, which can induce detrimental vibrations. Jerk-limited trajectories can be used as well to smoothly drive loading arms. A significant amount of work has been done to find efficient and elegant solutions to this problem of trajectory planning and/or vibration reduction, particularly for machining applications [EA01, JCPC05, OBGD10]. In addition to robotic manipulation, service robotics (collaborative) and mobile robotics have to solve the same problem but with online capability. Indeed in this recent context, robots attempt to instantaneously react to unpredicted events originating from the unstructured environment and potentially from the physical human-robot interaction. In the context of MLA, a tracking algorithm that makes the loading arm able to follow the manifold has to be developed. The ability to adjust trajectories online according to the environment, e.g. relative motions between the FLNG and the LNG carrier, is needed. Thus according to the context, the trajectory generation has to verify the following points:

- Trajectories should be modified during execution time (online ability) depending on external measurements or human commands. Therefore the generator has to handle non-zero initial conditions, and has to generate trajectories fast regarding a controller cycle time.
- Trajectories should be time-optimal in order to minimize the tracking delay

between the coupler and the manifold motions,

- The smoothness of the trajectories, at least jerk-limited, should be sufficient not to induce oscillation in the system, for an improved accuracy.

One can find existing solutions in the literature to solve the problem of time-optimal online trajectory generation. Jerk-limited trajectories were first usually defined analytically by computing optimal profiles offline then implemented in the systems ([EA01]). More recently, analytic solutions to the time-optimal and time-fixed jerk-limited online profile generation problem were proposed [JCPC05, HWR08]. The computing time of such algorithms is about 350 microseconds for one axis trajectory, which can be a significant limitation for multi-axis systems during one control cycle (typically 1 millisecond). In [KTW06, KW10], Kröger *et al.* introduce a new elegant framework based on the current state of the system and the final desired state, that provides time-optimal acceleration-limited trajectories (trapezoidal velocity). The jerk-limited solution is present in their recent works as the well-known Reflexxes Motion Library. Different approaches described in [Krö11], that can save computation time, are based on the analytical recalculation of the trajectories, only whenever a new event arrives to the trajectory generator.

Another interesting approach to naturally comply with the online capability of the trajectory generation consists in using a filter-based approach. In [Lu08], Lu presents an original jerk-limited time-optimal control scheme, i.e. a dynamic filtering or closed-loop filtering approach. The proposed controller is time-optimal according to the constrained jerk and is adapted to real-time use, but the kinematic constraints on the maximum values of the velocity and acceleration are not considered. A similar approach, but with enhanced capabilities, is described in [GB10]. The proposed dynamic filter-based trajectory generation can handle freely assignable bounds on the velocity, the acceleration and the jerk, but the time-fixed solution and consequently the multi-axis synchronization problem is not taken into consideration in this approach. Also, no information about the calculation time is given. A simpler method consists in using FIR (Finite Impulse Response) filters properties to shape the trajectories according to a given set of kinematic, time and frequency constraints. This open-loop approach conducts to less complex algorithms, which can be naturally adapted to the real-time trajectory generation. In [OBGD10], a FIR filter-based approach is exploited to generate the tool feedrate of a machining robot with limited jerk. The jerk-limited trajectory is obtained offline by convolving a pre-calculated low complexity acceleration-limited profile with a moving average filter, i.e. a FIR filter with all weight coefficients set equal to one. In [BM12], Biagiotti and Melchiorri generalize the FIR filter-based approach for the online trajectory generation. Starting from a rough step input, a cascade of n FIR filters generates a trajectory of order n respecting the kinematic

constraints. The time-fixed trajectory generation problem and multi-axis synchronization can be solved using this approach. However, the proposed online generator can only deal with symmetric kinematic constraints and the time-optimality of the trajectory is not assured between via-point. Moreover, it is not possible to specify on the fly desired values of time-derivative of the position (velocity, acceleration and jerk) different from zero at the via points. On the other hand, the strength of the previous FIR-filter based approach relies on the fact that the smooth online trajectory generation can be efficiently combined with the interesting properties of FIR filters in the frequency domain for vibration reduction.

On this subject, previous works exploiting the FIR filter-based approach [OBGD10, BO13] demonstrated that the FIR filter time, i.e. the constant jerk-time for a jerk-limited trajectory, can be tuned to cancel the motion-induced vibrations of an undamped system. In [Bea14], Béarée proposes an improvement by using asymmetric jerk profiles, i.e. by using non-equal FIR filter coefficients, to take into account the damping coefficient of the flexible system. This approach was generalized and improved in [BMM16] by using trajectories based on an exponential jerk profile and by deriving analytically the new FIR filter parameters that guarantee the residual vibration suppression.

This work proposes a different methodology which exploits the properties of FIR filtering to generate on the fly jerk-limited trajectories, based on initial acceleration-limited trajectories. The initial acceleration-limited profiles are adapted to handle non-zero initial conditions. As a result a fast and versatile trajectory generator is developed, that fulfills all the requirements for driving MLAs and many robotic applications.

4.1 Online trajectory generation with jerk limitation

The generation of time-optimal acceleration-limited trajectories can be easily solved analytically. This low computational complexity approach is well adapted for online trajectory generation, but results in unsmooth profiles with step accelerations (bang-bang or bang-cruise-bang type control) and triangular or trapezoidal velocity profiles. Considering a FIR filter defined for implementation as

$$a_{f,k} = \frac{1}{N} \sum_{i=1}^N c_i \cdot a_{k-i+1}, \quad (4.1)$$

CHAPTER 4. JERK LIMITED TIME OPTIMAL ONLINE TRAJECTORY GENERATION

with respectively $a_{f,k}$ and a_k the acceleration output and input value of the filter at time k . T_e , T_e the sampling time of the signal, N the number of taps of the filter calculated as the integer part of T_j/T_e , T_j the filter time (T_j is practically chosen as a multiple integer of T_e) and $c_i = \{c_1, \dots, c_N\}$ the filter coefficients. Convolution of an acceleration step function of value a_{\max} with a sliding average FIR filter ($c_i = 1, i \in \{1, \dots, N\}$) produces a ramp function with ending value a_{\max} and a slope value, i.e. a jerk value noted j_{\max} , given by

$$j_{\max} = a_{\max}/T_j. \quad (4.2)$$

Therefore as illustrated in Figure 4.1, an acceleration-limited profile may be turned into a jerk-limited profile by FIR filtering. Unfortunately, FIR filtering of a time-optimal acceleration-limited trajectory does not necessarily produce a time-optimal jerk-limited trajectory. Indeed, the jerk limitation given by (4.2) could be exceeded. Moreover, the initial acceleration and velocity conditions being not explicitly taken into account, there is no guarantee that the desired position will be reached.

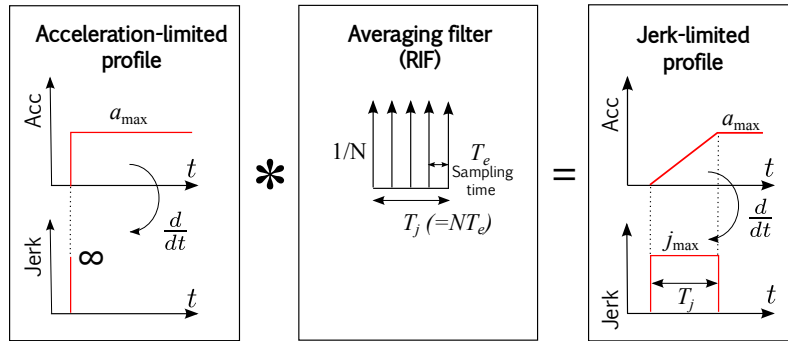


Figure 4.1: FIR filtering principle for jerk-limited trajectories synthesis.

The proposed approach, summarized in Figure 4.2, solves the latter problems in a systematic way:

1. The first stage consists in generating the time-optimal acceleration-limited (noted AL) trajectory (see Figure 4.4), which fulfills the requirements in terms of set-point, initial velocity and kinematic limitations on velocity and acceleration.
2. In order to ensure that the time-optimality, the jerk limitation and the acceleration continuity are respected by the final jerk-limited trajectory (noted JL), the initial AL trajectory may have to be *adapted* before the filtering. This adaptation stage is based on simple closed-form relations.

CHAPTER 4. JERK LIMITED TIME OPTIMAL ONLINE TRAJECTORY GENERATION

- Then a FIR filter is applied to the adapted AL profile to produce a JL acceleration profile. One note that the filter length is chosen according to the acceleration and jerk limitations. For each new event that modifies the position set-point, the current state of the trajectory generator becomes the initial conditions of the new trajectory.

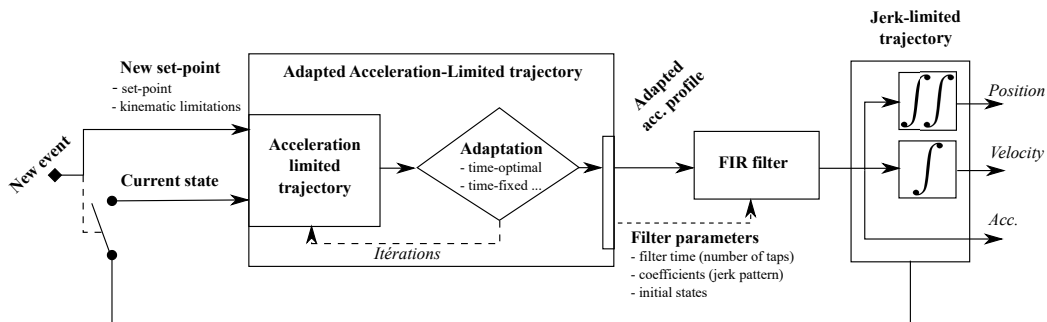


Figure 4.2: Proposed online trajectory generation algorithm based on FIR filtering of adapted acceleration-limited profiles.

Figure 4.3 presents example of trajectories without and with needed adaptations for jerk limitation and time-optimality.

In this chapter, the subscript f stands for "filtered", i.e. denotes the variables of the jerk-limited profile, which is the output of the algorithm. It is assumed that the final velocity and acceleration are zeros, since if no new set-point is given, the goal is reached and the motion stops.

CHAPTER 4. JERK LIMITED TIME OPTIMAL ONLINE TRAJECTORY GENERATION

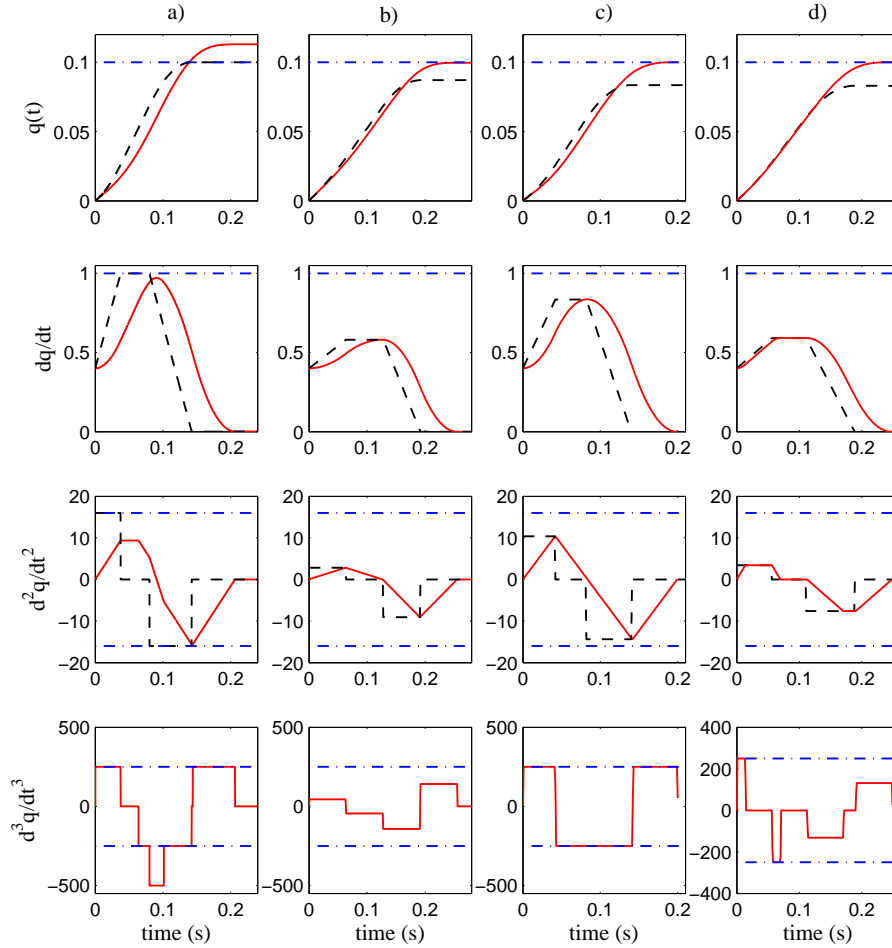


Figure 4.3: Examples of trajectories resulting from FIR filtering (averaging filter) of different acceleration-limited profiles. Solid and dashed lines indicate respectively the filtered and the initial profiles, dotted lines represent the kinematic constraints (set-point $q_e = 0.1m$, $v_m = 1m/s$, $v_{0f} = 0.4m/s$, $a_m = d_m = 16m/s^2$, $j_m = 250m/s^3$). a) Filtered trajectory resulting from a time-optimal acceleration-limited profile, b) the initial acceleration profile is adapted to generate jerk-time fixed trajectory ($T_j = a_m/j_m = 0.064ms$), c) the initial profile is adapted to generate time-optimal jerk-limited profile, d) the initial profile is adapted to generate time-fixed jerk-limited trajectory ($T = 0.25s$)

4.1.1 Acceleration-limited trajectory generator

The first stage of our methodology consists in generating the time-optimal AL trajectory, which respects the following kinematic constraints and boundary conditions :

$$\begin{cases} |v(t)| \leq v_{\max} \\ \text{if } t < T_a + T_v & |a(t)| \leq a_{\max} \\ \text{else} & |a(t)| \leq d_{\max} \end{cases} \quad (4.3)$$

The acceleration-limited profile, also known as bang-bang profile, can be build in three phases: first an acceleration phase during which the acceleration is constant: $|a(t)| = a_{\max}$. During the second phase the acceleration is zero, i.e. the maximal velocity has been reached and is constant: $|v(t)| = v_{\max}$. Finally in the third phase comes the deceleration, constant as well: $|a(t)| = d_{\max}$. The durations of these three phases are respectively noted T_a , T_v and T_d , as illustrated in Figure 4.4. The

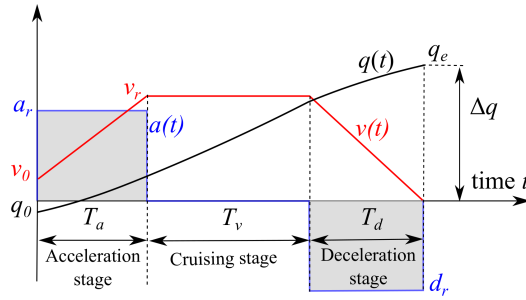


Figure 4.4: A classic acceleration-limited profile. a_r , d_r and v_r are the reached acceleration, deceleration and velocity values.

displacement Δq is given by relation 4.4:

$$\Delta q = q_e - q_0 = \frac{T_a(v_r + v_0)}{2} + T_v v_r + \frac{T_d v_r}{2}, \quad (4.4)$$

with:

$$T_a = \frac{v_r - v_0}{a_r}; \quad T_d = \frac{-v_r}{d_r}. \quad (4.5)$$

To ensure that the trajectory is time-optimal, the acceleration, deceleration, and cruising velocity values are set at the maximum values:

$$a_r = s \cdot a_{\max}; \quad d_r = -s \cdot d_{\max}; \quad v_r = s \cdot v_{\max},$$

where a_r , d_r and v_r are the reached acceleration, deceleration and velocity values and s is the sign of the velocity during the cruising phase. In order to take into

account a non-zero initial velocity, s can be determined by:

$$s = \text{sign}(q_e - q_{stop}), \quad (4.6)$$

where q_{stop} represents the position reached after the fastest full stop. If the initial velocity v_0 is greater than the maximum velocity: $s \cdot v_0 > s \cdot v_r$, the velocity has to be reduced to v_r . In this case, $a_r = -s \cdot a_{\max}$ and the profile as two deceleration phases, a_r and d_r have the same sign [HWR08]. Suitable values for T_a , T_d and T_v are then calculated. Let us note Δq_{min} the minimum displacement for which v_r is reached, when $T_v = 0$. If $s \cdot \Delta q \geq s \cdot \Delta q_{min}$ then the maximal velocity is reached during the motion. Consequently:

$$T_a = \frac{v_r - v_0}{a_r}; \quad T_v = \frac{\Delta q - \Delta q_{min}}{v_r}; \quad T_d = \frac{-v_r}{d_r}. \quad (4.7)$$

Otherwise, the maximal velocity is not reached and the velocity profile is wedge-shaped. The maximum reached velocity v_r is then updated:

$$v_r = s \cdot \sqrt{\frac{-\frac{v_0^2}{ar} - 2\Delta q}{\frac{1}{dr} - \frac{1}{ar}}}, \quad (4.8)$$

and

$$T_a = \max(0, \frac{v_r - v_0}{a_r}); \quad T_v = 0; \quad T_d = \max(0, \frac{-v_r}{d_r}).$$

Finally, the triplet (T_a, T_v, T_d) defines the time-optimal acceleration-limited profile which respects the acceleration and velocity bounds.

4.1.2 Adaptation of the initial AL profile for FIR filtering

In the general case the AL profile has to be modified before filtering. Non-zero initial conditions of the initial state of the desired trajectory leads, after simple filtering of length T_j , to errors on the final state, as shown by Figure 4.5 a) and b). Therefore the parameters (q_0, v_0) used to generate the initial AL profile have to be adjusted according to the real current state (q_{0f}, v_{0f}, a_{0f}) . Calculating the difference between the non-filtered and filtered profiles, the relationship between the initial parameters can be written as

$$v_0 = v_{0f} + \delta_v, \quad q_0 = q_{0f} + \delta_q, \quad (4.9)$$

with

$$\delta_v = \frac{T_j a_{0f}}{2}, \quad (4.10)$$

CHAPTER 4. JERK LIMITED TIME OPTIMAL ONLINE TRAJECTORY GENERATION

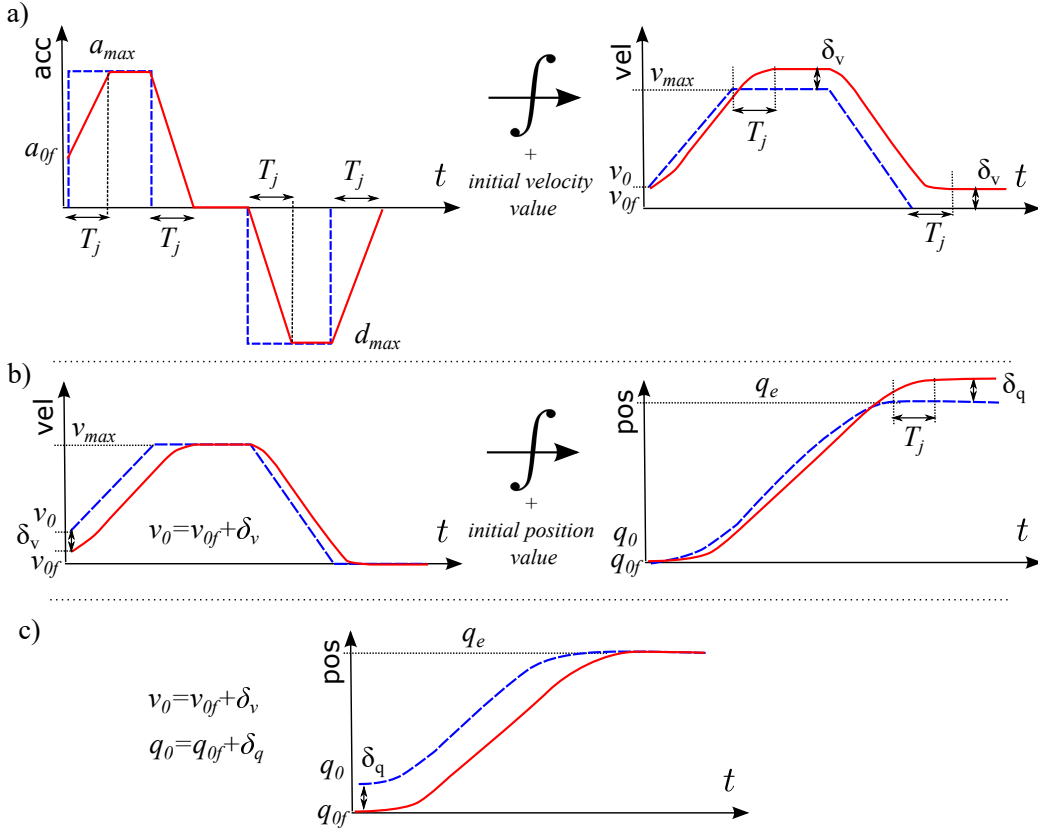


Figure 4.5: Principle of initial conditions definition for FIR filtering trajectory. a) Influence of the initial acceleration value on the filtered velocity: the maximum and final filtered velocity values present an overshoot of δ_v . b) Adaptation of the initial velocity condition v_0 of the acceleration-limited profile to fulfill the velocity constraints after filtering: the final filtered position presents an overshoot of δ_q . c) adaptation of the initial position condition q_0 of the acceleration-limited profile: the filtered trajectory fulfill the kinematic constraints.

and

$$\delta_q = v_{0f} \cdot \frac{T_j}{2} + a_{0f} \cdot \frac{T_j^2}{12}. \quad (4.11)$$

Once the AL profile is generated according to Equation 4.9, the final jerk-limited trajectory is ensured to be correct in terms of initial and final states.

Afterwards the test $T_v > T_j$ should be checked. If T_v is less than T_j , another adaptation of the AL profile is required to keep the jerk of the JL profile from exceeding its limits, as shown on Figure 4.6. Such adaptation consists in re-generating the AL profile with a lower value of v_r which satisfies $T_v = T_j$ and

relations (4.7).

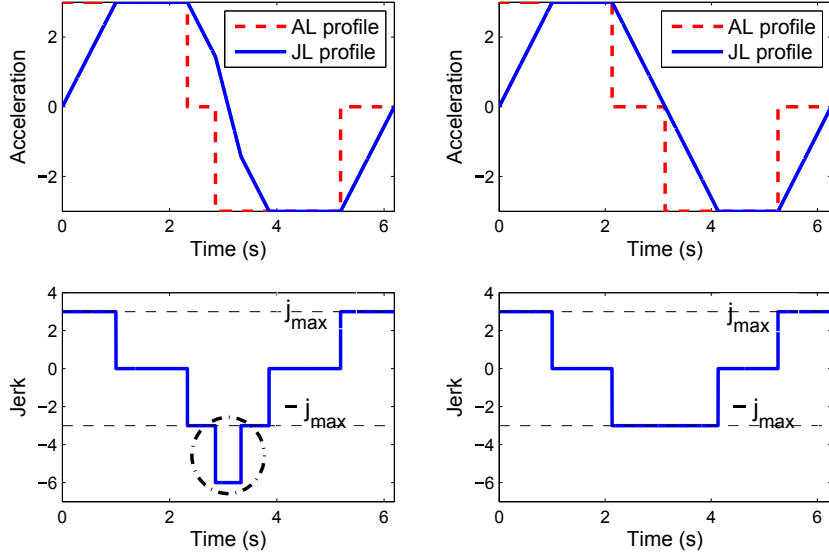


Figure 4.6: Example of an adaptation: Type II (see Fig. 4.13). To the left: non-adapted profile, $T_v < T_j$. To the right, adapted profile, $T_v = T_j$ and $|v_r| < v_{\max}$.

4.1.3 FIR Filtering and jerk patterns

Starting from the previously adapted AL profile, a JL trajectory can be obtained using a FIR moving average filter, as shown on Figure 4.7. The length of the filter T_j is classically chosen to reach the maximum allowed value of the jerk j_{\max} . Hence T_j depends on the maximum change of acceleration during a constant jerk stage:

$$T_j = \max \left\{ \frac{|a_r - a_{0f}|}{j_{\max}}, \frac{|a_r|}{j_{\max}}, \frac{|d_r|}{j_{\max}} \right\}. \quad (4.12)$$

In order to respect the desired initial acceleration of the profile, the coefficients of the filter should be initialized at a_{0f} . One notes that the resulting JL trajectory is not time-optimal because the jerk time is fixed instead of the maximum jerk value. Other jerk patterns can be generated by changing the coefficients of the filters. For instance, jerk patterns can be used to reduce residual vibration in the system as described in [Bea14]. Figure 4.8 presents two examples of trajectories generated using Damped-Jerk and sine squared Jerk patterns.

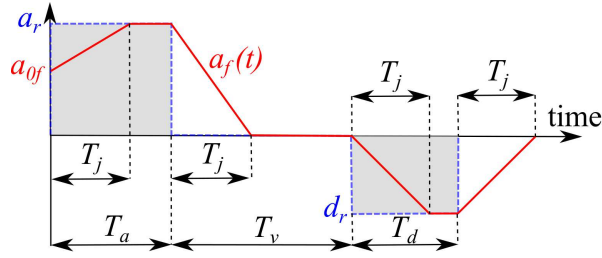


Figure 4.7: The initial acceleration-limited trajectory (blue dashed line) is filtered to give a jerk-limited profile (solid red line).

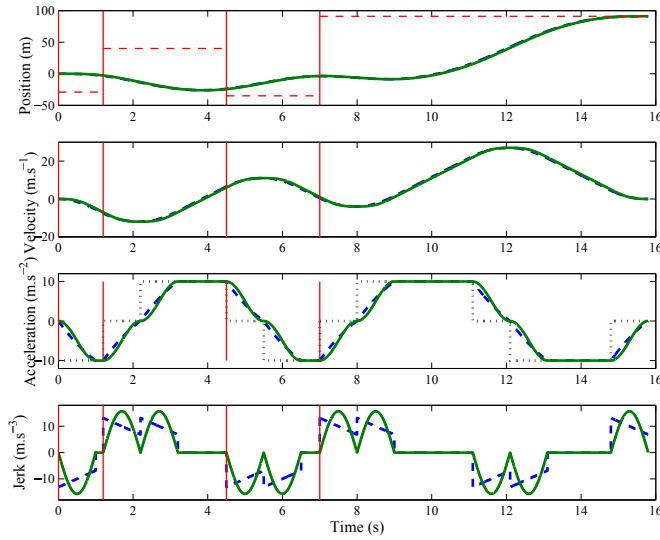


Figure 4.8: Example of trajectories with different jerk patterns: Damped-Jerk (dashed blue line) and sine squared Jerk (solid green line).

4.2 Time-optimal jerk-limited trajectories

Many industrial applications require time-optimal trajectories for productivity reasons. In the case of loading arms, such trajectories are needed to minimize the delay, i.e. the position error, between the coupler and the manifold during the pursuit stage (see Section 1.3.1.3). To ensure the time-optimality, the maximum jerk value should be fixed instead of the filter length. Therefore the filter length should be changed while filtering to satisfy the following relationships:

$$T_{ja} = \frac{|a_r - a_{0f}|}{\dot{j}_{\max}}; T_{jv} = \frac{|a_r|}{\dot{j}_{\max}}; T_{jd} = \frac{|d_r|}{\dot{j}_{\max}}, \quad (4.13)$$

where T_{ja} , T_{jv} and T_{jd} are the durations of the constant jerk stages, as shown in Figure 4.9.

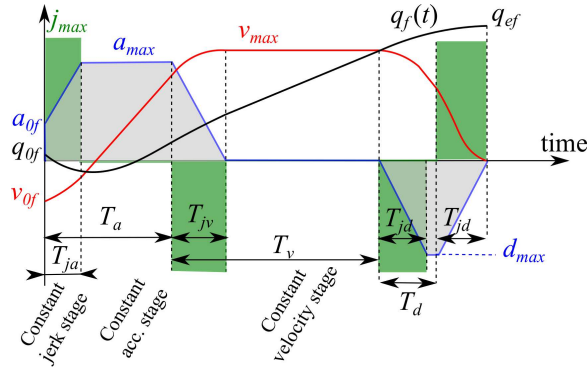


Figure 4.9: Time-optimal jerk-limited profile with non-zero initial conditions, each derivative saturates at its bound.

4.2.1 Jerk-limited full-stop

While operating, the MLA may have to stop its motion due to external conditions or human command. Simple stop, i.e. sudden closure of the hydraulic spool valves is very brutal and may lead to large oscillation of the arm and damages to the hardware. Even in emergency cases, such a brutal stop may be detrimental. By contrast, a jerk-limited stop smoothly stops the system. The length of the stop motion depends on the initial state of the system – velocity, acceleration – and the kinematic bounds.

The jerk-limited full-stop profile is the shortest acceleration profile for which the final kinematics parameters, i.e. position and acceleration, are zeros. According to the initial parameters v_{0f} and a_{0f} , such an acceleration profile can present different shapes, as shown on Figure 4.10.

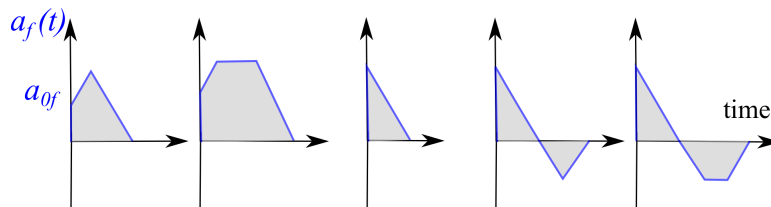


Figure 4.10: Examples of full-stop acceleration profiles.

The full-stop profile is also useful to compute the sign s which is need for the

CHAPTER 4. JERK LIMITED TIME OPTIMAL ONLINE TRAJECTORY GENERATION

AL generation. Indeed, the first stage of the generation consist in determining the direction, or sign $s \in \{-1, 1\}$, of the trajectory. This sign corresponds to the sign of the cruising velocity. [HWR08] states that s is given by the relation:

$$s = \text{sign}(q_e - q_{stop}), \quad (4.14)$$

where q_{stop} represents the position reached after the fastest full stop of the system. If $q_{stop} = q_e$ then the full-stop profile should be kept as a result with no further calculation. The calculation of q_{stop} consists in integration the acceleration, then the velocity profile:

$$v_{0f} + \int_{t_0}^{t_e} a_f(t) dt = 0 \quad (4.15)$$

$$q_{stop} = q_{0f} + \int_{t_0}^{t_e} \underbrace{\left(v_{0f} + \int_{t_0}^t a_f(\tau) d\tau \right)}_{v_f(t)} dt \quad (4.16)$$

4.2.2 Sign change

In the case where $s \cdot a_{0f} < 0$, the sign s may change during the first constant jerk phase. If the evaluation of the sign at $t = |a_{0f}/j_{max}|$ gives a result different than the initial sign s , the time T_p at which the value of s change should be found. Figure 4.11 shows such a trajectory.

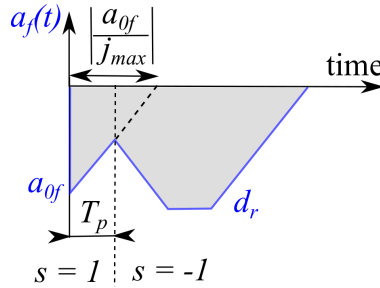


Figure 4.11: Example of an acceleration profile with a sign change at $t = T_p$.

In the case where a_f saturates at d_r , T_p is a real, positive root of a forth-order polynomial function:

$$a \cdot T_p^4 + b \cdot T_p^3 + c \cdot T_p^2 + d \cdot T_p + e = 0 \quad (4.17)$$

Otherwise T_p is a zero of a non-linear function, found by using an adapted Newton-Raphson method.

4.2.3 Adaptation of the AL profiles

The relationships between (q_0, v_0) and (q_{0f}, v_{0f}, a_{0f}) given by (4.10) and (4.11) cannot be used for time-optimal generation since the length of the filter is not constant in the general case. Equations (4.18) and (4.19) are similarly derived to take this difference into account.

$$\delta_v = s \cdot \frac{a_r a_{0f}}{j_{\max}} - s \cdot \frac{a_{0f}^2}{2j_{\max}}, \quad (4.18)$$

$$\delta_q = a_r \left(\frac{s \cdot v_{0f}}{2j_{\max}} + \frac{a_{0f}^2}{4j_{\max}^2} \right) - \frac{a_{0f}^3}{6j_{\max}^2} - s \cdot (a_r + d_r) \frac{v_r}{2j_{\max}}. \quad (4.19)$$

In addition to the adaptation previously described in 4.1.2, which makes sure that the jerk bound is respected, the AL profile should also be checked to make sure that the solution given after filtering is time-optimal. If $T_{ja} > T_a$ or $T_{jd} > T_d$, then the acceleration profile after filtering saturates at a value less than its bound, respectively a_{\max} or d_{\max} , as illustrated on Figure 4.12. In that case, the initial AL profile should be adapted in order to produce the desired time-optimal jerk-limited trajectory. Figure 4.13 presents the decision table used to select the adaptation to

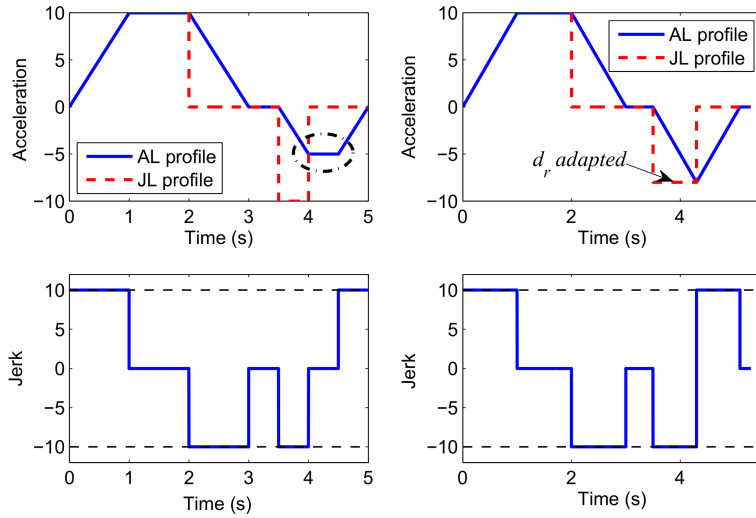


Figure 4.12: Example of an adaptation: Type III-b (see Fig. 4.13). To the left: non-adapted profile, $T_d < T_{jd}$. To the right, adapted profile, $T_d = T_{jd}$ and $|d_r| < d_{\max}$.

be applied to the AL profile. As an example, if the initial AL profile exhibits $T_d < T_{jd}$ and $T_v > T_{jv}$, a Type III-b adaptation is needed. In that case, the

CHAPTER 4. JERK LIMITED TIME OPTIMAL ONLINE TRAJECTORY GENERATION

deceleration stage does not saturate, i.e. $|d_r| < d_{\max}$. Therefore

$$T_d = T_{jd} \Rightarrow \frac{-v_r}{d_r} = \frac{-s \cdot d_r}{j_{\max}},$$

hence:

$$d_r = -s\sqrt{s j_{\max} v_r}. \tag{4.20}$$

Once the AL profile is adapted, it should be re-checked for a possible second adaptation, as shown in Figure 4.14.

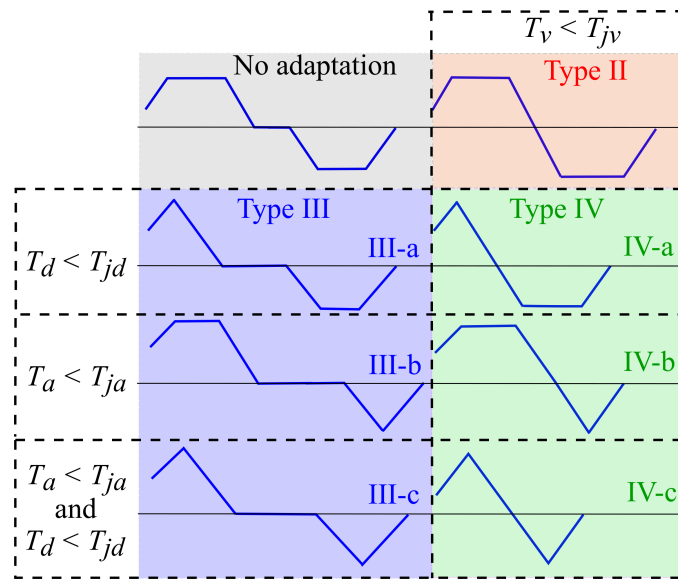


Figure 4.13: Decision table for the selection of the adaptation of the AL profile.

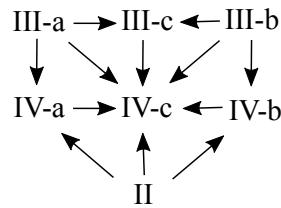


Figure 4.14: Decision tree which shows the possible successive adaptations.

4.2.4 Filtering

In order to keep the jerk at its maximum value j_{\max} , the length of the filter is dynamically switched according to relation (4.13). The trajectory starts at $t = 0$ with

a filter initialized at a_{0f} with a length T_{ja} . Then the filter is changed at $t = T_a$ to a length T_{jv} , initialized at a_r . Finally at $t = T_a + T_v$ the length of the filter is set to T_{jd} . Figure 4.9 shows the filter lengths.

4.3 Online constraints change

Many recent robotic applications require online adaptation of the kinematic bounds of the trajectory. For instance, the detection of human presence in the workspace of the robot can enable a "smooth" mode in which the kinematic limits are lowered, or the jerk pattern modified. In the case of loading arms, different sets of kinematic bounds can be associated to the different modes and stages of the MLA connection (see Section 1.3.1).

In the case where the velocity or acceleration limit is lowered during the motion, a transition stage may be required. If the initial acceleration and velocity are such that the new velocity limit is or will be exceeded, i.e. if:

$$s \cdot \left(v_{0f} + \frac{a_{0f}}{2} \cdot \left| \frac{a_{0f}}{j_{\max}} \right| \right) > s \cdot v_{\max}, \quad (4.21)$$

then the deceleration stage, noted $a_{ds}(t)$, should bring the velocity back into its news bounds as soon as possible. Let us note the duration of this stage T_{ds} , as shown in Figure 4.15. The deceleration stage corresponds to:

$$v_{0f} + \int_{t_0}^{T_{ds}} a_{ds}(t) dt = s \cdot v_{\max}. \quad (4.22)$$

For the fastest solution, the jerk is saturated:

$$v_{ds}(t) = -s \cdot \frac{j_{\max} t^2}{2} + a_{0f} t + v_{0f},$$

with $v_{ds}(T_{ds}) = s \cdot v_{\max}$, hence

$$-s \cdot \frac{j_{\max}}{2} T_{ds}^2 + a_{0f} T_{ds} + v_{0f} - v_{\max} = 0.$$

In the case where $T_{ds} > \left| \frac{-s \cdot a_{\max} - a_{0f}}{j_{\max}} \right|$ then a_{ds} saturates at $-s \cdot a_{\max}$.

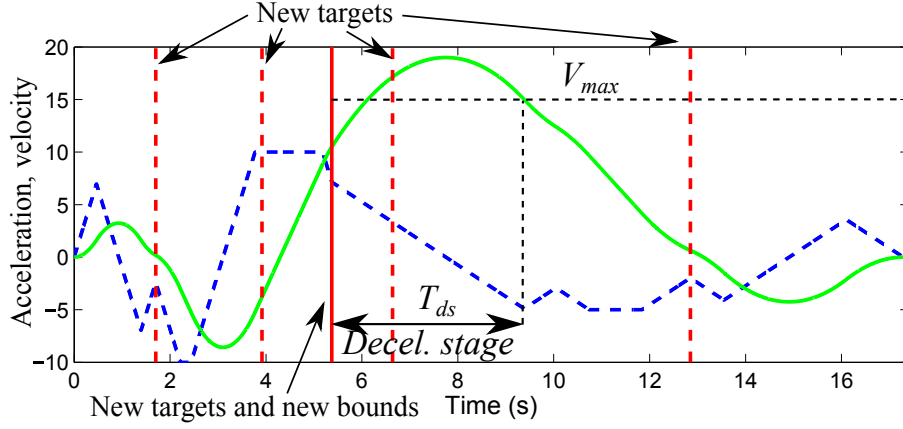


Figure 4.15: Example of a trajectory with a deceleration stage. Dashed blue line: acceleration. Full green line: velocity. The kinematic bounds are lowered at $t = 5.3$ s (vertical full line). A deceleration stage ensures that the velocity respects its new limit.

4.4 Time-fixed trajectory: Axis Synchronization

In the general case, several Degrees-Of-Freedom (DoF) are controlled simultaneously to reach a targeted position. Classically, it is wished that the motion of each DoF ends at the same time. Consequently, for a motion involving n DoF, with T_i the duration of the time-optimal trajectory for the i -th DoF, $n - 1$ trajectories have to be adjusted to the fixed time constraint T_{fix} given by the slowest DoF

$$T_{fix} = \max_i T_i. \quad (4.23)$$

This adjustment can be done in several, very different ways. Here, we propose to take benefits from the filtering strategy to easily compute the fixed-time solution for the JL profile. Indeed, without consideration of time-optimality, if an AL profile is directly convolved with a FIR filter of time duration T_j , the resulting profile is T_j seconds longer than the initial AL profile. Noting τ_{fix} the fixed time duration of the AL profile, τ_{fix} is given by $\tau_{fix} = T_{fix} - T_j$. The AL profile used here allows arbitrary initial velocities and the fixed-time solution for such a profile can be simply calculated. Considering the rescaling of the whole time evolution with the parameter $\alpha = \tau_{fix}/\tau_i$:

$$\tau_a = \alpha T_a; \tau_v = \alpha T_v; \tau_d = \alpha T_d. \quad (4.24)$$

The parameters to be determined are a_r and d_r , respectively the reached acceleration and deceleration. From (4.4) and (4.5) it is straightforward to derive the

CHAPTER 4. JERK LIMITED TIME OPTIMAL ONLINE TRAJECTORY GENERATION

relationships (4.25) and (4.26):

$$a_r = -\frac{q_0 + \tau_a \cdot v_0 + \tau_d \cdot v_0/2 + \tau_v \cdot v_0 - q_e}{\tau_a^2/2 + \tau_a \cdot \tau_d/2 + \tau_a \cdot \tau_v}, \quad (4.25)$$

$$d_r = -\frac{v_0 + \tau_a \cdot a_r}{\tau_d}, \quad (4.26)$$

where q_0 and v_0 are the ones used to generate the initial trajectory, i.e. the ones given by the relationships (4.10) and (4.11). Thus the axis synchronization problem for JL trajectories is solved with a set of simple equations. Since no iterative solver is required, these equations are almost instantaneous to evaluate. Equations (4.18) and (4.19) stand for trajectories with a jerk profile saturated at a given value j_{\max} . Since synchronized trajectories do not respect that condition anymore, another method has to be developed. In order to minimize the computation time, it is wished to avoid iterative resolutions of equations. By setting the jerk at its maximum value for the first acceleration phase and preserving the length of the filter for the deceleration phase T_{jd} , as shown on Figure 4.16, the problem is simplified. T_{ja} and T_{jv} can be expressed as

$$T_{ja} = s \cdot \frac{a_r - a_{0f}}{j_{\max}}, T_{jv} = s \cdot \frac{a_r}{j_{\max}}. \quad (4.27)$$

From the generic closure system:

$$\begin{cases} v_{0f} + \int_0^{t_e} a_f(t) dt = 0 \\ q_{ef} - q_{0f} + \int_{t_0}^{t_e} \left(v_{0f} + \int_{t_0}^t a_f(\tau) d\tau \right) dt = 0 \end{cases} \quad (4.28)$$

one can derive the system (4.29), for which the reached accelerations and deceleration a_r and d_r are solution.

$$\begin{cases} A \cdot a_r^2 + B \cdot a_r + C = 0 \\ d_r = -\frac{v_{0f} + (a_{0f} + a_r) \cdot T_{ja}/2 + a_r \cdot (\tau_a - T_{ja}) + a_r \cdot T_{jv}/2}{\tau_d} \end{cases} \quad (4.29)$$

with

$$\begin{aligned} A &= -\frac{a_{0f} + j_{\max} s \tau_a}{2j_{\max}^2} \\ B &= \frac{\tau_a(T_{jd} + \tau_a + \tau_d + 2\tau_v)}{2} + \frac{a_{0f}^2}{2j_{\max}^2} + \frac{a_{0f} s (T_{jd} + 2\tau_a + \tau_d + 2\tau_v)}{2j_{\max}} \\ C &= q_{0f} - q_{ef} + v_{0f} \left(\frac{T_{jd}}{2} + \tau_a + \frac{\tau_d}{2} + \tau_v \right) - \frac{a_{0f}^3}{6j_{\max}^2} \\ &\quad - s \cdot \frac{a_{0f}^2 (T_{jd} + 2\tau_a + \tau_d + 2\tau_v)}{4j_{\max}} \end{aligned}$$

This system gives an exact solution while $s \cdot a_{0f} \leq s \cdot a_r$. Otherwise, $T_{ja} = -s \cdot \frac{a_r - a_{0f}}{j_{\max}}$, thus the expression of A , B and C changes. This approach is very fast, since it only requires to find the roots of a second order polynomial function.

Figure 4.17 shows an example of synchronized jerk-limited trajectories.

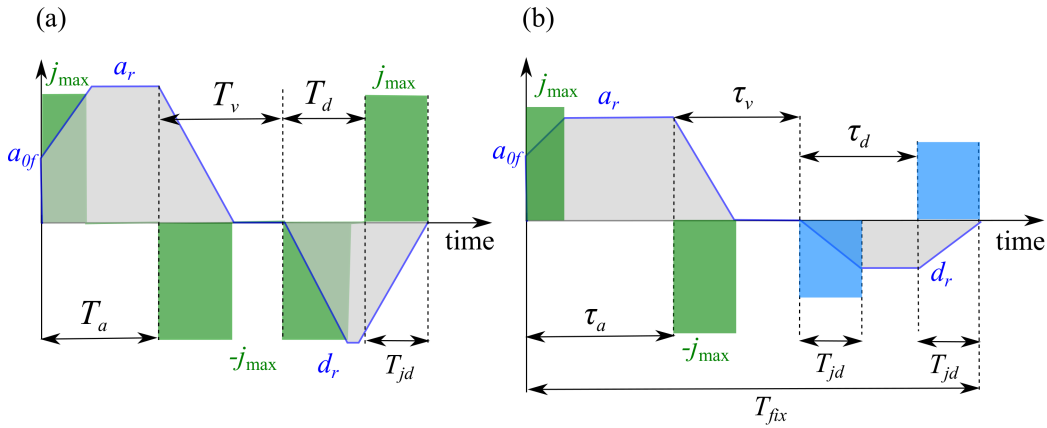


Figure 4.16: The approach chosen to deal with joint synchronization is to constrain the value of the jerk j_{\max} for the first acceleration stage and the filter length T_{jd} for the second one.

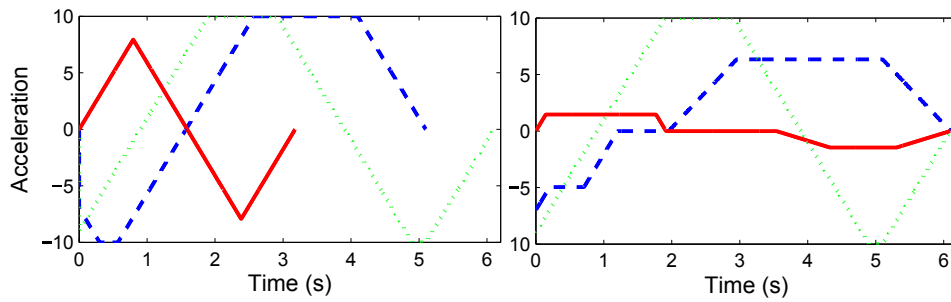


Figure 4.17: Synchronization of time-optimal trajectories: initial trajectories to the left, synchronized trajectories to the right.

4.5 Results

4.5.1 Simulation

The algorithm is implemented in C++ and tested for all types of configurations to validate its results. In any case the algorithm generates the solution in less than 1 microsecond on a regular laptop i7 / 2.7GHz running with Windows 7 as operating system. At the best of the author's knowledge this is the fastest time-optimal jerk-limited trajectory generator. A typical control cycle time being 1 ms, this algorithm can easily handle any multi-axis system and save a significant amount of time to the controller for other tasks, e.g. monitoring, obstacle avoidance or any data processing. Besides, such a small calculation time enable instantaneous reactions to unforeseen events, as introduced in [KTW06].

4.5.2 Experimental validation with a 7 axis robot

The algorithm is tested with a 7 DoF KUKA leightweigh LBR IIWA. The Fast Robot Interface (FRI) of the KUKA *Sunrise.Connectivity* collection of open interfaces was used for real time communication between the robot controller and an external computer with a rate of 1 ms, as shown by Figure 4.18.

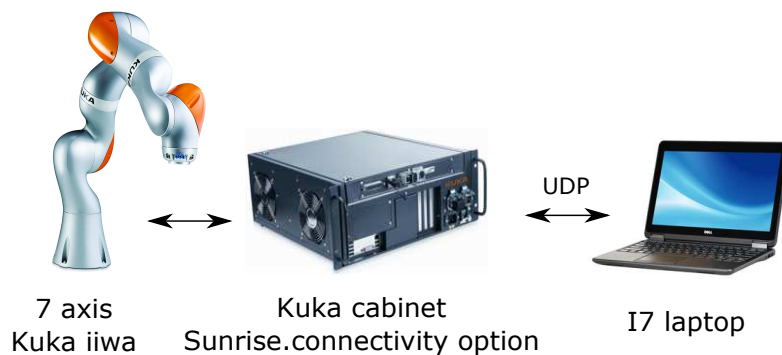


Figure 4.18: Experimental setup for the validation of the jerk-constrained trajectory generation.

Figures 4.19 and 4.20 show samples of experimental results with respectively synchronized and not synchronized joints. Dynamic new target references were randomly generated and the new trajectories updated online, with some changes in the kinematic limits. The joint positions are measured by from the joint encoders and the velocity and acceleration signals are obtained by time differentiation and subsequent smoothing.

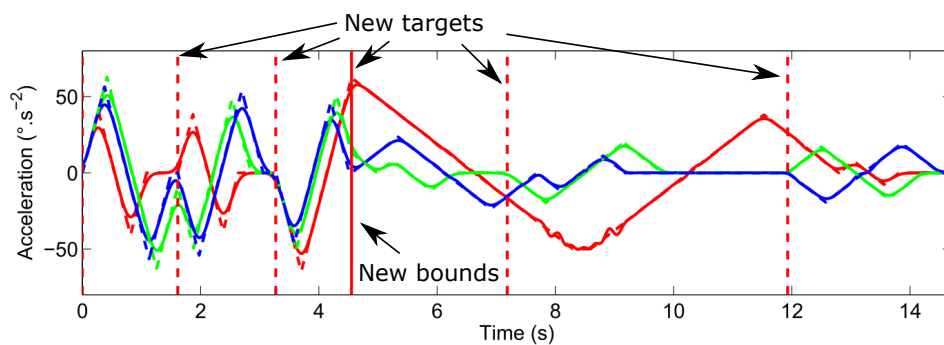


Figure 4.19: Experimental results for non-synchronized trajectories (only three joints shown). New targets are given on vertical lines. j_{\max} is lowered at the vertical full line. Dashed lines: reference acceleration, full lines: actual acceleration.

CHAPTER 4. JERK LIMITED TIME OPTIMAL ONLINE TRAJECTORY GENERATION

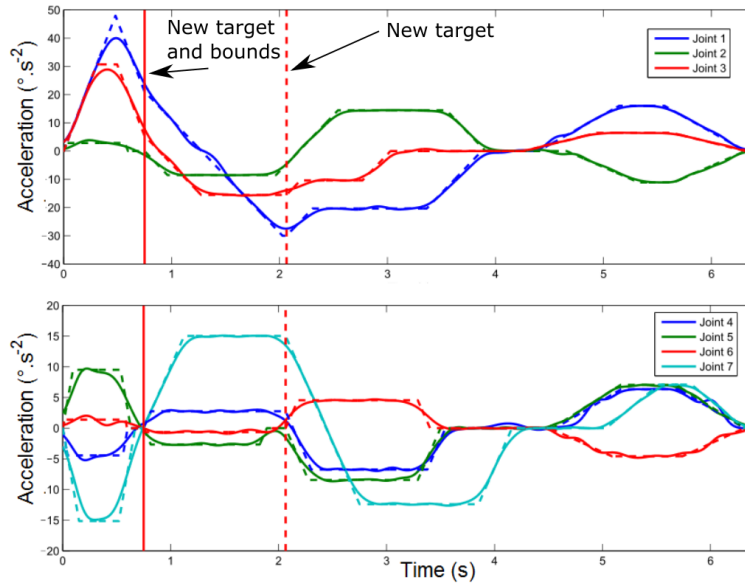


Figure 4.20: Experimental results for synchronized trajectories (7 joints). New targets are given on vertical lines. j_{\max} is lowered at the full vertical line. Dashed lines: reference acceleration, full lines: actual acceleration. Top graph: joints 1 to 3; bottom graph: joints 4 to 7.

These results demonstrate how the trajectory generator developed in this chapter can handle systems with many DoFs while respecting very a short cycle time. An additional experiment is set up. Two iiwa robots are setups in a master / slave configuration. The master robot follows a programmed path. A camera monitors the position of the tip of this master robot with a sampling time of 15 ms and sends this position to a computer online. The latter computer uses an inverse kinematic model of the slave robot to convert these measured Cartesian positions into robot configurations. The latter are then send to the jerk-limited trajectory generator which drives the slave robot joints. As result the slave robot follows the master robot with a jerk-limited motion. Figure 4.21 shows the setup of the experiment. The kinematic limits of the joints are set as: $(v_{\max}, a_{\max}, j_{\max}) = (100 \text{ s}^{-1}, 200 \text{ s}^{-2}, 200 \text{ s}^{-3})$.

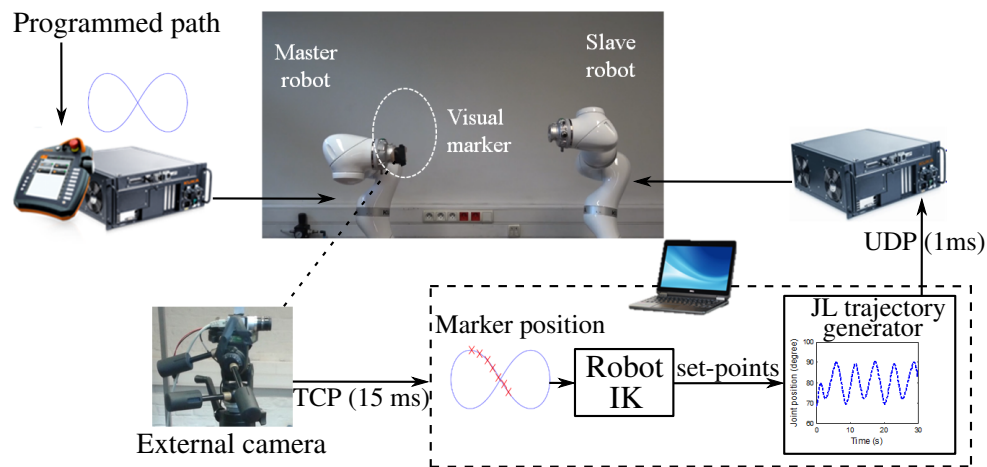


Figure 4.21: Setup of the master / slave experiment.

This experiment shows how a loading arm can be make follow a moving target with jerk-limited motions. A video of this test is available at http://pcabeset.free.fr/public/hidden/Master_slave_expe.mp4.

4.5.3 Marine loading arms

Jerk-limited trajectories are tested on the scaled OLAF model and the full scale DCMA. The trajectories are send in open-loop to the spool valves, and the response of the arm is observed. After empirical tuning of the kinematic limits for each joint, smooth motions of the arm are achieved. These motions are characterized by no residual oscillation, measured or visually observed, and a very "neat" full stop. Acceleration-limited and jerk-limited trajectories are briefly compared on the scaled OLAF model presented in Section 1.4.1. It is found, from sensor recordings and visual observation, that the scaled arm behaves similarly for both kind of trajectories, as illustrated by Figure 4.22. This may be explained by the low accuracy of the actuation system or this arm, and the natural filtering effect of the hardware.

On the other hand, the full scale DCMA presented in Section 1.4.2 is much more sensitive to the type of reference trajectory. This statement is based on visual observation because no sensor is available to measure the oscillation of the structure. Further study may include the measurement of such oscillation by using an external measurement system, e.g. a total station.

CHAPTER 4. JERK LIMITED TIME OPTIMAL ONLINE TRAJECTORY GENERATION

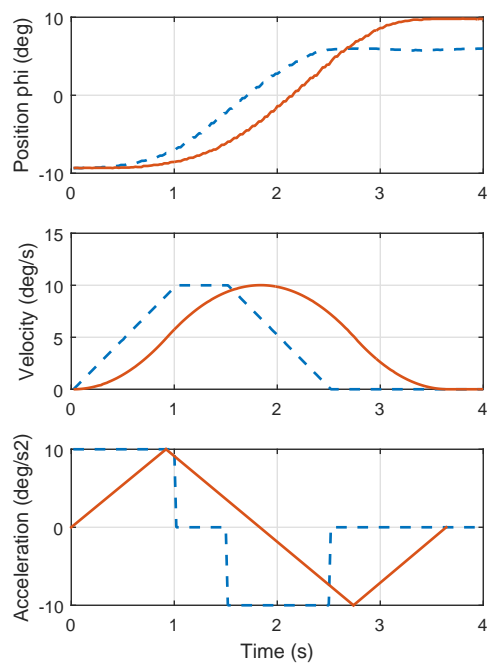


Figure 4.22: Typical joints responses to AL (dashed blue line) and JL (full red line) trajectories. Example of the slewing joint: top graph: measured position ϕ , middle and bottom graphs: reference velocity and acceleration. No residual oscillation are measured or seen on any of the motions.

Chapter 5

Active motion compensation with delay removal

The pursuit stage of the automatic connection procedure, as detailed in Section 1.3.1.3, aims to keep the coupler of the loading arm in front of the manifold. Due to the relative motion between the two vessels induced by the sea, the arm should continuously move to compensate this phenomenon. Vessel motion compensation, and more particularly heave compensation, is widely discussed in the literature. Motion compensation methods are classically classed as passive or active. Passive compensation uses passive systems with no external power consumption such as dampers. For example [NLW⁺09] proposes a heave platform mounted on pneumatic cylinders, for deep sea mining systems. This system is able to compensate 83% of the vertical motion of the vessel, according to the latter study. However such passive systems are not compatible with loading arms. First because of the size of loading arms, second because these systems would only compensate the FLNG absolute motion instead of the relative motion between FLNG and LNGC. In this project the solution to develop is clearly based on active compensation. Active motion compensation consists in using actuators together with sensors to measure the vessel motion and compensate it. A well known motion compensation application in the offshore industry is the dynamic positioning (DP) of vessels. Dynamic positioning is a common system which regulates the position and heading of vessels by using their propulsion systems. Closer to the application of this project come compensation systems applied to offshore cranes. [WTM12] presents a winch actuated compensation system for load transfer. This system uses an inertial measurement unit to estimate the vessel movements, and a winch to regulate a load position. K uchler *et al.* [KMN⁺11] also propose an active heave compensation system that keeps the load motion of a crane unaffected by the ship movement. This latter method uses a prediction algorithm to prevent any detrimental time delay in the load position control. Active

CHAPTER 5. ACTIVE MOTION COMPENSATION WITH DELAY REMOVAL

motion compensation can also be found in different systems, such as robotic tools for heart surgery. Kettler *et al.* [KPN⁺07] developed a robotic instrument that measures with ultrasound and compensates the motion of the target tissue with a single actuator. The pursuit stage of the automatic connection of loading arm corresponds to a stage where the loading arm uses its actuation system to compensate the relative motion between the FLNG and the LNGC, by controlling the position of the coupler. In other words, from the knowledge of the relative motion 0P_m , the loading arm should be driven in a way that keeps the pose of the coupler P_c constant in the manifold frame R_m (see Figure 1.11). More precisely, Equation (1.1) should be satisfied.

A motion tracking algorithm has therefore to be implemented. The pose of the manifold 0P_m is measured by some of the equipment detailed in Section 2.1, and is assumed known in this section. From Relation (1.1) the target manifold pose 0P_t is calculated (see Figure 1.14). The inverse kinematic model developed in Appendix A can thus express 0P_m as a target arm configuration $\mathbf{q}_t = [\phi, \alpha, \beta, \gamma]^T$ at any time t :

$$\mathbf{q}_t(t) = \mathbf{IK}({}^0P_t(t), {}^r\mathbf{q}_0(t)). \quad (5.1)$$

Consequently, the problem is kinematically decoupled and each joint is considered individually. Hence in this section the motion planning problem of a single joint is investigated. In order to benefit from the properties of time-optimal jerk-limited trajectories, the generator developed in Chapter 4 is used. Figure 5.1 shows a diagram of the tracking algorithm developed for a single joint.

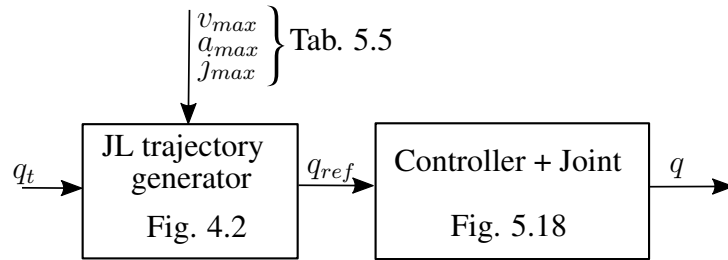


Figure 5.1: Simple jerk-limited tracking algorithm for a single joint.

Where:

- q_t is the target position for the joint considered,
- q_{ref} is the reference of the controller of the joint, computed by the trajectory generator,
- q is the measured position for the joint considered,

CHAPTER 5. ACTIVE MOTION COMPENSATION WITH DELAY REMOVAL

- v_{\max} , a_{\max} and j_{\max} are respectively the maximum velocity, acceleration and jerk used to constraint the trajectories of the joint.

A simulation is run under the reference vessels motions given in Section 3.3.2 with a the OLAF scaled model and the full scale DCMA as loading arms. The joints and the low-level controllers are not modeled in this simulation under the assumption that the kinematic limits of the trajectories are low enough to be accurately followed. The behavior of the joints and the controllers are implicitly accounted for by the trajectory generator, as further detailed in Section 5.3.1. The values used as kinematic limits are given in Table 5.5. In other words, it is assumed that $q = q_{ref}$. Figure 5.2 shows the evolution of the angular position of the three first joints (blue lines) with the target positions (dashed red lines).

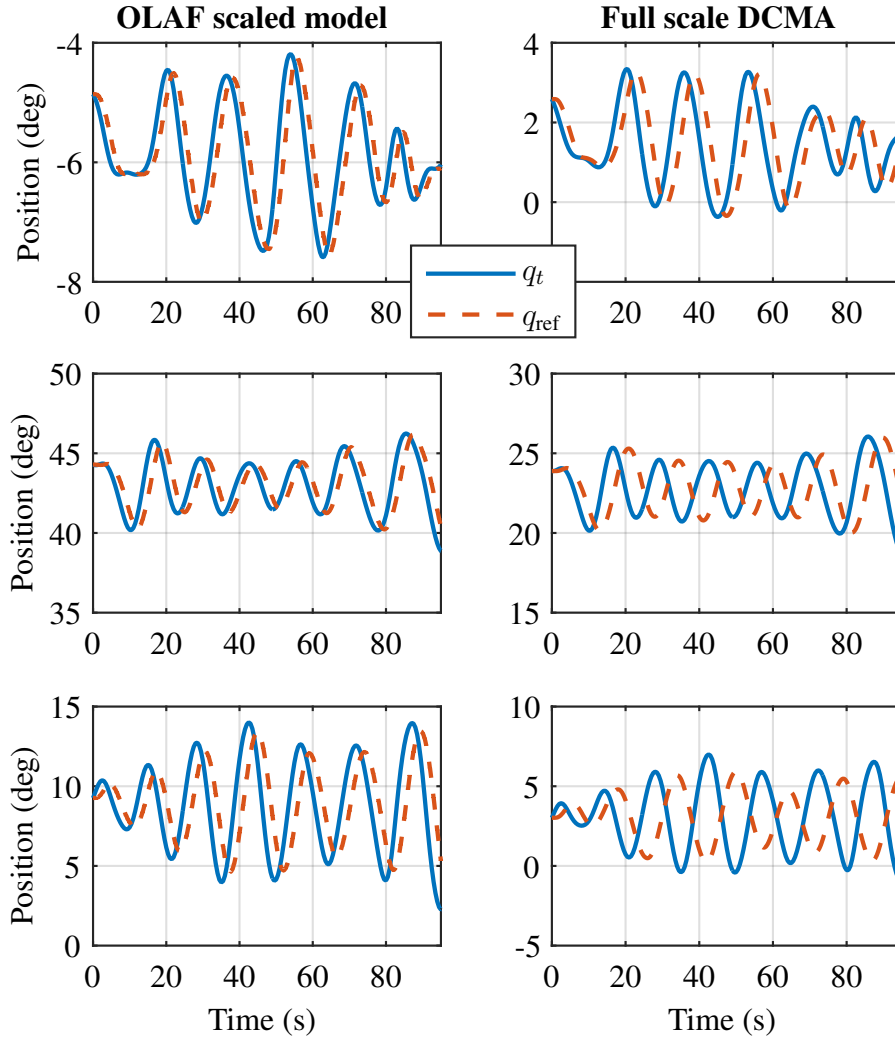


Figure 5.2: Evolution of the angular references q_{ref} of the three first joints (blue lines) with the target positions q_t (dashed red lines).

One can notice a delay between the target position and the planned position of the joints. This delay comes from the low kinematic bounds of the trajectories used to drive the joints. The tracking errors of the joints positions lead to significant error of the pose of the coupler. Figure 5.3 shows the evolution of the position error $X_{err}(t) = \|\mathbf{X}_c(t) - \mathbf{X}_t(t)\|$.

During this simulation, the maximal calculated position error is 1.3 meters for the full scale DCMA (for a tolerance of 10 cm). This significant error comes from

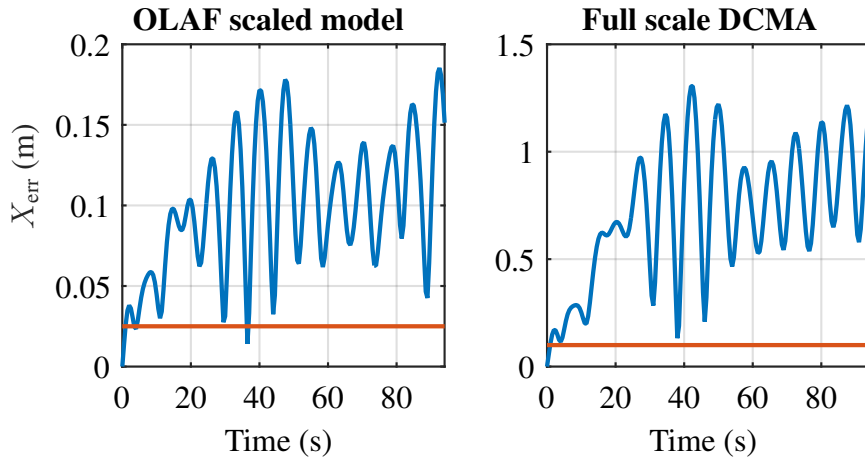


Figure 5.3: Evolution of the position error of the coupler. The maximum simulated error is 1.3 m for the full scale DCMA and 0.25 for the scaled OLAF. The red lines represent the tolerance of the coupling systems.

the kinematic limitation of the joints regarding the relative motion of the vessels. According to the position tolerance of the flanging system of the coupler, this error is too high for the automatic connection to be possible.

In the following section, a method to reduce or remove the pursuit delay is investigated.

5.1 Predictive planning

The pursuit error highlighted in the previous section, i.e. $q_t - q_{ref}$, has to be removed. One solution could be to higher the kinematic bounds set on the joints. The latter solution is not an option since these bounds are set according to the performance of the controllers and ensure that the arm is driven without vibration. By predicting the future vessels motions, the future joints references may be anticipated and the tracking delay canceled. However the knowledge of future references cannot be used as direct input for the trajectory generator. Indeed the pursuit delay is nonconstant and changes according to the state of the joint and its reference because of the use of the JL trajectory generator. Classically, tracking problems are solved by using tools such as model predictive control (MPC). Model predictive control is a popular strategy from the optimal control theory. This approach to control design takes advantage of the knowledge of future references to optimize the performance of the system over a window of time. In other words, predictive

CHAPTER 5. ACTIVE MOTION COMPENSATION WITH DELAY REMOVAL

control makes the system able to anticipate foreseen events. First successful applications of this technique appear in the literature in the late 1970, in the chemical industry [RRTP78]. Since then, this method was extensively studied, and applied in many fields of the industry, as surveyed in [QB03] and [MRRS00]. In the field of industrial robotics, predictive control is also widely used, mainly for low-level control. [VM05] presents a classic application where the dynamic model of a Puma robot is linearized and used to anticipate its behavior, thus increasing its tracking performance. On the other hand, Ghazaei *et al.* [AORJ15] use MPC applied to a fixed-time trajectory generation method for a ball catching scenario with an industrial manipulator. In this study, predictive control is set up to reduce the pursuit error highlighted on Figure 5.3. For a straightforward implementation the algorithm is developed in discrete time. The relationship between the continuous and discrete time is given by the relation:

$$t = kT_p, \quad (5.2)$$

where t is the continuous time, k the discrete time, integer, and T_p the cycle time for the predictive planning algorithm. Let us note in this section :

- k the current discrete time,
- H the receding horizon over which the predictive control is applied,
- q_i the past measured positions of the joint, at the past time $i \leq k$,
- $q_{i|k}$ the positions of the joint for the future time i , calculated at time k , $\forall i > k$,
- $\mathbf{q}|_k = [q_{k+1|k}, \dots, q_{k+H|k}]^T$, the predicted positions of the joint at time k over the horizon H ,
- \mathbf{w} the target motion time series, and w_k its value at time k ,
- $\mathbf{u}|_k = [u_{k|k}, \dots, u_{k+H-1|k}]^T$ the future inputs of the system, calculated at time k .

Predictive control aims to determine, at every time k , the input vector $\mathbf{u}|_k$ for which the future system outputs $\mathbf{q}|_k$ best fit with the target trajectory \mathbf{w} , as illustrated on Figure 5.4. This input vector is calculated as the solution of the optimization problem:

$$\mathbf{u}|_k = \min_{\mathbf{u}|_k} J_k, \quad (5.3)$$

CHAPTER 5. ACTIVE MOTION COMPENSATION WITH DELAY REMOVAL

where the cost function J_k penalizes the distance between the future system output $\mathbf{y}|_k = [y_{k+1|k}, \dots, y_{k+H|k}]$ and the reference trajectory w :

$$J_k = \sum_{i=k+1}^{k+H} \sigma_i (q_{i|k} - w_i)^2 + \lambda \sum_{i=k+1}^{k+H} (u_{i-1|k} - w_i)^2. \quad (5.4)$$

The scalar factors λ and σ_i are weights to be tuned according to the application. This cost function is made of two terms. The first one (left term) aims to reduce the error of the system. The second one aims to keep the solver algorithm from producing very large outputs, in order to ensure convergence. Once $\mathbf{u}|_k$ is calculated, its first element $u_{k|k}$ is sent as input to the system.

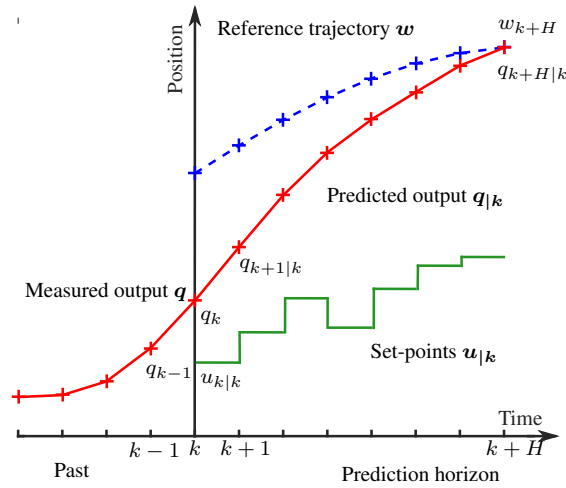


Figure 5.4: Predictive control aims to find the optimal set-points sequence $\mathbf{u}|_k$ to make the future outputs $\mathbf{q}|_k$ match the reference trajectory w .

Classically the predictive control works without trajectory generator, and directly drives the actuators of the system by using models of the latter. However in the case of the loading arm, such an approach requires models of the joints that include nonlinearities, e.g. dry friction, and vibration phenomena. It is important to include the vibration behavior of the structure in the models for the MPC not to excite the arm. Since such models, as for example finite elements models [BCG08], are complex to develop and since the knowledge of all vibration modes of the arm is missing, another approach is taken.

The time-optimal jerk-limited trajectory generator developed in Chapter 4 is kept before the joints, to ensure that they are smoothly driven and that no vibration is induced in the structure of the arm. Therefore the plant to control is the

CHAPTER 5. ACTIVE MOTION COMPENSATION WITH DELAY
REMOVAL

trajectory generator plus the joint with its own controller. For that reason the methodology developed here is called predictive planning. In this study the reference trajectory w is the target joint motion q_t of the joint considered, given by Equation (5.1):

$$w = [q_t(k+1), \dots, q_t(k+K)]. \quad (5.5)$$

The reference w comes from the prediction of the future vessels motion, as detailed in Section 5.2 and w is assumed known in this section. Figure 5.5 shows the architecture of the overall system.

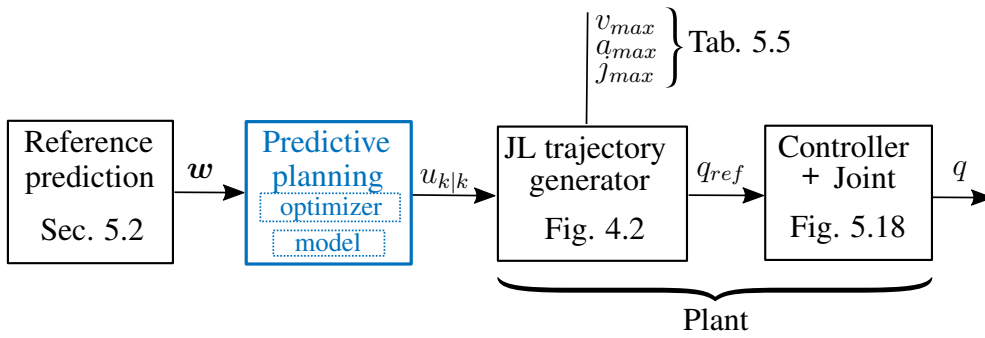


Figure 5.5: The predictive planning sends inputs to the trajectory generator.

A model of the plant is required to predict the outputs q_k . Let us note f this model such that:

$$\begin{cases} Q_{k+1} &= f(Q_k, u_k) \\ q_k &= CQ_k \end{cases}, \quad (5.6)$$

where $Q_k = [q_k \ \dot{q}_k \ \ddot{q}_k]^T$ denotes the state of the joint at time k and $C = [1 \ 0 \ 0]$. In this study it is assumed that the joint is able to follow accurately the trajectories produced by the trajectory generator, i.e. $q = q_{ref}$, from adequate tuning of the trajectory generator. Such a tuning is detailed in Section 5.3.1. Consequently, the joint and controller may be omitted in the model f of the plant, which is thus reduced to the trajectory generator only. Figure 5.6 illustrates the predictive planning algorithm.

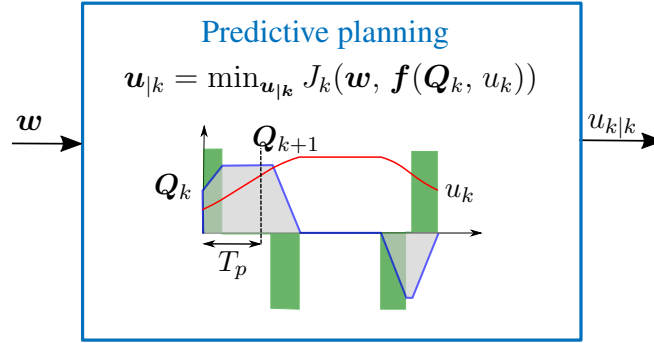


Figure 5.6: The predictive planning algorithm uses the jerk-limited trajectory generator as a model.

The use of the trajectory generator as a model makes it possible to guarantee that the state of the joint is bounded (v_{\max} , a_{\max} , j_{\max}). Therefore no constraint has to be added in the predictive planning problem. The absence of constraint in the algorithm is a significant advantage of this methodology. Indeed dealing with the constraints is a difficult problem, as widely discussed in the literature [BD96]. However f has no closed-form expression and is not linear. Consequently the optimization problem (5.3) is not straightforward to solve. Equation (5.3) can be written as:

$$\mathbf{u}_{|k} = \min_{\mathbf{u}_{|k}} \sum_{i=k+1}^{k+H} \sigma_i (\mathbf{C} \mathbf{f}(\mathbf{Q}_{i-1|k}, \mathbf{u}_{i-1|k}) - \mathbf{w}_i)^2 + \lambda \sum_{i=k+1}^{k+H} (\mathbf{u}_{i-1|k} - \mathbf{w}_i)^2. \quad (5.7)$$

An implementation of the classic Levenberg-Maquardt algorithm [Mor78] is used to numerically solve the problem (5.7). This algorithm is chosen because it converges fast enough to adequate solutions for this predictive planning problem, as discussed below. In this study it is assumed that the optimizer does converge. The choice of the horizon H is relative to the dynamic of the system and the target trajectory. A too long horizon would make the optimization problem difficult and too slow to solve, while a too short horizon would not ensure that the system anticipates the evolution of the target [BD96].

The simulations run at the beginning of this chapter are repeated with the predictive planner, as a comparison. Figure 5.7 shows the results of that simulation. The horizon length is empirically chosen as $H = 4$ for the OLAF scaled model and $H = 10$ for the full scale DCMA. The parameters λ and σ_i are set as : $\lambda = 1.10^{-4}$ and $\sigma_i = 1, \forall i$. With these settings the algorithm convergence time is below 0.2 seconds.

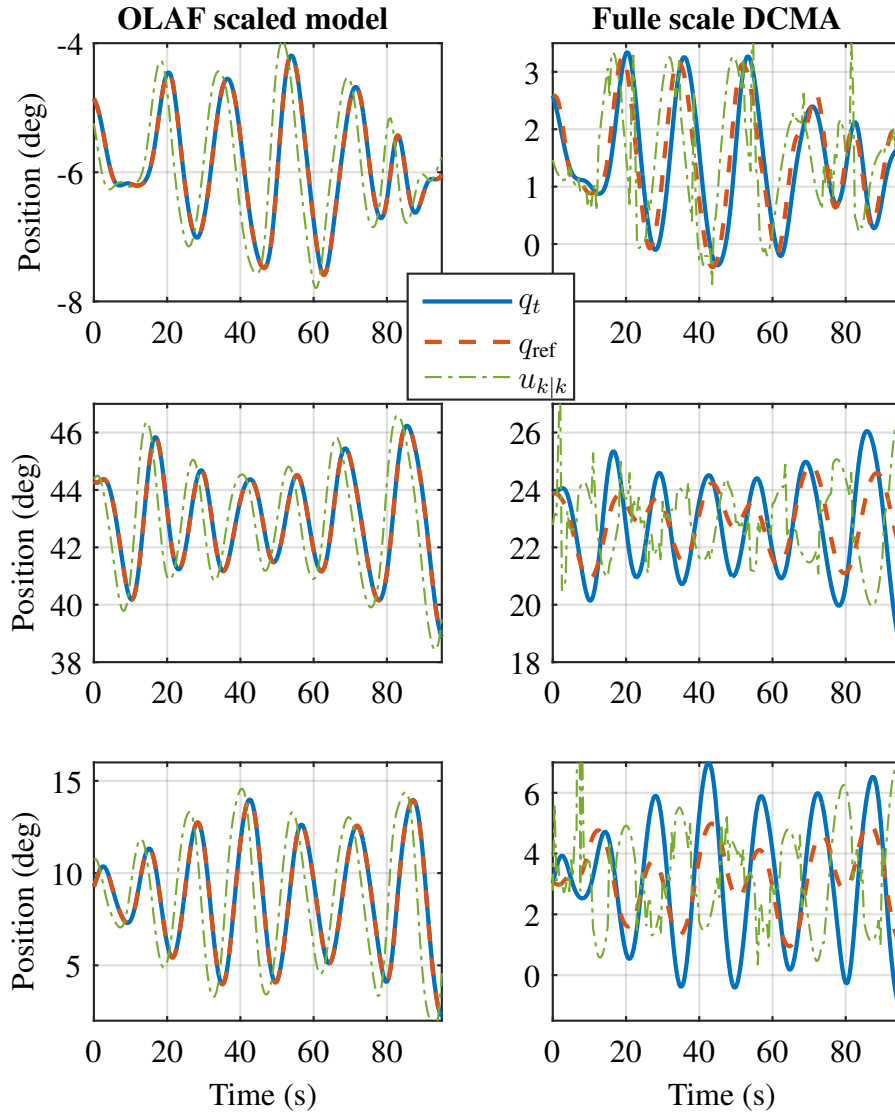


Figure 5.7: Predictive planning: simulation results. Evolution of the angular position q of the three first joints (blue lines) with the target positions q_t (dashed red lines). The set-points $u_{k|k}$ generated by the optimization algorithm is plotted by the dot-dashed green lines.

Let us first consider the results for the OLAF scaled model. The set-points sequence generated by the predictive planning algorithm successfully drives the joints position along their reference. As shown on Figure 5.8, the position error $X_{err}(t)$ is significantly reduced below 0.005 m so that this error is small enough

CHAPTER 5. ACTIVE MOTION COMPENSATION WITH DELAY REMOVAL

for the automatic connection to be possible. Unfortunately the results of the simulation with the full scale arm are not as successful. Even though the position error is significantly reduced (see Figure 5.3), the resolution algorithm does not converge toward a solution that cancels this error for the reason that the kinematic limits of the arm joints are too low. In other words, the bounds set up in Table 5.5 are respectively lower than the derivatives of the target positions. Therefore no optimization can make the arm track the target motion.

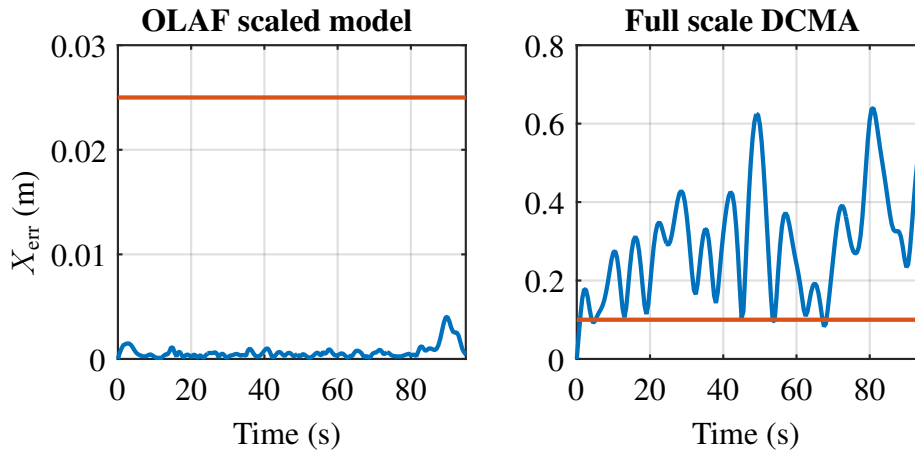


Figure 5.8: Evolution of the coupler position error $X_{err}(t)$ with the predictive planning operating. The red lined represents the tolerance of the coupling systems.

This simulation shows that the use of a predictive control strategy nearly cancels the pursuit error, so that the latter error is small enough for the automatic connection to be possible. In the case where the arm has not the capability to follow the target motion, as simulated for the full scale arm, either the kinematic bounds of the joint should be changed by improving the system, or a slower target motion should be waited for. The predictive planning is no further studied in this project, nevertheless the author highlights that:

- The convergence of the optimization algorithm is not proven. Any failure of the solver to successfully converge could lead to unexpected motion of the loading arm. This is a serious safety issue which should be investigated.
- The robustness of the solver to the initial conditions of the system is not discussed. Even though the optimization algorithm always converges in practice, this question should be studied.
- The robustness of this system to errors in the estimation of w is not studied either. The knowledge of this robustness is important for the development of the predictor of q_t , detailed in the next section.

In order to implement the predictive control, the target trajectory $\mathbf{q}_t(t)$, which has been assumed known so far, has to be predicted. The next section deals with this matter.

5.2 Vessel motion prediction

An accurate prediction of the carrier motion is required by the predictive control developed in the previous section. More specifically, the evolution of the pose ${}^0\mathbf{P}_m$ of the manifold during a sliding horizon H is needed. The future evolution of the orientation ${}^r\mathbf{q}_0$ is also needed by the inverse kinematics function of the loading arm, although this later prediction is not detailed in this section. From the complicated nature of the sea waves, currents and wind, vessel motion prediction is a difficult task and is widely discussed in the literature. In order to develop an active heave compensation system for a crane mounted on a vessel, [KMN⁺11] uses a prediction algorithm based on superposition of sine signals. [FGLA11] compares such a predictor with an Auto-Regressive predictor, using data measured on a real ship. In his study the latter predictor gives better results. Ship motion prediction is also used in aircraft landing operations. In this context [YPGU08] builds a phase-lead prediction model for ship dynamics, while [KBM05] develop a prediction procedure based on artificial neural networks. The previous prediction methods assumed that the past vessel motion is known, often recorded by inertial measurement units. Another approach consists in measuring the remote incoming waves at the surface of the ocean in order to predict the ship motion. [DHN⁺10] implements such a technique by means of a monitoring radar system. While the prediction is significantly enhanced over the latter approaches, using this method is expensive and sensitive hardware is needed onboard. It is difficult to compare the methods found in the literature, since in each study the results are given for different ships on different sea states and according to different performance criteria.

In this study it is chosen to investigate the use of Artificial Neural Networks (ANN) as prediction algorithm. Artificial neural networks are mathematical structures inspired from the inner working of biological brain, as extensively described in [Kri07]. ANNs first appear in the literature in the 1940s with the work of Warren McCulloch and Walter Pitts [MP43]. As computing possibilities have greatly increased in the recent years, artificial neural networks became a practical solution to many industrial issues [LMF⁺01]. The adaptability, polyvalence as well as the easiness of implementation of this technique make ANNs a popular choice in many fields, such as robotics [KCB⁺12], system modeling, image processing or

data mining. For the same reasons, an artificial neural network is chosen in this study to solve the vessel motion prediction problem.

5.2.1 Structure of the neural network

The structure of a neural network should be chosen according to the problem to solve. Our prediction problem can be formulated as follow. At any time k , given N_i past recorded samples of the pose ${}^0\mathbf{P}_m$, the evolution of ${}^0\mathbf{P}_m$ should be estimated for the H steps ahead. Moreover this estimation should be accurate enough for the needs of the predictive control algorithm developed in the previous Section. In other words, the neural network should behave as a function $\hat{\mathbf{f}}$:

$$\hat{\mathbf{f}} : \mathbb{R}^{6 \times N_i} \rightarrow \mathbb{R}^{6 \times H}$$

$$[\mathbf{P}_{m, k+1|k}, \dots, \mathbf{P}_{m, k+H+1|k}] = \hat{\mathbf{f}}(\mathbf{P}_{m, k}, \dots, \mathbf{P}_{m, k-N_i}) \quad (5.8)$$

where $\mathbf{P}_{m, k}$ is the measured value of ${}^0\mathbf{P}_m$ at time k and $\mathbf{P}_{m, k+j|k}$ is the value of ${}^0\mathbf{P}_m$ at time $k+j$, calculated at k . The sampling time is noted T_n .

For times series prediction and function approximation, three-layered feed-forward ANNs have demonstrated good results in the literature [Kri07]. So far the studies investigating vessel motion prediction concentrates on one dimension only, generally the heave. Figure 5.9 presents the structure of such an ANN where:

- y_k is the value of the considered time series at time k ,
- $\mathbf{Y}_k = [y_k, \dots, y_{k-N_i}]^T$ the input vector,
- N_i is the number of inputs,
- N_n is the number of neurons in the hidden layer,
- \mathbf{W}_h and \mathbf{W}_o are the matrices of the weights in the hidden and output layers,
- b_h and b_o the biases of the hidden and output layers.
- \mathbf{f}_h and \mathbf{f}_o the activation functions of the hidden and output layers.

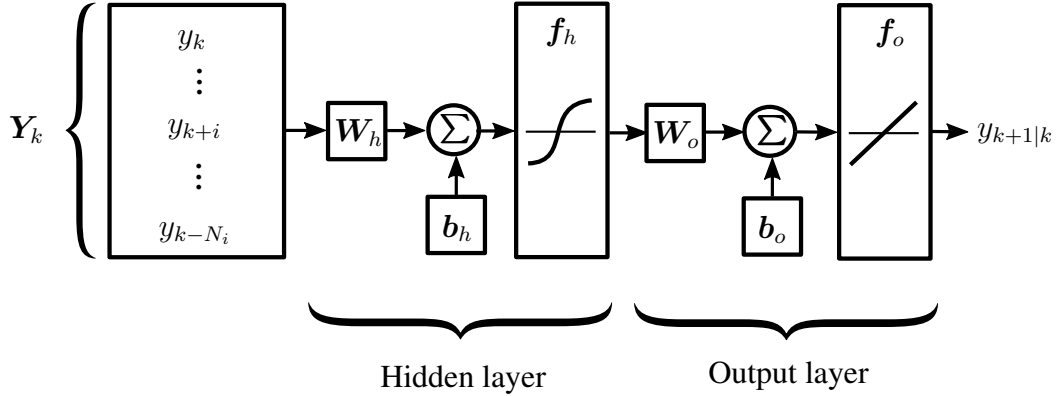


Figure 5.9: Generic structure of a three-layered feedforward neural network.

A three-layered neural network consists of an input vector \mathbf{Y}_k , an hidden layer $\mathbf{f}_h(\mathbf{W}_h \cdot \bullet + \mathbf{b}_h)$, and an output layer $\mathbf{f}_o(\mathbf{W}_o \cdot \bullet + \mathbf{b}_o)$. Together these layers correspond to the relation:

$$y_{k+1|k} = \mathbf{f}_o(\mathbf{W}_o \mathbf{f}_h(\mathbf{W}_h \mathbf{Y}_k + \mathbf{b}_h) + \mathbf{b}_o) \quad (5.9)$$

One should note that the activation functions \mathbf{f}_h and \mathbf{f}_o are elementwise functions. Classically, \mathbf{f}_h is chosen as a log-sigmoid or tangent-sigmoid function. The latter is chosen in our study:

$$\mathbf{f}_h(\mathbf{v}) = \left[\frac{2}{1 + e^{-2v_1}} - 1, \dots, \frac{2}{1 + e^{-2v_{N_i}}} - 1 \right]^T \quad (5.10)$$

Using a nonlinear activation function makes the ANN able to approximate nonlinear functions. The tangent-sigmoid function is similar to the tangent hyperbolic function, but is faster to evaluate numerically. Consequently the training of the ANN is made faster. The activation function of the output layer \mathbf{f}_o is chosen as the identity function:

$$\mathbf{f}_o(\mathbf{v}) = \mathbf{v} \quad (5.11)$$

The choice of the activation functions relies on the experience brought by the literature [Kri07]. The neural network previously described may be used to predict one dimension of ${}^0\mathbf{P}_m$. Six of such neural networks would thus be needed to predict ${}^0\mathbf{P}_m$. Another approach is to use a single network to predict the six dimension of ${}^0\mathbf{P}_m$ simultaneously. The size of the input vector N_i is then six times the number of past samples used in the prediction:

$$\mathbf{Y}_k = [\mathbf{P}_{m,k}^T, \dots, \mathbf{P}_{m,k-N_i}^T]^T \quad (5.12)$$

The neural network is defined by the function:

$$\mathbf{P}_{m, k+1|k} = \mathbf{f}_o (\mathbf{W}_o \mathbf{f}_h (\mathbf{W}_h \mathbf{Y}_k + \mathbf{b}_h) + \mathbf{b}_o) \quad (5.13)$$

The main advantage of using a single ANN to predict all six components of ${}^0\mathbf{P}_m$ is that the network may be able to find correlation between these dimensions and use it to improve its performances.

The predictive control developed in the previous section require a prediction of ${}^0\mathbf{P}_m$ for the H steps ahead. In order to use the ANN for several steps ahead prediction, a loop is made from the output to the input. In others words, for any integer $i > 0$ the predicted vector $\mathbf{P}_{m, k+i|k}$ is used to compose the vector $\mathbf{Y}_{k+i|k}$ and then calculate $\mathbf{P}_{m, k+i+1|k}$. Figure 5.10 shows the structure of such a closed-loop network.

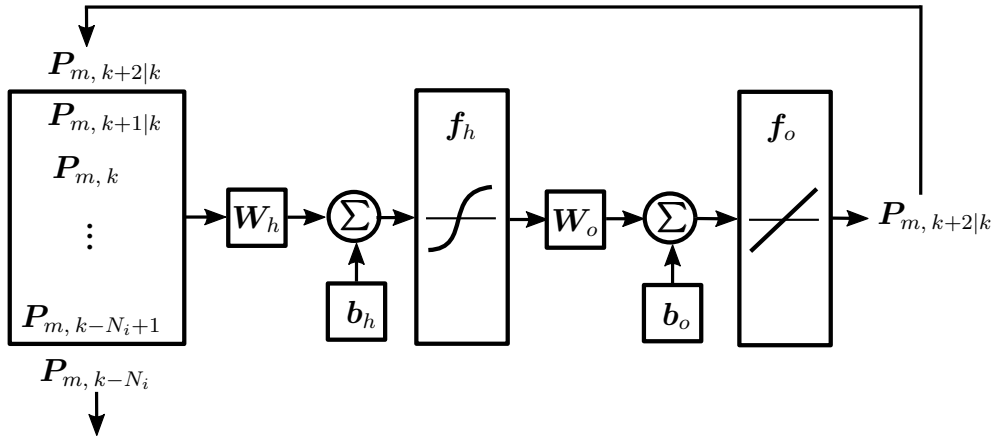


Figure 5.10: Estimated samples are used as inputs to make multiple step ahead prediction.

The values of N_i and N_n , which correspond respectively to the size of the input vector and the height of W_h , are to be found experimentally. Indeed the literature does not offer any systematic way to calculate this values.

5.2.2 Training of the neural network

Once the structure of a neural network is chosen, the latter has to be trained before it can be used. The training stage consists in optimizing the weights and biases, i.e. the values of the elements of W_h , W_o , b_h and b_o , so that the error between the predicted and target outputs is minimized. These weights and biases are randomly

initialized. The training of an ANN is a non-linear optimization problem which consists in minimizing the quantities $P_{m, k+1} - P_{m, k+1|k}$, for any k . More precisely, a cost function called objective function in the context of ANNs, is defined as:

$$J = \sum_k (P_{m, k+1} - P_{m, k+1|k})^2 \quad (5.14)$$

This type of training is called supervised learning, where the target result of the ANN is known. Figure 5.11 summarizes the supervised learning scheme. The literature offers many iterative algorithms to solve this optimization problem, e.g. the conjugate gradients, Levenberg-Marquardt or the quasi-Newton algorithms [Kri07]. Supervised learning may also be used *while* the network is used. The learning is then called "adaptative". Adaptative learning is beyond the scope of this study.

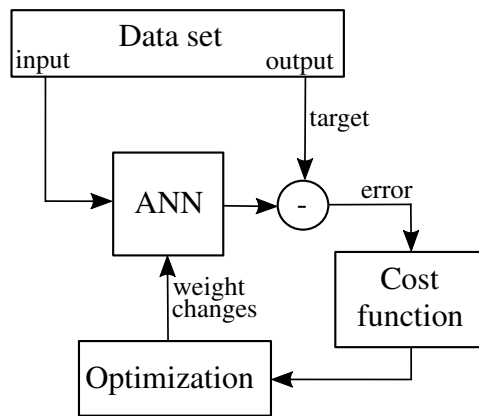


Figure 5.11: Generic diagram for the training of artificial neural networks [MV06].

A large amount of data is necessary for the training. In this study the training data correspond to a 3 hours time series of 0P_m , generated according to the method presented in Section 3.3.2. The choice of the optimization algorithm used in the training stage mostly impact the duration of this stage. It was found from empirical tests that, for this study, the Levenberg-Maquardt algorithm ensures the fastest convergence, and also finds better optima than conjugate gradients and quasi-Newton algorithms.

5.2.3 Results

In order to validate the method developed in this section, the data set is divided in two subsets for cross-validation: a training subset which corresponds to 70% of

CHAPTER 5. ACTIVE MOTION COMPENSATION WITH DELAY REMOVAL

the original data set, and a validation subset of 30%. These datasets are respectively 126 minutes long and 54 minutes long, initially sampled at 0.02 seconds. These data will be re-sampled to a more suitable sample time T_n , as detailed below. Two different structures of ANN are compared below: one that predicts separately each component of the vessels motion, and another that process all motion components together.

First, a set of six one-dimension neural networks are trained for the motion prediction of each of the surge, sway, heave, roll, pitch and yaw signals, with the training subset, according to the structure presented in Figure 5.12. In a second time a six-dimensional network is also trained according to the structure presented in Figure 5.13.

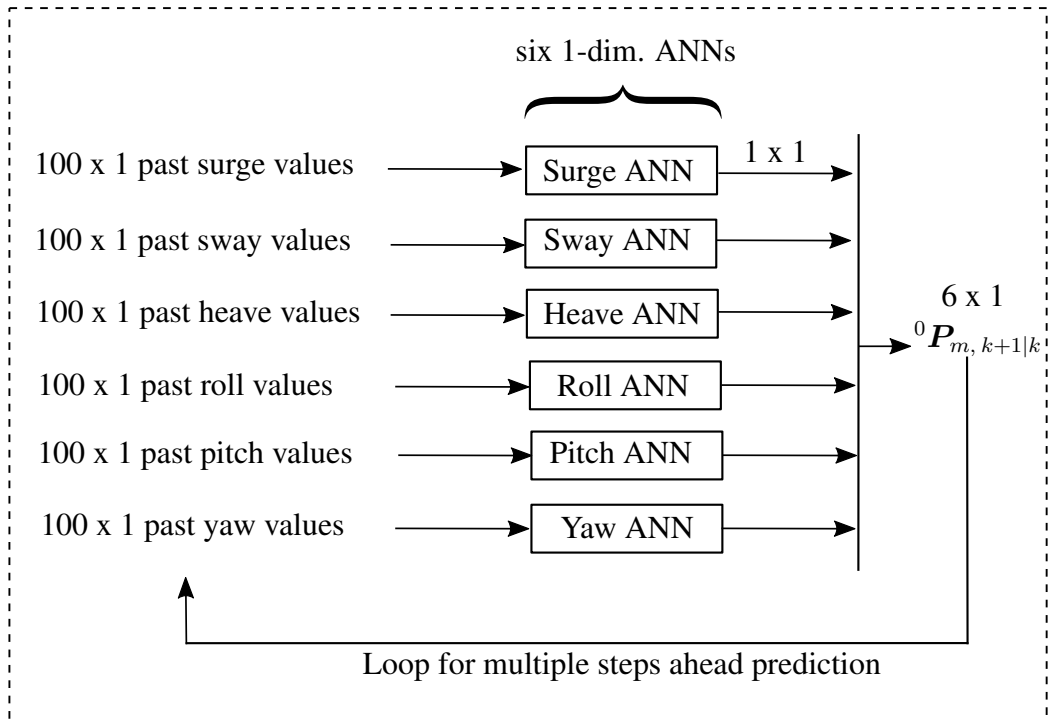


Figure 5.12: Six one-dimension artificial neural networks are trained for the motion prediction. Each of them follow the structure shown in Figure 5.9.

CHAPTER 5. ACTIVE MOTION COMPENSATION WITH DELAY REMOVAL

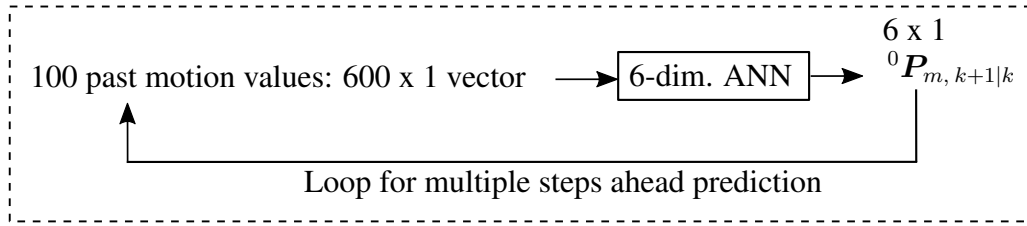


Figure 5.13: A single six-dimension artificial neural network is trained for the motion prediction.

Because of the high computational cost of the training of such ANNs, the training is time-consuming with the available processing units. Consequently the parameters N_i , T_n and N_n are tuned empirically. These parameters are, for each structure, near the optimal values. In particular, this tuning is careful not to overestimate the number of neurons, to prevent overfitting [DBDJH14]. The values of these parameters are detailed in Table 5.1.

Table 5.1: Parameters values

	One-dim. ANNs	Six-Dim ANNs
N_i	100	100
T_n (s)	0.8	0.8
N_n	5	10

Let us note the prediction error produced at time k for j samples ahead:

$$e_{j|k} = P_{m, k+j} - P_{m, k+j|k} \quad (5.15)$$

Figure 5.14 shows a typical prediction of the one-dimension ANN for the heave signal at one time sample k , with the prediction error.

CHAPTER 5. ACTIVE MOTION COMPENSATION WITH DELAY REMOVAL

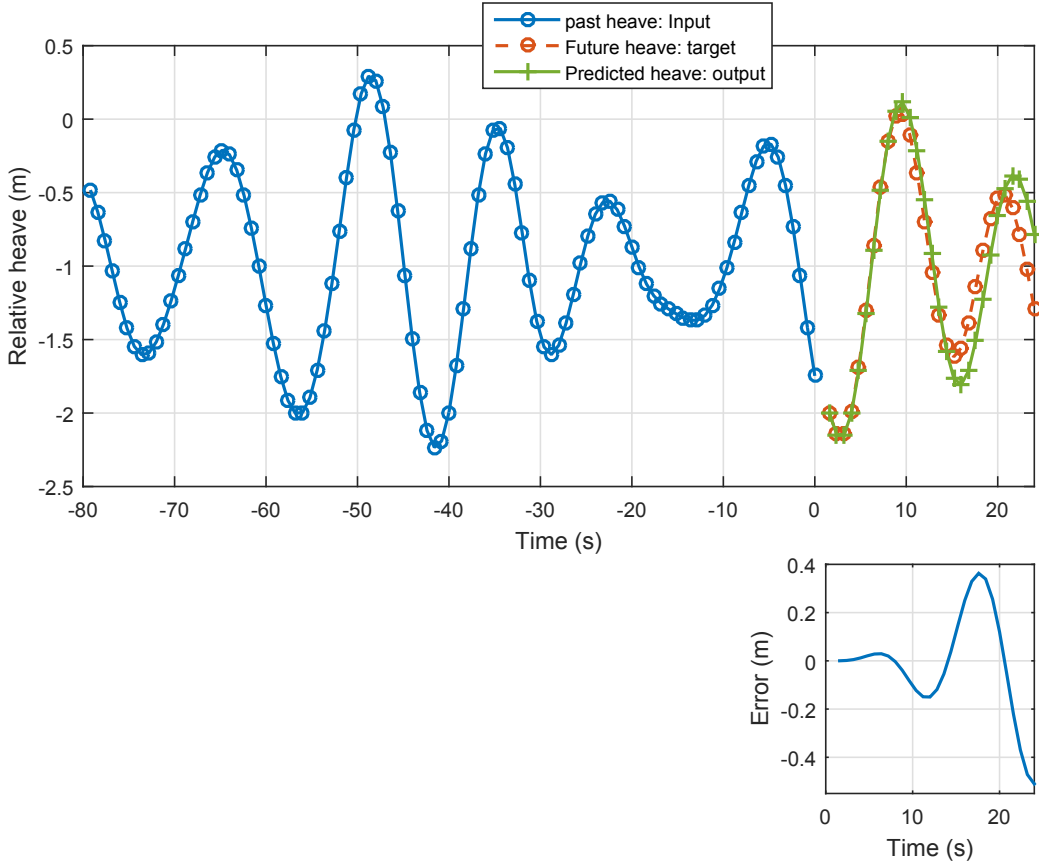


Figure 5.14: Example of heave prediction by the one-dimension ANN. This prediction is only based on the past heave motion (blue samples), and previous predictions (green samples) to predict multiple steps ahead. Bottom graph: prediction error

Let us define $\boldsymbol{\mu}_e(j)$ and $\boldsymbol{\sigma}_e(j)$ the 6×1 vectors of the mean prediction error regarding the prediction length j , over all the samples k of the validation dataset, and its standard deviation:

$$\boldsymbol{\mu}_e(j) = \frac{1}{N_k} \sum_{k=1}^{N_k} \mathbf{e}_{j|k}, \quad (5.16)$$

$$\boldsymbol{\sigma}_e(j) = \sqrt{\frac{1}{N_k - 1} \sum_{k=1}^{N_k} (\mathbf{e}_{j|k} - \boldsymbol{\mu}_e(j))^2}, \quad (5.17)$$

with N_k the number of samples in the validation dataset. Figure 5.15 shows the evolution of $\boldsymbol{\mu}_e(j)$ and $\boldsymbol{\sigma}_e(j)$:

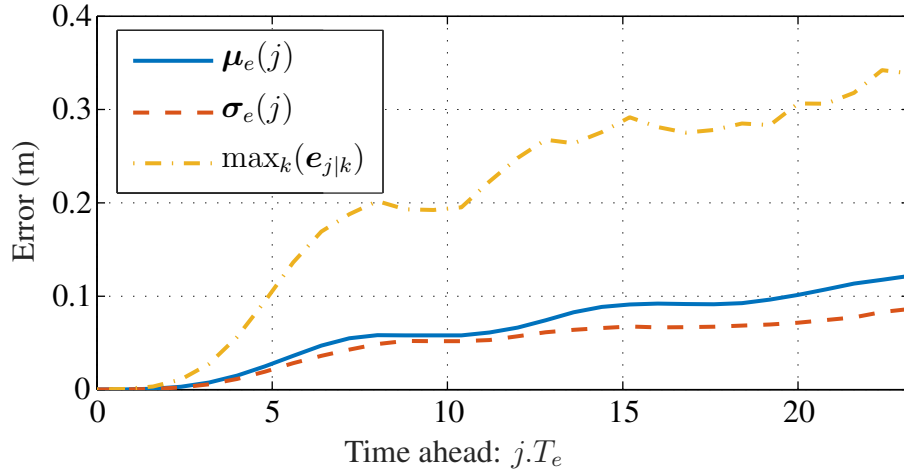


Figure 5.15: Study of the evolution of the prediction error regarding the length of the prediction j : Case of the heave prediction by a one-dimension ANN.

Table 5.2 presents the performance results at $j = 5$, i.e. $5T_n = 4$ seconds ahead. This value corresponds to the horizon required by the predictive planning developed in the previous section.

Table 5.2: Results at $j = 5$.

	$\mu_e(5)$	$\sigma_e(5)$	$\max_k(e_{5 k})$
Surge (mm)	17	12	55
Sway (mm)	25	17	70
Heave (mm)	20	16	66
Roll ($\cdot 10^{-4}$ rad)	7	4	17
Pitch ($\cdot 10^{-4}$ rad)	5	4	16
Yaw ($\cdot 10^{-4}$ rad)	8	5	23

A single six-dimension ANN, as presented on Figure 5.13, is then trained and evaluated in the same conditions than the previous one-dimension ANNs. Figure 5.16 shows the evolution of $\mu_e(j)$ and $\sigma_e(j)$, compared to the results of the one-dimension ANN and Table 5.3 presents the performance results.

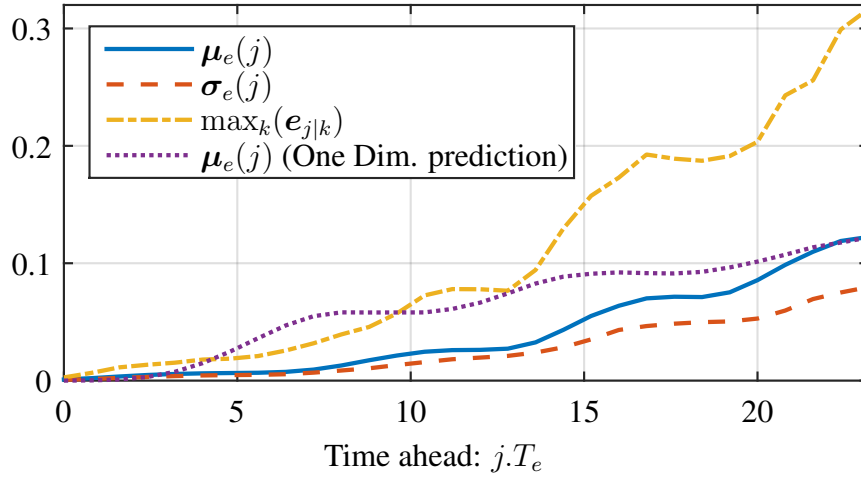


Figure 5.16: Study of the evolution of the prediction error regarding the length of the prediction j : Case of the heave prediction by a six-dimension ANN.

Table 5.3: Results at $j = 5$.

	mean(\bar{e}_5) (One dim.)	std(\bar{e}_5)	max(\bar{e}_5)
Surge (mm)	0.9 (17)	8.9	18.5
Sway (mm)	1.4 (25)	9.9	20.2
Heave (mm)	0.3 (20)	6.9	13.4
Roll ($\cdot 10^{-4}$ rad)	0.1 (7)	2.6	5.7
Pitch ($\cdot 10^{-4}$ rad)	0.3 (5)	1.8	4.9
Yaw ($\cdot 10^{-4}$ rad)	0.1 (8)	1.1	2.5

It clearly appears that the prediction of one six-dimension ANN is significantly more accurate than the prediction of six one-dimension ANNs for the first 20 seconds ahead, as illustrated by Figure 5.17. This difference can be explained by the ability of neural network to find couplings and correlations between the input signals. Hence six-dimension ANNs can achieve a deeper analysis of the input vector, while one-dimension ANNs are limited to the analysis of one component of the motion. This explanation makes sense, because the components of the vessel motion are indeed physically coupled [IG09, HX98], and the motion simulation takes this coupling into account via the RAO, as presented in Section 5.1.

CHAPTER 5. ACTIVE MOTION COMPENSATION WITH DELAY REMOVAL

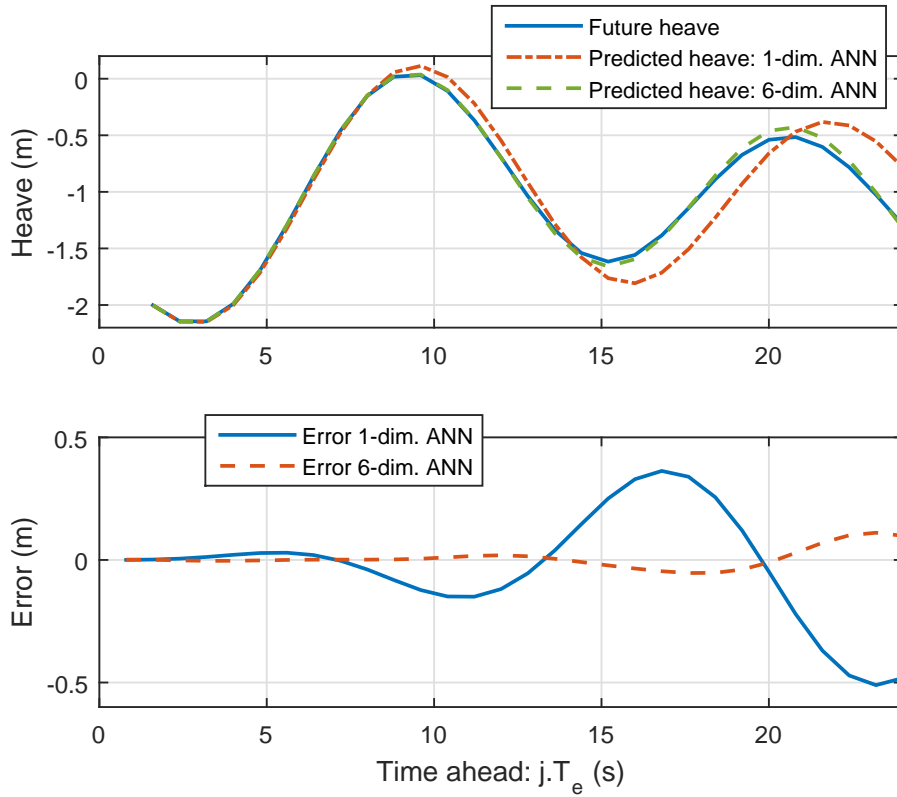


Figure 5.17: Comparison of the one-dimension ANN and the six-dimension ANN for heave prediction at one time sample.

A C++ implementation of the neural network was developed. It was measured that one evaluation of the six-dimension neural network last less than $1 \mu s$. This computational cost is very low regarding a classic cycle time of an industrial robot, and even lower regarding the cycle time of the predictive control developed in Section 5.1. The performance of the ANNs developed in this section, in terms of prediction accuracy, is sufficient for the predictive control to work. This is demonstrated by reproducing the simulation run in Section 5.1, with predicted motion. It was found that such small prediction errors does not affect the results given by the predictive planning.

Although the results from this section are satisfying the needs of the automatic connection system, some investigation is still needed:

- There exists many different structures of ANN. It is possible that using another structure, such as a recurrent ANN improve the results, as suggested by [CMA94].

- The robustness of the ANN to measurement noise is to be studied. Can the ANN accept raw data from the measurement tools ?
- The robustness of the ANN to other sea states has not been investigated. How much the prediction accuracy decreases for a smoother, or harder sea ?
- According to the answer of the previous question, it may be interesting to develop an adaptive ANN, with the ability to evolve online.
- In this project the ANNs are trained with simulated vessel motion only. Does an ANN trained with simulated motion works with real motion? Does six-dimension ANNs find more correlations between dimensions when trained with real data ?

5.3 Experimental validation

In this section the different elements developed in this project are assembled together to build the final automatic connection solution. Then the overall automatic connection procedure is tested. Prior to any test the low-level joints controllers are needed. The next section presents the development of such controllers.

5.3.1 Joints controllers synthesis

The development of low-level controllers for the joints of the loading arm is essential. The purpose of these controllers is to make it possible for the joints to follow their target motion with maximum accuracy and dynamic performance. The automatic control of a system such as an hydraulic loading arm is challenging. In particular, the hardware presents the following difficulties:

- backlashes in the slewing transmission,
- nonlinear effects in the proportional valves (Figure 3.10) and the cables,
- dry friction in the joint,
- flexible elements which easily oscillate.

The controllers are build around classic proportional-integral-derivative (PID) controllers:

$$\text{PID} = k_p \epsilon + k_d \frac{d\epsilon}{dt} + k_i \int \epsilon dt, \quad (5.18)$$

CHAPTER 5. ACTIVE MOTION COMPENSATION WITH DELAY REMOVAL

This structure is popular in the industry for its versatility and its easiness of tuning. Some additional components are added to the controllers in order to improve their performances

- A feedforward velocity action tuned in open-loop produces the main part of the control signal.
- An asymmetric feedforward acceleration component helps to compensate the dry friction, as shown on Figure 5.19. This action only activates after that the joint velocity reaches zero to help the joint start its motion.
- An active-damping loop reduces undesired oscillation of the joint. This element is used only for the OLAF scaled model, since no oscillation are observable by the sensors of the full scale arm.

Figure 5.18 shows the architecture of the controllers.

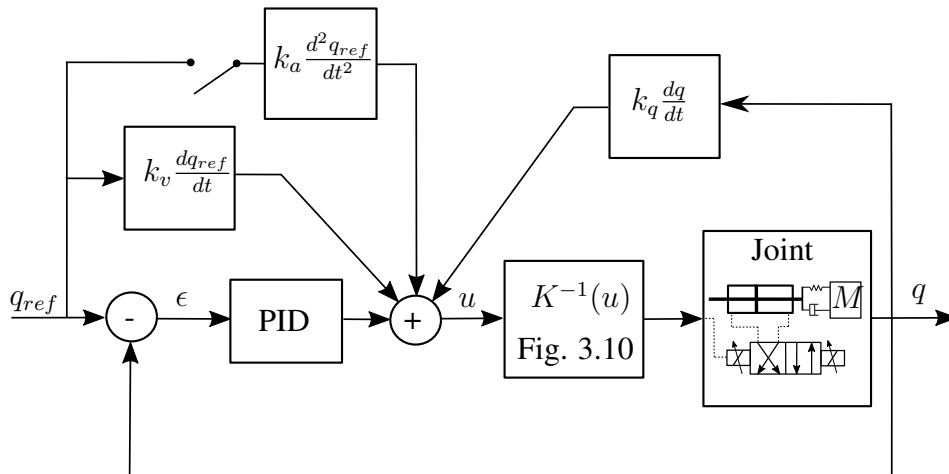


Figure 5.18: Diagram of a joint controller.

The sampling time of the controller T_e is limited by the programmable logic controller (PLC) capabilities, at $3 \cdot 10^{-2}$ second. The controllers are tuned as follow, starting with all parameters set to zero. First the open loop component k_v is increased until the joint correctly achieve rest-to-rest, point-to-point motion over jerk-limited trajectories, for which the kinematic bonds are chosen arbitrarily. Then the PID gains k_p , k_i and k_d are successively tuned according to the classic Ziegler–Nichols method [ZN42]. Finally the parameters k_q and k_a are adjusted to respectively damp residual oscillation and help to compensate the effects of dry friction, as shown on Figure 5.19. Dry friction makes it difficult to drive the

CHAPTER 5. ACTIVE MOTION COMPENSATION WITH DELAY
REMOVAL

joints at low speed, especially when the sign of the velocity changes. The output of the controller rapidly raises until the joint suddenly moves. This phenomenon is only observed for the OLAF scaled model. Table 5.4 shows the final controllers parameters.

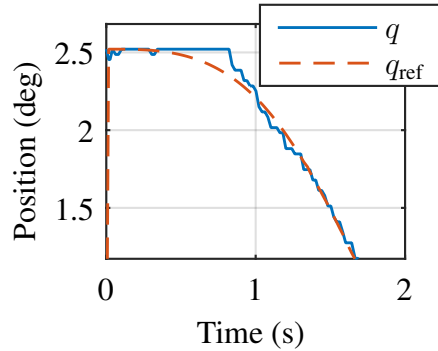


Figure 5.19: Typical effect of the dry friction in the joint: the joint "sticks" to its position when its velocity changes of sign. Example of the slewing joint (joint 1) of the OLAF scaled model.

Table 5.4: Controller parameters

Joint:	OLAF scaled model			full scale DCMA		
	1	2	3	1	2	3
k_p	2.3	2.5	5.0	1.25	1.8	4.4
k_i	0.4	1.0	1.0	0.0	0.0	0.0
k_d	0.8	0.0	0.0	0.0	0.0	0.0
k_v	1.1	1.0	1.1	1.0	1.0	1.0
k_a	0.8	0.1	0.5	0.0	0.0	0.0
k_q	0.1	0.1	0.0	0.0	0.0	0.0

In order to estimate the instant derivative of the joint position despite the noise of the signal, a second order polynomial curve is fitted on the last N_d samples. The coefficients \mathbf{a} of the parabola are given by:

$$\mathbf{a} = (\mathbf{X}^T \mathbf{X})^{-1} \mathbf{X}^T \mathbf{y} \quad (5.19)$$

where \mathbf{X} is the $N_d \times 3$ Vandermonde matrix of the time samples, \mathbf{y} the $N_d \times 1$ vector of the position samples. Best results are obtained for $N_d = 16$.

CHAPTER 5. ACTIVE MOTION COMPENSATION WITH DELAY REMOVAL

For each joint, kinematic limits for the reference jerk-limited trajectories are tuned. These limits are set to the highest values for which the joints controllers follow accurately their jerk-limited reference. This bounds value are tuned so that the controllers errors $q - q_{ref}$ are less than 0.2 degrees. This value is chosen so that the controller errors lead to a Cartesian coupler error that is half the coupler tolerance, in the worst case. In the case of the full scale DCMA, these kinematic limits are lowered until no oscillation of the structure are seen visually. Table 5.5 gives the tuned kinematic limits. Figure 5.20 shows typical results of the inboard controllers.

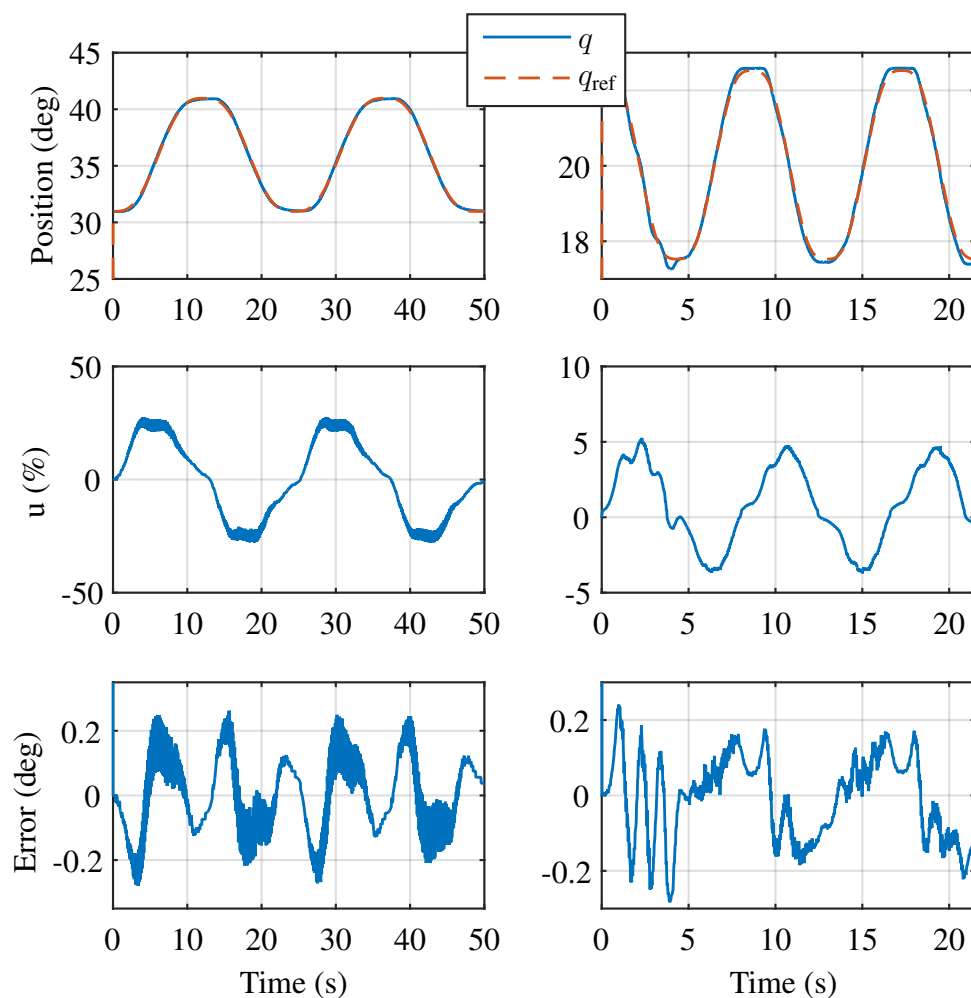


Figure 5.20: Typical joints responses to jerk-limited trajectories, example of the inboard joints. Left graphs: full scale DCMA, right graphs: OLAf scaled model.

Finally functional joints controllers are available. As long as the references

Table 5.5: Kinematic parameters that match to the controllers capabilities

Joint:	OLAF scaled model			full scale DCMA		
	1	2	3	1	2	3
v_{\max} (deg/s)	10.0	5.0	10.0	5.0	6.0	8.0
a_{\max} (deg/s ²)	5.0	4.0	5.0	0.3	0.4	0.3
j_{\max} (deg/s ³)	2.0	2.0	5.0	0.2	0.3	0.2

given to these controllers respect the kinematic limits given in Table 5.5, the assumption $q = q_{ref}$ is made. This assumption make it possible not to use models of the joints in the predictive planning, as detailed in Section 5.1, and thus greatly simplify the overall system. However these kinematic bounds are restrictive and significantly limit the ability of the system to compensate the relative vessels motion during harsh sea condition, as detailed in Section 5.3.2.2. Other relevant control strategies are available in the literature such as optimal control or model predictive control. Such advanced methods could make the kinematic limits higher, thus improve the dynamic capabilities of the loading arm. However such methods are not straightforward to implement and are beyond the scope of this project.

5.3.2 Final tests

All software and hardware elements presented in this project are embedded in a single hierarchical framework, so that they can efficiently operate together. The lowest-level elements of this framework are the hardware systems: the loading arm with its PLC, and the total station. Then comes the low-level communication layer which links the hardware with the different algorithms. Among them first comes the low-level joints controllers which drive the cylinders, and take set-points from the jerk-limited trajectory generator. In parallel, the datastream from the total station is processed by the ANN and translated in the joint space by the inverse kinematic model of the arm (which has been calibrated beforehand). Finally, the predictive planning algorithm, which can be considered as the highest-level element of this framework, collects the prediction and gives references to the trajectory generator. The diagram shown in Figure 5.21 illustrates the architecture of the framework.

The models and algorithms developed along this project came with practical implementation issues. In particular, a special care to safety was taken during the

CHAPTER 5. ACTIVE MOTION COMPENSATION WITH DELAY REMOVAL

coding of each element of this framework. Before its use with the real arm, a series of tests were conducted to make sure that the whole system is fail-safe. Indeed any failure of any element of the framework could lead to unexpected motion of the loading arm, and severe damage to the hardware. A jerk-limited emergency stop button was developed, in order not to stop the loading arm with brutal step inputs in case of emergency.

The settings of the final tests slightly differ from a real offshore setup:

- For both arms the swivel joint (joint 5) has no position sensor and cannot be used. Consequently the manifold (\mathbf{X}_m) is kept in the plane ($\mathbf{y}_0, \mathbf{z}_0$) and the slewing joint (joint 1) is not used. Moreover without joint 5 the arm cannot compensate non-zero relative orientation of the vessels. Therefore the orientation of both vessels are kept zero.
- The frames R_0 of the arms is static during the test, no FLNG motion is simulated. Indeed the full scale arm has no mean to be moved in such way. The scaled arm could be moved via the FLNG hexapod, but no measurement system is available to monitor this motion. Therefore the test benches of the arms are used to simulate the relative motion ${}^0\mathbf{X}_m$ instead of the LNG motion ${}^r\mathbf{X}_m$.
- For practical reasons, combinations of sine signals are used to simulate ${}^0\mathbf{X}_m(t)$ in the test benches, instead of a simulated sea state. Therefore artificial neural networks are replaced by a simple linear regression to recognize the phase and offset of the motion.

5.3.2.1 Test with the OLAF scaled model

The LNGC hexapod (see Section 1.4.1) is driven with sine motion along \mathbf{y}_0 and \mathbf{z}_0 :

$${}^0\mathbf{X}_m(t) = \begin{bmatrix} 0 \\ A \sin(2\pi ft) \\ A \sin(2\pi ft) \end{bmatrix} + C, \quad (5.20)$$

where C is a constant vector so that ${}^0\mathbf{X}_m(0)$ is at the center of the flanging area. The chosen values of the parameters are given in the table below:

$A_y =$	0.15 m
$A_z =$	0.40 m
$f_y =$	0.05 Hz
$f_z =$	0.03 Hz

CHAPTER 5. ACTIVE MOTION COMPENSATION WITH DELAY REMOVAL

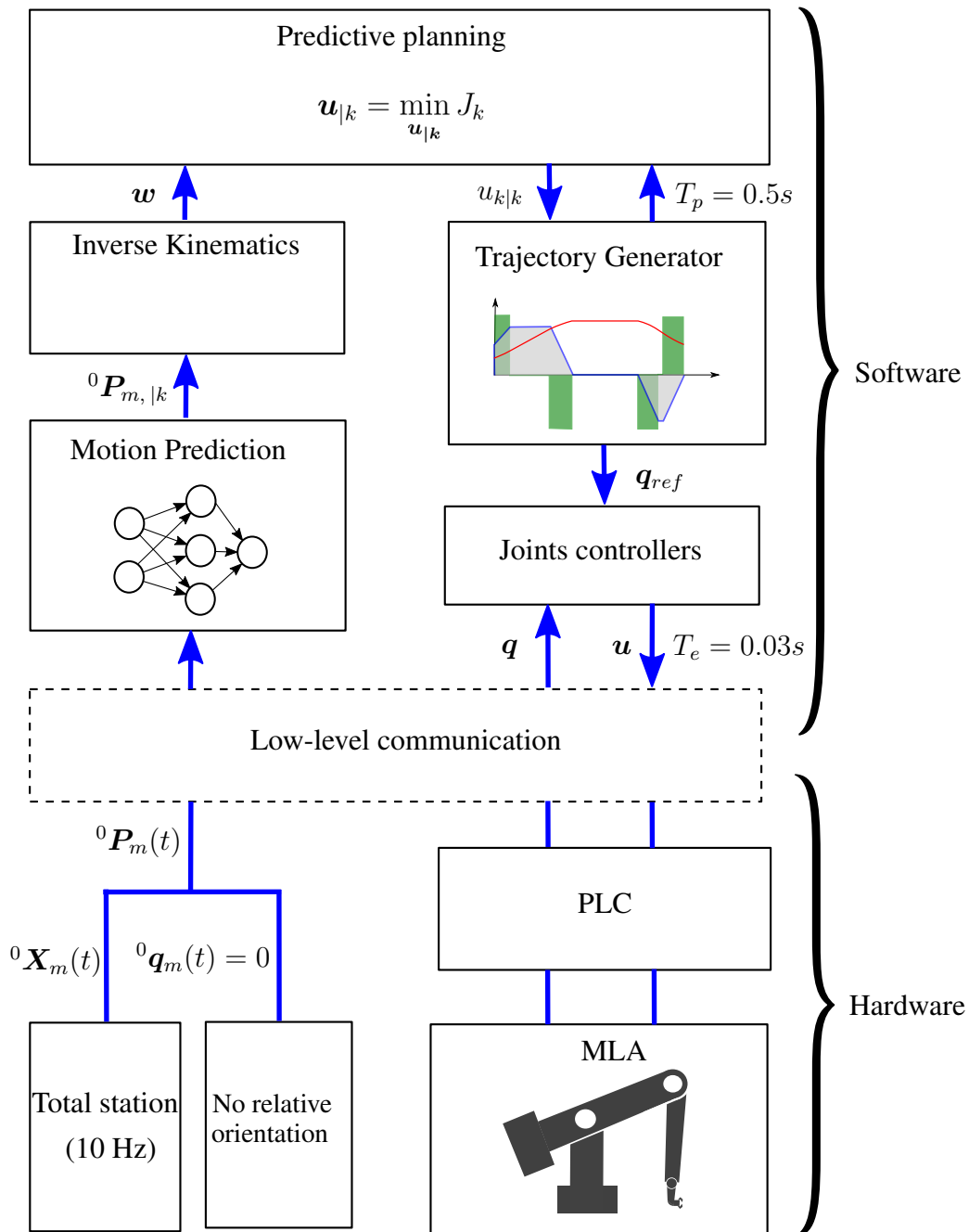


Figure 5.21: Architecture of the hierarchical framework developed and implemented for the OLAF scaled model and the full scale DCMA.

The values of A_z and A_y correspond to maximal amplitudes of the reference sea state (see Section 3.3.2), with a 1/4 scaling. However frequencies f_z and f_y

CHAPTER 5. ACTIVE MOTION COMPENSATION WITH DELAY REMOVAL

are lower than the real main motion frequency 0.1 Hz (see Figure 3.15). These settings correspond to a test run during the development. Unfortunately the test at full frequency has not been conducted for practical issues. However this test, together with the simulation presented in Figure 5.7 and the controller tuning presented in Figure 5.20, confirm the validity of the overall approach. The arm follows automatically the manifold, thanks to the measurements of the total station. The distance d_p defined in Equation (1.1), at which the coupler follows the manifold, is set to 1.5 m, to avoid any collision in case of failure. Figure 5.25 shows the arm during its motion. The predictive planning is switched on at $t = 140$ s. Figure 5.22 shows the evolution of the joint position q , the controller set-point q_{ref} and the reference trajectory w for the inboard and outboard joints. Figure 5.23 show the controller error $q_{ref} - q$, the planning error $w - q_{ref}$ and the total error $w - q$.

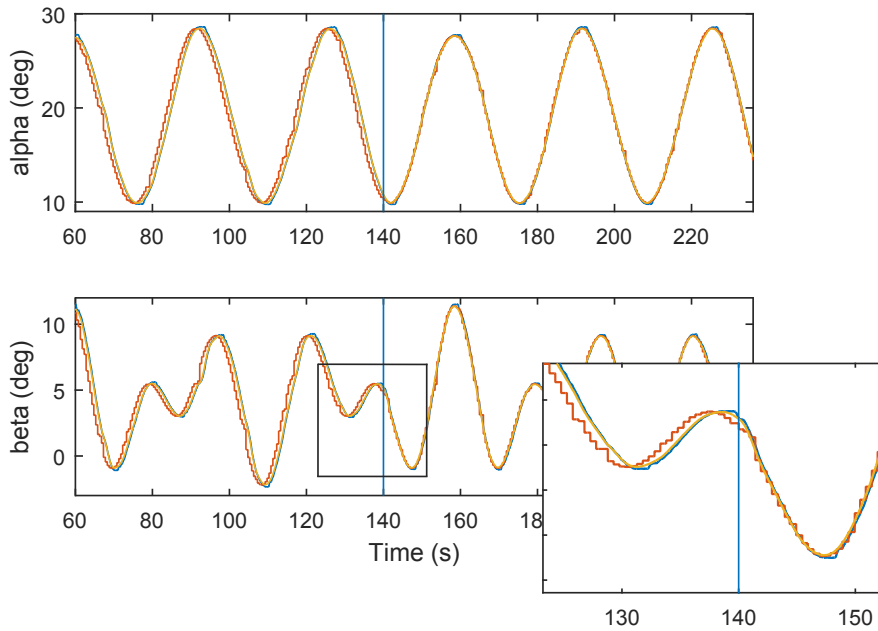


Figure 5.22: Evolution of the joint position q (blue line), controller set-point q_{ref} (orange line) and the reference w (red line). The predictive planning is switched on at $t = 140$ s. Top graph: inboard joint ($q = \alpha$), bottom graph: outboard joint ($q = \beta$).

From the observation of Figures 5.22 and 5.23, one can see that before using the predictive planning, the total error is mainly (mean ratio for joint 2: 90%) due to the planning pursuit error. When the predictive planning is enabled the pursuit error is canceled, and the remaining error comes from the difficulties of the controllers to deal with dry friction (see 5.3.1). Figure 5.24 shows the residual

CHAPTER 5. ACTIVE MOTION COMPENSATION WITH DELAY REMOVAL

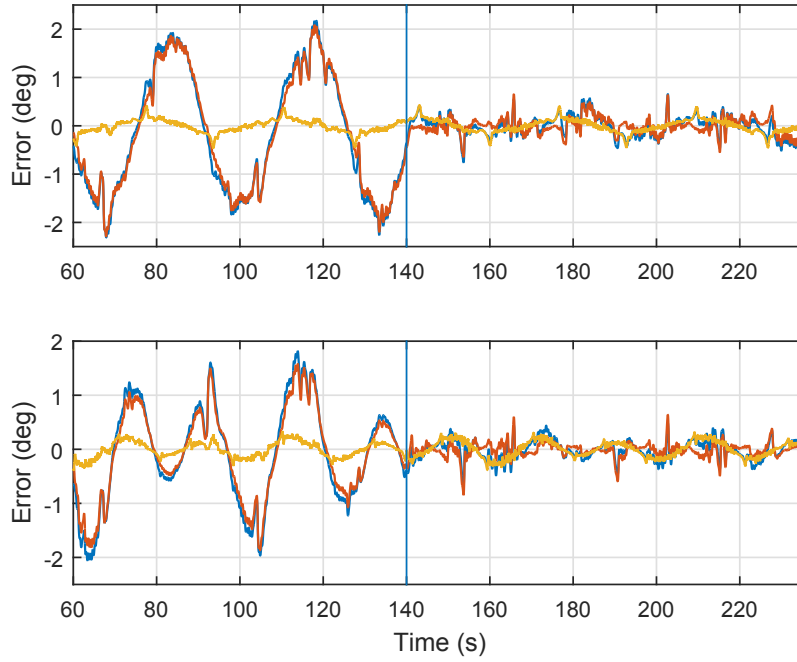


Figure 5.23: Evolution of the controller error $q_{ref} - q$ (orange line), planning error $w - q_{ref}$ (red line) and total error $w - q$ (blue line). Top graph: inboard joint ($q = \alpha$), bottom graph: outboard joint ($q = \beta$). The predictive planning is switched on at $t = 140$ s (vertical line).

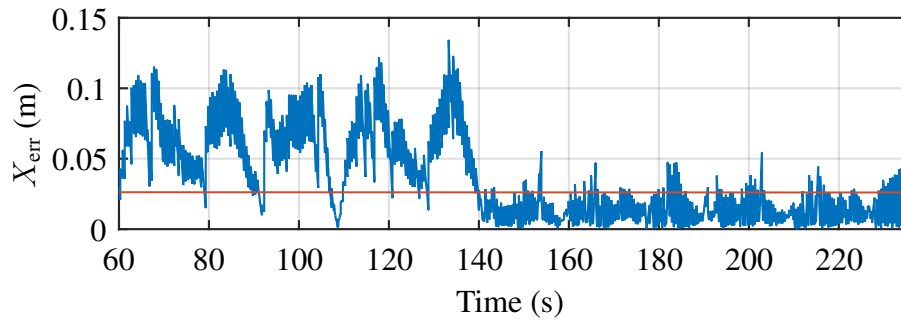


Figure 5.24: Evolution of the total error in terms of coupler position $X_{err}(t) = \|\mathbf{X}_c(t) - \mathbf{X}_m(t)\|$. Red line: coupler tolerance.

position error. When the predictive planning is on, this error is below 0.025 m, which is sufficient for the connection if all other error sources (e.g. geometric accuracy) are assumed zeros.

This experiment shows that the predictive planning successfully removes the

CHAPTER 5. ACTIVE MOTION COMPENSATION WITH DELAY REMOVAL



Figure 5.25: The OLAF scaled model automatically follows the manifold.

pursuit delay. No automatic connection was attempted with this arm, because its coupler is not suitable, and the final accuracy is not sufficient (see 2.2).

5.3.2.2 Tests with the full scale DCMA

Similar tests are conducted with the full scale DCMA. These tests aim to validate the entire work of this project by automatically connecting the loading arm on the moving manifold. The manifold of the test bench is driven by Cartesian sine motion as described by Equation (5.20). The values of the motion parameters are given below:

$$\begin{array}{r} \overline{\overline{A_y = 0.4 \text{ m}}} \\ \overline{\overline{A_z = 1.0 \text{ m}}} \\ \overline{\overline{f_y = 0.025 \text{ Hz}}} \\ \overline{\overline{f_z = 0.033 \text{ Hz}}} \end{array}$$

These parameters correspond to a slower sea state. The manifold velocity was reduced for several reasons. First the kinematic limits found in Table 5.5 do not permit to follow the full speed reference sea state. Then it is observed that in spite of these restrictive kinematic limits, oscillation unseen by the sensors appears very easily when the arm moves. In particular it is strongly suspected that the transmission cable (See 1.4.2) has a low stiffness and induces oscillation in the outboard arm and in the Style 80. It has been calculated afterward that some other mechanical parts in the power transmission are largely deformed when the arm is driven, and thus may participate to oscillation induction. These oscillations makes the arm too inaccurate for the coupler to flange on the manifold. No sensor were fitted at the right place to measure these oscillations, and therefore no data are available to support the above statements. As explained in Chapter 3, oscillation in the structure is not observable by the position monitoring system.

The coupler automatically follows the manifold, according the reference of the predictive planning, at a distance $d_p = 2.5$ m. This pursuit stage takes place similarly as the one run on the OLAF scaled model, with a planning error under 0.1 degree. However the controllers error reaches 0.2 degree. This error appears because the gains of the controllers are lowered to reduce oscillation of the arm while the kinematic limits are kept unchanged regarding the values presented in Section 5.3.1. Figure 5.26 and Figure 5.27 respectively show the joints errors and the corresponding coupler position error. The latter is below 0.04 meters which is, even added with the 25.5 mm arm accuracy (see Section 2.2.3), under the coupler tolerance.

Once the synchronization between the coupler and the manifold is done, the distance d_p is set to 30 mm. This change of d_p has for effect to smoothly drive the coupler near the manifold, while keeping the synchronous motion compensation.

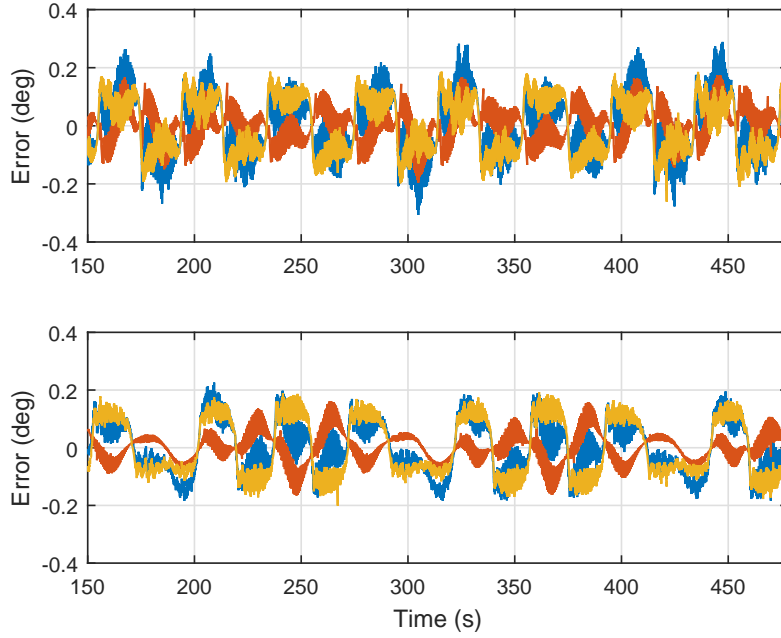


Figure 5.26: Evolution of the controller error $q_{ref} - q$ (orange line), planning error $w - q_{ref}$ (red line) and total error $w - q$ (blue line). Top graph: inboard joint ($q = \alpha$), bottom graph: outboard joint ($q = \beta$).

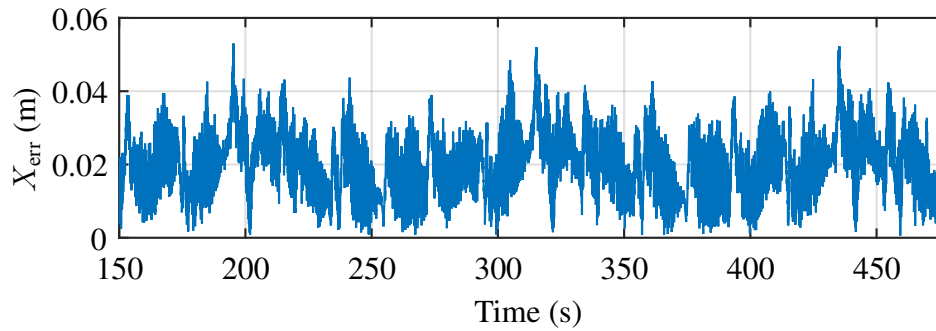


Figure 5.27: Evolution of the calculated total error in terms of coupler position $X_{err}(t) = \|\mathbf{X}_c(t) - \mathbf{X}_m(t)\|$.

Figure 5.29 shows the coupler synchronously following the manifold. This very small value of d_p proved necessary to make the flanging possible. Under visual supervision, the flanging instruction is manually sent to the arm at a time where the velocity of the heave is zero, i.e. at the top or bottom of an heave oscillation. That way the oscillation in the arm is lower. This instruction simultaneously starts

CHAPTER 5. ACTIVE MOTION COMPENSATION WITH DELAY REMOVAL

the flanging operation and switches the arm in freewheel mode (see Chapter 3), as detailed in Section 1.3.1. In other words, the actuation system of the loading arm is disabled before that the arm is connected. The flanging system is fast enough to "catch" the manifold before it moves away from the coupler, which is now steady. Figure 5.30 shows the arm connected to the manifold. At this stage the arm is pulled by the manifold, and comply with the relative motion of the vessel. In a real case, this is the moment where the LNG would be offloaded.

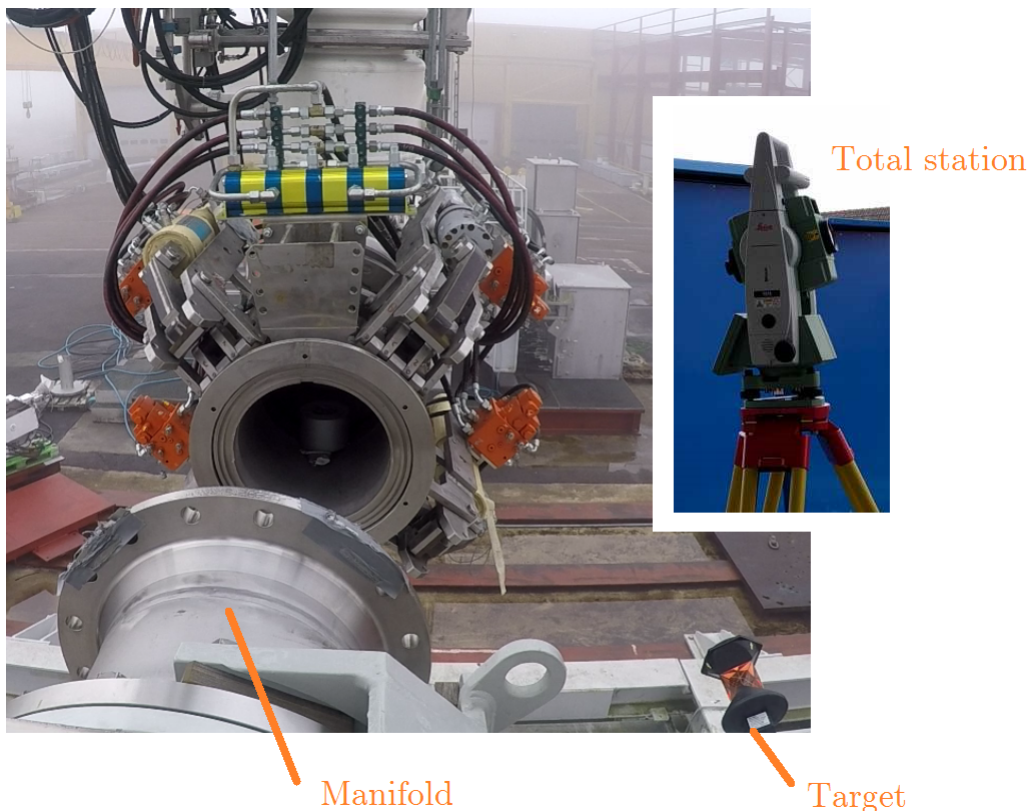


Figure 5.28: The full scale DCMA automatically follows the manifold.

This test was successfully reproduced 10 times, over a period of two days. It demonstrates the feasibility of the automatic connection of a loading arm, and shows that the methodology developed in this project adequately solves the challenges of the automatic connection. With these final experiments the objectives of the project are met, with as only restriction the lower frequency of the vessel.

CHAPTER 5. ACTIVE MOTION COMPENSATION WITH DELAY
REMOVAL

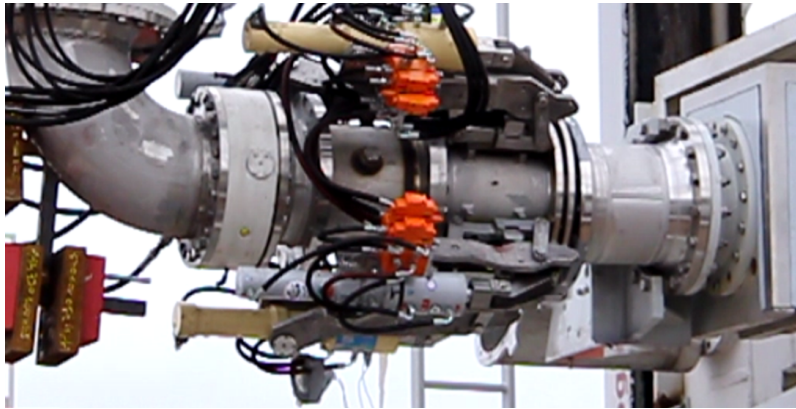


Figure 5.29: The loading arm moves very closely (<4 cm) to the manifold, to make the flanging possible.

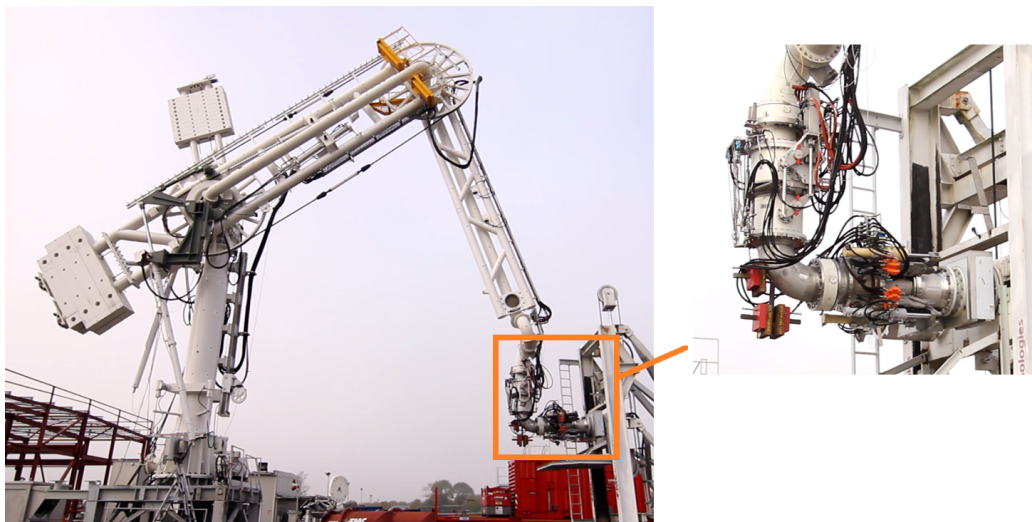


Figure 5.30: The full scale DCMA is successfully connected to the manifold.

Chapter 6

General conclusion and perspectives

Marine loading arms are challenging systems to control, mainly because these systems were not designed to be robotized. Nevertheless it is chosen to robotize the existing equipment rather than designing whole new robotic loading systems. This choice is motivated by economical reasons and by the perceptive to generalize this robotization process to a wide scope of other systems, e.g. landing platform for helicopters, bridges between moored vessels. As a result the main challenges of this project lie in the hardware of the MLA and more particularity in its low stiffness and its hydraulic actuation system. The final methodology consists of several main components (namely trajectory generation, predictive planning, motion prediction and calibration) which are developed according to the needs of the system. The next section summarizes the work done during this project. Then some perspectives are presented.

6.1 Summary of the results

Solving the automatic connection problem starts with measuring and improving the accuracy of the loading arm. Different sources of inaccuracy such as deflection in the structure, offsets in the joints and errors to the parts nominal dimensions can be compensated by model-based calibration. The results of **repeatability measurement and calibration procedures** applied to both the 1/4 scaled model and the full scale loading arm are:

- the repeatability of the OLAF scaled model is 27 mm and 9 mm for the full scale DCMA,
- the calibration procedure improve the accuracy from 40.1 mm to 27.1 mm for the scaled model and from 421 mm to 25.5 mm for the full scale arm.

- the total station, tool used for surveying and building construction, is adequate and make the latter operations much faster than with a classic metrology laser tacker.

An **experimental study** investigates the hardware capabilities by conducting a series of tests on both a 1/4 scaled loading arm and a full size one. These tests characterize the actuated joints of the arms in terms of performance and behavior. These tests also include actual modal analyses of the structures of the arms, which give some of their vibration modes and operational shapes. Together these tests shows that:

- Marine loading arms have a flexible structure, with a first measured mode at 0.37 Hz for the full scale arm.
- The oscillation of the structure of the full scale arm is not observable by its sensors. Hence no active damping is possible. This is a major difference with the scaled model for which the hydraulic circuit is flexible regarding the stiffness of the structure.
- The FLNG motion spectra (max 0.15 Hz) are below the measured modes of the structure (max 0.37 Hz). Therefore the FLNG motion should not excite the structure of the loading arm. However these spectra are close and one should be careful to keep them separated when designing structures of arms (See Figure 3.16). Moreover only the modes along x_0 and responding to an excitation along x_0 were measure by the modal analysis. It is strongly suspected that lower modes are present, in particular in the plan (y_0, z_0) . As a result further investigations are needed.

Then a dynamic model of a marine loading arm including the effects of the non-inertia base (FLNG) is developed. This model is used to simulate the joints torques induced by the inertia effects from the FLNG. It is shown that:

- the inertia effects from the FLNG motion induce non negligible joints torques.
- The latter simulated joints torques do not interfere with the proper working of the loading arm, in terms of maximum joint torque and vibration induction.

This result makes interesting the research study where From *et al.* [FGLA11] proposes a methodology which uses these inertia effects to reduce the power needed by the onboard robot. One may note that this method require a motion prediction algorithm and a dynamic model of the arm, already available in this project.

In order to reduce the oscillation of the structure induced by the actuation system, hence increase its accuracy, smooth trajectories are needed to drive the joints. A fast and versatile **online jerk-limited trajectory generator** is developed to deal with the trajectory planning problem of the joints. This generator is able to generate trajectories that are:

- jerk-limited, under the chosen jerk, acceleration and velocity limits,
- time-optimal, according to these limits,
- dynamic, i.e. that accept any initial state in terms of acceleration velocity and position,
- possibly synchronized to deal with multi-axis systems,
- generated in less than $1 \mu s$.

These features and this very low calculation time make it possible to use this trajectory generator for many real-time applications, even in the case of systems with multiple joints. It is also fast enough to be directly used by the optimization algorithm of the predictive planning. Jerk-limited trajectories are a tool for smoothly driving the joints of the loading arm, and also a way to describe the response of the joints. In other words, it is shown that the joints controllers follow accurately jerk-limited trajectories generated under adequate kinematic limits. Hence no model is necessary to describe the behavior of the joints, but only sets of kinematic bounds.

The **active vessels motions compensation** makes the coupler of the loading arm follow the manifold. The time delay of the pursuit is removed by a predictive planning algorithm that gives the ability to loading arms to anticipate the vessels motions. This algorithm generates optimal targets for the jerk-limited trajectory generator. It is found that:

- this approach makes it possible to significantly reduce the tracking error, so that the automatic dynamic connection is possible,
- this is nevertheless only possible if the kinematics limits of the joints are higher than the reference trajectory.

The reference trajectory of the predictive planning algorithm is fed by an **artificial neural network** which predicts the vessels motions. It is shown that:

- the proposed neural network is accurate enough for the predictive planning algorithm to work,

- by processing all motion components together instead of separately, the prediction is much more accurate.

This project ends with a functional prototype of automatic connection system and paves the way towards its industrialization. The goals of the project are met and the feasibility of the robotization of loading arms is demonstrated. The manufacturer's requirement not matched by the final prototype is the severity of the sea state under which the system can operate, i.e. the amplitude and frequency of the relative vessels motion. In view of improving this system, and turning it into a robust and reliable product, some elements should be considered, as presented in the next section.

6.2 Perspectives

Some points that are not covered by this study, but that seem nonetheless necessary, are listed below:

- First of all and probably most of all, a complete risk and failure mode analysis should be carried out. Loading arms are sensible systems operating in a sensible environment and their robotization should be developed to be fail-safe.
- The study of the influence of the wind is beyond the scope of this thesis. However it is visually observed that the wind induces non negligible oscillation of the structure. An investigation of the effects of the wind is thus recommended because they could compromise the proper functioning of the automatic connection system.
- Neither path planning nor collision avoidance are studied in this project. These elements are important to make sure that the arm does not collide other arms of elements of the vessels.
- It might be interesting to develop an automatic re-calibration procedure: the external conditions (thermal expansion), the transportation of the loading arm, may slightly change the geometry of the structure and make the factory calibration obsolete.
- An experimental study that measures the real coupler tolerance in all directions can lead to a better, optimized, management of the flanging operation.
- The very low stiffness of many parts of the loading arms structure is the main obstacle that keeps the system from reaching better performance. A way to make these parts more stiff could be investigated.

Bibliography

- [AORJ15] M Mahdi Ghazaei Ardakani, Björn Olofsson, Anders Robertsson, and Rolf Johansson. Real-time trajectory generation using model predictive control. In *Automation Science and Engineering (CASE), 2015 IEEE International Conference on*, pages 942–948. IEEE, 2015.
- [BCG08] Olivier Brüls, Alberto Cardona, and Michel Géradin. Modelling, simulation and control of flexible multibody systems. In *Simulation Techniques for Applied Dynamics*, pages 21–74. Springer, 2008.
- [BD96] Patrick Boucher and Didier Dumur. *La commande prédictive*, volume 8. Editions Technip, 1996.
- [Bea14] Richard Bearee. New damped-jerk trajectory for vibration reduction. *Control Engineering Practice*, 28:112–120, 2014.
- [BM12] Luigi Biagiotti and Claudio Melchiorri. Fir filters for online trajectory planning with time-and frequency-domain specifications. *Control Engineering Practice*, 20(12):1385–1399, 2012.
- [BMM16] L. Biagiotti, C. Melchiorri, and L. Moriello. Optimal trajectories for vibration reduction based on exponential filters. *IEEE Transactions on Control Systems Technology*, 24(2):609–622, March 2016.
- [BO13] Richard Bearee and Adel Olabi. Dissociated jerk-limited trajectory applied to time-varying vibration reduction. *Robotics and Computer-Integrated Manufacturing*, 29(2):444–453, 2013.
- [Bus04] Samuel R Buss. Introduction to inverse kinematics with jacobian transpose, pseudoinverse and damped least squares methods. *IEEE Journal of Robotics and Automation*, 17(1-19):16, 2004.
- [CDPV06] Francois Caron, Emmanuel Duflos, Denis Pomorski, and Philippe Vanheeghe. Gps/imu data fusion using multisensor kalman filtering:

BIBLIOGRAPHY

- introduction of contextual aspects. *Information fusion*, 7(2):221–230, 2006.
- [CFC⁺08] Heping Chen, Thomas Fuhlbrigge, Sang Choi, Jianjun Wang, and Xiongzi Li. Practical industrial robot zero offset calibration. In *Automation Science and Engineering, 2008. CASE 2008. IEEE International Conference on*, pages 516–521. IEEE, 2008.
- [CMA94] Jerome T Connor, R Douglas Martin, and Les E Atlas. Recurrent neural networks and robust time series prediction. *IEEE transactions on neural networks*, 5(2):240–254, 1994.
- [Cra05] John J Craig. *Introduction to robotics: mechanics and control*, volume 3. Pearson Prentice Hall Upper Saddle River, 2005.
- [DBDJH14] Howard B Demuth, Mark H Beale, Orlando De Jess, and Martin T Hagan. *Neural network design*. Martin Hagan, 2014.
- [DHN⁺10] Jens Dannenberg, Katrin Hessner, Peter Naaijen, Henk van den Boom, Konstanze Reichert, et al. The on board wave and motion estimator owme. In *The Twentieth International Offshore and Polar Engineering Conference*. International Society of Offshore and Polar Engineers, 2010.
- [DJC07] Jens-Uwe Dolinsky, ID Jenkinson, and GJ Colquhoun. Application of genetic programming to the calibration of industrial robots. *Computers in Industry*, 58(3):255–264, 2007.
- [EA01] Kaan Erkorkmaz and Yusuf Altintas. High speed CNC system design. part I: jerk limited trajectory generation and quintic spline interpolation. *International Journal of machine tools and manufacture*, 41(9):1323–1345, 2001.
- [EGZ⁺04] AY Elatta, Li Pei Gen, Fan Liang Zhi, Yu Daoyuan, and Luo Fei. An overview of robot calibration. *Information Technology Journal*, 3(1):74–78, 2004.
- [FGLA11] Pål J From, Jan T Gravdahl, Tommy Lillehagen, and Pieter Abbeel. Motion planning and control of robotic manipulators on seaborne platforms. *Control engineering practice*, 19(8):809–819, 2011.
- [GB10] Oscar Gerelli and Corrado Guarino Lo Bianco. A discrete-time filter for the on-line generation of trajectories with bounded velocity, acceleration, and jerk. In *Robotics and Automation (ICRA), 2010 IEEE International Conference on*, pages 3989–3994. IEEE, 2010.

BIBLIOGRAPHY

- [GFDL14] Claudio Gaz, Fabrizio Flacco, and Alessandro De Luca. Identifying the dynamic model used by the kuka lwr: A reverse engineering approach. In *Robotics and Automation (ICRA), 2014 IEEE International Conference on*, pages 1386–1392. IEEE, 2014.
- [GYN00] Chunhe Gong, Jingxia Yuan, and Jun Ni. Nongeometric error identification and compensation for robotic system by inverse calibration. *International Journal of Machine Tools and Manufacture*, 40(14):2119–2137, 2000.
- [HWR08] Robert Haschke, Erik Weitnauer, and Helge Ritter. On-line planning of time-optimal, jerk-limited trajectories. In *Intelligent Robots and Systems, 2008. IROS 2008. IEEE/RSJ International Conference on*, pages 3248–3253. IEEE, 2008.
- [HX98] MR Haddara and Jinsong Xu. On the identification of ship coupled heave–pitch motions using neural networks. *Ocean Engineering*, 26(5):381–400, 1998.
- [IEA15] IEA. *World Energy Outlook*. International Energy Agency, 2015.
- [IG09] RA Ibrahim and IM Grace. Modeling of ship roll dynamics and its coupling with heave and pitch. *Mathematical Problems in Engineering*, 2010, 2009.
- [ISO98] ISO. Iso 9283:1998 - manipulating industrial robots – performance criteria and related test methods., 1998.
- [JAG14] Anthony Jubien, Gabriel Abba, and Maxime Gautier. Joint stiffness identification of a heavy kuka robot with a low-cost clamped end-effector procedure. In *Informatics in Control, Automation and Robotics (ICINCO), 2014 11th International Conference on*, volume 2, pages 585–591. IEEE, 2014.
- [JB13] Ahmed Joubair and Ilian A Bonev. Comparison of the efficiency of five observability indices for robot calibration. *Mechanism and Machine Theory*, 70:254–265, 2013.
- [JCPC05] Soon Yong Jeong, Yun Jong Choi, PooGyeon Park, and Seung Gap Choi. Jerk limited velocity profile generation for high speed industrial robot trajectories. In *Proceedings of the 16th IFAC world congress, Prague, Czech Republic*, 2005.

BIBLIOGRAPHY

- [JGJ14] Anthony Jubien, Maxime Gautier, and Alexandre Janot. Dynamic identification of the kuka lwr robot using motor torques and joint torque sensors data. In *World Congress of the International Federation of Automatic Control (IFAC)*, pages 1–6, 2014.
- [JP02] J. M. J. Journee and Jakob Pinkster. Introduction in ship hydromechanics. *Delft University of Technology*, 2002.
- [KB02] Wisama Khalil and Sébastien Besnard. Geometric calibration of robots with flexible joints and links. *Journal of Intelligent and Robotic systems*, 34(4):357–379, 2002.
- [KBM05] Ameer Khan, Cees Bil, and Kaye E Marion. Ship motion prediction for launch and recovery of air vehicles. In *OCEANS, 2005. Proceedings of MTS/IEEE*, pages 2795–2801. IEEE, 2005.
- [KCB⁺12] Rongjie Kang, Hélène Chanal, Thomas Bonnemains, Sylvain Pate-loup, David T Branson, and Pascal Ray. Learning the forward kinematics behavior of a hybrid robot employing artificial neural networks. *Robotica*, 30(05):847–855, 2012.
- [KD04] Wisama Khalil and Etienne Dombre. *Modeling, identification and control of robots*. Butterworth-Heinemann, 2004.
- [Kim99] Sun-Wook Kim. *Contact dynamics and force control of flexible multi-body systems*. PhD thesis, McGill University Montreal, Quebec, Canada, 1999.
- [Kło05] Jacek Kłosiński. Swing-free stop control of the slewing motion of a mobile crane. *Control Engineering Practice*, 13(4):451–460, 2005.
- [KMN⁺11] Sebastian Küchler, Tobias Mahl, Jörg Neupert, Klaus Schneider, and Oliver Sawodny. Active control for an offshore crane using prediction of the vessel’s motion. *Mechatronics, IEEE/ASME Transactions on*, 16(2):297–309, 2011.
- [KPN⁺07] Daniel T Kettler, Richard D Plowes, Paul M Novotny, Nikolay V Vasilyev, J Pedro, and Robert D Howe. An active motion compensation instrument for beating heart mitral valve surgery. In *2007 IEEE/RSJ International Conference on Intelligent Robots and Systems*, pages 1290–1295. IEEE, 2007.
- [Kri07] David Kriesel. *A brief Introduction on Neural Networks*. Citeseer, 2007.

BIBLIOGRAPHY

- [Krö11] Torsten Kröger. Opening the door to new sensor-based robot applications—the reflexxes motion libraries. In *Robotics and Automation (ICRA), 2011 IEEE International Conference on*, pages 1–4. IEEE, 2011.
- [KTW06] Torsten Kröger, Adam Tomiczek, and Friedrich M Wahl. Towards on-line trajectory computation. In *Intelligent Robots and Systems, 2006 IEEE/RSJ International Conference on*, pages 736–741. IEEE, 2006.
- [KW10] Torsten Kröger and Friedrich M Wahl. Online trajectory generation: Basic concepts for instantaneous reactions to unforeseen events. *Robotics, IEEE Transactions on*, 26(1):94–111, 2010.
- [Lee13] Bum-Joo Lee. Geometrical derivation of differential kinematics to calibrate model parameters of flexible manipulator. *International Journal of Advanced Robotic Systems*, 10, 2013.
- [LMF⁺01] Barry Lennox, Gary A Montague, Andy M Frith, Chris Gent, and Vic Bevan. Industrial application of neural networks—an investigation. *Journal of Process Control*, 11(5):497–507, 2001.
- [Lu08] Yu-Sheng Lu. Smooth speed control of motor drives with asymptotic disturbance compensation. *Control Engineering Practice*, 16(5):597–608, 2008.
- [LWL13] Dana Lowell, Haifeng Wang, and Nic Lutsey. Assessment of the fuel cycle impact of liquefied natural gas as sued in international shipping. Technical report, International council on clean transportation, 2013.
- [Mar14] Philip Christian Marmolejo. An economic analysis of floating liquefied natural gas (flng). B.s. thesis, MIT, 2014.
- [Mar15] Darwin Jayson Mariano. Is flng the answer to southeast asia’s rising energy demand? In *13th FLNG World Congress*, June 2015.
- [Mor78] Jorge J Moré. The levenberg-marquardt algorithm: implementation and theory. In *Numerical analysis*, pages 105–116. Springer, 1978.
- [MP43] Warren S McCulloch and Walter Pitts. A logical calculus of the ideas immanent in nervous activity. *The bulletin of mathematical biophysics*, 5(4):115–133, 1943.

BIBLIOGRAPHY

- [MRRS00] David Q Mayne, James B Rawlings, Christopher V Rao, and Pierre OM Scokaert. Constrained model predictive control: Stability and optimality. *Automatica*, 36(6):789–814, 2000.
- [MV06] George D Magoulas and Michael N Vrahatis. Adaptive algorithms for neural network supervised learning: a deterministic optimization approach. *International Journal of Bifurcation and Chaos*, 16(07):1929–1950, 2006.
- [NB13] Albert Nubiola and Ilian A Bonev. Absolute calibration of an abb irb 1600 robot using a laser tracker. *Robotics and Computer-Integrated Manufacturing*, 29(1):236–245, 2013.
- [NGM⁺15] M Neubauer, H Gatringer, A Mueller, A Steinhauser, and W Hoebarth. A two-stage calibration method for industrial robots with joint and drive flexibilities. *MECHANICAL SCIENCES*, 6(2):191–201, 2015.
- [NLW⁺09] Jia Ni, Shaojun Liu, Mingfeng Wang, Xiaozhou Hu, and Yu Dai. The simulation research on passive heave compensation system for deep sea mining. In *2009 International Conference on Mechatronics and Automation*, pages 5111–5116. IEEE, 2009.
- [NPK96] Bradley J Nelson, Nikolaos P Papanikolopoulos, and Pradeep K Khosla. Robotic visual servoing and robotic assembly tasks. *Robotics & Automation Magazine, IEEE*, 3(2):23–31, 1996.
- [NZK15] Hoai-Nhan Nguyen, Jian Zhou, and Hee-Jun Kang. A calibration method for enhancing robot accuracy through integration of an extended kalman filter algorithm and an artificial neural network. *Neurocomputing*, 151:996–1005, 2015.
- [OBGD10] Adel Olabi, Richard Béarée, Olivier Gibaru, and Mohamed Damak. Feedrate planning for machining with industrial six-axis robots. *Control Engineering Practice*, 18(5):471–482, 2010.
- [ODB⁺12] Adel Olabi, Mohamed Damak, Richard Bearee, Olivier Gibaru, and Stephane Leleu. Improving the accuracy of industrial robots by off-line compensation of joints errors. In *Industrial Technology (ICIT), 2012 IEEE International Conference on*, pages 492–497. IEEE, 2012.

BIBLIOGRAPHY

- [QB03] S Joe Qin and Thomas A Badgwell. A survey of industrial model predictive control technology. *Control engineering practice*, 11(7):733–764, 2003.
- [RRTP78] Jacques Richalet, A Rault, JL Testud, and J Papon. Model predictive heuristic control: Applications to industrial processes. *Automatica*, 14(5):413–428, 1978.
- [SGMP12] Marco Sabatini, Paolo Gasbarri, Riccardo Monti, and Giovanni Battista Palmerini. Vibration control of a flexible space manipulator during on orbit operations. *Acta astronautica*, 73:109–121, 2012.
- [SK16] Bruno Siciliano and Oussama Khatib. *Springer handbook of robotics*. Springer, 2016.
- [SYJA09] Jorge Santolaria, José-Antonio Yagiüe, Roberto Jiménez, and Juan-José Aguilar. Calibration-based thermal error model for articulated arm coordinate measuring machines. *Precision Engineering*, 33(4):476–485, 2009.
- [VM05] A Vivas and V Mosquera. Predictive functional control of a puma robot. In *ACSE 05 Conference, 19-21 December 2005, CICC, Cairo, Egypt, 2005*.
- [WKP⁺12] Yier Wu, Alexandr Klimchik, Anatol Pashkevich, Stéphane Caro, and Benoît Furet. Optimality criteria for measurement poses selection in calibration of robot stiffness parameters. In *ASME 2012 11th Biennial Conference on Engineering Systems Design and Analysis*, pages 185–194. American Society of Mechanical Engineers, 2012.
- [WTM12] TT Wong, Collin HH Tang, and M Mailah. Winch driven active heave compensation for load transfer in overhead crane system. In *Intelligent and Advanced Systems (ICIAS), 2012 4th International Conference on*, volume 1, pages 34–39. IEEE, 2012.
- [YPGU08] Xilin Yang, Hemanshu Pota, Matt Garratt, and Valery Ugrinovskii. Ship motion prediction for maritime flight operations. In *Proc. World Congress IFAC, 2008*.
- [ZN42] John G Ziegler and Nathaniel B Nichols. Optimum settings for automatic controllers. *trans. ASME*, 64(11), 1942.

BIBLIOGRAPHY

- [ZWR94] Hanqi Zhuang, Kuanchih Wang, and Zvi S Roth. Optimal selection of measurement configurations for robot calibration using simulated annealing. In *Robotics and Automation, 1994. Proceedings., 1994 IEEE International Conference on*, pages 393–398. IEEE, 1994.

Appendix A

Inverse kinematics of a marine loading arm

The configuration of a serial manipulator is fully described by its configuration (joints positions) \mathbf{q} . The forward kinematics function calculates the pose of the end-effector of the robot in the Cartesian space according to its configuration. The forward kinematics function is presented in Section 2.2, with Equation 2.3 which can be rewritten, for a loading arm, as:

$${}^0P_c = \mathbf{FK}(\mathbf{q}) \quad (\text{A.1})$$

The inverse kinematics function \mathbf{IK} on the other hand, gives the adequate configuration \mathbf{q} to reach the desired coupler pose 0P_c . Such a configuration depends of the orientation ${}^r\mathbf{q}_0$ of the FLNG, because of the Style 80 which acts as a pendulum. The function \mathbf{IK} can be written as:

$$\mathbf{q} = \mathbf{IK}({}^0P_c, {}^r\mathbf{q}_0) \quad (\text{A.2})$$

While the forward kinematics function is straightforward to establish in the general case, the inverse kinematics may be more challenging to derive. Indeed the geometry of some serial mechanisms is such that there is no closed-form expression of the inverse kinematics function [Bus04]. However in the case of loading arms a closed-form solution is found, under the assumption that the Style 80 is steady under the effect of gravity, and that its center of mass is aligned with \mathbf{y}_4 , i.e. :

$$\mathbf{y}_5 \cdot \mathbf{z}_e = 0 \Leftrightarrow \theta = 0, \quad (\text{A.3})$$

where θ is the measure of the inclinometer of the Style 80, as shown on Figure 2.14. The steadiness of the Style 80 is already considered as true for the connection operation. The alignment of its center of gravity with \mathbf{y}_4 is true for small

APPENDIX A. INVERSE KINEMATICS OF A MARINE LOADING ARM

values of q_4 , according to the nominal specifications from the manufacturer. If inexact, this alignment is corrected anyway by the calibration process presented in Chapter 2. Equation A.3 makes it possible solve the inverse kinematics problem with closed-form expressions, if the orientation ${}^r q_0$ of the FLNG is known.

The forward and inverse kinematic functions rely on a geometric model of the arm which is parametrized according the classic modified Denavit-Hartenberg (DH) convention [KD04]. Figure A.1 shows that geometric model.

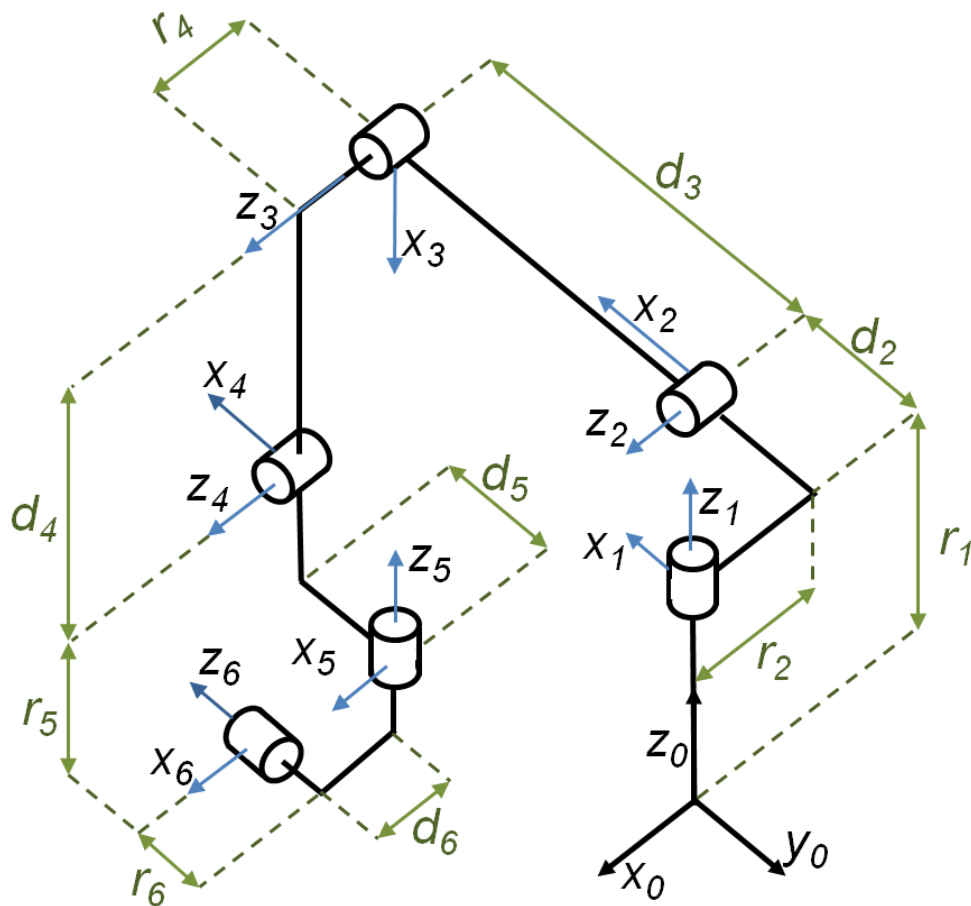


Figure A.1: MLA in zero position: Modified DH model.

with the parameters defined as proposed by Kahlil *et al.* [KD04]:

- axis z_j is along the axis of joint j ,
- axis x_j is along the common perpendicular with axes z_j and z_{j+1} . If the latter axes are parallel, a choice as to be made,

APPENDIX A. INVERSE KINEMATICS OF A MARINE LOADING ARM

- α_j : angle between axes \mathbf{z}_{j-1} and \mathbf{z}_j corresponding to a rotation about \mathbf{x}_{j-1} ,
- d_j : distance between \mathbf{z}_{j-1} and \mathbf{z}_j along \mathbf{x}_{j-1} ,
- q_j : angle between axes \mathbf{x}_{j-1} and \mathbf{x}_j corresponding to a rotation about \mathbf{z}_j ,
- r_j : distance between \mathbf{x}_{j-1} and \mathbf{x}_j along \mathbf{z}_j ,

This structured definition of the parameters makes it possible to define the transformation matrix of frame R_j in the frame R_{j-1} as:

$${}^{j-1}\mathbf{T}_j(q_j) = \begin{bmatrix} \cos(q_j) & -\sin(q_j) & 0 & d_j \\ \cos(\alpha_j)\sin(q_j) & \cos(\alpha_j)\cos(q_j) & -\sin(\alpha_j) & -r_j\sin(\alpha_j) \\ \sin(\alpha_j)\sin(q_j) & \sin(\alpha_j)\cos(q_j) & \cos(\alpha_j) & r_j\cos(\alpha_j) \\ 0 & 0 & 0 & 1 \end{bmatrix}. \quad (\text{A.4})$$

Hence the forward kinematic function of a loading arm is given by:

$${}^0\mathbf{T}_6(\mathbf{q}) = {}^0\mathbf{T}_1(q_1) \times \cdots \times {}^5\mathbf{T}_6(q_6). \quad (\text{A.5})$$

In this whole study the the sixth joint of loading arm is ignored because is does not change the geometry of the arm, as precised in Section 1.2.

The inverse kinematic function of a loading arm relies on the following relations and the hypothesis (A.3). It can be derived as a geometry problem, as detailed bellow. The target coupler vector \mathbf{z}_6 is constraint as by the orientation manifold, plus (A.3). Hence

$$\mathbf{z}_6 = -{}^0R_c({}^0\mathbf{q}_c) \cdot \mathbf{y}_0 - ({}^0R_c({}^0\mathbf{q}_c) \cdot \mathbf{y}_0 \cdot \mathbf{z}_r) \cdot \mathbf{z}_r. \quad (\text{A.6})$$

Let us note :

- $\cos(q_i) = c_i$ and $\sin(q_i) = s_i, \forall i$,
- $c_\psi = \|\mathbf{z}_6 \wedge \mathbf{z}_0\|$,
- $s_\psi = -\mathbf{z}_6 \cdot \mathbf{z}_0$.

q_1 is derived as:

$$q_1 = \arctan 2 \left(-\frac{\mathbf{x}_r \cdot {}^0\mathbf{X}_c - r_6 \cdot \mathbf{z}_6 \cdot \mathbf{x}_0 + d_6 \cdot \mathbf{z}_6 \cdot \mathbf{y}_0}{\mathbf{y}_r \cdot {}^0\mathbf{X}_c + c_\psi \cdot r_6 \cdot \mathbf{z}_6 \cdot \mathbf{y}_0 - c_\psi \cdot d_6 \cdot \mathbf{z}_6 \cdot \mathbf{x}_0} \right) - \arcsin \left(\frac{r_2 + r_3}{\sqrt{(\mathbf{x}_r \cdot {}^0\mathbf{X}_c + r_6 \cdot \mathbf{z}_6 \cdot \mathbf{x}_0 + d_6 \cdot \mathbf{z}_6 \cdot \mathbf{y}_0)^2 + (\mathbf{y}_r \cdot {}^0\mathbf{X}_c + c_\psi \cdot r_6 \cdot \mathbf{z}_6 \cdot \mathbf{y}_0 - c_\psi \cdot d_6 \cdot \mathbf{z}_6 \cdot \mathbf{x}_0)^2}} \right) \quad (\text{A.7})$$

Let us then note:

APPENDIX A. INVERSE KINEMATICS OF A MARINE LOADING ARM

- $X_b = \mathbf{x}_r \cdot {}^0\mathbf{X}_c + r_6 \cdot \mathbf{z}_6 \cdot \mathbf{x}_0 + d_6 \cdot \mathbf{z}_6 \cdot \mathbf{y}_0 - (c_1 \cdot r_3 - s_1 \cdot c_\psi \cdot d_5 - s_\psi \cdot s_1 \cdot r_5 + c_1 \cdot r_2 - s_1 \cdot d_2)$,
- $Y_b = \mathbf{y}_r \cdot {}^0\mathbf{X}_c + c_\psi \cdot r_6 \cdot \mathbf{z}_6 \cdot \mathbf{y}_0 - c_\psi \cdot d_6 \cdot \mathbf{z}_6 \cdot \mathbf{x}_0 - (s_1 \cdot r_3 + c_1 \cdot c_\psi \cdot d_5 + c_1 \cdot s_\psi \cdot r_5 + s_1 \cdot r_2 + c_1 \cdot d_2)$,
- $Z_b = \mathbf{z}_r \cdot {}^0\mathbf{X}_c - s_\psi \cdot r_6 \cdot \mathbf{z}_6 \cdot \mathbf{y}_0 + s_\psi \cdot d_6 \cdot \mathbf{z}_6 \cdot \mathbf{x}_0 - (s_\psi \cdot d_5 + c_\psi \cdot r_5 + r_1)$.

Finally the other joints angles are calculated as:

$$\sin(q_3) = \frac{d_3^2 + d_4^2 - (X_b^2 + Y_b^2 + Z_b^2)}{2 \cdot d_3 \cdot d_4}, \quad (\text{A.8})$$

$$\cos(q_3) = \sqrt{1 - s_3^2}, \quad (\text{A.9})$$

$$q_3 = \arctan\left(\frac{s_3}{c_3}\right), \quad (\text{A.10})$$

$$q_2 = \arctan\left(\frac{d_4 \cdot c_3}{d_4 \cdot s_3 - d_3}\right) - \arctan\left(-\frac{Z_b}{(Y_b \cdot c_\psi + X_b \cdot s_\psi)}\right), \quad (\text{A.11})$$

$$q_4 = \arctan\left(\frac{s_\psi}{c_\psi}\right) - q_2 - q_3, \quad (\text{A.12})$$

$$q_5 = \arctan\left(-\frac{\mathbf{z}_6 \cdot \mathbf{x}_0}{\mathbf{z}_6 \cdot \mathbf{y}_0}\right) - q_1. \quad (\text{A.13})$$

Appendix B

Résumé en Français

Cette annexe propose une synthèse, rédigée en langue française, du mémoire de thèse. Dans un souci de concision, seule la méthodologie et les principaux résultats sont présentés ici.

Cette thèse a pour objectif la robotisation de bras de chargement de gaz naturel liquéfié (GNL), de sorte que ceux-ci puissent fonctionner automatiquement, avec des performances accrues. Les bras de chargement de gaz sont des structures articulées dans lesquelles du méthane peut s'écouler à température cryogénique. En haute mer, ces bras sont installés sur le pont de navires-usines (FLNG) et se connectent à des méthaniers pour leur transférer du gaz. En raison de problèmes de sécurité et de performances, il est souhaité que ces bras de chargement soient robotisés pour qu'ils se connectent automatiquement. Cette thèse, en partenariat entre le laboratoire LSIS et la société FMC Technologies, a pour objectif la conception et l'implémentation d'un système de connexion automatique pour les bras de chargement.

L'opération de connexion nécessite un pilotage de grande précision, relativement aux dimensions d'un bras de chargement. En effet le système terminal de bridage du bras a une tolérance de positionnement de 10 cm, pour un bras mesurant plus de 15 m. Pour cette raison le bras est d'abord étalonné pour augmenter sa précision statique. Ensuite, des analyses modales expérimentales mettent en évidence l'importante souplesse de la structure des bras de chargement. Par conséquent un générateur de trajectoires « douces », à jerk limité, est développé afin de piloter le bras sans le faire vibrer. Enfin, un système de compensation actif visant à compenser les mouvements relatifs des deux navires est mis en place. Cette compensation combine la génération de trajectoires douces avec une composante prédictive basée sur des réseaux de neurones. Cette dernière permet de prédire et d'anticiper les mouvements des navires sur l'océan, afin d'annuler tout retard dans

la compensation. Finalement, cette thèse présente la première connexion automatique d'un bras de chargement, et démontre la validité de cette approche.

Ce résumé est organisé de la manière suivante. La première section présente les bras de chargement et les objectifs du projet. Ensuite, la méthodologie d'étalonnage employée dans ce projet est présentée dans la deuxième section, puis appliquée sur des bras de chargement. Une étude expérimentale des systèmes étudiés menée dans la troisième section précède le développement d'un générateur de trajectoires en section 4. Enfin la cinquième section détaille le développement d'une méthode de compensation active et prédictive des mouvements des navires.

B.1 Présentation des bras de chargement et de la connexion automatique

Les bras de chargement sont des structures articulées supportant une canalisation également articulée. Cette dernière est appelée « ligne produit », et permet au GNL de s'écouler. Les bras de chargement sont actionnés par des vérins hydrauliques, et maintenus au repos par un système de contrepoids. En bout du bras se trouve le « Style 80 », libre d'osciller autour de son axe, tel un pendule. Ce Style 80 est équipé d'un système de bridage hydraulique conçu pour se connecter au manifold d'un méthanier client, ce dernier se trouvant dans la zone de connexion. La figure B.1 montre les différents composants d'un bras de chargement.

Afin de réaliser la connexion du bras au méthanier, un système d'assistance constitué d'un câble, de treuils et de cônes de mise en position est utilisé. La figure B.2 présente le système de connexion.

Ce système de connexion n'est cependant pas satisfaisant, pour les raisons suivantes :

- ce système est coûteux relativement au prix global du bras,
- ce système pose des problèmes de sécurité, car son dysfonctionnement peut entraîner un risque d'arrachement du manifold.
- ce système nécessite le transfert et l'installation d'éléments mécaniques du FLNG vers le méthanier. Un tel transfert d'équipage et d'équipements pose des problèmes de législation.

Ce projet étudie la possibilité d'automatiser l'opération de connexion afin de s'affranchir du système de connexion existant. La figure B.3 introduit les principales notations des repères utilisés dans cette étude.

APPENDIX B. RÉSUMÉ EN FRANÇAIS

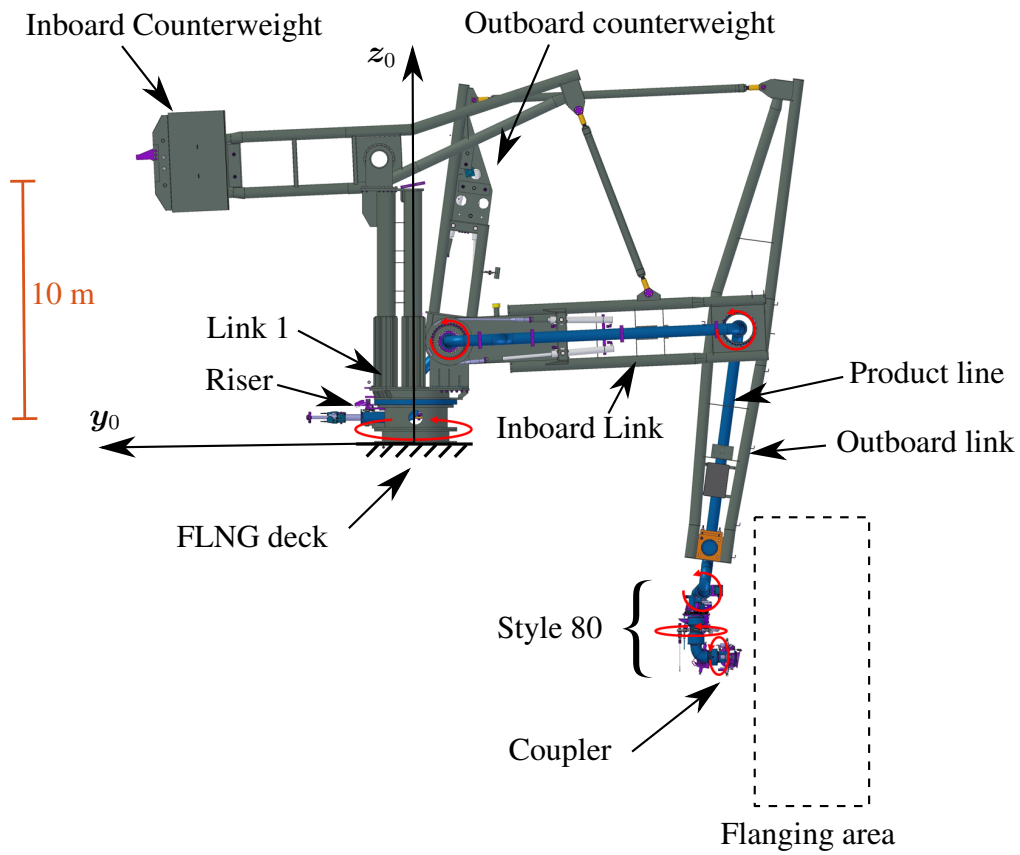


FIGURE B.1 : Un bras de chargement de type OLAF (Offshore Loading Arm Footless).

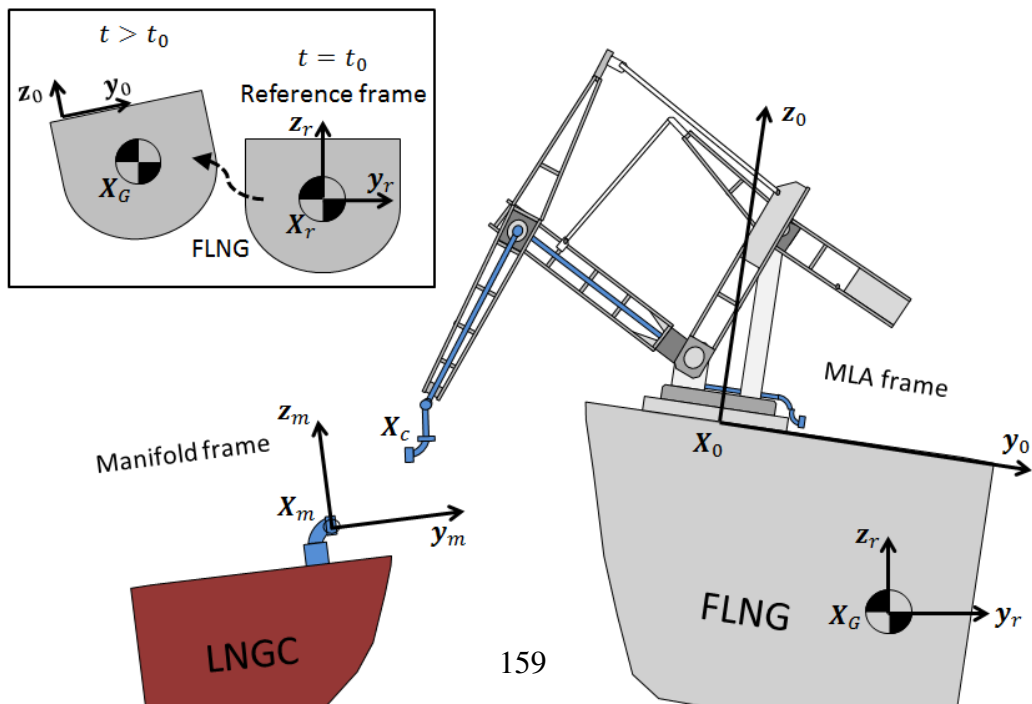


FIGURE B.3 : Principales notations de repères.

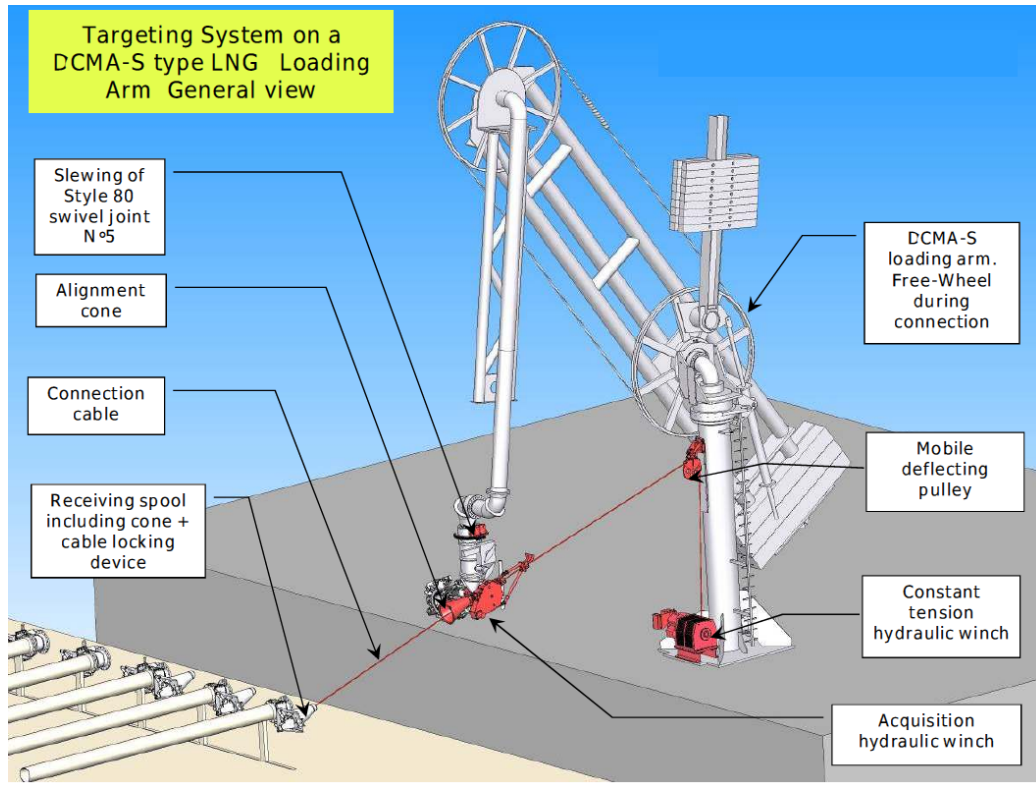


FIGURE B.2 : Le système de connexion actuel est basé sur un câble tendu entre les deux navires. [Credit : FMC Technologies].

Avec en particulier :

- les positions (3×1) sont notées \mathbf{X} ,
- les orientations (3×1) sont notées \mathbf{q} ,
- les poses (6×1) sont notées $\mathbf{P} : \mathbf{P} = \begin{bmatrix} \mathbf{X} \\ \mathbf{q} \end{bmatrix}$,
- ${}^f \mathbf{v}$ représente le vecteur \mathbf{v} dans le repère f .

Les principaux repères utilisés dans cette étude sont définis ci-dessous :

- Un repère de référence R_r est construit selon $(\mathbf{X}_r, \mathbf{x}_r, \mathbf{y}_r, \mathbf{z}_r)$, avec \mathbf{X}_r le centre de gravité du FLNG à l'instant initial t_0 , \mathbf{x}_r l'axe longitudinale du FLNG à t_0 projeté sur le plan horizontal, et \mathbf{z}_r l'axe vertical. Ce repère est supposé galiléen.

APPENDIX B. RÉSUMÉ EN FRANÇAIS

- Le repère du bras R_0 , avec z_0 l'axe de sa première articulation, orthogonal au pont du FLNG.
- Le repère du manifold R_m ayant pour origine X_m le centre du manifold. Sont orientation est notée q_m .
- Le centre du coupler est noté X_c et le centre de gravité du FLNG est noté X_G .

Un procédure de connexion automatique est établie comme cahier des charges du projet. Cette procédure comprends trois étapes :

- le déploiement du bras, qui sort de sa configuration de stockage pour placer le coupler en face du manifold,
- la phase de suivi, durant laquelle le coupler suit le manifold, c'est à dire compense les mouvements relatifs des navires sur l'océan, à une distance d_p , comme illustré par la figure B.4,
- la connexion, où le coupler avance vers le manifold et se connecte.

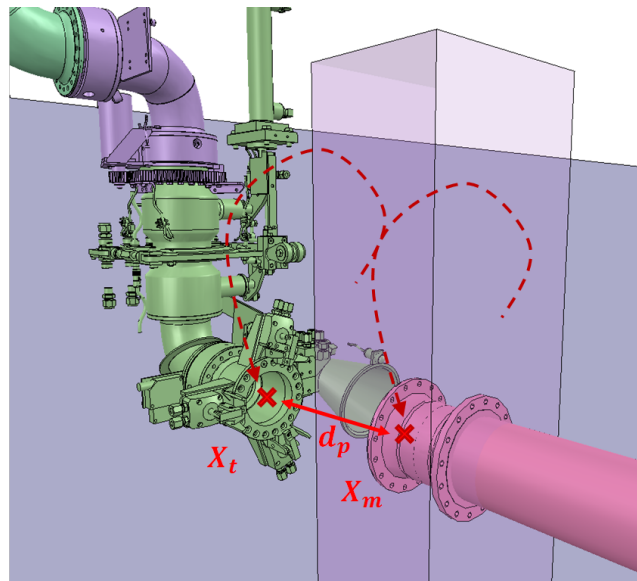


FIGURE B.4 : Phase de suivi : le coupler (vert) suit le manifold (rose) à une distance d_p .

La mise en place de cette connexion automatique est soumise à certaines contraintes. D'abord, la structure mécanique du bras ne doit pas être modifiée. Ensuite, la solution choisie doit minimiser les équipements nécessaires sur le méthanier client. Enfin, tout matériel utilisé doit être certifié ATEX (atmosphère explosive).

APPENDIX B. RÉSUMÉ EN FRANÇAIS

Le développement d'une telle connexion automatique présente des obstacles techniques :

- la tolérance du coupler est seulement de 10 cm, pour un bras de plus de 15 mètres,
- le système doit fonctionner dans des conditions de haute mer, sous le vent et les mouvements des navires,
- les bras de chargement ne sont pas conçus comme des robots, leurs structures sont flexibles et présentent des non-linéarités telles que des frottements secs et des jeux.

Ce projet combine les études théoriques et expérimentales. Pour ces dernières, une maquette de bras de chargement à l'échelle 1/4 est disponible. Cette maquette est installée sur un hexapode à 6 degrés de liberté (DDL), capable de reproduire les mouvements du FLNG. Un second hexapode supportant un manifold à l'échelle 1/4 est installé devant la maquette, pour servir de cible à celle-ci. La figure B.5 montre ces éléments. Un bras de chargement à l'échelle 1 de type DCMA (double counterweight marine arm), présenté par la figure B.6, est disponible à la fin de ce projet pour valider la méthode développée durant ce projet.



FIGURE B.5 : Maquette OLAF connectée au manifold.



FIGURE B.6 : Un bras échelle 1 est disponible pour les essais finaux.

En raison de la grande précision nécessaire pour la connexion d'un bras, une procédure d'étalonnage est mise en place.

B.2 Positionnement précis d'un bras de chargement

La très faible tolérance du coupler devant les dimension du bras pause la question de la répétabilité et de la précision de ce dernier. Dans cette partie de l'étude, la répétabilité des bras à disposition est mesurée, puis ces dernier sont calibrés. Bien que les bras soient peu rigides, aucun effet non-géométrique n'est pris en compte dans cet étalonnage. En effets, la zone de connexion dans laquelle le bras doit être précis est petite devant le bras et les phénomènes non-géométriques sont supposés constants dans ce volume. Cette hypothèse est confirmée par l'étalonnage des

APPENDIX B. RÉSUMÉ EN FRANÇAIS

bras.

La répétabilité des bras dans la zone de connexion est mesurée selon la norme ISO 9283 [ISO98], à l'aide d'une station totale de topographie, comme montré sur la figure B.7. Il est surprenant de constater que le bras DCMA a une répétabilité de 9 mm tandis que celle de la maquette à l'échelle 1/4 est seulement de 27 mm.



FIGURE B.7 : La station total mesure la position du coupler. Photographie de la maquette OLAF.

Un étalonnage géométrique est mené selon de manière classique sur les bras de chargements. La précision du bras DCMA échelle 1 est améliorée de 421 mm à 25.5 mm et celle de la maquette OLAF de 40.1 mm à 27.1 mm. Cette étalonnage est basé sur un modèle géométrique de bras de chargement, paramétré selon la convention de Denavit-Hartenberg. La précision finale du bras DCMA représenté 25.5% de la tolérance de son coupler, et est donc suffisante pour rendre la connexion automatique possible.

B.3 Etude expérimentale d'un bras de chargement

Afin de préparer la synthèse des lois de commande des bras de chargement, le comportement du système d'actionnement et de la structure de ces derniers est étudié de manière expérimentale.

Dans un premier temps, une analyse modale est menée sur les deux spécimens disponibles. Les structures sont excitées par des mouvements (maquette) ou des efforts (bras échelle 1) en sinus glissant, et les réponses des structures en termes de vitesse selon x_0 (normal au plan de la structure) sont mesurées par un vibromètre laser. Les réponses fréquentielles des structures sont données par la figure B.8, et les déformées opérationnelles par la table B.1.

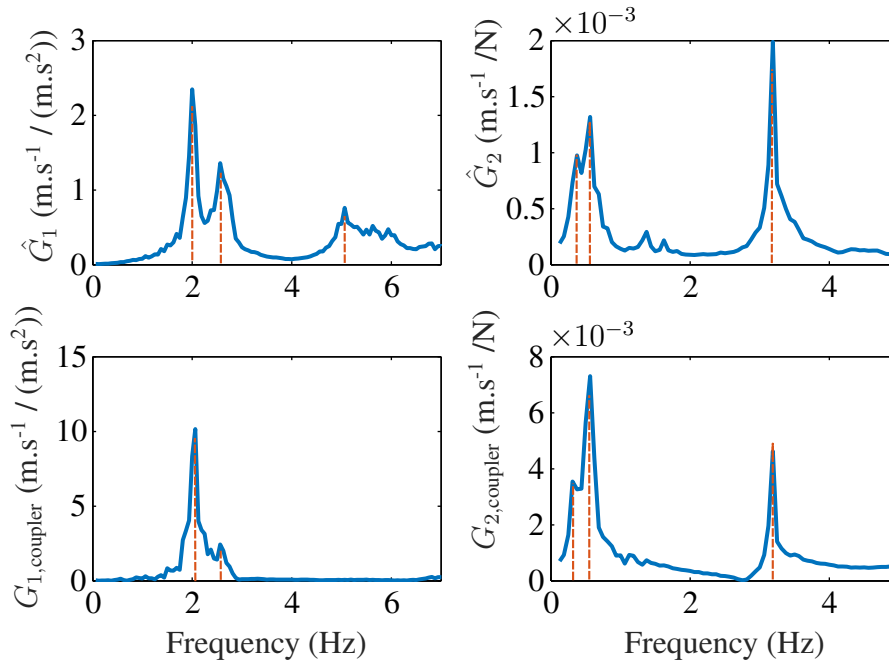


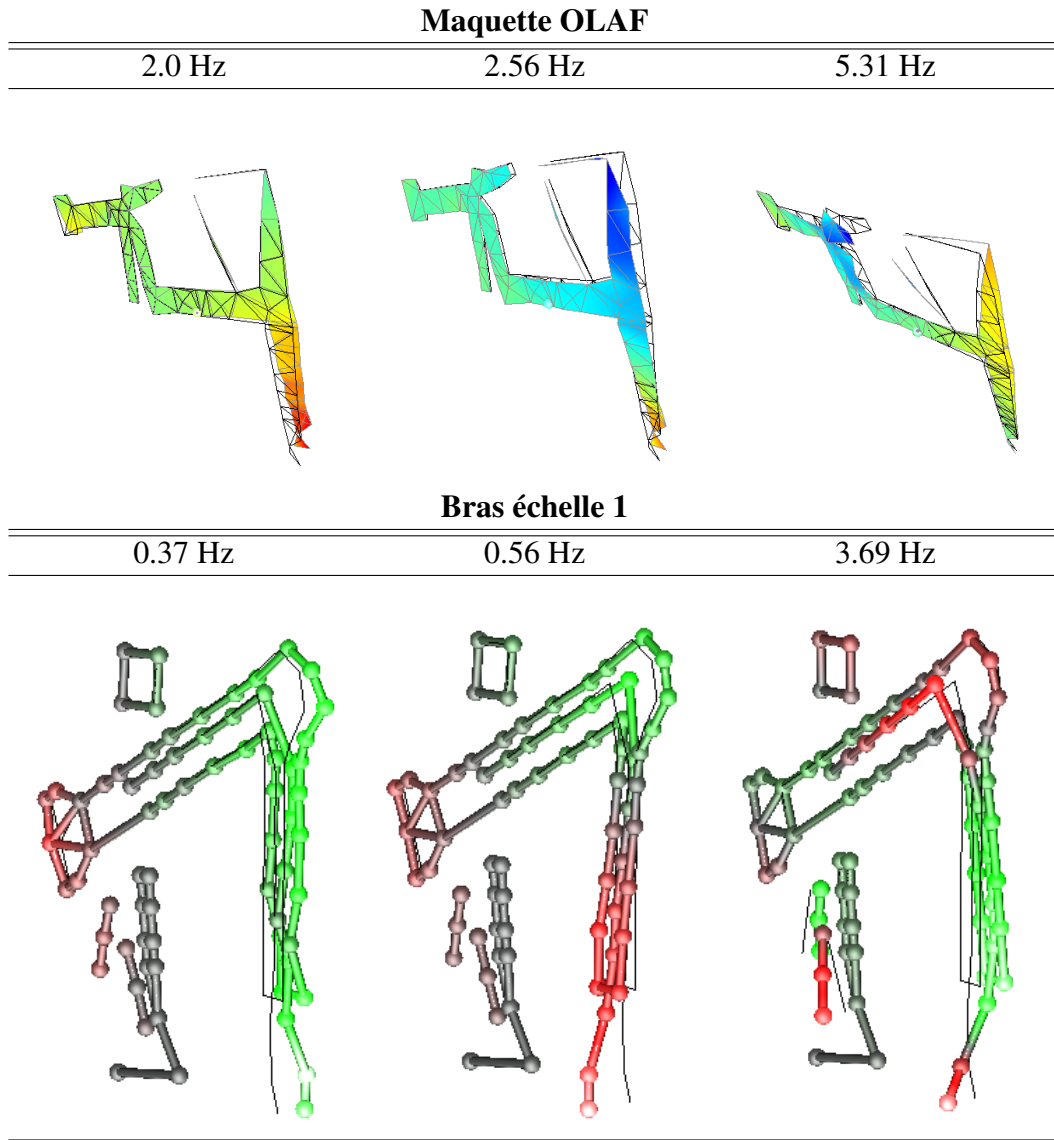
FIGURE B.8 : Réponses fréquentielles des bras selon x_0 , soumis à des excitations selon x_0 . Courbes de gauches : maquette, courbes de gauches : bras échelle 1. haut : moyennes spatiales, bas : réponses au niveau du coupler. Résolution fréquentielle = $6.25 \cdot 10^{-2}$ Hz.

Ensuite, les réponses fréquentielles des actionneurs des deux bras sont mesurées et comparées aux réponses des structure, comme le montre la figure B.9.

Les essais précédant montrent que la maquette et le bras échelle 1 ont des comportements différents : La structure de la maquette est rigide par rapport aux

APPENDIX B. RÉSUMÉ EN FRANÇAIS

TABLE B.1 : Premiers modes mesurés : fréquences et déformées opérationnelles



capacités des actionneurs. Ce n'est pas le cas de du bras échelle 1, dont la structure oscille facilement. Ces résultats, complétés par une observation visuelle des systèmes en question, montrent que :

- Les oscillations de la maquette engendrées par la commande viennent de flexibilités dans le circuit hydraulique, ainsi que dans les câbles de trans-

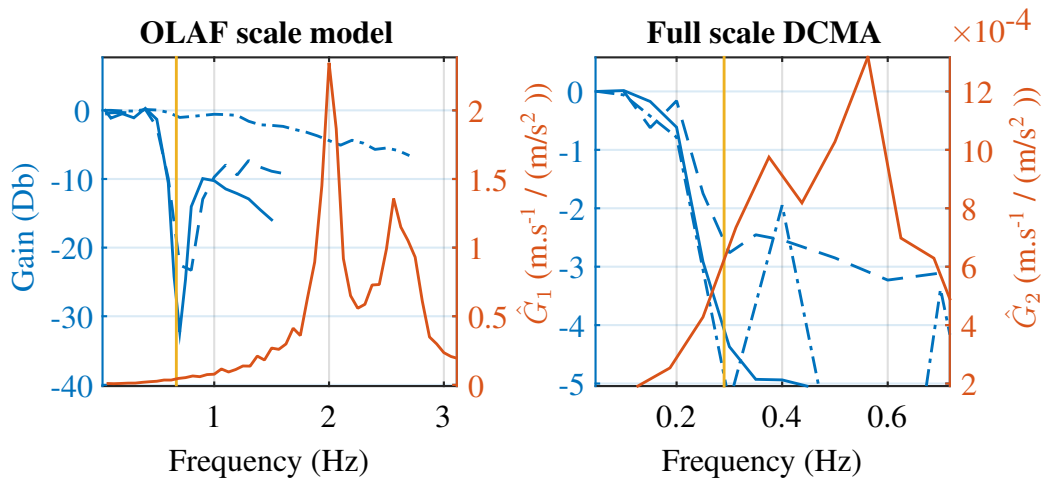


FIGURE B.9 : Les réponses fréquentielles des axes (lignes bleues, continue : axe 1, pointillée : axe 2, mixte : axe 3) sont comparée aux réponses fréquentielles moyennées des bras (lignes rouges). Les fréquences d’oscillation mesurées des Styles 80 sont représentées par les lignes oranges verticales.

mission. Seule une partie de ces oscillation est observable par les capteurs qui mesurent la position des tiges des vérins.

- Pour le bras échelle 1, aucune oscillation n’est visible par ces capteur.

Afin de ne pas exciter ces modes vibratoire via la commande, des trajectoires douces sont utilisées pour piloter les axes des bas. La partie B.4 traite de la génération de telles trajectoires.

L’influence des mouvements du FLNG supportant le bras de chargement est étudiée. Des simulations montrent que le contenu fréquentiel de ces mouvements est disjoint des réponses fréquentielles des structures des bras (voire figure 3.16). Par conséquent il est supposé que ces mouvements n’excitent pas la structure. Un modèle dynamique d’un bras, incluant les mouvements du FLNG, est construit, basé sur l’algorithme de Newton-Euler. Ce modèle est utilisé pour simuler des effets d’inerties sur la structure du bras, induit par les mouvements du FLNG. Il est calculé que ces effets sont significatifs en termes de couples articulaires, et qu’il est donc envisageable de les prendre en compte dans la planification de mouvements.

B.4 Génération de dynamique trajectoires

Afin de piloter les bras de chargement sans les faire osciller, des trajectoires « douces » sont utilisées. Plus précisément, les trajectoires à jerk limité sont populaire de le domaine de la robotique, car elle permettent de piloter des systèmes sans provoquer de vibrations, et sont moins agressives vis-à-vis du matériel. La littérature concernant la génération de trajectoires à jerk limité est riche, cependant une approche allant plus loin en termes de réduction des vibration est étudiée. Un générateur de trajectoires est développé, avec les contraintes suivantes :

- les trajectoires générées doivent respecter des limites de vitesse, accélération et jerk paramétrables,
- ces trajectoire doivent être optimales en temps,
- celles-ci doit accepter un état initial non nul (vitesse et accélération) pour pouvoir être générées dynamiquement,
- enfin la génération d’une trajectoire doit être rapide devant le temps de cycle d’un contrôleur, pour pouvoir être utilisée en temps réel.

La méthode employée ici est basée sur les propriétés des filtres à réponse impulsionnelle finie (RIF). La convolution d’un tel filtre avec un profil d’accélération à accélération limitée (créneaux) produit un profil à jerk limité (trapèzes), comme le montre la figure B.10.

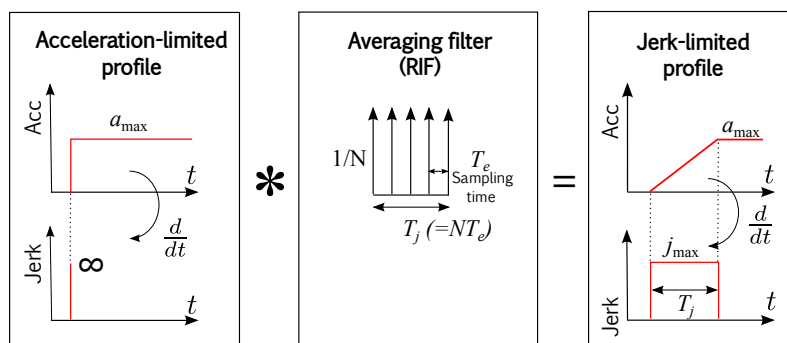


FIGURE B.10 : Des filtre RIF sont utilisés pour la synthèse de trajectoires à jerk limité.

Le générateur est construit selon l’architecture présentée par la figure B.11. Lorsqu’une nouvelle référence est envoyée au générateur, un profil à accélération limitée est d’abord généré. Ensuite, ce profil est adapté selon l’état actuel du système (c’est à dire l’état initial de la nouvelle trajectoire) et selon les limites

cinématiques. Ce profil est enfin filtré pour créer la nouvelle trajectoire.

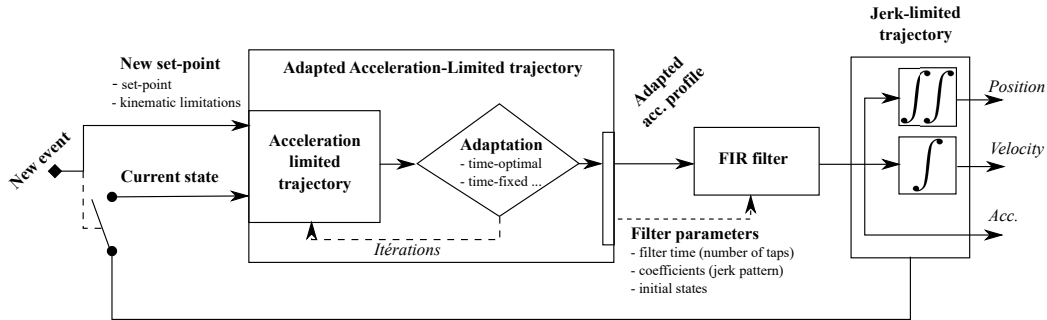


FIGURE B.11 : Architecture du générateur de trajectoires.

Les trajectoires à accélération limitée sont simples et rapides à générer de même que les filtre RIF sont faciles à implémenter et rapide d'exécution. Ainsi cette approche mène à une solution facilement implantable dans des systèmes industriels, et peu couteux en temps de calcul. La figure B.12 présente une trajectoire à accélération limitée classique. Ce profile, généré en premier lieu, est ensuite filtré par un filtre à moyenne glissante pour produire un profile à accélération limitée, comme présenté par la figure B.13.

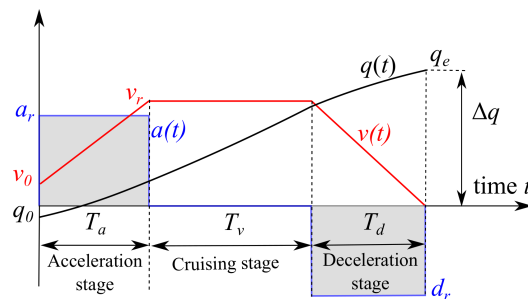


FIGURE B.12 : Un profile à accélération limitée. a_r , d_r and v_r sont les limites atteintes en termes d'accélération, de décélération et de vitesse.

Pour permettre la gestion d'états initiaux quelconques, il est nécessaire d'adapter spécialement le profile à accélération limitée initial. En effet, le filtrage d'une trajectoire ayant un état initial non nul produit naturellement une erreur sur l'état finale de la trajectoire résultante. Une telle adaptation. consiste à modifier l'état initial servant à générer la trajectoire à accélération initiale. La figure B.14 illustre cette adaptation.

Afin de générer des trajectoires optimales, le jerk doit être saturé à sa limite maximale. Pour ce faire, la durée du filtre est ajustée de manière dynamique. Plus

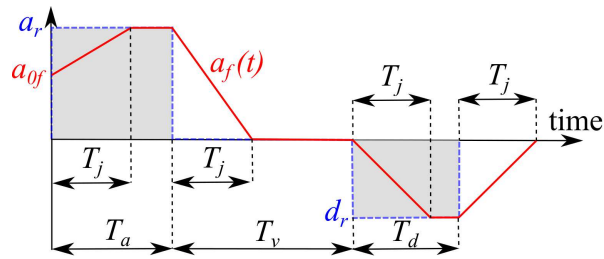


FIGURE B.13 : Le profile à accélération limitée initial (en bleu pointillé) est filtré pour produire un profile à jerk limité (ligne rouge).

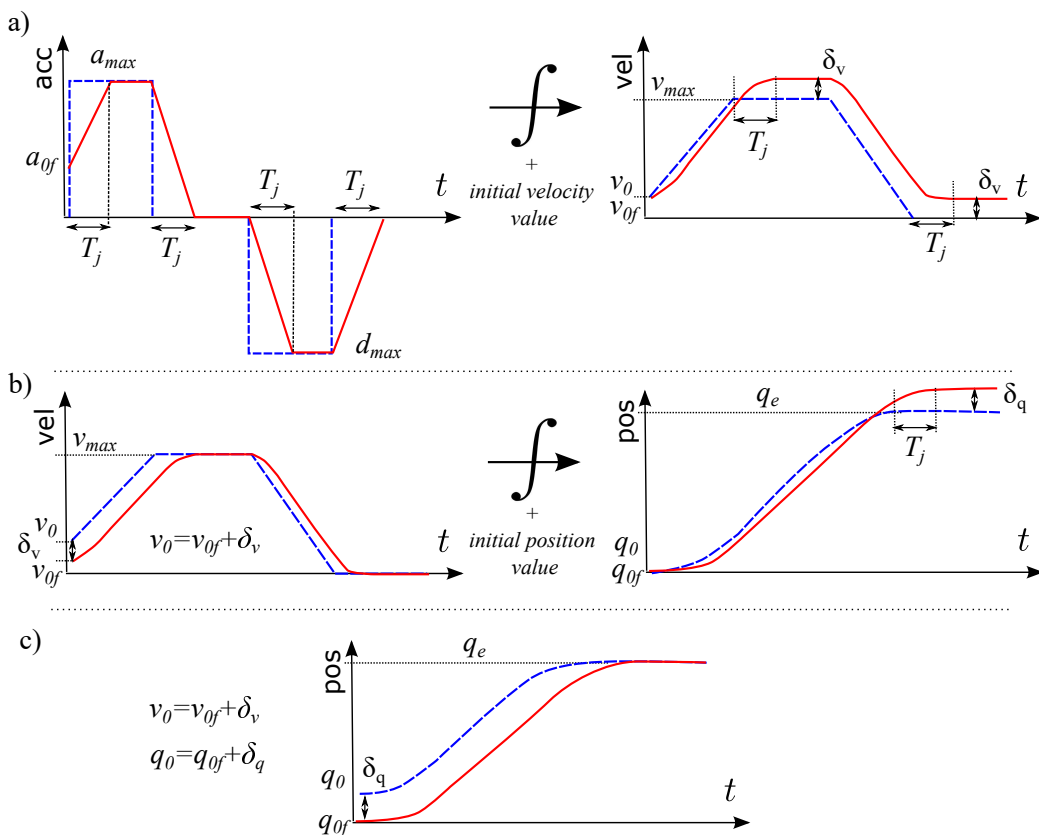


FIGURE B.14 : Adaptation des conditions initiales du profile à accélération limitée avant filtrage. a) Influence de l'accélération initiale sur la vitesse finale : Les vitesses maximales et finales présentent un dépassement de δ_v . b) Adaptation de la vitesse initiale v_0 du profile à accélération limitée : la position après filtrage présente un dépassement δ_q . c) Adaptation de la position initiale q_0 du profile à accélération limitée : la trajectoire finale remplit ses critères cinématiques.

précisément, le filtre prend successivement trois durées différentes (T_{ja} , T_{jv} , T_{jd}) qui correspondent respectivement au phase d'accélération, de vitesse constante et de décélération du profile initial. La figure B.15 présente une trajectoire à jerk limité optimale en temps générée de manière dynamique.

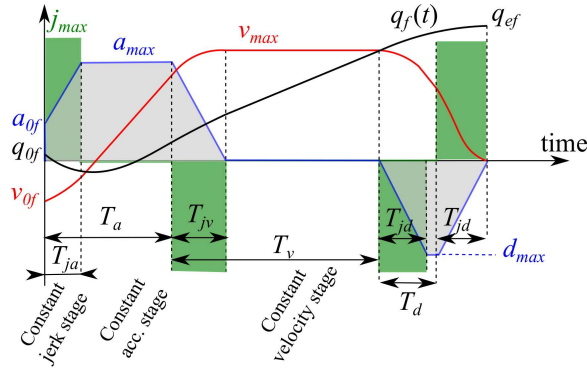


FIGURE B.15 : Time-optimal jerk-limited profile with non-zero initial conditions, each derivative saturates at its bound.

L'algorithme est également capable de générer des trajectoires à durée fixée, afin de synchroniser plusieurs trajectoires d'axes. De plus, il est possible d'ajuster les limites cinématiques de manière dynamique afin d'adoucir ou de ralentir le système en réponse à des événements extérieurs imprévus. Ce générateur de trajectoires a été implémenté en C++ avec un soin particulier à l'optimisation du code en termes de vitesse d'exécution. Les temps de génération mesurés sont inférieurs à $1 \mu s$ pour tout types de trajectoires. Ce temps de calcul court permet de gérer des systèmes à multiples degrés de liberté tout en gardant un temps de cycle bas.

B.5 Compensation active avec annulation du retard

B.5.1 Méthodologie

Les limites cinématiques qui contraignent les trajectoires articulaires entraînent un retard dans le suivi du manifold, et donc une erreur de position. Ces limites sont pourtant nécessaires pour s'assurer que les contrôleurs d'axes suivent leurs consignes, et qu'ils n'engendrent pas d'oscillations dans la structure. L'erreur due au retard du système peut être annulée en utilisant une méthode prédictive, qui permet d'anticiper les mouvements de la cible. Un algorithme de prédiction est donc développé pour prédire l'évolution de la pose du manifold ${}^0P_m(t)$.

APPENDIX B. RÉSUMÉ EN FRANÇAIS

Cette méthode de prédiction est basé sur un réseau de neurones artificiel avec une structure de perceptron multicouche, contenant une couche cachée de dix neurones ayant une fonction d'activation en tangente sigmoïde. Ce réseau utilise les mesures de pose passées (100 derniers échantillons) pour prédire les poses future. La figure B.16 montre la structure du réseau de neurones. La figure B.17 compare la méthode de prédiction lorsque les composantes du mouvement sont prédites séparément et lorsqu'elles sont prédite dans un même réseau. Dans ce dernier cas, le réseau de neurone est capable d'améliorer sa prédiction en s'appuyant sur des couplages physiques entre les dimensions.

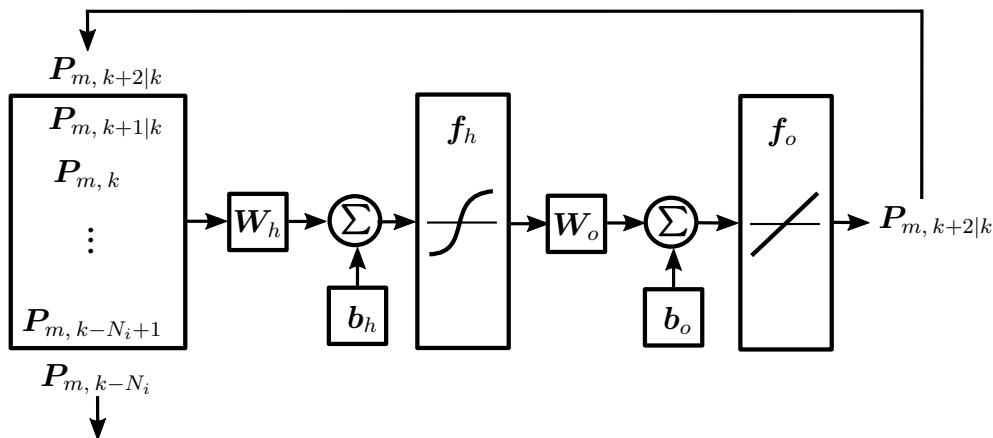


FIGURE B.16 : Un perceptron multicouche est utilisé pour prédire l'évolution du mouvement relatif des navires.

Le problème de suivit de cibles est, dans l'industrie, généralement résolu en utilisant des commandes prédictives. Ce type de contrôle optimal vise à minimiser l'erreur du système contrôlé sur une fenêtre de temps glissante, à l'aide d'un modèle de ce système. Pour les bras de chargement, cette manière de procédé ne semble pas adéquate. En effet les modèles des axes du bras doivent inclure leurs non-linéarités, plus les phénomènes vibratoires du bras, afin de ne pas exciter ces derniers. Par conséquent, le générateur de trajectoires à jerk-limité est maintenu en amont des axes, et la commande prédictive utilise un modèle de l'ensemble générateur plus axe. Les contraintes cinématiques de la planification de trajectoires étant réglées pour que les contrôleurs suivent leur référence sans erreur, la modélisation des axes est négligée. La figure B.18 montre l'architecture général d'une telle « planification prédictive », pour un axe.

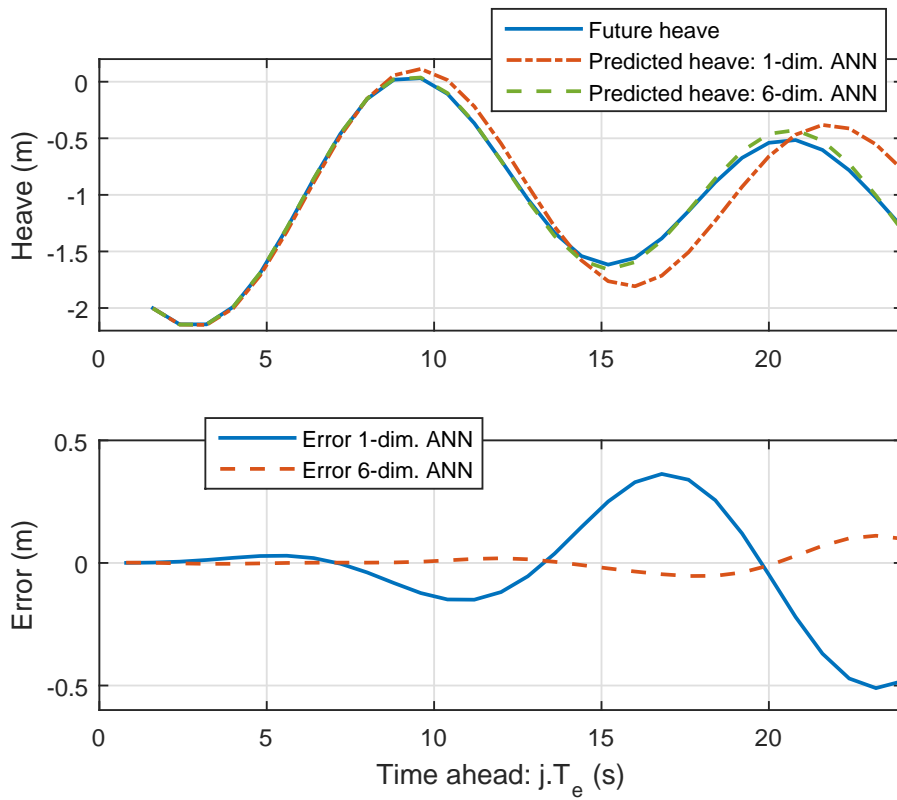


FIGURE B.17 : Comparatif de performances lorsque les dimensions sont prédites séparément ou ensemble.

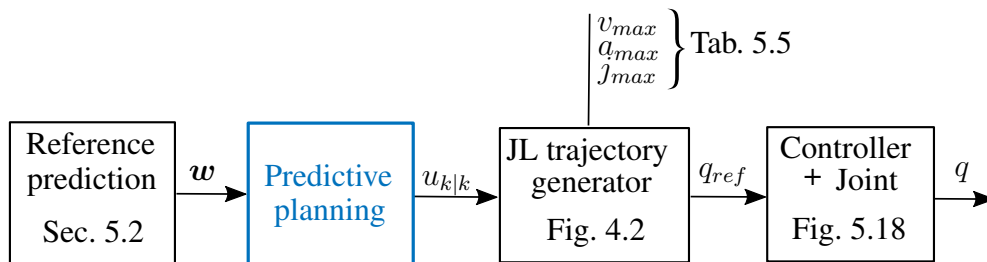


FIGURE B.18 : La planification prédictive pilote le générateur de trajectoires.

La planification prédictive optimise un vecteur de référence $u_{|k}$ de manière à minimiser la distance entre la sortie q et la trajectoire w sur un horizon futur de longueur H . Cette optimisation utilise l'algorithme de Levenberg-Marquardt avec le générateur de trajectoires développé dans la section précédente.

La future trajectoire w doit être prédite pour faire fonctionner la planifica-

tion prédictive. w est l'expression de l'évolution future de la pose relative entre le FLNG et le LNGC, dans l'espace articulaire. A chaque instant, déterminer w revient donc à déterminer la pose 0P_m sur l'horizon H futur, puis à utiliser le modèle géométrique inverse du bras pour l'exprimer dans l'espace articulaire. Cette méthodologie est validée en simulation, puis implémentée pour être validée de manière expérimentale.

B.5.2 Validation expérimentale

Des contrôleurs sont développés pour piloter les vérins. Ces contrôleurs, présentés par le schéma figure B.19, sont construits autour de correcteurs de type PID.

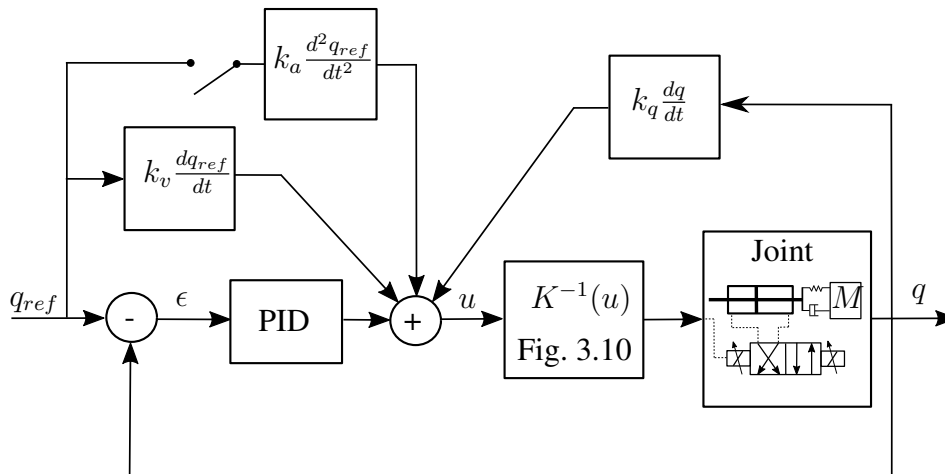


FIGURE B.19 : Schéma d'un contrôleur d'axes.

La méthodologie développée durant ce projet est implémentée sur un bras de chargement en vue d'une validation expérimentale, selon l'architecture présentée par la figure B.20. Compte tenu des dimensions du système des et puissances mises en jeu, un soin particulier est apporté à l'aspect sécurité. Notamment, des limiteurs des pressions soigneusement tarés sont installés en amont des vérins, et la partie logicielle est implémentée pour une gestion de toute exception.

Les résultats expérimentaux démontrent la validité de la méthodologie employée. En effet le bras de chargement se connecte avec succès au manifold cible, qui décrit un mouvement généré par des signaux sinusoïdaux. Cet essai constitue, à la connaissance de l'auteur, la première connexion automatique d'un bras de chargement offshore.

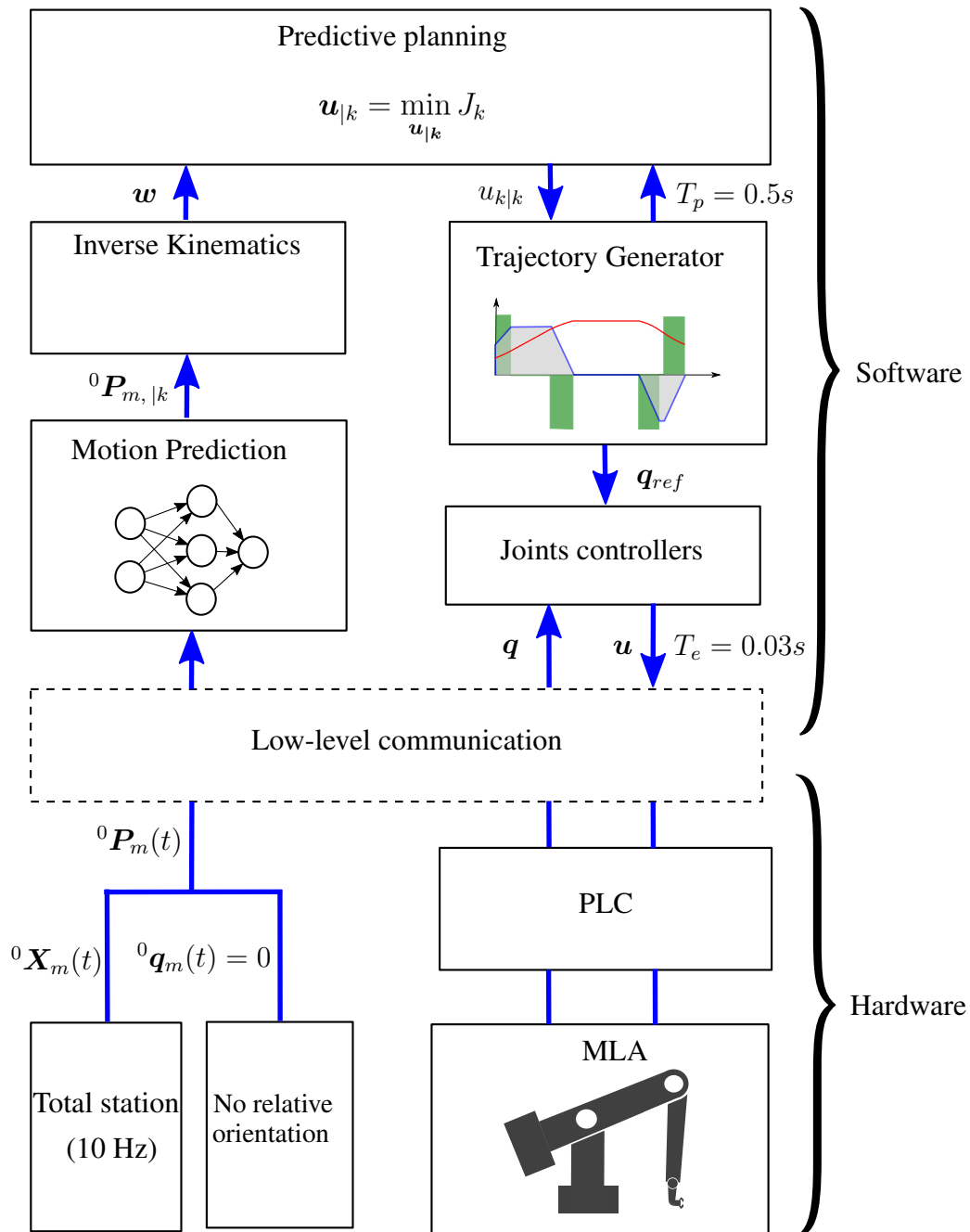


FIGURE B.20 : Architecture hiérarchique de la solution finale.

B.6 Conclusion

Les bras de chargement sont des systèmes dont la robotisation est un réel défi, principalement parce qu'ils n'ont pas été conçus dans cette optique. Il est ce-



FIGURE B.21 : Le bras de chargement est connecté avec succès au banc de test.

pendant choisi de robotiser les équipements existant plutôt que de concevoir et construire de nouveaux systèmes robotiques dédiés. Ce choix est motivé par des raisons économiques, mais également en vue d'appliquer le processus de robotisation à d'autres systèmes, comme par exemple des passerelles ou encore des pistes d'atterrissage. Les principales difficultés de ce projet résident dans la grande flexibilité de la structure du bras, ainsi que dans son système d'actionnement.

La solution finale résultante de ce projet est constituée de plusieurs composants technologiques, qui ont été développés spécialement pour ce projet. Plus précisément, après une étude expérimentale approfondie de bras de chargement, un étalonnage géométrique est mené sur la structure du système pour en améliorer la précision. Ensuite un générateur de trajectoires à jerk limité optimales en temps est développé pour adéquatement piloter le bras de chargement sans en exciter la structure. Ce générateur permet de générer des trajectoires de manière dynamique, et ne demande qu'un temps de calcul très bas afin de pouvoir être employé dans des applications en temps réel. Enfin un système de compensation active des mouvements des navire est développé. Ce système se base sur un algorithme de planification prédictive de trajectoires qui permet au bras de suivre le manifold sans retard, tout en conservant les bénéfices du générateur de trajectoires à jerk limité. La prédiction de l'évolution future du mouvement relatif des navires, nécessaire au fonctionnement de la planification prédictive, est assurée par un perceptron multichouche. Finalement, cette solution est implémentée et validée expérimentalement sur un bras de chargement de type DCMA.

COMMANDE D'UN BRAS DE CHARGEMENT DE GAZ NATUREL LIQUEFIE EN MILIEU MARIN

RESUME : Un bras de chargement de gaz est une structure articulée dans laquelle du méthane peut s'écouler à température cryogénique. En haute mer, ces bras sont installés sur le pont de navires-usines et se connectent à des méthaniers pour leur transférer du gaz. En raison de problèmes de sécurité et de performances, il est souhaité que le bras de chargement soit robotisé pour qu'il se connecte automatiquement. Cette thèse a pour objectif l'automatisation de la connexion. Cette opération nécessite un pilotage de grande précision vis à vis de la taille du bras. Pour cette raison le bras est d'abord étalonné pour augmenter sa précision statique. Ensuite, des analyses modales expérimentales mettent en évidence l'importante souplesse de la structure des bras de chargement. Pour cette raison un générateur de trajectoires « douces », à jerk limité, est développé afin de piloter le bras sans le faire vibrer. Enfin, un système de compensation actif visant à compenser les mouvements relatifs des deux navires est mis en place. Cette compensation combine la génération de trajectoires douces avec une composante prédictive basée sur des réseaux de neurones. Cette dernière permet de prédire et d'anticiper les mouvements des navires sur l'océan, afin d'annuler tout retard dans la compensation. Finalement, cette thèse présente la première connexion automatique d'un bras de chargement, et démontre la validité de cette approche.

Mots clés : Bras de chargement, gaz naturel liquéfié, génération de trajectoires, compensation active, commande prédictive, réseau de neurones, étalonnage de systèmes sériels.

AUTOMATIC CONTROL OF A MARINE LOADING ARM FOR OFFSHORE LNG OFFLOADING

ABSTRACT : Marine loading arms are articulated structures that transfer liquefied gas between two vessels. The flanging operation of the loading arm to the receiving tanker is very sensitive. This thesis aims to robotize a loading arm so it can flange automatically. The required accuracy for the connection is very high. A calibration procedure is thus proposed to increase the accuracy of loading arms. Moreover a jerk-limited trajectory generator is developed to smoothly drive the arm without inducing oscillation. This element is important because the structures of loading arms have a very low stiffness and easily oscillate, as highlighted by modal analyses. A predictive active compensation algorithm is developed to track without delay the relative motion between the two vessels. This algorithm relies on an artificial neural network able to predict the evolution of this relative motion. Finally this thesis presents the first automatic connection of an offshore loading arm. The success of the final tests validate the feasibility the automatic connection and the validity of this approach.

Keywords : Marine loading arm, liquefied natural gas, active motion compensation, trajectory generation, predictive control, artificial neural network, robot calibration.